# Real Time PCR Measurement by Fluorescence Anisotropy

by

Bryan Lee Crane

B.S., Mechanical and Aerospace Engineering
University of Missouri-Columbia, 1999

S.M. Mechanical Engineering,
Massachusetts Institute of Technology, 2001

Submitted to the Department of Mechanical Engineering
in Partial Fulfillment of the Requirements for the Degree of

DOCTOR OF PHILOSOPHY IN MECHANICAL ENGINEERING
at the
MASSACHUSETTS INSTITUTE OF TECHNOLOGY

FEBRUARY 2005





Signature of Author.....
Department of Mechanical Engineering
October 1, 2004

Certified by.....
Ian W. Hunter
Hatsopoulos Professor of Mechanical Engineering
Thesis Supervisor

Accepted by.....
Lallit Anand
Chairman, Department Committee on Graduate Students

# Real Time PCR Measurement by Fluorescence Anisotropy

by

Bryan Lee Crane

Submitted to the Department of Mechanical Engineering
on October 1, 2004 in Partial Fulfillment of the Requirements for the
Degree of Master of Science in Mechanical Engineering

## Abstract

Real-time polymerase chain reaction (PCR) is the gold-standard for quantitation in both mutation and gene expression analyses. Already this technique has found valuable clinical application in disease diagnosis and progression evaluation. As the number of known gene-disease correlations continues to rise, there will be increased demand for higher throughput and decreased cost for these analyses. Present real-time PCR measurement is based upon the fluorescent intensity of either intercalating dyes or oligonucleotide probes. Intercalating dye methods suffer from a lack of binding specificity, while probe methods are expensive and require increased assay optimization.

In this thesis, a new method is presented for monitoring real-time PCR that utilizes the fluorescent anisotropy (FA) of labeled primers. FA, when measured at constant temperature, is indicative of the molecular mass to which the fluorophore is attached. Specificity is improved with the FA method over the use of intercalating dyes since the selective binding of primers is required for signal change. Assay complexity and cost are reduced compared to fluorogenic probe methods since the probes are eliminated.

The design of a prototype instrument, which successfully implements this new method, is presented. Instrument and assay performance are compared to intercalating dye assays run in commercially available instrumentation. Theoretical limits on performance are also presented and compared to experimental results. Excellent repeatability and linearity are observed with respect to these benchmarks. This new method, having both high specificity and low optimization complexity, is expected to be particularly applicable to the demanding robustness requirements of nano-scale PCR.

Thesis Supervisor: Ian W. Hunter
Title: Hatsopoulos Professor of Mechanical Engineering

# Acknowledgements

I am grateful to many people for their support and encouragement over the course of this thesis work.

My advisor, Prof. Ian Hunter, has provided a rich environment for rapid learning and experimentation. I deeply admire his depth and breadth of knowledge as well as his fearlessness in diving into new frontiers of research.

All the many members of the BioInstrumentation Lab over the years, but especially Robert David, Cathy Hogan, and Andrew Taberner, have been of great help in solving the challenges of my thesis. In addition to his insights, I thank Robert for his patience with the burdens of my experiments (which sometimes included darkness and uncomfortable temperatures) in our little room of no windows.

I am grateful to Prof. Bill Thilly for the hours he spent with me explaining methods of investigating genetic correlations with disease. Heelo Sudo, of the Thilly Lab, played a key role in many of the early experiments both providing the testing material and running control experiments in parallel to my own.

Prof. Peter So and Prof. George Barbastathis both provided many helpful comments that steered the course of this work. I appreciate the time and insight they gave in serving on my thesis committee.

All my friends, especially Matthew Spenko, Ben Paxton, Steve Buerger, Patrick Anquetil, and Max Berniker, have contributed to making graduate school a great adventure. No matter how our careers may scatter us, I take with me many memories of good times at Kinnard, Pearl, and 529.

Colleen Murphy has also been a big part of my life for some time now. Her interest in and support of my academic pursuits are only a few of the many reasons I enjoy being with her so much.

Finally, I wish to thank my family for all of their support, encouragement, and love. Your examples of dedication, caring, and hard work always guide me no matter how far from home I may be.

# Contents

# List of Acronyms and Abbreviations

| | |
|---|---|
| A/D | Analog to Digital (converter) |
| CCD | Charge Coupled Device |
| CRI | Cambridge Research & Instrumentation, Inc. |
| CV | Coefficient of Variation |
| DMM | Digital Multimeter |
| DNA | Deoxynucleic Acid |
| EDM | Electro-discharge Machining |
| FA | Fluorescence Anisotropy |
| FEA | Finite Element Analysis |
| LED | Light Emitting Diode |
| MAMA | Mismatch Amplification Mutation Assay |
| mRNA | messenger Ribonucleic Acid |
| PCR | Polymerase Chain Reaction |
| PID | Proportional-Integral-Derivative |
| PMT | Photomultiplier Tube |
| RH | Relative Humidity |
| RMS | Root Mean Square |
| RTD | Resistance Temperature Detector |
| RT-PCR | Reverse Transcription PCR |
| SDA | Strand Displacement Amplification |
| SNP | Single Nucleotide Polymorphism |
| ssDNA | single stranded DNA |

## Chapter 1

# Introduction

A series of discoveries in the mid-1900's sparked a rapid advance in molecular biology and mankind's ability to understand biological processes. In 1941, Beadle and Tatum showed that a "gene" codes for a single protein* (Nobel Prize 1958) (Beadle and Tatum, 1941). Three years later, Avery elucidated the component of the cell that was acting as this "gene": its deoxyribonucleic acid (DNA) (Avery, MacLeod, and McCarty, 1979).

In 1953, Watson and Crick published their famous paper (Watson and Crick , 1953) describing the structure of the DNA molecule as a long sequence of paired nucleotides (Nobel Prize 1962). This structure implied the means by which genetic data was encoded and the means for replication of this information during cell division. In 1958, semi-conservative replication was proven by Meselson and Stahl (Meselson and Stahl, 1958).

These and subsequent discoveries have opened the door to a new understanding of disease and its treatment. Specific DNA mutations present at birth (germinal) or developed over time (somatic) have begun to be correlated with disease. This growing understanding of molecular biology provides insights for models describing disease

* More accurately, their 1941 paper tests a one gene – one enzyme hypothesis, in this case enzymes that were composed of single proteins (however some enzymes are composed of multiple proteins).

progression, for identifying disease state at progressively early points in life, and for developing drug therapies to treat disease.

Key to the accelerating pace of discovery has been the development of new assays and instrumentation for molecular biology. The invention of DNA sequencing (Lewin, 1997) and the polymerase chain reaction (PCR) (Saiki, Scharf, Faloona, et. al, 1985) significantly lowered the barriers to direct reading of an organism's DNA. Driven by increasingly high throughput sequencing machines, the Human Genome Project completed a "working draft" of the human genome in 2000, years ahead of schedule (Lander, Linton, Birren, et. al, 2001; Venter, Adams, Myers, et. al, 2001). The invention of oligonucleotide arrays (Pease, Solas, Sullivan, et. al, 1994) and real-time PCR analysis (Livak, Flood, Marmaro, et. al, 1995) has propelled efforts to identify and quantitate mRNA expression which has led to increasingly detailed knowledge of the proteins and pathways of disease.

There remains much to be learned about disease progression and its genetic correlates. The Human Genome Project provided an invaluable mapping for the general sequence of various organisms. Newer efforts such as the "Hap Map" seek to compile information regarding patterns of frequently occurring polymorphisms (Gabriel, Schaffner, Nguyen, et. al, 2002). However, many believe that understanding and combating our many common diseases will require information on a statistically finer scale than "general sequence" or "frequently occurring polymorphism" mappings can provide (Couzin, 2002). Methods to measure these low frequency mutational events and subtle shifting of gene expression are needed to study these diseases. Moreover, in the future, improved methods will be required to cheaply and efficiently test patients for the presence of known gene-disease correlations. Real-time PCR presently stands as the gold-standard for such analyses (Bustin, 2000); however the assay and its measurement can be difficult and complex (Bustin, 2002; Lunge, Miller, Livak, et. al, 2002). Significant assay optimization is often required for accurate results.

In this thesis, a new method for monitoring the real-time PCR assay is described. This method is motivated by a desire to eliminate certain reagents, simplifying the assay, while maintaining a high level of accuracy in its results. Such an advancement will

enable experiments and screening applications that are currently prohibitively costly and difficult.

## 1.1. The Basics of PCR

The polymerase chain reaction provides a method of making copies of DNA in a specified region of a genomic sample. Most genetic measurement techniques do not have enough sensitivity to perform adequate measurement without amplification of the target sequence. As such, PCR is an essential preliminary step for most current genetic analyses including sequencing and oligonucleotide array analysis.

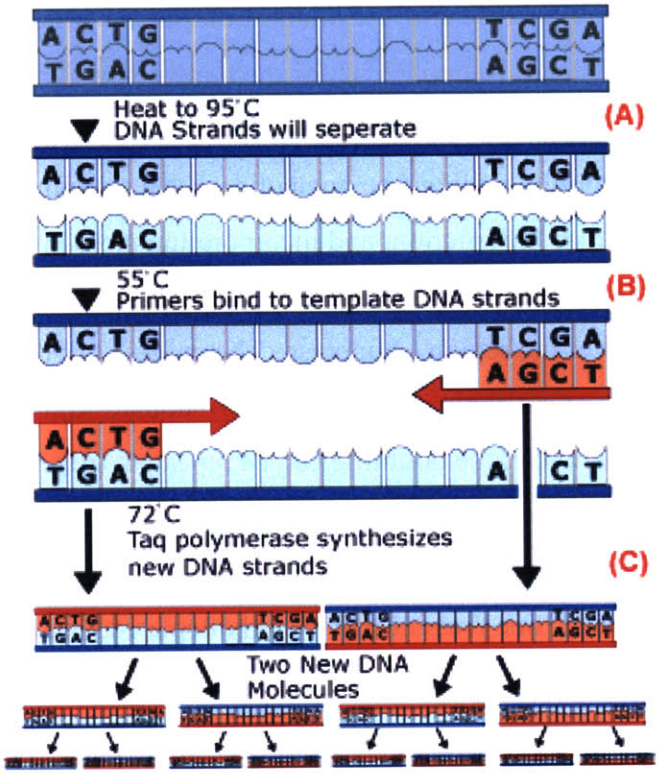


**Figure 1-1. PCR process: (A) Denaturation, (B) Primer Annealing, (C) Extension (Taken from http://genetics.nbii.gov/basic2.html).**

The polymerase chain reaction is typically composed of three steps. These are illustrated in Figure 1-1. Initially, the genetic sample is suspended in aqueous solution with several additional reagents. The first step, called denaturation, requires heating this solution to ~ 95 °C. At this temperature, the hydrogen bonds across nucleotides are

broken causing the previously double-stranded DNA to move to a single stranded conformation. The second step of PCR, called annealing, requires the PCR solution to be cooled to between 45-65 °C. During this step, short oligonucleotides, present in great excess in the initial PCR solution, bind to their complimentary sequence on the single stranded genomic samples. Two unique sequences of oligonucleotides are included in any PCR reaction. When used in human genetic analysis, these oligonucleotides, called forward and reverse primers, are typically ~20 base pairs in length in order to uniquely identify a single region of the genome. The primer pair unambiguously defines the start and end of the sequence which is to be copied. Primer binding enables an additional reagent to react. A polymerase enzyme binds at the site on which the primer has bound. The PCR solution is then raised to 72 °C for the third step called extension. At this temperature, polymerase enzyme becomes active. The polymerase moves sequentially down the genomic sample, pulling free nucleotides (that compliment the nucleotide to which it is to bind) from the solution, and incorporating them in the direction of its travel. This process transforms the previously single stranded genomic sample into a double stranded molecule over the region of interest. The process has thereby separated a double-stranded genomic sample and produced two double stranded molecules. By repeating this thermal cycle, the doubling can be repeated. As the number of cycles increases, PCR reagents are depleted and the polymerase enzyme is degraded. As a result, a loss of efficiency occurs such that all of the target sequences are not replicated at every cycle. Eventually, one reagent will be fully depleted, and no further copies will be made.

## 1.2. Quantification of starting copy number

Real-time PCR methods are used to quantitate the initial number of template copies in a genetic sample. The copies are typically present initially in such a low quantity or concentration that it is not possible to measure them. Through the amplification process of PCR, sufficient sample (and signal proportional to that sample) is generated for quantitative measurement.

During the amplification cycles in which the reagents of PCR are present in great excess, the amplification process performs near full exponential efficiency. Given sensitivity sufficient for detection during the exponential period, the cycle at which the measured signal (proportional to template copy number) rises above background is repeatably related to the initial template copy number.

An example of a real-time PCR result is shown in Figure 1-2 below. A dilution series (i.e., the second sample is a 10× dilution of the first, the 3rd sample a 100× dilution, etc.) of starting template was amplified in this experiment. A threshold signal level is defined at which the signal has risen above the measurement noise. The cycle at which each curve crosses this threshold is defined as the threshold cycle (Ct). The Ct is plotted against the log of the starting template number in the lower part of Figure 1-2. Dilution series such as this one are typically run as standard curves along with samples of unknown quantity. By comparison of the Ct of the unknown with those of the standards, quantitation can be done.

The method of manual threshold definition and calculation of the intersection point of the amplification curves with the threshold has been the traditional means of generating data from which to interpolate the starting copy quantity of the unknown sample. More recently, variations on this method have been introduced that are more amenable to complete automation and less susceptible to instrument drift (Roche Applied Science, 2003). These methods center on the use of the first derivative of the amplification signal. For these methods, the crossing point is defined as the cycle at which the first derivative reaches a maximum. This point corresponds to the last cycle before amplification efficiency starts to decline.

Two strategies are employed in creating the standard curves. For absolute quantitation, a set of standard curves must be generated from a dilution series that began with a sample whose starting copy number was known. The absolute quantitation of this reference sample is typically done by absorbance measurements. In addition to care in the absorbance measurement, absolute quantitation requires accurate pipetting in creating the dilution series.

Relative quantitation is an alternative for which standard curve preparation is less difficult. In this case, the experimental sample quantitation is expressed only relative to

some basis sample. Basis samples can include stock DNA or RNA. Another example is the use of the DNA or RNA from an untreated control subject. So-called "housekeeping" genes are frequently used as references for RNA quantitation (Bustin, 2002).

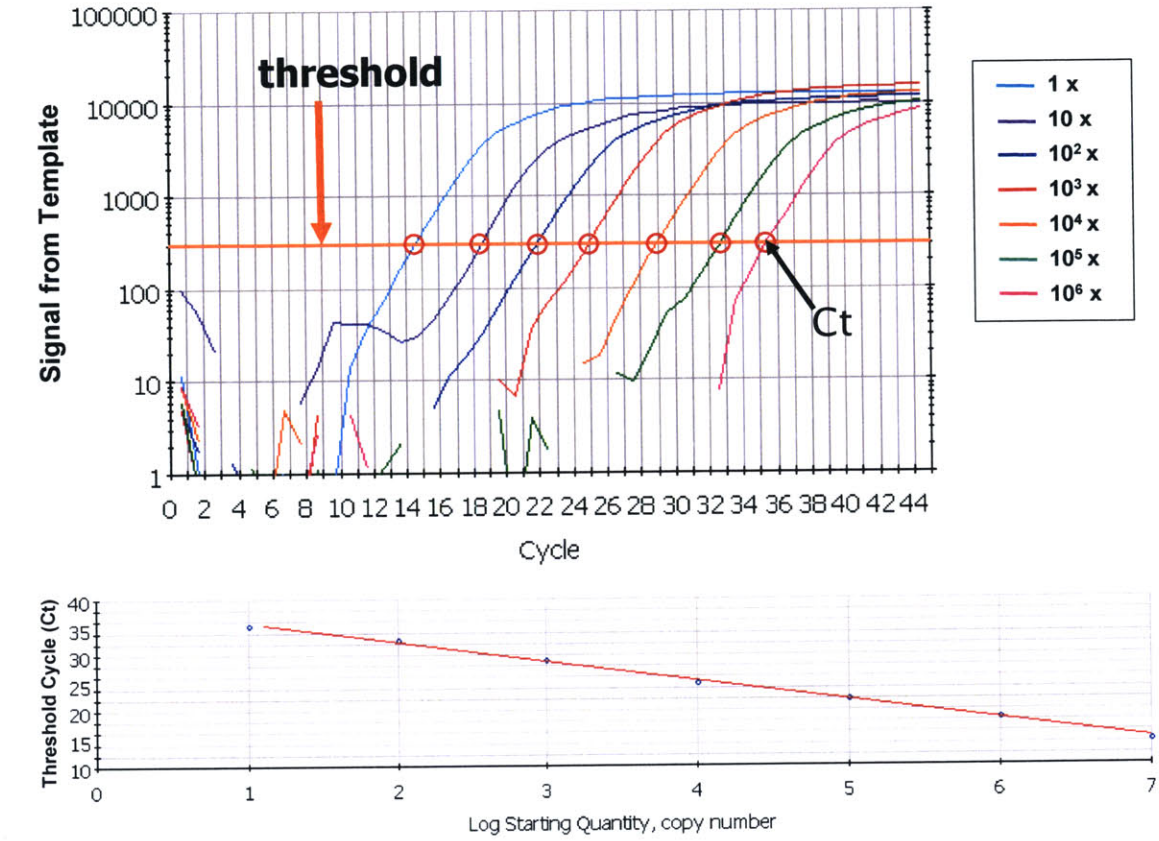


**Figure 1-2. Example of real time PCR dilution series data. [Upper] Exponential amplification continues past the threshold cycle (Ct) for amplification at each starting copy number. [Lower] Starting concentration has a log-linear relation to Ct. (http://www.med.sc.edu:85/pcr/realtime-home.htm)**

## 1.3. Applications

### *1.3.a. DNA mutation analysis*

Extensive efforts are presently being conducted to improve the knowledge and utilization of correlations between DNA mutations and disease, where much of this work is focused on single nucleotide polymorphisms (SNPs) (Holden, 2002) (Schmith, Campbell, Sehgal, et. al, 2003). SNPs are locations in the human genome in which the allele frequently varies across individuals, e.g. greater than 1% of the population carries a

variant at any SNP site. It is believed that localized patterns of these SNPs will create identifiable sub-populations (haplotypes) that are correlated with a particular phenotype (Gabriel, Schaffner, Nguyen, et. al, 2002). This hypothesis is based upon on the observation of recombination between intact sub-lengths of parental chromosomes during meiosis. Sub-regions of the DNA are thereby expected to exhibit "linkage" uniquely identifying a genetic lineage. Phenotypes to which haplotypes are correlated could include those with a predisposition to inherited disease or unique profiles of drug metabolism or efficacy. Genetic tests based on SNPs are already available for diseases such as cystic fibrosis, Huntington's disease (Roses, 2000), Rett Sydrome (Amir, Van den Veyver, Wan, et. al, 1999), and sickle cell anemia (Waterfall and Cobb, 2002). SNP genotypes have also been identified for familial cancers of the breast, ovary, colon, and melanoma (Ross and Ginsburg, 2002). More than 25 SNP genotypes also have been identified that are predictive of drug response (Evans and Relling, 2004). Among this list is a recently FDA approved genetic test/drug therapy (Gleevec) combination for identifying and treating a sub-population of people afflicted with chronic myeloid leukemia (CML) (Halapi and Hakonarson, 2002).

The high frequency nature of SNPs results in low requirements on detection sensitivity. At most, a genomic sample from a single individual is expected to be heterozygous for a specific allele. There are many measurement techniques that can meet the demands of such analysis including real time PCR, sequencing, oligonucleotide arrays, single-base extension assays (Nikiforov, Rendle, Goelet, et. al, 1994), and pyro-sequencing (Ronaghi, Uhlen, and Nyren, 1998).

A second class of DNA mutation analysis, that of rare mutant analysis, focuses on diseases with some level of environmental causality. Cancers are the largest cause of death in the United States after heart disease, where lung, breast, colon, and prostate cancer are the most pervasive (Mokdad, Marks, Stroup, et. al, 2004). Cancers are believed to require a series of mutations to reach malignancy (Armitage and Doll, 1954; Nordling, 1953; Knudson, 1971). It is further hypothesized that some or all of these mutations are environmentally induced or promoted (Thilly, 2003). Indeed, environmental causality is strongly established for cancers of the skin (Brash, Rudolph, Simon, et. al, 1991).

Environmentally induced mutations are inherently localized in select tissues. As a result, cells containing the causal or symptomatic mutations are at very low ratios to normal cells during much of the disease's progression. To study rare genotypic variants, the detection of point mutations at fractions from $10^{-3}$ to $10^{-7}$ mutant/wild type copies is required (Parsons and Heflich, 1997). Rare mutation analysis also requires specificity, reproducibility, and accuracy. Most techniques used to analyze SNPs do not meet these requirements. Presently the most effective means of studying rare mutations in many applications is through the use of a special type of real-time PCR that preferentially amplifies the allele of interest (a.k.a. allele-specific PCR).

The earliest reported method for allele-specific PCR is known as the Amplification Refractory Mutation System (ARMS) (Newton, Graham, Heptinstall, et. al, 1989). The basis of the technique is that oligonucleotides with a 3' mismatch do not function as efficient primers for polymerase extension under appropriate conditions. Thus primers are designed to match a mutant allele and thus preferentially amplify it relative to the wildtype. This technique was shown to be effective for mutant fractions of $10^{-1}$ mutants per wildtype (Cotton, 1997). Beyond this limit, the difference between the amplification efficiency of mutant alleles and wildtype alleles was not sufficient for the mutant signal to rise above the background signal of the wildtype.

The mismatch amplification mutation assay (MAMA) was developed to extend the sensitivity (mutant fraction detection limit). This assay is based on the observation that primer/template combinations with but a single mismatch in any of the last three 5' PCR primer bases are generally extended by Taq DNA polymerase (under appropriate conditions) but that primers containing any two mismatches are not extended (Cha, Zarbl, Keohavong, et. al, 1992). Primers are thus designed to complement the desired mutant sequence in the mutant site but not in an adjacent base pair. This automatically creates a double mismatch in the wildtype sequence. The result is selective amplification of the mutant sequence. The technique is illustrated in Figure 1-3. The potential of this assay was demonstrated by Cha et al. who described successful discrimination to a fraction of $10^{-5}$ mutant/wildtype and used it for the first direct measurement of point mutations from genomic DNA in animal tissue. Though the MAMA assay was originally analyzed by

post-PCR slab gel methods, its application to real-time PCR analysis has also been demonstrated (Glaab and Skopek, 1999).

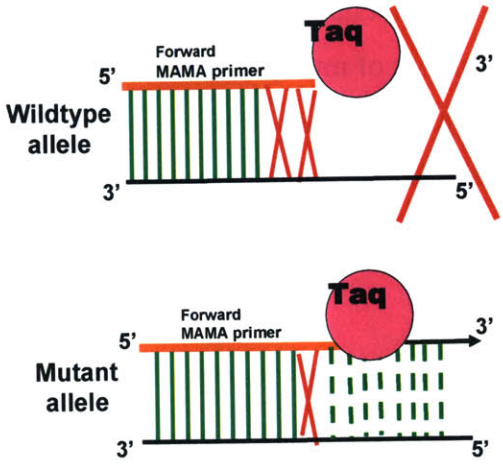


**Figure 1-3. Illustration of MAMA PCR concept. The MAMA primer contains a double mismatch for the wildtype allele making extension highly improbable. The MAMA primer has only a single mismatch for the mutant allele, and extension proceeds with high efficiency.**

Other variations on the theme of allele-specific PCR include PCR Amplification of Specific Alleles (PASA) (Sommer, Cassady, Sobell, et. al, 1989), the Allele-specific Competitive Blocker PCR (ACB-PCR) (Orou, Fechner, Utermann, et. al, 1995), and the Mutation-Specific PCR Assay (MSPA) (Yano, Uchida, Yuasa, et. al, 1997).

Allele specific PCR has found utility in *in vivo* animal model studies of environmental mutagens (Dobrovolsky, Chen, and Heflich, 1999; Chen, Harrington-Brock, and Moore, 2002) and wide use in research on carcinogenesis in humans (Horikoshi, Lenz, Danenberg, et. al, 1994; Kirby, Batist, Fotouhi-Ardakani, et. al, 1996; Bezieau, Devilder, Avet-Loiseau, et. al, 2001; Laghi, Orbetegli, Bianchi, et. al, 2002).

Rare mutation analyses such as these hold great promise not only for the study of environmental mutagens and improved models of cancer progression, but also for clinical applications detecting cancerous cell mutations very early in the disease cycle. However, while SNP genotyping has already found clinical applications as described earlier, rare mutant analysis has not.

There are two limitations to greater implementation of rare mutant genetic testing as a clinical diagnostic. The first is the present limited, but growing, availability of gene-

disease correlations. Analysis cost is the second limitation which affects not only future wide spread implementation of rare mutant genetic testing but also limits today's ability to rapidly prove rare-mutation correlation. A growing list of available rare mutatant genetic tests which potentially include screening for multigenic, multiallelic mutations across a set of multiple samples of multiple tissues will put significant pressures on instrument throughput and analysis cost. If we are to achieve truly routine screening, an affordable, robust assay of minimal complexity (thereby maximally amenable to high throughput formatting) will be required.

*1.3.b. Gene Expression (mRNA quantification)*

Many cellular decisions concerning survival, growth, and differentiation are reflected in altered patterns of gene expression. This expression occurs via the messenger molecule, mRNA. Quantification of mRNA has therefore been key to applications seeking to understand gene function, cell signaling pathways, and disease progression.

Real time PCR methods have found wide-ranging applications to mRNA analysis by utilizing reverse-transcription to convert the mRNA back to DNA. This combination of methods is referred to as RT-PCR (reverse transcription polymerase chain reaction).

Applications of real-time RT-PCR include quantifying the regulation and expression of drug resistance markers in tumor cells (Ramachandran and Melnick, 1999), monitoring responses to chemotherapy (Desjardin, Perkins, Wolski, et. al, 1999), providing a molecular assessment of tumor stage (Bustin and Dorudi, 1998), detecting circulating tumor cells in cancer patients (Ghossein and Rosai, 1996), and detecting bacterial (Hill, 1996) and viral (Holodniy, 1994) pathogens including HIV (Connor et al. 1993; Piatak et al. 1993b; Furtaqdo et al. 1995).

As with DNA-based diagnostics, wide-spread implementation of mRNA-based clinical diagnostics requires, first, that many more correlations between expression and disease be found and, second, that there exists an affordable, accurate means of detecting the expression indicator. The search for expression-disease correlation is largely being conducted with oligonucleotide arrays (a.k.a. "gene-chip") instrumentation. First developed by Fodor, this technology attempts to identify undefined mRNA expression by

washing a reverse-transcribed DNA sample over millions of unique sets of oligonucleotides (Pease, Solas, Sullivan, et. al, 1994). Each set is bound to a specific location on a glass substrate. Fluorescence methods are then used to identify which oligonucleotides captured the unknown sample, thus elucidating the identity of the expressed mRNA. Gene-chips are fraught with challenges including transcriptional errors, sensitivity, and non-specific binding. Because of these challenges, gene-chips present role is primarily that of identification and only approximate quantification. Though of lower throughput, real-time RT-PCR remains the gold standard by which RNA expression is quantified.

Just as for DNA-based diagnostics, the throughput requirements and associated cost pressures on mRNA-based diagnostics will only increase as further correlations, especially multigenic, multi-allelic correlations, between expression and disease are discovered. Fine changes in gene expression indicative of disease state are unlikely to be quantified with adequate accuracy by gene-chip analysis. If such resolution is required, real-time RT-PCR is expected to have a substantial role in clinical diagnostics. To achieve routine clinical diagnostic analysis of gene expression, an affordable, robust assay of minimal complexity will be required.

## 1.4. Existing Methods of Real-Time PCR Measurement

### *1.4.a. Intercalating Dyes*

The first description of a real time PCR method was given by Higuchi (Higuchi, Dollinger, Walsh, et. al, 1992). In their work, ethidium bromide was added to the PCR. Ethidium bromide undergoes a large fluorescence enhancement on binding to double stranded DNA. Thus, measured fluorescent intensity over the course of PCR is theoretically linearly proportional to the number of DNA copies present. In subsequent development, an improved dye, SYBR-green, replaced ethidium bromide (Morrison, Weis, and Wittwer, 1998). SYBR-green is favored because its fluorescence enhancement is twice that of ethidium bromide and for its improved safety (ethidium bromide is a known mutagen) (www.probes.com).

The major advantage to the use of intercalating dyes for real-time PCR is their universal nature, i.e., they can be used on any target sequence. This allows "bulk" purchase and lowers their cost.

There are, however, important disadvantages to the use of intercalating dyes. The primary limitation of intercalating dyes are their lack of specificity. Primer-dimer formation and non-specific amplification create false increases in measured signals that are indistinguishable from amplification of the target sequence. The indiscriminate binding of intercalators to double stranded DNA also poses a problem for PCR with genomic DNA template. At best steric-hinderance prevents the intercalator from binding to the non-targeted genomic DNA. Another best case scenario is that the effective background signal from genomic bound intercalator will be constant over the course of the reaction. Neither best-case can be expected to exist fully in practice, the result of which is a drifting background level routinely observable in the results of real-time PCR with intercalating dyes. Such a drift may also be caused by another problem with intercalating dyes, non-constant binding ratios. It has been shown that when an intercalating dye is at high concentration relative to double-stranded DNA, more dye molecules will bind per DNA base-pair than when the intercalator is at lower relative concentration (Marino, Devaney, Davis, et. al, 1998).

*1.4.b. Hybridization Probes*

An alternative to the use of intercalating dyes with greater specificity was described by Heid et al. in 1996. This method, which they called Taqman, was later commercialized by Applied Biosystems (ABI). In the Taqman assay, fluorogenic probes anneal to template DNA downstream from the point of primer annealing and are subsequently cleaved by the 5' exonuclease function of the Taq polymerase during extension. Cleavage frees the fluorophore of proximity to the quencher molecule generating an increase in fluorescence for each PCR cycle (Holland, Abramson, Watson, et. al, 1991; Heid, Stevens, Livak, et. al, 1996). This technique is shown in box A of Figure 1-4.

Other hybridization probe methods have subsequently been reported and commercialized. These techniques are reviewed in detail elsewhere (Mackay, Arden, and

Nitsche, 2002; Bustin, 2000). Briefly, these include three techniques that are based upon the use of hairpin oligoprobes shown in boxes B, D, and E of Figure 1-4. In each technique, hybridization of the oligoprobe forces the hairpin structure apart thereby freeing the fluorophore from proximity to a quenching molecule. Box B depicts the earliest hairpin technology, known as Molecular Beacons, in which the hairpins simply hybridize during the annealing stage to provide signal proportional to the number of DNA copies present (Tyagi and Kramer, 1996). In the extension phase, the polymerase displaces the Molecular Beacon returning it, intact, to free solution. Sunset primers, shown in Box D, work similarly, however, these oligoprobes are incorporated into the product rather than being repeatedly displaced (Whitcombe, Theaker, Guy, et. al, 1999). The commercial embodiment of this technique, known as Amplifluor primers, utlize a three primer strategy (two of which are unlabeled) that allows the hairpin to be universal for any sequence (www.probes.com). Scorpion primers, depicted in Box E, require a more complex design in which a portion of the hairpin hybridizes in two locations on one strand of the target sequence (Nazarenko, Bhatnagar, and Hohman, 1997). The final technique shown in Figure 1-4 (Box C) is the use of a pair of labeled oligonucleotides designed to hybridize in adjacent positions on the target sequence. The fluorescent labels are selected such that the emission band of one overlaps the exciation band of the second fluorophore. When this pair of labels are closely located, fluorescence resonant energy transfer (FRET) efficiently couples the energy from the first to the second fluorophore. This enables detection of signal at the emission band of the second fluorophore proportional to the number of target copies present (Wittwer, Herrmann, Moss, et. al, 1997; Cardullo, Agrawal, Flores, et. al, 1988).

At present, Taqman probes remain the most popular method but market preferences continue to evolve. There are relative advantages and disadvantages of each. However, all these techniques share a set of disadvantages that are common to the category.

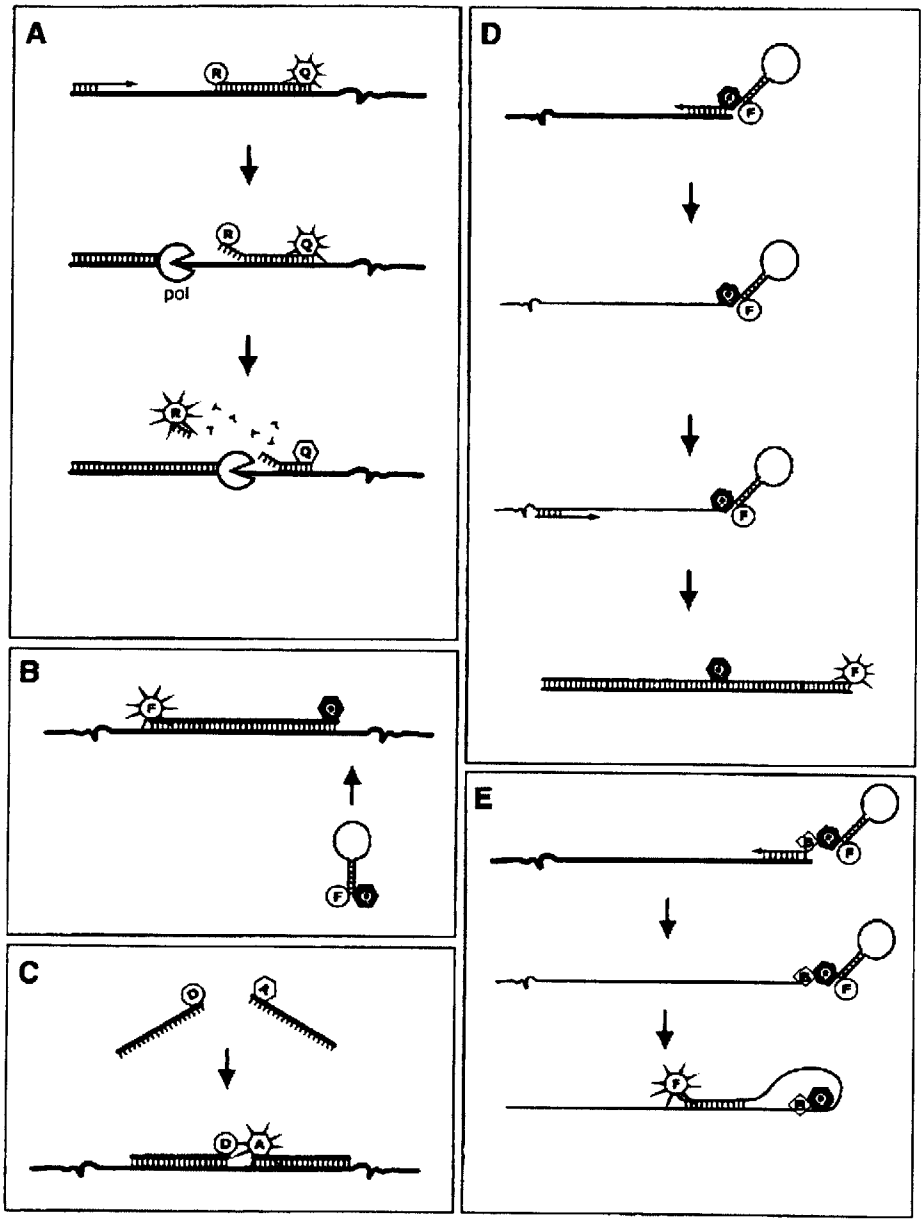


**Figure 1-4. Hybridization techniques used in real-time PCR. [A] 5' Nuclease oligoprobes (a.k.a. Taqman probe) [B] Hairpin oliogoprobes (a.k.a. Molecular Beacons), [C] Adjacent oligoprobes (a.k.a. Hyb Probes), [D] Sunrise Primers (a.k.a. Amplifluor primers), [E] Scorpion primers. Figure taken from (Mackay, Arden, and Nitsche, 2002).**

Hybridization probe assays are highly sensitive to spatial placement of the primers and probe. The spatial location along the target sequence defines the sequence of the primer and probe oligonucleotides and thereby their melting temperatures. Melting temperatures must be compatible with PCR temperatures for annealing and extension. This is an especially tricky problem for hairpin structures. The probes sequence is also

critical for two more reasons. First, it is known that nucleotides affect fluorescence uniquely (Livak, Flood, Marmaro, et. al, 1995). Thus the nucleotide sequence proximate to the reporter or quencher dyes can affect experimental results. Second, evidence also indicates that the sequence is correlated to the effectiveness with which the polymerase is able to hydrolyze the probe. A sequence that is G-rich at the 5' end of a Taqman probe (at the reporter dye) appears to more difficult to displace (Lunge, Miller, Livak, et. al, 2002). The relative spatial location of the primers and probe (defined by their sequence) also affects hydrolysis. The processivity of Taq DNA polymerase is approximately 50-75 nucleotides (Abramson, 1995). It is reasoned that the observed reduction in hydrolysis efficiency in reactions whose primer-probe spacing is greater than this interval is explained by this processivity limit (Lunge, Miller, Livak, et. al, 2002). The final concern regarding the sequence of primers and probe is that of specificity and primer-dimer/ primer-probe duplex formation. Such events can obviously affect assay performance.

The concentration of reagents in the reaction can also adversely affect hybridization probe assay performance. The best signal in a hybridization probe reaction comes when all the probe molecules have left their "free-solution-state" having otherwise been cleaved, bound, or incorporated. If the number of probe molecules (i.e., given a comparison in constant volume, the concentration) is too high, the assay will only convert a small percentage of molecules from their low to high fluorescent state. Thus the percentage change in the solution's fluorescence will be diminished. In addition to concern over having too many probes, having too few is also problematic. When the probe concentration is too low, competition for binding sites will result in hybridization of the original template prior to probe binding. The optimal amount of probe depends on the efficiency of the PCR. The concentration of $MgCl_2$ must also be optimized. With specific regard to fluorogenic probe assays, increased $MgCl_2$ concentration is known to enhance the quenching ability of TAMRA. It can also have implications for PCR extension efficiency (Bassler, Flood, Livak, et. al, 1995).

The challenges described above have predominantly been explored in assay volumes of 20 to 100 μL. Conducting these assays in smaller volumes holds great promise for cost reduction but further increases the difficulty of performing a repeatable,

accurate assay. Shrinking the volume of PCR increases the surface area of the solution volume that contacts the PCR vessel. Surface chemistries can thereby become increasingly detrimental to the performance of reagents, especially DNA polymerase. Multiple studies have been preformed analyzing passivation strategies to create surfaces suitably inert for PCR (Shoffner, Cheng, Hvichia, et. al, 1996; Cheng, Shoffner, Hvichia, et. al, 1996; Taylor, Winn-Deen, Picozza, et. al, 1997). While these studies have shown success, lower reaction efficiencies are typically observed compared to that of standard PCR (Taylor, Winn-Deen, Picozza, et. al, 1997). As the reaction shrinks and the degree of parallelization of the measurement increases, concerns over evaporation, image uniformity, and stochastic errors increase. Combining the complexities of existing hybridization probe assays with the complexities of micro-scale analysis is a daunting proposition.

## 1.5. Conclusion

In this thesis, a new method for monitoring real-time PCR based on fluorescence anisotropy (FA) is proposed and tested. Utilizing the properties of polarized light and fluorescent emission, FA can be used as a gauge for the size of a molecule to which a fluorophore is attached. The instrument that is developed tracks the FA of fluorescently labeled forward primer molecules as they are incorporated into amplified products during the PCR. Additional reagents such as intercalating dyes or probe molecules are no longer required.

FA-based detection holds significant advantages over competing detection methods. Unlike intercalating fluorophore signals, the FA of fluorescently labeled primers only changes when the primer molecule uniquely binds to its target. Spurious signals from indiscriminate binding of the intercalator to double-stranded DNA are eliminated. Another advantage of the FA real-time PCR method is that it results in an amplified PCR product which is not saturated with intercalating dye. Such contamination is undesirable for research applications in which sequencing or other DNA post-processing is employed.

When compared against the use of hybridization probes, FA based detection greatly simplifies reaction optimization. This not only enables faster assay development but also improves assay robustness. Greater robustness eases the transition to smaller PCR volumes. The combination of eliminating the fluorogenic probe and facilitating decreased reaction volume has the potential for orders of magnitude reduction in PCR costs. Finally, all these benefits come without sacrificing the most desirable feature of fluorogenic probes: a signal which changes only when unique binding of an oligonucleotide sequence occurs.

This thesis describes the design and development of a real time PCR instrument in which FA is used to monitor the amplification. The results demonstrate the feasibility of this approach and include comparison of the theoretical and experimental sensitivity and performance. The prototype is shown to be highly repeatable achieving comparable performance to that of existing real-time PCR assays and instrumentation.

# Chapter 2

# Fluorescence Anisotropy

## 2.1. Background

*2.1.a. Maximum Anisotropy*

Fluorophores are known to behave as radiating dipoles. When such dipoles are excited by plane-polarized light, they emit polarized fluorescence into a fixed plane (Perrin, 1926). To understand the principles of fluorescence anisotropy, first consider a single molecule whose absorption and emission axes are parallel. Assume this molecule is oriented with its dipole axis at an angle $\alpha$ relative to the z-axis and $\varphi$ relative to the y-axis as shown in Figure 2-1 and that the excitation energy is polarized along the z-axis. The intensity of the light radiating from this dipole can be resolved into polarization components (i.e., intensities along two orthogonal observation axes). These are computed as the square of the electric field projected onto these observation axes. Taking the Z-axis as the vertical observation axis and the Y-axis as the horizontal observation axis, these projections are given by

$$I_V(\alpha,\varphi) = \cos^2\alpha \qquad \textbf{2-1}$$

$$I_H(\alpha,\varphi) = \sin^2\alpha \sin^2\varphi . \qquad \textbf{2-2}$$

In real experiments, a solution will contain many fluorophores with a random distribution of orientations. The anisotropy measured from this solution will be an average based on all the molecules that are excited. Since the molecules have an equal probability of lying at any angle, φ, from 0 to 2π and are excited with the same efficiency at any angle, φ, from 0 to 2π, the φ dependence in Equation 2-2 is averaged to 1/2 for solutions containing many fluorophores (the average value of $\sin^2\varphi$ is ½ when φ spans from 0 to 2π).

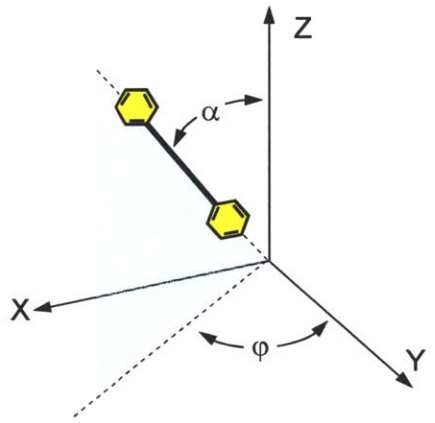


**Figure 2-1. A single fluorescent molecule can be approximated as a radiating dipole with parallel excitation and emission axes.**

Although the probability of excitation is the same for a dipole oriented at any angle φ, it is not so for dipoles at different values of α. Moreover, molecules that are randomly oriented are not distributed equally at all angles α. If the probability that an excited molecule is oriented at α is defined as f(α), then we can integrate across all α to compute the measured intensities for a collection of fluorophores as

$$I_V = \int_0^{\pi/2} f(\alpha)\cos^2\alpha \, d\alpha \,, \qquad \textbf{2-3}$$

$$I_H = \frac{1}{2}\int_0^{\pi/2} f(\alpha)\sin^2\alpha \, d\alpha \,. \qquad \textbf{2-4}$$

Fluorescence anisotropy is computed as the normalized difference given by

$$FA=\frac{I_V-I_H}{I_V+2\cdot I_H}. \qquad \textbf{2-5}$$

Substituting Equations 2-3 and 2-4 into 2-5 and making use of the identity $\sin^2\alpha = 1-\cos^2\alpha$, the equation for FA becomes

$$FA=\frac{3}{2}\cdot\frac{\int_0^{\pi/2} f(\alpha)\cos^2\alpha\, d\alpha}{\int_0^{\pi/2} f(\alpha)\, d\alpha}-\frac{1}{2}. \qquad \textbf{2-6}$$

The probability that an excited molecule lies at angle $\alpha$ is a function of two factors. The first factor is the number of molecules that lie at angle $\alpha$. The second factor is the efficiency with which molecules at different $\alpha$ orientations are excited.

The number of molecules oriented at an angle between $\alpha$ and $\alpha+d\alpha$ is proportional to the surface area on a sphere from $\alpha$ to $\alpha+d\alpha$. This quantity is proportional to $\sin\alpha\, d\alpha$.

Since fluorescent molecules act like radiating dipoles, they exhibit a probabilistic excitation called photo-selection. Molecules with their absorption axis aligned parallel to the electric field of the polarized excitation have the highest probability of excitation. This probability falls off as $\cos^2\alpha$.

The probability that an excited molecule lies at an angle, $\alpha$, is the product of these two factors and is given as

$$f(\alpha)=\cos^2\alpha\sin\alpha. \qquad \textbf{2-7}$$

Substituting Equation 2-7 into Equation 2-6, the evaluated integral simplifies to FA = 0.4. This result is referred to as the maximum (or fundamental) anisotropy and defines the anisotropy that would be observed for a randomly distributed, but immobile, collection of radiating dipoles which have parallel absorption and emission axes. Thus it is observed that a collection of immobile fluorophores, excited by plane polarize light,

yields partially depolarized light. Departure from our assumptions of parallel absorption and emission axes further decreases the maximum anisotropy.

### *2.1.b. Mobile Fluorophores*

Rotational diffusion of fluorophores, such as by Brownian motion, during the excited lifetime of the fluorophore causes further depolarization. These effects are described for an idealized spherical molecule by Perrin's equation (Perrin, 1926) which models the observed FA as

$$FA = r_0 / (1 + \tau/\theta), \qquad \textbf{2-8}$$

where $r_0$ is the maximum (fundamental) anisotropy, $\tau$ is the fluorescence lifetime, and $\theta$ is the rotational correlation time. This correlation time is given by

$$\theta = (\mu \cdot V)/(R \cdot T), \qquad \textbf{2-9}$$

where $\mu$ is the solvent viscosity, T is the temperature, R is the gas constant, and V is the molecular volume. For measurements at constant viscosity and temperature, FA depends on molecular size in free solution. The concept of using FA to measure molecular mass (volume) is illustrated conceptually in Figure 2-2.

An example plot of Perrin's equation is given in Figure 2-3. The plot was generated with the assumptions that $r_0$=0.4, $\tau = 4\times10^{-9}$ s, and that $\theta$ was related to the molecular mass by a proportionality constant of $\beta = \mu/(R\times T\times\rho) = 0.4$ ns/kDa, where $\mu$ = 0.001 kg/(m s) (i.e., that of water), R = 8.3145 J/(K mole), T = 298 K (room temperature) and $\rho$ = 1000 kg/m$^3$ (i.e., density of water). This proportionality constant is approximated in (Owicki, 2000) and www.probes.com/handbook/boxes/1572.html.

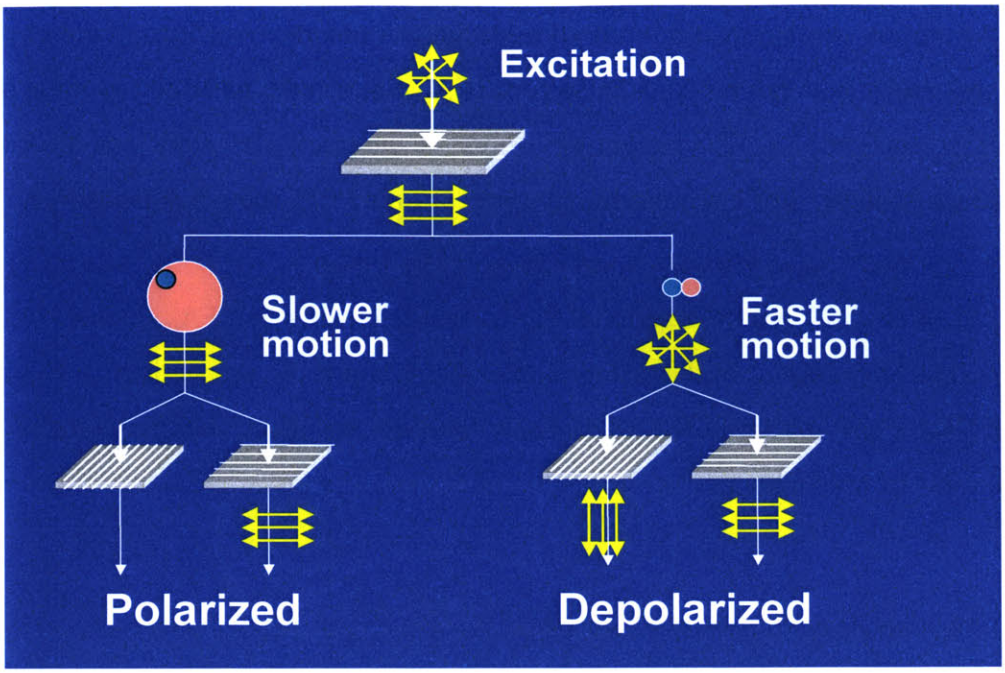


**Figure 2-2. Conceptual illustration of Fluorescence anisotropy mass discrimination.**

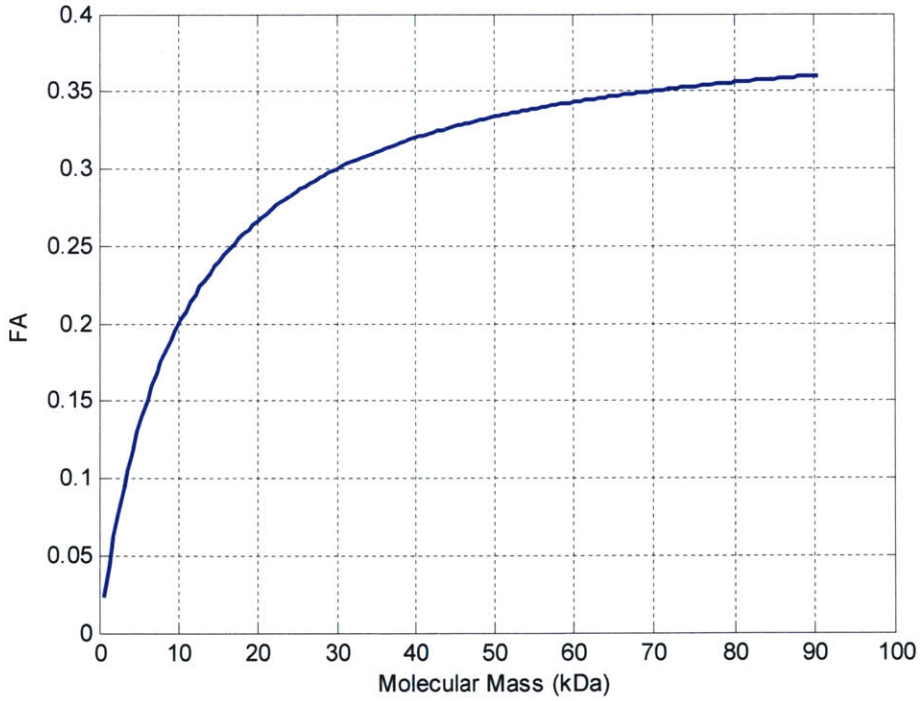


**Figure 2-3. Example plot of Perrin's equation.**

A solution containing a mixture of molecules of unique mobility and thereby unique anisotropy will exhibit a net anisotropy ($FA_{net}$) that is the weighted average of these unique anisotropies. The weighting factors are the fractional intensities (f) of each of the unique species. For FA measurement of real-time PCR, the net anisotropy is

$$FA_{net} = f_{primer} FA_{primer} + f_{product} FA_{product} + f_{other} FA_{other}, \quad \textbf{2-10}$$

where $f_{primer}$ and $f_{product}$ are the fractional fluorescent intensities and $FA_{primer}$ and $FA_{product}$ are the unique anisotropies of the primer and product molecules, respectively. The terms $f_{other}$ and $FA_{other}$ account for polarized intensity from other sources such as scattered light or autoluminescent molecules.

### *2.1.c. Previous Applications of FA to DNA*

FA has previously been applied to DNA analysis by many researchers for genotyping by hybridization (Chen, Levine, and Kwok, 1999; Latif, Bauer-Sardina, Ranade, et. al, 2001; Gibson, Gillard, Whitcombe, et. al, 1997). In such applications, the maximum required sensitivity was the detection of heterozygous alleles. Murakami et al. appear to have been the first to use FA to monitor DNA-DNA hybridization (Murakami, Nakaura, Nakatsuji, et. al, 1991). They showed that a solution of labeled probes exhibited increased FA when mixed with complimentary oligonucleotides. Non-complimentary oligonucleotides resulted in no change in FA.

Ye et al. have explored the use of FA as a tool for approximate confirmation of successfully amplification comparing the FA of PCR solution before and after amplification (Ye, Ikebukuro, and Karube, 1998). These results showed the ability to uniquely identify mixtures of labeled primer and labeled product when the ratios differed by 20%, i.e., they could differentiate a sample containing 100% primer and 0% product from one that contained 80% primer and 20% product.

More recent work used FA for genotyping in a single base extension assay (Chen, Levine, and Kwok, 1999). FA measurement monitored the incorporation of one of four dye-labeled terminators (dNTA, dNTT, dNTC, or dNTG), each having a unique spectral signature. In a solution of identical oligonucleotides, it was demonstrated that FA measurement at each of the four emission wavelengths could differentiate which of the

bases were incorporated. Results demonstrated that homozygosity for any allele or heterozygosity for any allele pair could be determined.

Building on this work, Latif et al. showed that FA could be used to evaluate the Taqman PCR assay at completion (Latif, Bauer-Sardina, Ranade, et. al, 2001). In their work, the FA of the fluorescent label of two sets of allele specific probes were monitored (the fluorophore's emission wavelength was differed between the two sets). Hybridization of either probe (or both probes) with the targets and subsequent cleavage by the Taq polymerase induced a detectable change in FA. By utilizing FA instead of the typical intensity measurements, the researchers were able to eliminate the quencher molecule from the Taqman probe. The FA results were concurrent with the standard Taqman assay utilizing intensity measurements.

Only one group has used FA measurements for real-time DNA measurement. Walker and colleagues have demonstrated the use of FA in real time monitoring of strand displacement amplification (SDA). SDA is based upon the ability of a restriction enzyme to nick a hemi-modified recognition site and the ability of a polymerase to displace a downstream DNA strand during replication. Their application of FA to real-time SDA was hindered by its $10^8$ fold amplification limit, and its restriction to relatively small targets (~60 bp). These authors demonstrated limited success only after incorporating a DNA binding protein into the assay (Spears, Linn, Woodard, et. al, 1997; Walker, Linn, and Nadeau, 1996b; Walker, Nadeau, and Linn, 1997).

## 2.2. Achieving adequate dynamic range for template quantitation

Application of FA to measurement of primer incorporation during the PCR process brings with it a number of complications. Foremost among these challenges is the typically limited dynamic range of FA measurement.
The dynamic range of an instrument is defined as the measurement range (difference between maximum and minimum signal) divided by the measurement resolution.* The resolution is typically taken as at least twice the standard deviation of the measurement.

* Note that this definition of dynamic range differs from that reported by some assay/instrument manufacturers, in particular Applied Biosystems (ABI). In their product literature they describe a "$10^5$ dynamic range." By this claim, they mean the instrument can provide quantitation of starting template

The range attainable with FA is fundamentally constrained by the underlying physics as seen in Equation 2-8. Applications of FA to DNA measurement face more constraint from dynamic range than is implied by this equation or illustrated graphically in Figure 2-3. Perrin's equation assumes spherical molecules, whereas short lengths of DNA have a rod-like structure. Because the additional mass is structured in this way, the additional mass does not slow the Brownian motion as dramatically as if the molecule were spherical. Confounding this effect is that fluorescent labels on DNA are typically not rigid allowing a limited degree of freedom between the target molecule and fluorophore. Figure 2-3 indicates that a 6 kDa primer molecule and a 60 kDa product would be expected to exhibit a change in FA of ~230 mP. Initial experiments performed for this dissertation measured a range of only 71 mP from primer to product (Crane, Sudo, Thilly, et. al, ).

Instrument resolution, the second piece of the dynamic range puzzle, has seen steady improvement in recent years. Older literature and some commercially available instruments report a typical resolution of a few mP. A survey of instrument manufacturers shows that the best resolution currently attainable in commercial instruments is 0.5 mP♦ (Affinity Fluorescence Multimode Reader, Cambridge Research Instruments). At this noise level, the theoretical dynamic range would be ~1:230 (=230 mP / (2×0.5mP)). Early feasibility experiments for this thesis indicated dynamic range could be limited to less than 1:180 (Crane, Sudo, Thilly, et. al ,). Walker et al. report dynamic ranges of only 10 for their assay/instrument combination, noting that such a dynamic range was unacceptable for accurate quantitation of SDA (Walker, Linn, and Nadeau, 1996b), however the product DNA used in these experiments were only 50mers as opposed to 100mers as assumed above.

---

concentrations over five orders of magnitude that are linear with $C_T$, the cycle at which the fluorescence rises above background.

♦ This standard deviation was recorded for an assay in which the fluorophores were at 1 nM concentration. It is not unreasonable to expect the CRI instrument performs better at the 200 nM fluorophore concentration found in the PCR. No data are available on CRI instrument performance on concentrations this high.

*2.2.a. How much is enough?*

Given the limitations on measurement feasibility encountered by Walker and colleagues due to a small dynamic range for FA measurement, it is prudent to ask how much dynamic range is required for accurate quantitation. The easiest approach to answering this question is to reference existing real-time PCR instrumentation.

The Roche Lightcycler real-time PCR instrument is described in detail in Chapter 5. Given its availability in the BioInstrumentation lab, it was used as the benchmark for all FA real-time PCR instrument comparison. All commercial instrumentation (to the author's knowledge) share a common problem for the purpose of dynamic range comparison. Intensity measurement data taken by the instrument, even in its rawest form, always include a background subtraction that is transparent to the operator. Intercalators and hybridization probes both have some fluorescence in their "no-signal" state (i.e., at cycle 1). This fluorescent intensity is measured by the instrument, assumed to represent background, and subtracted from all future measurements. The challenge arises in knowing if any additional scaling was done on the reported data. If the data are multiplied by a scaling factor *after* the background has been subtracted, the dynamic range can appear much larger than it actually is.

In Chapter 4, experiments are described in which intercalator assays were performed both in the Lightcycler and the FA instrument. By comparing these data sets, it was possible to determine that the Lightcycler does not scale its readings after background subtraction. Hence, its data can be used to estimate the dynamic range required for accurate real time PCR measurements.

Figure 2-4 shows the Lightcycler amplification of four replicates of 20 ng of genomic control DNA (4312660, Taqman Control Genomic DNA (Human), Applied Biosystems) using a Roche master mix containing SYBR-green (3003230, Lightcycler Fast Start DNA Master SYBR Green I, Roche) according to their recommended protocol. Figure 2-5 shows nine different amplification curves from both genomic control and cellular DNA using a Roche master mix containing hybridization probes (2015102, Lightcycler DNA Master Hybridization Probes, Roche) according to their recommended protocol. Both results are typical of our experience with the Lightcycler.

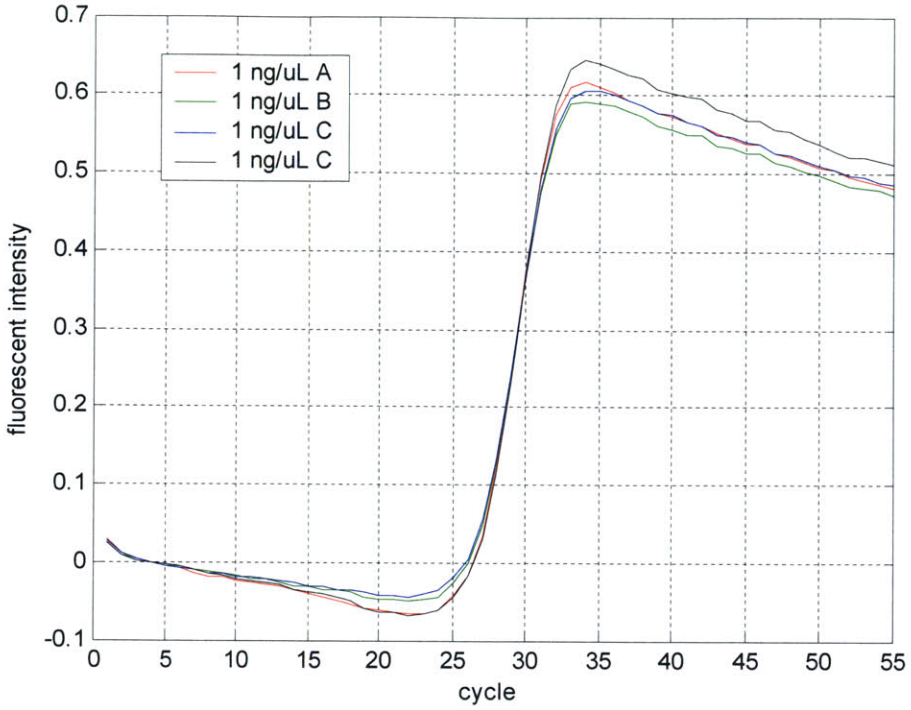


**Figure 2-4. Four replicates amplifying 20 ng of genomic DNA in the Lightcycler using an intercalator assay.**

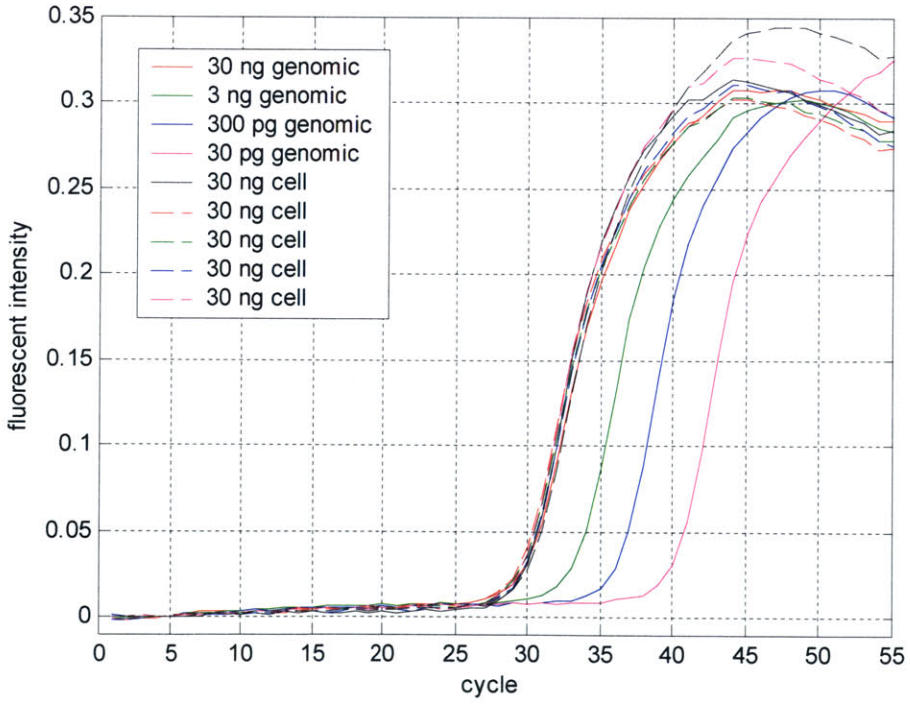


**Figure 2-5. Amplification of a dilution series of genomic DNA and five replicates of cellular DNA.**

The SYBR green results shown in Figure 2-4 exhibit drift in the early PCR cycles which is common in SYBR green assays. De-trending the intensity measurements of the early cycles allows computation of the standard deviation of the intensity measurement that ignores the signal drift. Computing the standard deviation of each signal over the first 20 cycles yields an average standard deviation across the four replicates of 0.0017 intensity units. The typical range observed in these experiments is 0.68 intensity units yielding a dynamic range of ~1:200.

The hybridization probe results shown in Figure 2-5 do not exhibit substantial early cycle drift. The standard deviation of the intensity measurements taken over the first 20 cycles is, on average, 0.002 intensity units. The typical range observed is 0.314 intensity units yielding a dynamic range of ~1:83.

The early feasibility results indicated a dynamic range of better than 1:180 could be achieved with FA measurement of primer incorporation into product. Discoveries discussed in Chapter 3 and Chapter 4 required instrument and assay modifications from these early prototype measurements which were detrimental to dynamic range. The factors that can be used to improve dynamic range in FA measurement of real time PCR are discussed below.

### *2.2.b. Increasing Dynamic Range Through Fluorophore Selection*

In most cases an assay designer is highly constrained in his/her selection of practical fluorophores. Cost constraints (fluorophores can differ dramatically in price) and especially instrumentation configuration limit available choices. Thus it is critical that instrumentation design carefully consider optimal fluorophores.

Dynamic range can be maximized by optimal selection of fluorescence lifetime ($\tau$), a property unique to each fluorophore. Plots of Perrin's equation are shown graphically in Figure 2-6 for a variety of fluorescence lifetimes. Observe that a fluorophore with a 1 ns fluorescence lifetime has maximum sensitivity for molecules ranging in size from 0 to 10 kDa. Substantially less sensitivity is observed, for example, if a molecule were converted from 30 to 100 kDa.

For real-time PCR, the fluorophores will initially be joined to 20-mer primer molecules. During PCR, these primers will be incorporated into product DNA based on target sequences typically on the order of 100 bp in length. Given that a set of $10^{10}$ molecules of dsDNA 100 bp in length has a mass of ~ 1 ng, a single primer molecule (ssDNA) has a molecular mass, $m_1$, of 6 kDa. Likewise, product DNA has a mass, $m_2$, of 60 kDa.

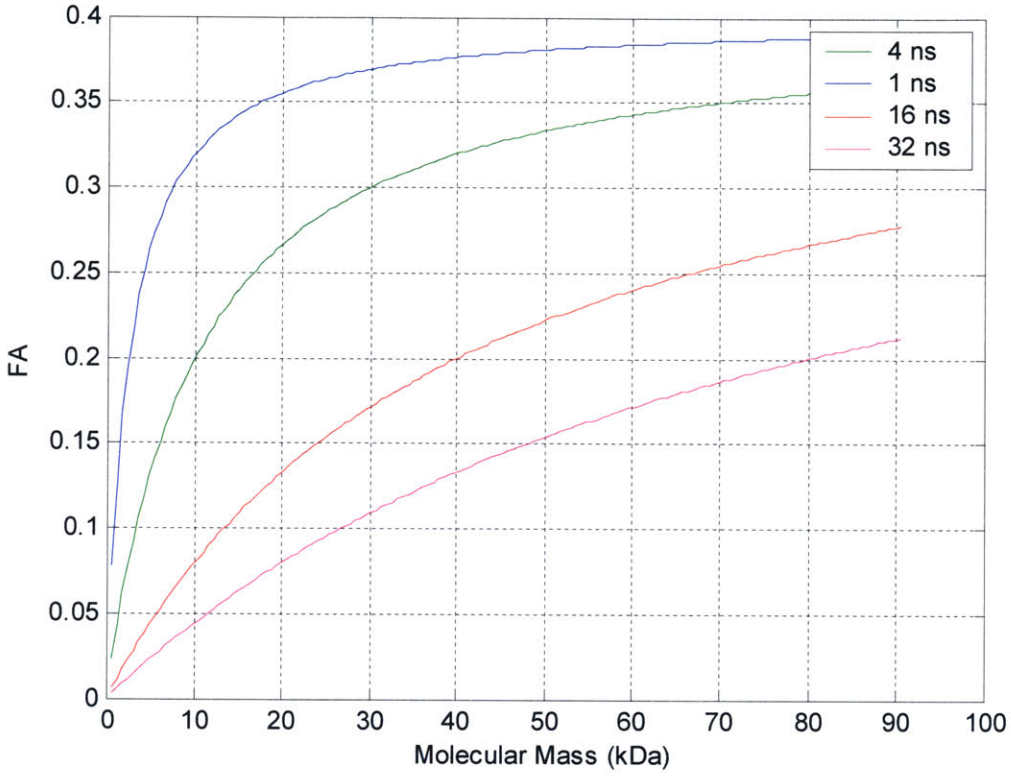


**Figure 2-6. Perrin's equation relating molecular mass and fluorescence anisotropy (FA) for various fluorescence lifetimes.**

An approximation for the optimal fluorescence lifetime may be found by constructing the equation for range from Perrin's equation and maximizing it. This equation, defining range as a function of fluorescence lifetime, is simply the difference between the anisotropy at the final mass, $m_2$, and the anisotropy at an initial mass, $m_1$. This relationship is plotted in Figure 2-7. The optimal lifetime for maximum range can be found by differentiating this relationship and setting it to zero. This operation leads to

$$\tau = \frac{m_1\sqrt{m_2} - m_2\sqrt{m_1}}{(\sqrt{m_1} - \sqrt{m_2})\cdot\beta}, \qquad \text{2-11}$$

where β is, as described above, a proportionality constant between the rotational correlation time and molecular mass.

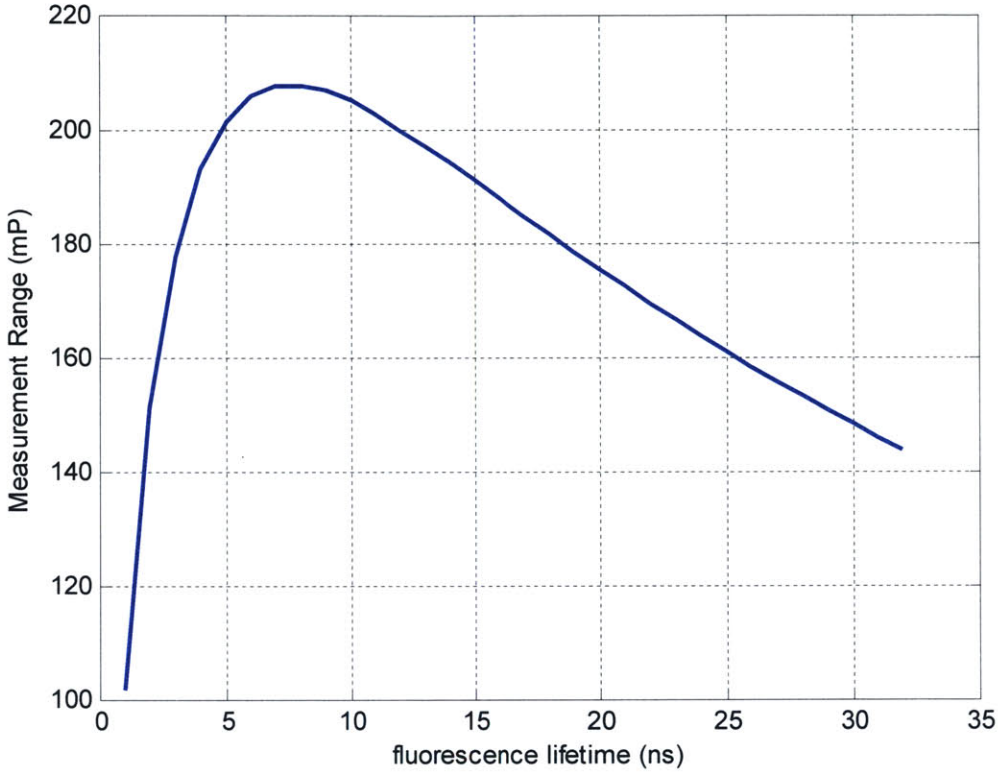


**Figure 2-7. Fluorescence anisotropy range for conversion of primer to product as a function of fluorescence lifetime.**

Equation 2-11 indicates the range is maximized for $\tau$ = 7.6 ns, given the assumptions described above. The maximum range, according to Perrin's equation, is 207 mP. Unfortunately, this estimate of optimal fluorescence lifetime is only approximate. DNA is not at all spherical, and as such, a 6 kDa primer does not behave like a 6 kDa sphere. It is likewise for the 60 kDa product DNA. Since both effectively behave as smaller molecules (faster rotation), it is reasoned that Perrin's equation provides an over-estimate of the optimal lifetime.

Table 2-1 provides a list of fluorophores that can be conjugated to DNA. Typical fluorophores such as fluorescein, TAMRA, and rhodamines have fluorescent lifetimes of

less than 4.3 ns. BODIPY conjugates can have lifetimes that are almost 50% longer, however one pays a price in terms of cost and Stokes shift width (narrow Stokes shift is undesirable since it limits discrimination between emission and excitation).

**Table 2-1. Common fluorescent conjugates and their fluorescent lifetimes**

| Fluorophore | Lifetime (ns) | Stokes Shift (nm) | Cost | Reference |
|---|---|---|---|---|
| Cy2 | 0.6 | 13 | $150 | A |
| NBD-hexanoic acid | 1.1 | 56 | $190 | A |
| NBD-F | 1.3 | 60 | $190 | A |
| NBD-Cl | 1.3 | 72 | $190 | A |
| TAMRA | 2.3 | 30 | $150 | A |
| Alexa Fluor 568 | 3.6 | 25 | $1,130 | B |
| FITC | 3.7 | 24 | $90 | A |
| Alexa Fluor 598 | 3.9 | 27 | $1,130 | B |
| Alexa Fluor 488 | 4 | 24 | $1,130 | C |
| Alexa Fluor 546 | 4 | 17 | $1,130 | B |
| fluorescein | 4.1 | 24 | $105 | A |
| 5-carboxyfluorescein | 4.2 | 36 | $105 | A |
| Rhodamine 123 | 4.2 | 26 | $320 | A |
| Rhodamine 6G | 4.2 | 24 | $320 | A |
| Rhodamine Green (RG) | 4.2 | 26 | $320 | A |
| Oregon Green 488 | 4.3 | 30 | $300 | A |
| Oregon Green 514 | 4.4 | 17 | $300 | A |
| BODIPY493 | 5.9 | 10 | $320 | A |
| BODIPY505 | 5.9 | 10 | $320 | A |

Notes:

Cost taken based on 1umol concentration from www.synthegen.com, Nov 25, 2003

*Reference* A: Nunnaly, B.K. et al, 1997

*Reference* B: www.probes.com/handbook/sections/0103.html

*Reference* C: www.probes.com/handbook/boxes/1572.html

Absent from this table are fluorescent lifetimes for popular conjugates such as 6-Hexachlorofluorescein (HEX), 6-Tetrachlorofluorescein (TET), and 6-carboxy-4',5'-dichloro-2',7'- dimethoxyfluorescein (JOE), which are not currently available in the literature. Also absent are nucleic acids stains such as ethidium bromide ($\tau$ = 19 ns), YOYO-1 ($\tau$ = 2.1 ns), and TOTO-1 ($\tau$ = 2.2 ns) (Sailer, Nastasi, Valdez, et. al, 1997). These dyes undergo a significant increase in fluorescence upon binding to dsDNA and therefore are less useful for FA application.

As observed in Figure 2-7, Perrin's equation predicts only limited sensitivity of optimized range to the fluorescence lifetime when the lifetime is in the region just below the optimal. This fact, compounded by the trade-offs present in the use of BODIPY conjugates, leads to the conclusion that any of the fluorophores with 4+ ns fluorescence lifetimes are suitable for use in this instrument.

### *2.2.c. Increasing Dynamic Range through Optimal Measurement Temperature*

Noting that Perrin's equation is also a function of temperature, another prudent question is whether there exists an optimal measurement temperature to maximize range. Again assuming the range is defined by Perrin's equation and molecules going from an initial mass of $m_1$ = 6 kDa to a mass of $m_2$ = 60 kDa (and including the additional assumptions described previously), the measurement range at temperatures from ambient to 373K is plotted in Figure 2-8. Because smaller molecules create greater depolarization (lower anisotropy) at decreasing temperature than larger molecules, the FA range is observed to increase with increasing temperature. Note however that the sensitivity of the range to temperature is low. For a 100K change in measurement temperature only a 5% increase in range is predicted. Temperature sensitivity is discussed more in the next section.

While Perrin's equation predicts that increasing measurement temperature can improve measurement range, there are important un-modeled dynamics to consider in the bond of the fluorophore to the primer. These dynamics are difficult to define quantitatively, however qualitatively it can be expected that at increasing measurement temperature the stiffness of this bond will decrease causing the fluorophore to increasingly exhibit motions that are independent of the motion of the mass to which it is attached. This concern is revisited in Chapter 4.

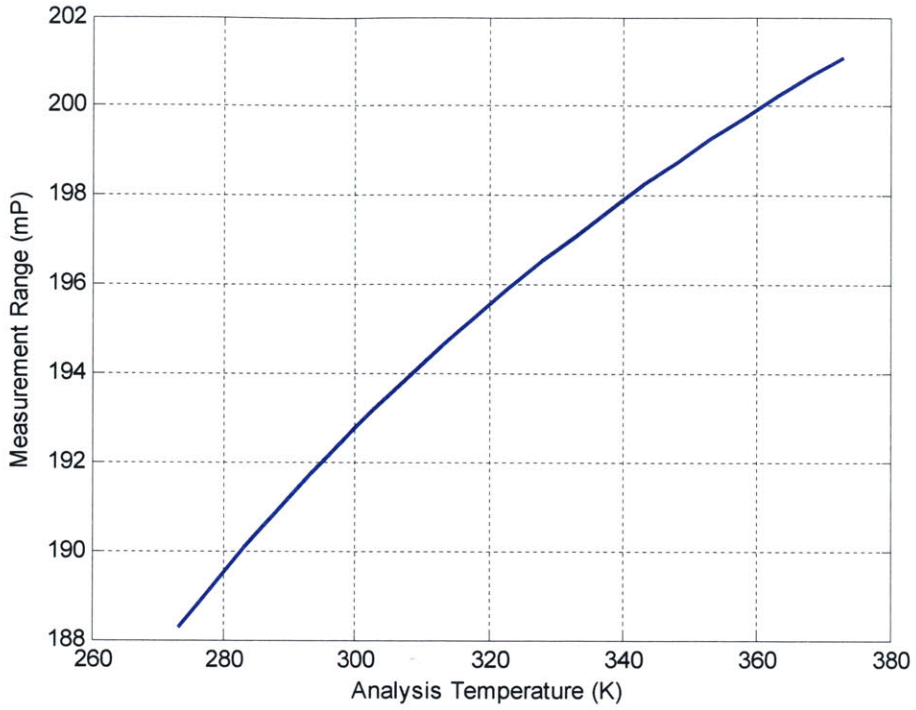


**Figure 2-8. FA range dependence on measurement temperature based on Perrin's Equation.**

*2.2.d. Increasing Dynamic Range through Resolution Enhancement: Temperature Stability*

Because of the temperature dependence of FA, a fluctuating solution temperature will result in a fluctuating FA measurement. Therefore, specifications on FA accuracy and variability define the requirements for temperature accuracy and stability for the thermal control system of the FA instrument.

To approximate the temperature sensitivity of FA measurement, Perrin's equation is differentiated with respect to temperature, yielding

$$\frac{d}{dT}(FA) = \frac{-r_o \cdot \mu \cdot V \cdot \tau \cdot R}{(\mu \cdot V + \tau \cdot R \cdot T)^2} \cdot \qquad \textbf{2-12}$$

Inserting the values for the parameters indicated in previous sections, Equation 2-12 is plotted in Figure 2-9. Observe from this figure that FA measurement of a solution of primer molecules at room temperature will have an FA/temperature sensitivity of ~0.31 mP/K. Product molecules are predicted to have a sensitivity of ~0.16 mP/K. The

sensitivity of a mixture is found by the average of the individual sensitivities weighted by the fractional intensity of the product and primer.

It was noted previously that Perrin's equation is based on the assumption of a spherical molecule. It was further noted that because of this structure, the effective volume in the context of Perrin's equation of the rod-like DNA molecules can be interpreted as smaller than is implied by its molecule weight. Thus, in this case, Perrin's equation is expected to *underestimate* the sensitivity of FA measurement to temperature.

While the discrepancy between the model's assumption and the actual structure of the measured molecules prohibits drawing a clear relationship, the analysis still provides helpful insights that can be used to generate a temperature stability specification, which is addressed in the next chapter.

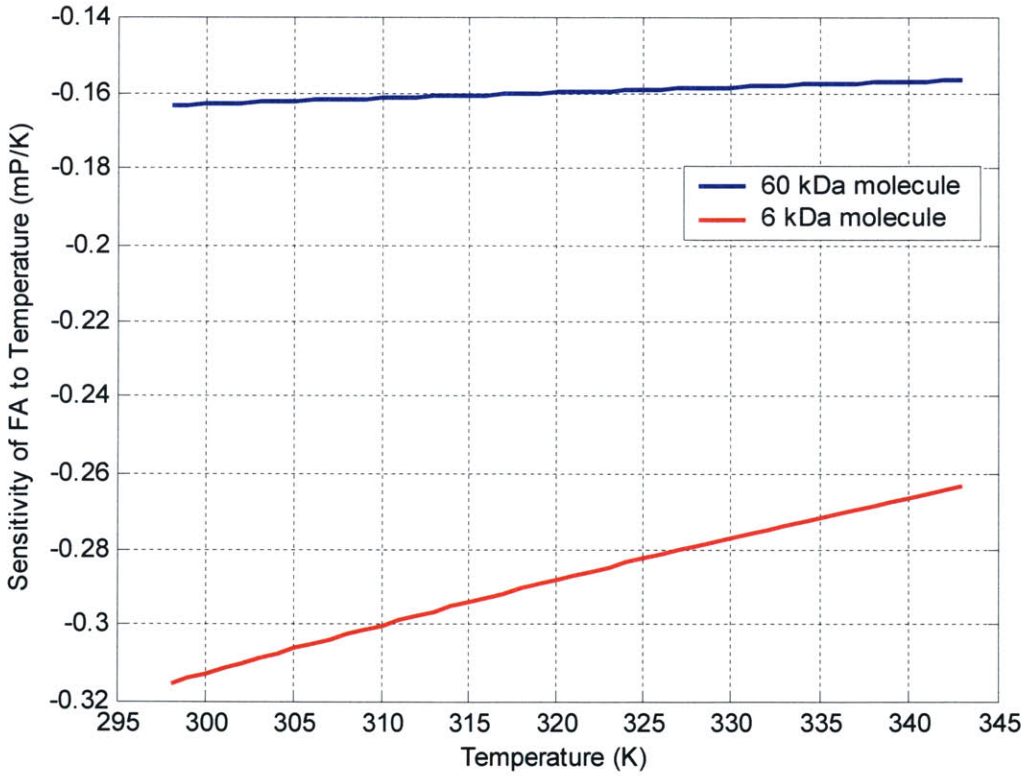


**Figure 2-9. Temperature sensitivity of FA measurement as a function of temperat**

# Chapter 3

# Design of Sample Holder

In this chapter, the design of the sample holder is presented. The sample holder includes not only a structure to confine the reagents of PCR but also the means of establishing its thermal control and optical alignment.

## 3.1. Design Requirements

### *3.1.a. Optical Considerations*

The optical system is discussed in detail in Chapter 4. To be compatible with the optical system, the sample holder should include a means for three dimension position adjustment for optical alignment and minimize reflected excitation intensity into the optical system.

### *3.1.b. Thermal Control*

The PCR solution must be moved through a series of temperatures to create the reaction. In one of these temperature steps, the FA of the solution must be measured. The specification for the necessary stability of the measurement temperature can be estimated from Perrin's equation as described in Chapter 2. This analysis shows an FA temperature sensitivity of *at least* 0.31 mP/K. Given an allowable fluctuation of ±0.01 mP, thermal fluctuations must be less than ±0.03 K. The allowable error for FA caused by thermal fluctuations (±0.01 mP) is set ~10× lower than the targeted resolution for two

reasons. First, the sensitivity estimate is a minimum sensitivity and thus room must be allowed for an experimentally observed larger sensitivity. Second, thermal fluctuations are only one of many factors contributing to error in the FA measurement. Temperature stability for other stages of the PCR process are much less important. The Roche Lightcycler, a real-time PCR instrument[♣] against which the FA instrument is benchmarked in this thesis, has a thermal stability of $< \pm 0.3$ °C.

There are additional design requirements for the dynamic temperature control performance. Taq polymerase is highly sensitive to temperatures >95 °C, therefore it is important that the controller not allow temperature overshoot when stepping to this level. An additional requirement is that of rapid temperature ramp rates to shorten reaction time. The FA instrument was designed to ramp at rates similar to those exhibited by the Roche Lightcycler, ~ 7°C/s.

### *3.1.c. Biological Considerations*

Efficient performance of the polymerase enzyme is critical to the success of the PCR reaction. As mentioned above, the Taq enzyme is known to be sensitive to temperatures above 95°C. Damage to the enzyme can also be caused by surface interactions (Shoffner, Cheng, Hvichia, et. al, 1996). Care must be taken to select a bio-compatible material to interface with the PCR solution.

Another important design requirement is that of cleanliness. Contaminants might be expected to damage the enzyme. Contaminates could also include DNA/RNA that would bias the PCR quantitation.

### *3.1.d. Evaporation Prevention*

The specific gravity of saturated water vapor at 95°C is ~20× greater than at room temperature. In an unsealed container, the PCR solution will quickly evaporate. Even small amounts of evaporation will cause concentration changes potentially affecting the reaction kinetics and the FA measurement.

---

[♣] As is explained in greater detail in Chapter 5, no existing real-time PCR instrument, including the Roche Lightcycler, uses FA to monitor real-time PCR. The temperature stability required of the Lightcycler are determined only by the needs of simple intensity measurement and reagent performance.

## 3.2. Final Sample Holder Design

### *3.2.a. Sample Holder Hardware*

Several iterations of the sample holder design were fabricated and tested before the final version was developed. Lessons learned from these earlier prototypes are described in the next section. The final version of the sample holder is shown in Figure 3-1.

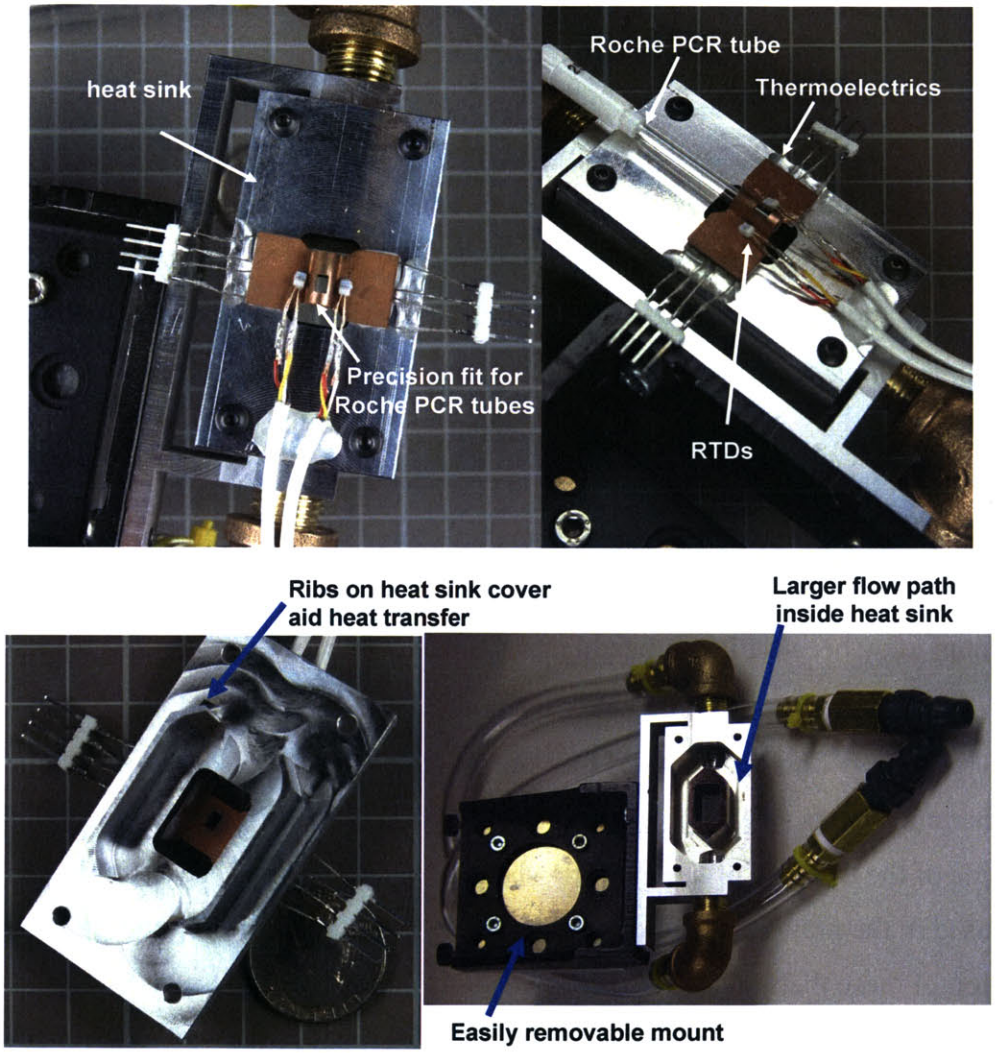


**Figure 3-1. Final Version of Sample Holder: (upper) Large aluminum heat sink stabilized temperature of backside of thermoelectric units. These units are sandwiched between the heat sink and copper sample holder. Two RTDs are bonded to sample holder face. Roche PCR tube fits tightly in precision bore of sample holder; (lower left) back side of heat sink cover plate features ribs to improve thermal contact to flowing, temperature regulated water; (lower right) Heat sink cover mounts to this heat sink base. Base has wide channel to allow rapid water circulation. Base is attached to easily removable mount.**

The sample holder is designed around 100 μL Roche PCR tubes normally used in its Lightcycler real-time PCR machine. These borosilicate tubes are 3.17 mm in diameter with 350 μm side walls. In the construction of the PCR tube, this glass tube is interference fit into a white plastic top. A removable plastic cap fits tightly in the top providing an effective seal against evaporation. These tubes are robust and of high optical quality. Designed for disposable use, each tube is less that $0.50 when purchased in reasonable quantity. Because they are designed for use in PCR instrumentation, their biocompatibility and cleanliness are assured.

The PCR tube mounts in a butterfly-shaped holder. The bore in which the PCR tubes rests was precisely sized to allow minimal clearance beyond the upper tolerance of the diameter of the PCR tubes. A series of PCR tubes were measured establishing the tolerance bounds on the capillary dimension as 3.160 mm to 3.187 mm. The bore was machined by multi-pass electro-discharge machining (EDM). In practice, even after this careful machining of the bore, a small amount of thermally conductive grease was striped down opposing sides of the tube before placing it into the sample holder in order to reduce the thermal resistance across the tube/copper interface.

The butterfly-shaped holder was manufactured from copper. In selecting this material, a low thermal time constant was desired . Copper was selected over an aluminum alloy because it exhibits higher thermal conductivity (Cu = 387 W/m·K, Al = 167 W/m·K) and lower specific heat capacity (Cu = 385 J/kg·K, Al = 896 J/kg·K).

The copper holder provides the thermal connection between the PCR tube and four thermoelectrics (www.melcor.com, HOT-2.0-18-F2A) that are mounted on the backside of the "wings" of the butterfly shape (2 on each side). The same thermoelectrics were used in the previous iteration of the device. Analysis regarding the sizing and selection of these thermoelectrics is provided in Section 3.3.

Two resistance temperature detectors (RTD) (F3105, www.omega.com) were mounted on the face of the butterfly-shaped copper holder for use in temperature control feedback loop. Multiple RTDs were used in order to build redundancy into the design. In fact, the connection to one of the RTDs was broken at some point during use. All RTD measurements utilized a 4-wire measurement configuration to minimize error caused by lead resistances.

The thermoelectrics transferred heat between the butterfly-shaped sample holder and a large aluminum heat sink. Aluminum was selected because of its high specific heat capacity-density product (for Al , $c_p \cdot \rho$ = 896 J/kg·K·2700 kg/m$^3$). Alternatives such as acrylic also provide a large heat capacity (for acrylic, $c_p \cdot \rho$ = 1470 J/kg·K·1120 kg/m$^3$), but at the expense of thermal conductivity and thermal expansion. Water, whose temperature was regulated by a recirculator (Model 1167, VWR), flowed through the heat sink to prevent drifting of the heat sink temperature. The thermal modeling of Section 3.3 clarifies how a varying heat sink temperature effectively acts as a disturbance to the thermal controller. The large size of this heat sink combined with its temperature regulation via circulating water minimizes this disturbance.

The heat sink was fastened to a mounting plate. Holes in the mounting plate mated with 4 precision pins fixtured to a 3-axis positioning stage. This mounting style allowed the sample holder assembly to be easily removed from the positioning stage and repeatably returned to its original position.

### *3.2.b. Control Strategy and Implementation*

As described in the introduction, PCR typically requires three temperature stages. The PCR protocols included denaturation (typically conducted at 95 °C), annealing (typically conducted at 50 °C) and extension (typically conducted at 72 °C).

In order to achieve rapid ramp rates, a non-linear bang-bang controller was digitally implemented as shown in Figure 3-2. This evolved from control schemes used in earlier prototypes of the sample holder. The aggressive nature of the bang-bang control method provided a reliable means to rapidly step to the desired temperature despite the thermal resistance of the glass capillary in the heat transfer path.

In Figure 3-2, the measured temperature at the RTD, $T_{act}$, is compared against the set temperature, $T_s$, to compute the error, e. An "if" statement selects the appropriate controller to apply (H1, H2, or H3) given the magnitude of the error. At the beginning of each stage, the H1 controller was used. For H1, the current output, i, was set to a constant maximum value. The H1 controller was selected by the "if" statement until $T_{act}$ had overshot $T_{set}$ by an amount specific to each PCR stage. This overshoot event

triggered a switch to the H2 controller. For H2, the current output, i, was again set to a constant value, but this time this value was set at a low level. The H2 output current was set at ¼ of the steady state current required to maintain $T_{set}$ at equilibrium. The H2 controller remained in the loop until the temperature error returned to within limits specific to each PCR step. With this condition met, the third controller, H3, was engaged. H3 was a simple Proportional-Integral-Derivative controller. The gains for the PID control were the same for all PCR steps. Computer simulation of the modeled system to roughly determine acceptable gain parameters (See Section 3.3.d). Further tuning was performed experimentally. A summary of the "if" statement switching rules is shown in Figure 3-3. Further insight into the discretization of the H3 controller is provided in Section 3.3.e.

This control strategy was implemented digitally as part of a Visual Basic 6.0 program which controlled the instrument's operation. Four-wire RTD measurements were read by an Agilent 34970A data acquisition unit. This measurement was transmitted to the PC by IEEE 488 communication. At every cycle, a command was sent to a bipolar current supply (BOP50-8D, KEPCO), again by IEEE 488 communication, refining the current sent to the thermoelectric.

The Agilent 34970 data acquisition unit uses a dual-slope analog-to-digital A/D converter chip which integrates incoming charge on a precision capacitor for a specified period of time. This time interval is typically an integral number of power line cycles (PLC) such that 60 Hz noise is sharply attenuated. The data acquisition unit was configured to integrate charge for 1 PLC in this application. This, however, did not define the sampling rate. Communication with the data acquisition system requires that an ASCII command be sent and processed to initiate the scan, dump the scan to the acquisition system's buffer, and finally retrieve the results. Switching between channels in conducting the scan is performed by mechanical relays (as opposed to MOSFET devices). In practice, it is the communication, processing, and switching that limit sample rate with the Agilent 34970. A sampling rate of 1 sample per 170 ms was achieved in the final implementation. While slow in terms of rates achievable by other acquisition systems, the Agilent 34970 provided adequate speeds with excellent noise rejection. RMS noise levels on temperature measurement were typically below 1 mK.

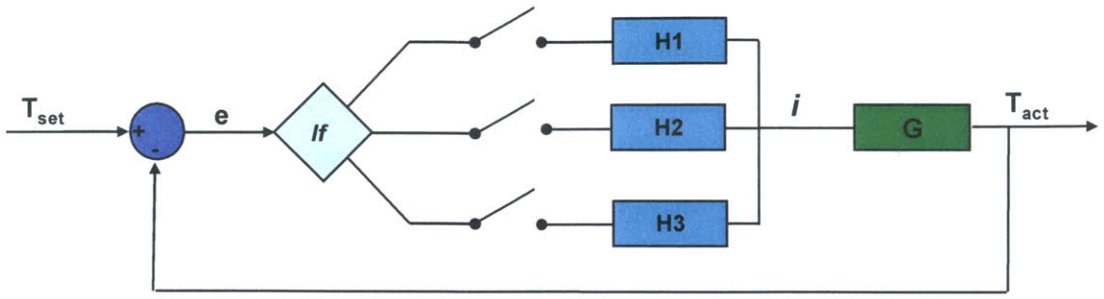


**Figure 3-2. Block diagram for control loop.**

$$H1 \quad ==> \quad i = i_{max}$$

$$H2 \quad ==> \quad i = i_{small}$$

$$H3(s) = \frac{i(s)}{e(s)} = K_P + \frac{K_I}{s} + K_D \cdot s$$

$$i_j = i_{j-1} + K_P \cdot (e_j - e_{j-1}) + K_I \cdot e_j \cdot \Delta t + \frac{K_D \cdot (e_j - 2 \cdot e_{j-1} + e_{j-2})}{\Delta t}$$

**Figure 3-3. Summary of "If" statement switching rules.**

The resulting thermal profile is shown in Figure 3-4 below. A direct measurement of the PCR solution temperature was desired in order to adjust the control parameters and demonstrate thermal performance. An RTD identical to those used on the front surface of the sample holder was made submersible by coating its electrical leads in thin layer of nail polish. Measurements taken by this RTD are shown by the dashed green curve.

Because the polymerase can be damaged by temperatures above 95 °C, the controller was designed to approach the denaturation temperature less aggressively than the target temperatures of other stages. The slower rise observed in Figure 3-4 A was done purposefully recognizing that the thermal time constant of the RTD (> 500 ms ) forces the measured temperature to reflect a dampened, delayed version of the actual solution temperature. Additionally, the low thermal conductivity of water causes for a

radial gradient in temperature within the capillary. The measured RTD temperature reflects only an average of this gradient.

Figure 3-4 B is an enlarged plot of the extension stage thermal profile. FA measurement is engaged after the software detects that the measured temperature (at the externally mounted RTD) has stabilized based on an eight point average. The internally measured temperature, again shown by the dashed green line, indicates temperature fluctuations less than ±0.03 °C.

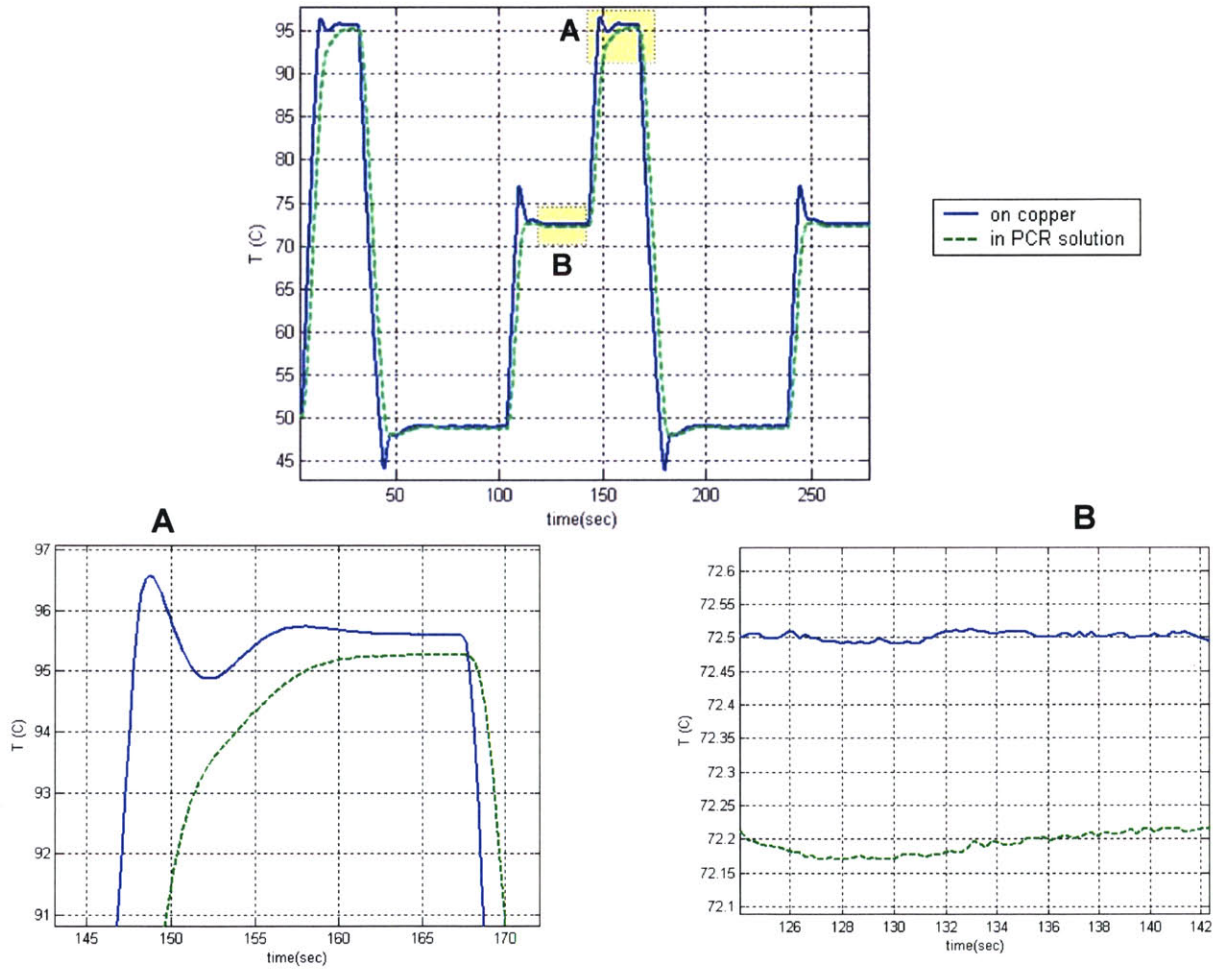


**Figure 3-4. Example thermal profile data for final controller design. Upper plot shows two complete thermal cycles. Highlighted squares A and B are shown expanded in bottom left and right, respectively. The solid blue line is the temperature measured at the copper ($T_{act}$). The dashed green line is the temperature measured by an RTD submerged in the PCR solution.**

## 3.3. Lessons from Earlier Design Iterations

### *3.3.a. Initial Prototype*

The first sample holder constructed for this thesis is shown in Figure 3-5. The sample holder was designed around a commercially available cuvette (20 μL, Hellma 105.252-QS). The unit is assembled from custom machined copper components joined by thermally conductive epoxy (Omegabond 101, Omega, Inc.). A resistance temperature detector (RTD) (F3105, www.omega.com) was mounted external to the cuvette to monitor the sample holder temperature. Two thermoelectrics (TM-2581, TE Technology, Inc.) were used to modulate sample holder temperature. One side of the thermoelectrics is held at constant temperature by liquid cooled heat sinks.

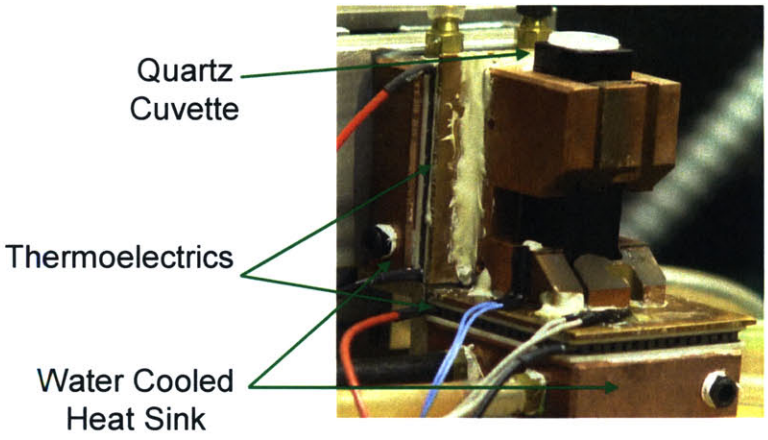


**Figure 3-5. Prototype sample holder utilizing a quartz cuvette.**

Achieving fast ramp rates, fast settling times, and stable steady state performance was found to be difficult with this sample holder design. The sizable thermal mass of the sample holder as well as the thermal resistance of the epoxy created a large time constant for the system.

In an effort to achieve better performance, a non-linear digital controller was implemented. A diagram of the controller is shown in Figure 3-6. The system is set up as a simple feedback system with the caveat that an if-statement conditionally switches the controller (H1 or H2) computing the input ($i$) to the plant.

Such a configuration was particularly desirable in this case because it allowed a large gain controller (H1) to define the input initially (to achieve fast ramp rates). Then, when the error (e) between the set temperature ($T_{set}$) and the actual temperature ($T_{act}$) was reduced to a pre-defined level, the if-statement could change the controller to one of lower gain (H2) (to guarantee stability, avoid overshoot, and achieve the steady state performance specs).

The controllers (H1 & H2) for this prototype were simple proportional-integral (PI) controllers with saturation limiters to prevent them from commanding plant inputs (currents) greater than the thermoelectrics could handle. An example of the system performance is shown in Figure 3-7. Unfortunately, this combination of sample holder geometry and control strategy did not provide adequate performance. Observe in the figure that while adequate ramp rates were achieved, the stability near the set temperature is poor. While it might be arguable that the stability for the PCR steps (Denature, Anneal, and Extend) were adequate, the stability during the FA measurement was clearly not.

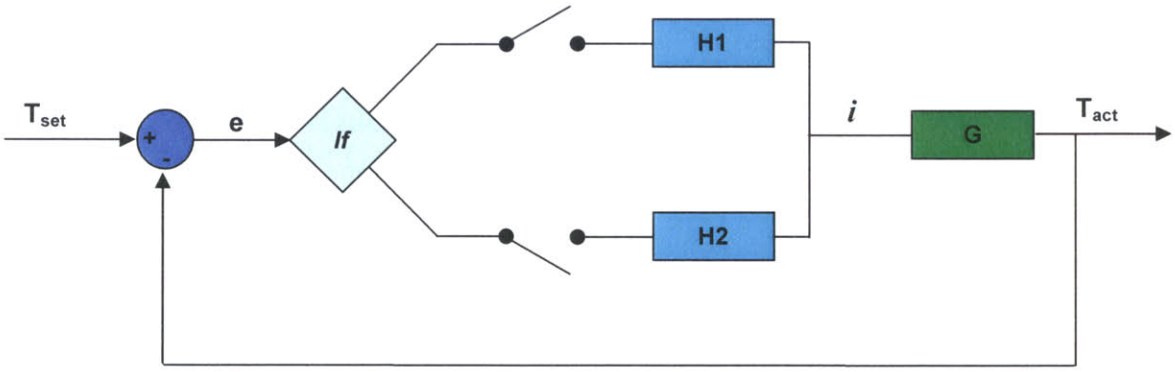


**Figure 3-6. Diagram of controller implemented for FA detection system.**

After applying and tuning several variations on the controllers and achieving unsatisfactory results, it was decided that significant modifications were necessary in the plant (sample holder). The large time constant (i.e., the product of its thermal capacitance and resistance) of the existing system created a slow pole that limited the dynamic performance. High gains were also not possible (discussed in more detail for

revised prototype design) because of loss of stability and the non-linearities caused by saturation limits of the thermoelectrics. Therefore, a redesign was needed.

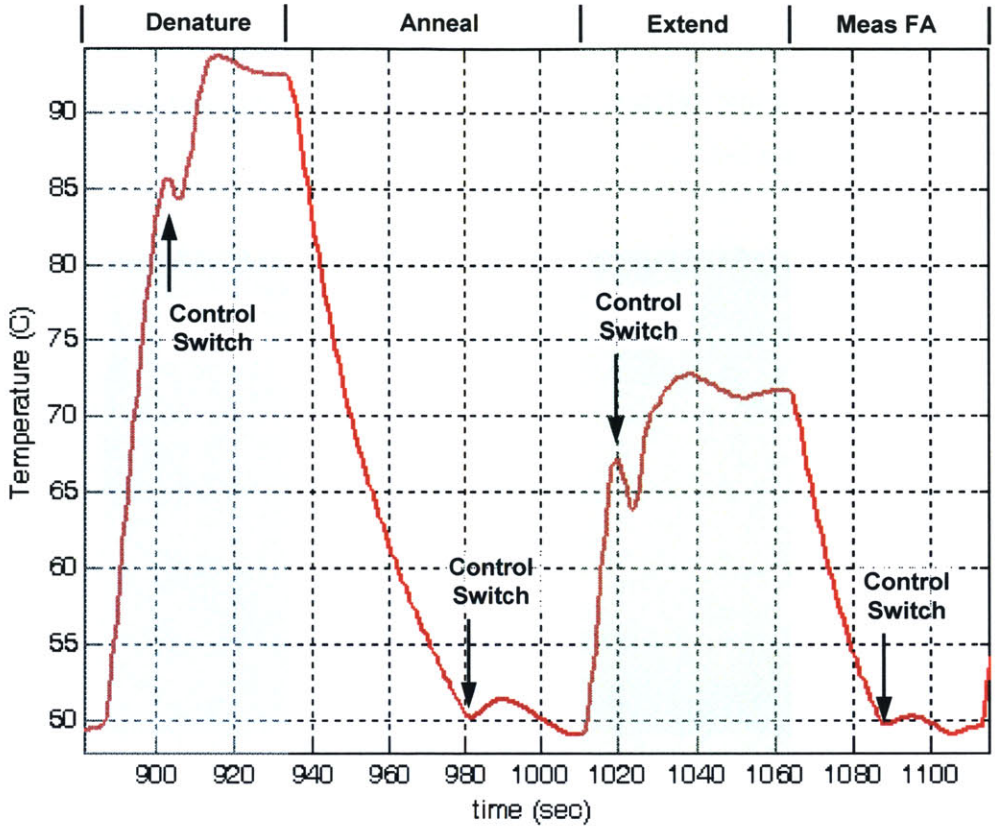


**Figure 3-7. An example of the dynamic thermal performance for the first sample holder prototype and its controller.**

*3.3.b. A design of reduced thermal time constant*

A new sample holder was designed with the intent of minimizing thermal capacitance and resistance. The first design change reviewed the decision to use a commercial sample cuvette. There is a large legacy of instrumentation that utilizes standard cuvettes. These instruments are all built to house a cuvette that has base dimensions of 10 mm × 10 mm. As small volume analysis has come into demand, the side walls of the cuvette have simply become thicker. This thickness of glass or plastic acts as a large thermal resistance between the thermoelectrics and the DNA sample. Another reason to eliminate the commercial cuvette was sample volume requirements. The 15 uL cuvette employed in the initial sample holder prototype was selected because

it was the smallest volume cuvette that could be found that had a suitable internal geometry for FA measurement (smaller volume cuvettes exist in a "flow through" arrangement such as those for cytometry, however these were unsuitable). For these reasons, the use of a commercial cuvette was eliminated. Instead, the new design was based on an integrated sample volume. An example concept for an integrated sample volume is shown in Figure 3-8.

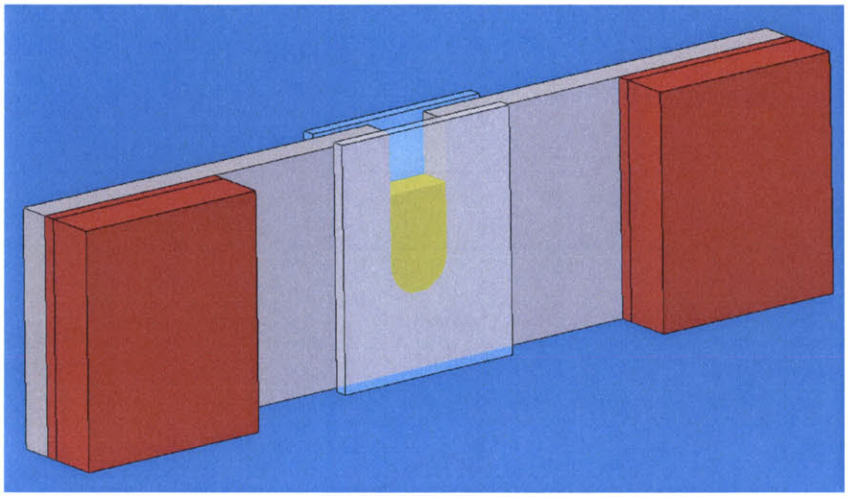

**Figure 3-8. Concept for new sample holder. Red components are thermoelectrics, yellow represents the sample, gray is the main sample holder substrate.**

A trade off existed in making the sample holder large enough to accommodate the necessary thermoelectrics (to achieve the desired ramp rates) while still keeping the system as small as possible. The sizing requirements for the thermoelectrics and the main substrate can be roughly approximated by constructing a simplified model. In creating this model, first note that the design of Figure 3-8 is symmetric. Therefore, it is necessary to model only one half of the system. Next, assume that all thermal resistances are negligible. This is not an acceptable assumption in defining the dynamic behavior of the plant; however, it will suffice for rough sizing of the thermoelectrics. This assumption allows the thermal capacitance of the silicon and water to be represented as a single lumped capacitance that is the sum of their individual capacitances. The rest of the model defines the thermoelectric.

Physics of Thermoelectrics

Thermoelectric modules are solid-state heat pumps that operate on the Peltier effect. This effect is a phenomenon by which heat and current flows are coupled at the junction of two dissimilar materials. A thermoelectric module, illustrated in Figure 3-9, consists of an array of p- and n- type semiconductor elements heavily doped with electrical carriers. The array of elements is soldered so that it is electrically connected in series and thermally connected in parallel. This array is then affixed to two ceramic substrates, one on each side of the elements.

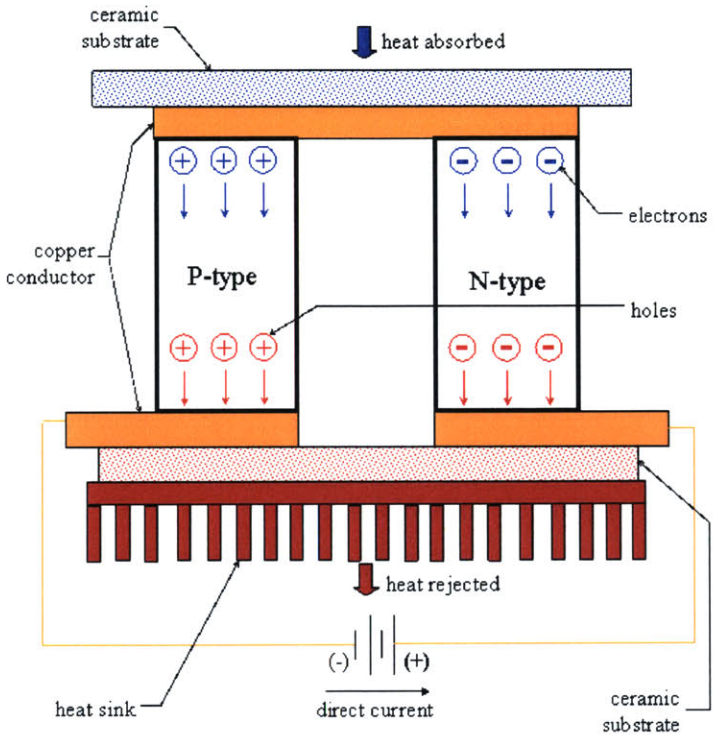


**Figure 3-9. Illustration of thermoelectric structure and function.**
**(Figure taken from www.tetech.com.)**

When an electron moves from the copper conductor to the p-type semiconductor, it does so by filling a "hole" in a semiconductor atom's valence band. This brings the atom to a lower energy level and heat is released. When an electron leaves the p-type semiconductor at the opposite end, a "hole" is created. Thus energy is absorbed. A similar but opposite process occurs in the n-type semiconductor. Electron conduction

occurs through conduction bands. The atom moves to a higher energy state thus absorbing energy. When the electron exits the n-type semiconductor, its energy state is reduced, releasing energy. Thus, in p-type semiconductors, a heat flux exists in opposite direction to that of the current flux. In n-type semiconductors, the heat flux flows in the same direction as the current flux.

Because of the series arrangement of p- and n- type materials in the thermoelectric, heat is always absorbed at one side and released at the other. The direction of the current flow defines which is which. The magnitude of the heat flow is related to the current by a material property of each semiconductor known as the Peltier coefficient ( $\Pi_n$ ). The heat flow creates a temperature gradient across the device which in turn creates a competing conductive heat flow. The net rate of energy transfer across the thermoelectric is thus given by

$$Q = I \cdot (\Pi_1 - \Pi_2) - \left( \frac{A_1 \cdot k_1}{L} + \frac{A_2 \cdot k_2}{L} \right) \Delta T , \qquad \textbf{3-1}$$

where I is the current through the thermoelectric, $A_1$ and $k_1$ are the total cross sectional area and thermal conductivity, respectively, of the p-type semiconductor, and $A_2$ and $k_2$ are the total cross sectional area and thermal conductivity, respectively, of the n-type semiconductor. The parameter, L, represents the thickness of the semiconductor elements (constrained by geometry to be the same).

This model of the thermoelectric heat transfer ignores thermal capacitance as well as joule heating. These details will be added to the model in a later section.

*First Order System Model*

A circuit diagram describing the model presently defined for the system plant is shown in Figure 3-10. The thermoelectric is represented by the flow source $Q_p$ and the thermal resistance $R_p$. Note that these terms correspond to the components of Equation 3-1,

$$Q_p = I \cdot (\Pi_1 - \Pi_2) \qquad \textbf{3-2}$$

and

$$Rp = \frac{A_1 k_1}{L} + \frac{A_2 k_2}{L} . \qquad \textbf{3-3}$$

The thermal capacitances of the sample holder substrate and sample solution are given by $C_{si}$ and $C_w$, respectively. The capacitance of the transparent material (glass) is neglected. The final component shown in the model is a "battery" (voltage source) which defines Tph as a constant. This voltage source represents the use of a water cooled heat sink that maintains a constant temperature on one side of the thermoelectric.

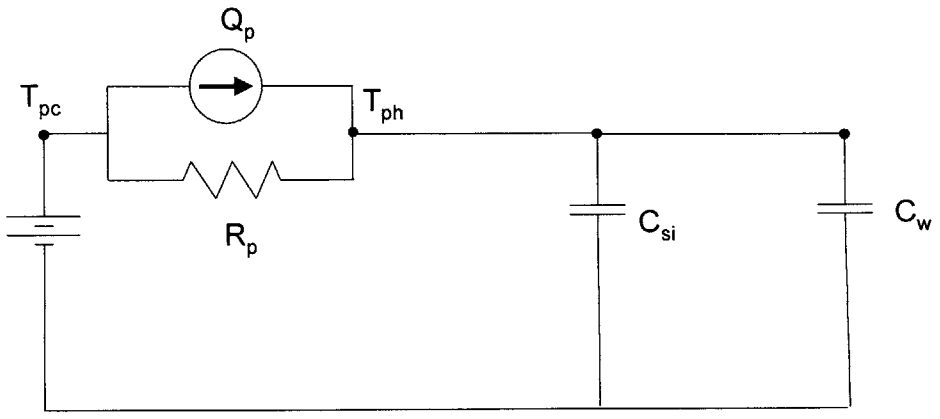


**Figure 3-10. Equivalent circuit diagram representing simplified heat transfer model.**

Kirkhoff's current law can then be applied to the node marked $T_{pc}$. The summation of flows at this node are given by

$$Q_p = \frac{\left(T_{ph} - T_{pc}\right)}{R_p} + \left(C_{si} + C_w\right) \cdot \frac{dT_{pc}}{dt} \qquad \textbf{3-4}$$

Material Selection

In order to compute specifications required of the thermoelectric, the material for the main sample holder substrate must be defined. As described earlier, the entire design seeks to minimize the thermal time constant. As such the material desirably has high thermal conductivity and low specific heat.

In addition, other non-thermal design considerations were highly relevant in material selection. Matched thermal expansion coefficients for the transparent material and the main sample holder substrate were desirable to prevent delamination of the bonded materials. In addition, matched thermal expansion coefficients minimize internal

stresses in the transparent medium. Such stresses can result in birefringence adding error to FA measurements.

Compatibility with the biological molecules under analysis was also a critical factor. The polymerase enzyme is known to be easily affected by undesirable surface chemistries. Any surface contacting the sample solution should be inert.

The best combination of materials was found to be silicon for the sample holder substrate and a silicon dioxide glass for the transparent material. Silicon dioxide is a highly inert material that is routinely used for many biological applications. Silicon has been shown to have compatibility issues with PCR however chemical modifications of the surface (such as deposited or thermally grown silicon dioxide) are known to correct this problem (Shoffner, Cheng, Hvichia, et. al, 1996; Cheng, Shoffner, Hvichia, et. al, 1996). While the thermal conductivity of silicon dioxide is not high (k = 1.13 W/m·K), the primary thermal pathway is through the silicon. Silicon has a large thermal conductivity (k = 148 W/m·K) and reasonably low specific heat (712 J/kg·K).

Thermoelectric Selection

Special thermoelectrics manufactured with high temperature solder are required for this application because of the temperatures at which DNA denaturation is performed (>94 °C). This limited the selection of commercially available thermoelectrics. Even more limiting was a desire to buy in-stock thermoelectrics. Several manufacturers listed products in the size and power range desired, but quoted a delivery time of multiple months.

The high-temperature thermoelectrics chosen for the application were selected from Melcor, Inc. (www.melcor.com). An example of the available selection is given in Table 3-1.

The thermoelectric selected for the task was the HOT 2.0-18-F2A from TE Technology, Inc. The specifications given for thermoelectrics include the maximum heat pumping capability, $Q_{max}$, and the maximum temperature differential, $DT_{max}$. The maximum heating pumping rate occurs and is measured when there is no temperature gradient across the thermoelectric, i.e., $T_{pc} = T_{ph}$. The maximum temperature difference occurs when the net amount of heat pumped by the thermoelectric is zero, i.e., in

Equation 3-1, Q = 0. $R_p$ can be approximated from these specifications where $R_p = DT_{max} / Q_{max.}$ A graphical representation of Equation 3-1 based on the specs of the chosen thermoelectric is shown in Figure 3-11.

**Table 3-1. Example list of commercially available small package, high-temperature thermoelectrics. (Adapted from www.melcor.com)**

| Catalog # | Imax (Amps) | $T_H$ = 25°C | | | Dimensions (mm) | | |
|---|---|---|---|---|---|---|---|
| | | Qmax[1] (Watts) | Vmax (Volts) | DTmax (°C) | width | length | thickness |
| H OT 1.2-18-F2A | 1.2 | 1.46 | 2.18 | 64 | 6 | 7.2 | 2.7 |
| H OT 1.2-24-F2A | 1.2 | 1.97 | 2.7 | 64 | 6.6 | 10.8 | 2.5 |
| H OT 1.2-30-F2A | 1.2 | 2.43 | 3.63 | 64 | 6.2 | 12.3 | 2.4 |
| H OT 1.2-31-F2A | 1.2 | 2.51 | 3.87 | 64 | 8.8 | 11 | 2.7 |
| H OT 1.2-65-F2A | 1.2 | 5.34 | 7.8 | 64 | 13.2 | 13.2 | 2.7 |
| H OT 1.5-18-F2A | 1.5 | 1.82 | 2.18 | 64 | 6 | 7.2 | 2.4 |
| H OT 1.5-24-F2A | 1.5 | 2.42 | 2.7 | 64 | 6.6 | 10.8 | 2.2 |
| H OT 1.5-30-F2A | 1.5 | 3.03 | 3.63 | 64 | 6.2 | 12.3 | 2.2 |
| H OT 1.5-31-F2A | 1.5 | 3.13 | 3.87 | 64 | 8.8 | 11 | 2.4 |
| H OT 1.5-65-F2A | 1.5 | 6.57 | 7.8 | 64 | 13.2 | 13.2 | 2.4 |
| H OT 2.0-18-F2A | 2 | 2.43 | 2.18 | 64 | 6 | 7.2 | 3.6 |
| H OT 2.0-24-F2A | 2 | 3.32 | 2.7 | 64 | 6.6 | 10.8 | 2 |
| H OT 2.0-30-F2A | 2 | 4.04 | 3.6 | 64 | 6.2 | 12.3 | 1.8 |
| H OT 2.0-31-F2A | 2 | 4.18 | 3.7 | 64 | 8.8 | 11 | 2.2 |
| H OT 2.0-65-F2A | 2 | 8.76 | 7.8 | 64 | 13.2 | 13.2 | 2.2 |

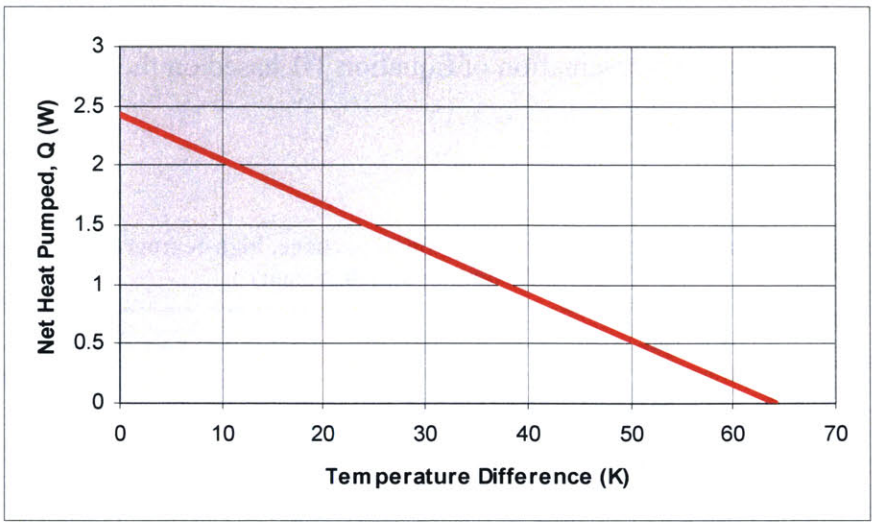


**Figure 3-11. Relationship between net amount of heat pumped and the temperature difference across the thermoelectric as given by Equation 3-1 for model HOT 2.0-18-F2A.**

Effective sizing of the selected thermoelectric is demonstrated under the following assumptions. First, assume $T_{pc}$ is set to 50 °C by the water cooled heat sink. Next, assume that the thermoelectric is to be sized for 3 uL (allowing for excess capacity in case of need to work at volumes larger than the targeted 1 uL for trouble shooting purposes). In addition, assume a total silicon substrate volume of 210 $mm^3$. Using symmetry of the system, one half of these volumes can be used to size the thermoelectric needed on each end of the sample holder. The thermal capacitance for the silicon, given by $C = \rho \cdot V \cdot c_p$ where $\rho$ is the density (2328 $kg/m^3$), V is the volume (105 $mm^3$), and $c_p$ is the specific heat (712 J/kg K), is $C_{si}$ = 0.174 J/K. The thermal capacitance for the water, with parameters $\rho$ = 1 kg/L, V = 1.5 $mm^3$, and $c_p$ = 4182 J/kg K, is $C_w$ = 0.006 J/K.

Given a desired ramp rate dT/dt = 3 °C /s from a start point of $T_{ph}$ = 70 °C, the required thermoelectric pumping power may be computed. Plugging all values into Equation 3-4, the power is found as $Q_p$ = 1.22 W. This calculation states that a thermoelectric with a $Q_{max} = Q_p$ and an effective thermal resistance of $R_p$ can increase the temperature of thermal masses ($C_{si}$+$C_w$) initially at 70 °C at a rate of 3 °C /s.

The $Q_{max}$ for the HOT-2.0-18-F2A is 2.43 W. While other thermoelectrics would have also met these specifications, at the time of ordering, this was one of the few models in stock at suitable quantity. To allow for excess capacity given the simplifying

assumptions of this model, the new design used 2 of these thermoelectrics on each end. While a 4× underestimate in the required power was unlikely, over-powering the system had the added bonus of keeping the required input current very low. As will be discussed, joule heating of the thermoelectric acts as a non-linear heat source that can be problematic for modeling and control. Utilizing more thermoelectric capacity than necessary allows joule heating problems to be minimized by keeping the current low.

*Prototype II Design*

The final design of prototype II is shown in Figure 3-12 integrating all four thermoelectrics (red). These mount to a silicon sample holder substrate to which two pieces of Pyrex glass also bond. The PCR solution is housed in the region between the Pyrex sheets.

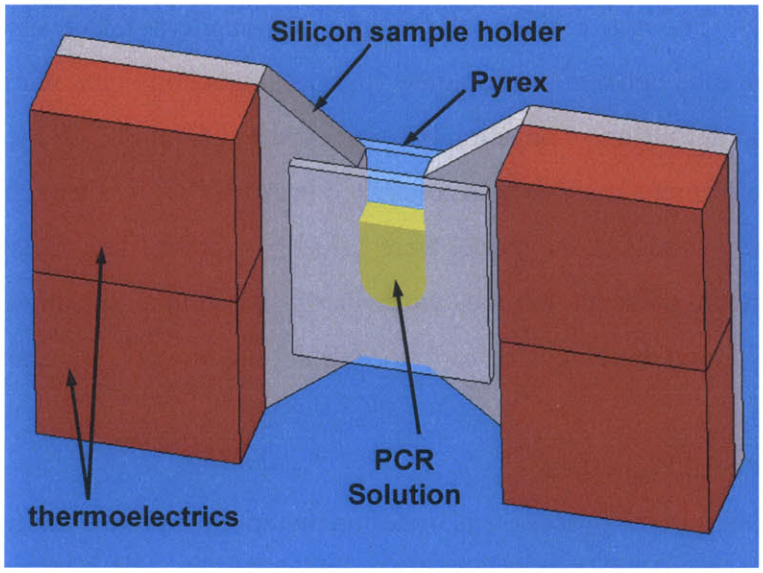


**Figure 3-12. Final design for sample holder includes 4 thermoelectrics, model HOT-2.0-18-F2A.**

*3.3.c. Steady State Thermal Variation: Finite Element Analysis (FEA)*

The simplified model of Figure 3-10 allowed the selection of thermoelectrics of sufficient pumping capacity to attain the desired dynamic performance (in particular, the desired ramp rate). Another design concern is the steady state performance. At equilibrium a temperature distribution will exist across the sample holder. The end points of this distribution will be regulated by the action of the thermoelectric. Points in

between will be subject to convective heat loss and thus deviate from that of the regulated thermoelectrics. The lumped parameter model of Figure 3-10 is not adequate to describe this distribution. This distribution was studies with a new model using finite element analysis.

The process began with the solid model similar to that shown in Figure 3-12 created in SolidEdge v14. The model was an assembly of seven components. These include the two pieces of $SiO_2$ (Pyrex) glass, the silicon substrate, and four parts modeling the four thermoelectrics. These four parts did not represent the unique volumes of the four thermoelectrics as is shown in Figure 3-12. Instead, a single volume was created for each pair of thermoelectrics except for a thin planar volume located at the interface of the substrate. This description is clarified by inspecting Figure 3-13, which contains the steady state results of the analysis. The volumes in grey represent each pair of thermoelectrics. The blue region at the interface of the thermoelectrics and the silicon substrate (in orange) is defined as a separate volume. The component distinctions are important for load definition. The assembly was exported from SolidEdge as a parasolid.

The finite element analysis was conducted in ANSYS 7.0. Once the parasolid was imported, the volumes of the model were "glued" together. This function assures that mesh points from adjacent volumes are properly shared upon meshing. Next, using the "smart mesh" automated meshing tool in ANSYS, the model was meshed.

Definition of Material Properties

The next step in the process was to define material properties for each of the separate volumes of the model. Individual volumes originally defined in the parasolid model persist even after "gluing" and meshing. Only four material types were used. The materials, the relevant properties, and their values are shown in Table 3-2.

The thermoelectrics are, in reality, assembled from a variety of materials such as the alumina ceramic plates on their exterior, the n- and p- type bismuth semiconductors sandwiched inside, and the solder and deposited copper layers that complete the electrical connection between the bismuth elements. Modeling all of these components would have required fine geometric detail. ANSYS, by default, uses a finer mesh in regions of fine geometry to adequately describe heat transfer in these regions. The number of mesh

points is limited both by reasonable limits on computation time and by the limits of the Bioinstrumentation Lab license for ANSYS. Thus it was desirable to keep the geometry of the model simple and describe material properties that reflected the thermal behavior of the thermoelectric assembly.

Material properties were computed to correctly reflect the thermal capacitance and resistance of the thermoelectric assemblies. The actual thermal resistance was computed from the specifications given in Table 3-1 where $R = DT_{max}/Q_{max}$. The net thermal resistance was found to be 32 W/m·K. The net thermal capacitance was computed by summing the capacitances of the individual components where each capacitance is given by $C = \rho \cdot V \cdot c_p$. Densities ($\rho$) for alumina and bismuth are 3960 kg/m$^3$ and 7530 kg/m$^3$, respectively. Specific heat capacities ($c_p$) are 850 J/(kg K) and 544 J/(kg K) for alumina and bismuth, respectively. Dimensions to compute volumes were measured by a micrometer (0.01 mm resolution). The net capacitance was found to be 0.278 J/K.

**Table 3-2. Material properties defined in ANSYS analysis**

| Material | Thermal Conductivity (W/m·K) | Specific Heat Capacity (J/kg·K) | Mass Density (kg/m$^3$) | Product of Density and Heat Capacity (J/m$^3$K) |
|---|---|---|---|---|
| Silicon (Si) | 148 | 712 | 2328 | 1.66E+06 |
| Pyrex ($SiO_2$) | 1.13 | 753 | 2230 | 1.68E+06 |
| Water ($H_2O$) | 0.61 | 4182 | 1000 | 4.18E+06 |
| "Thermoelectric" | 1.36 | 850 | 3960 | -- |

The thermoelectric model was composed of a rectangular volume whose cross sectional (face) area was the same as the (face) area of the actual thermoelectrics. The specific heat capacity of alumina was arbitrarily chosen to be the specific heat capacity of the thermoelectric model. The thermal capacitances were made the same by adjusting the thickness of the model. The corrected thickness was 1.9 mm. This number is smaller than the actual thickness (2.6 mm), which is consistent with both the use of a specific heat value that was higher than the mean of the materials and consistent with neglecting

the air space between bismuth elements. With the volume thus defined, the thermal resistance of the model was made the same as the actual thermoelectric by computing an "equivalent" thermal conductivity. The corrected thermal conductivity for the model was 1.36 W/m·K. Thermal conductivities for alumina and bismuth are 30 W/m·K and 1.5 W/m·K, respectively. The conclusion that the model's thermal conductivity should be less than either of these is again consistent with the model's basic solid shape which neglects the air space present between the bismuth elements in the actual thermoelectric.

Boundary Conditions

Two boundary conditions were applied in the model. The first was that of convective heat loss to all free surfaces. For the solution shown in Figure 3-13, a convection coefficient of 5 $W/m^2K$ and an ambient temperature of 295 K were assumed.

The second boundary condition was to impose a constant temperate on the back surface of the thermoelectrics (i.e., the surface of the thermoelectrics opposite that of their interface with the silicon substrate). This boundary condition models the water cooled heat sink to which the thermoelectrics are mounted. The constant temperature defined for the solution shown in Figure 3-13 was $T_c = 323$ K.

Loading

Ideally the thermoelectric heat pumping would be modeled by an imposed heat flux. Unfortunately, the definition of such surface loads produced nonsensical results. Available load settings of this type seem to be intended for surface rather than volumetric modeling in ANSYS, which may explain the solution failure. Alternatively the failure may have been due to a conflict between the heat flux load and the constant temperature boundary condition. These two were defined on separate but co-planar surface areas on each side of the thermoelectric.

An alternate strategy was thus employed to model the heat pumping phenomenon of the thermoelectrics. As discussed, the Peltier effect causes energy to be released as electrons travel across the junction of dissimilar materials. Therefore, rather than define a heat flux, a load was imposed for volumetric heat generation in the thin volume of the thermoelectric defined at the interface of the grey thermoelectric and the orange silicon

substrate shown in Figure 3-13. It was reasoned that this heat generation would well mimic the physics of energy release due to the changing energy levels of the electrons at this plane of material interfaces. The volumetric heat generation load was defined such that 1 W was being "pumped" by each of the four thermoelectrics.

The FEA solution for the steady state thermal distribution, given the conditions described above, is shown in Figure 3-13. An alternate view of the same solution is shown in Figure 3-14. Inspecting these figures, observe that a temperature difference of ~0.2 K exists between the surface of the silicon substrate (in orange) and the sample solution. It is at the regions colored by orange in Figure 3-13 where the RTD is mounted.

In Figure 3-14, observe that the distribution of temperature of the sample solution spans a range of ~0.1 K. This range is 3× greater than the specification for control stability defined at the beginning of this chapter. This is acceptable for two reasons. First, the presence of a thermal gradient in the sample solution is not a problem as long as the gradient is constant with time and static in space. While thermal gradients tend to induce convective flows, it is believed that these gradients are small enough that the resulting flows are slow enough to render the solution nearly static. The second reason that this is acceptable is that some error in FA caused by this distribution is allowable in the error budget.

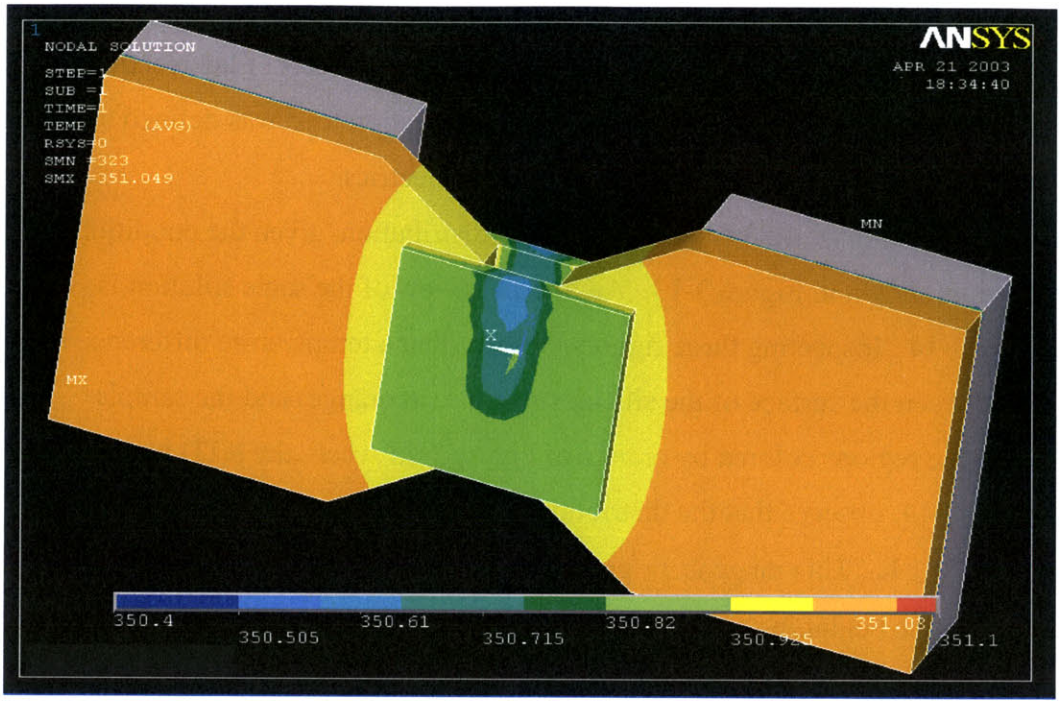


**Figure 3-13. Steady state temperature solution for finite element analysis of sample holder subject to convective load of h = 5 W/m$^2$K.**

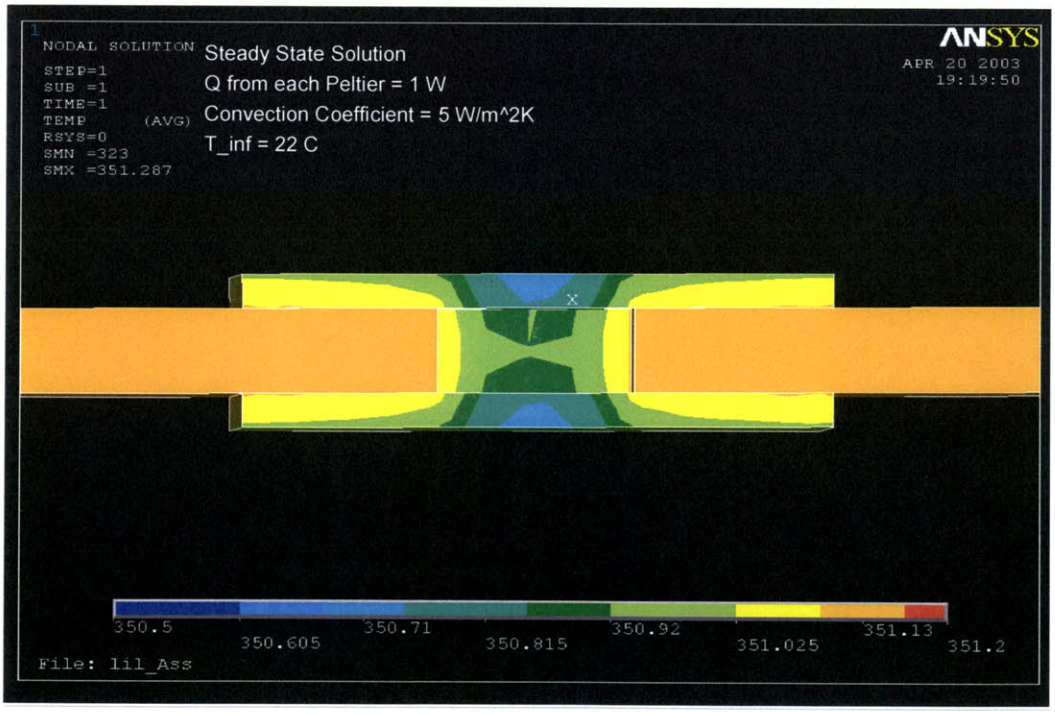


**Figure 3-14. Steady state temperature solution for finite element analysis of sample holder subject to convective load of h = 5 W/m$^2$K, zoomed view of fluid sample region to show distribution of sample temperatures.**

### *3.3.d. Thermal Modeling of Prototype 2*

The previous section showed that with a constant input from the thermoelectrics in the absence of disturbances an acceptable steady state temperature distribution would result. In practice, disturbances are present. These include fluctuations in the rate of convective (and radiative) heat loss as well as variations in the "cold side" temperature of the thermoelectric (i.e., the heat sink).

A controller must be used to compensate for these disturbances so that the predicted steady state response can be achieved. The controller also allows improved dynamics in stepping from one set temperature to another.

#### Analysis of Plant

The first step taken in developing the control for this system was to further analyze the system by building a lumped parameter model. The model demonstrated which parameters of the design were most critical to its performance, allowing subsequent designs to be more easily refined. It also clearly identified the inputs and outputs of the system. Variations in inputs act as disturbances and thus are desirably identified and addressed. The lumped parameter model also allowed definition of system time constants which defined the limit for the acceptable sampling time of the controller.

Another motivation for modeling the plant was consideration of model-based control methods. As will be shown, the model that captures the important dynamics of the plant includes non-ignorable non-linearities. This complexity along with the plant's multi-input, multi-output (MIMO) status discouraged such strategies.

Finally, the model provides a means of tuning the system gains in simulation rather than in hardware.

#### Equivalent Circuit Model

The equivalent circuit model shown in Figure 3-10 contains too many simplifications for this analysis. A more detailed equivalent circuit model is shown in Figure 3-15. This model again makes use of the symmetry of the problem such that only half of the sample holder (and therefore only two thermoelectrics) are modeled. As before, the thermal capacitances of (one half of) the sample solution and silicon substrate

are given by $C_w$ and $C_{si}$, respectively. Likewise the thermal resistances of the solution and silicon substrate are given by $R_w$ and $R_{si}$, respectively.

The components shown within the gray-shaded rectangle model the thermoelectric. The thermal capacitances and resistances, $C_{al}$ and $R_{al}$, are those of the ceramic substrates in which the thermoelectric semiconductors are sandwiched (see Figure 3-9). These ceramic substrates are made of alumina (hence the subscript). The heat pumped by the Peltier effect is given by $Q_p$ (see Equation 3-2). The thermal resistance of the semiconductor material that was given as $R_p$ in Figure 3-10 is now split in half to allow the insertion of a heat source, $Q_J$, and a thermal capacitance, $C_b$. The resistance is now labeled $R_b$ to reflect that it refers only to the resistance of the semiconductor elements (which are bismuth telluride). $Q_J$ models the joule heating associated with the flowing current. $C_b$ allows for the thermal mass of the semiconductor elements.

Finally, a resistance between the thermoelectric and the constant temperature of the heat sink has been added and labeled $R_S$.

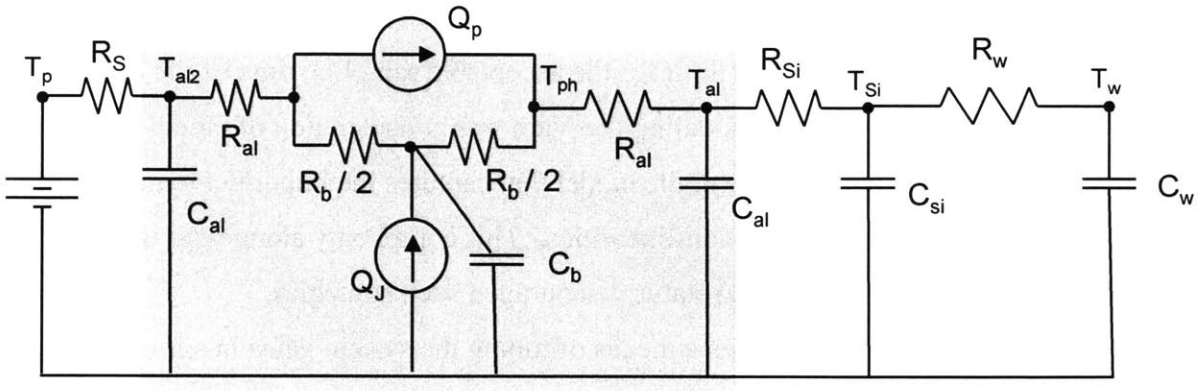


**Figure 3-15. More detailed equivalent circuit model of system. Components modeling the thermoelectric are shown backed in gray.**

This model has been created by inspection of the physical components of the system. A photograph of the system components is shown in Figure 3-16 for comparison. Computation of the relative scale of the individual components is now relevant to determine if any may be neglected.

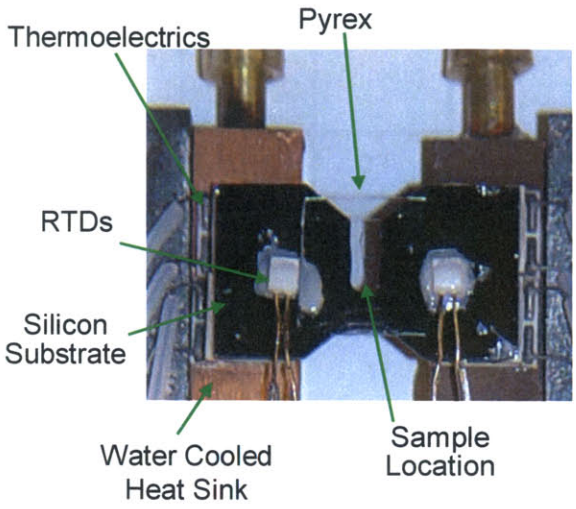


**Figure 3-16. Photo of sample holder.**

Approximate values for the thermal capacitance of each component are shown in Table 3-3, where again $C = \rho \cdot V \cdot c_p$. The volume given for $C_{al}$ represents that of two pieces of alumina, one from each thermoelectric (single side only). The volume for the bismuth is likewise based on that of the sum of the 36 semiconductor elements from each of two thermoelectrics. The volume for the silicon was derived from the computer CAD model and represents one half of the total volume of the silicon. Finally, the capacitance calculation for the water is based upon a 3 μL total volume as assumed previously.

Thermal resistances, shown in Table 3-4, are computed as $R = L/(k \cdot A)$ where L is the effective length of the thermal path, k is thermal conductivity, and A is the cross sectional area of the conductor. The effective length of the thermal path can be difficult to define as can be the cross sectional area in complex geometries.

**Table 3-3. Comparison of thermal mass magnitudes**

| | Material | Heat Capacity (J/kgK) | Mass Density ($kg/m^3$) | Volume ($mm^3$) | Capacitance (J/K) |
|---|---|---|---|---|---|
| $C_{al}$ | alumina | 760 | 3890 | 49.5 | 0.146 |
| $C_b$ | $Bi_2Te_3$ | 16 | 7730 | 30.4 | 0.004 |
| $C_{si}$ | silicon | 712 | 2328 | 105 | 0.174 |
| $C_w$ | water | 4182 | 1000 | 1.5 | 0.006 |

**Table 3-4. Comparison of thermal resistance magnitudes**

| | Material | Thermal Conductivity (W/mK) | Effective Length (mm) | Effective Cross Sectional Area ($mm^2$) | Resistance (K/W) |
|---|---|---|---|---|---|
| $R_{al}$ | alumina | 30 | 0.33 | 75 | 0.15 |
| $R_b$ | $Bi_2Te_3$ | 3 | 0.9 | 33.7 | 8.90 |
| $R_{si}$ | silicon & epoxy | 148 | 1 | 72 | 1.14 |
| $R_w$ | water | 0.61 | 0.5 | 1.5 | 546.45 |

$R_{al}$ is computed based on an "effective length" of the thermal path of one half the thickness of the alumina. The cross sectional area is the sum of the area of two pieces of alumina from a single face of the thermoelectrics. The thermal conductivity of pure (100%) alumina ($Al_2O_3$) is 30 W/m·K (www.matweb.com). This website however, lists more than 36 types of alumina variations with thermal conductivities ranging from 15 to 35.6 W/m·K.

The resistance, $R_b$, can be computed based on the geometry of the array of $Bi_2Te_3$ elements soldered in a 6x6 array onto each ceramic substrate. Limiting the accuracy of this calculation are tolerances on the element size that are large in comparison with their dimensions. In addition, fine detail in the geometry (such as solder fillets and material interfaces) may also have an appreciable impact on the actual resistance. Finally, as

shown in Figure 3-18, the thermal conductivity of $Bi_2Te_3$ is a function of doping level* which is also subject to manufacturing tolerances. The conductivity listed in Table 3-4 was again found at www.matweb.com (however the doping level is not specified). These assumptions of geometry and thermal conductivity yield an $R_b$ of 8.9 K/W. Another approach to estimating $R_b$ is, as discussed before, to use the maximum specifications, $R=DT_{max}/Q_{max}$. This approximation only holds for the assumptions of Figure 3-10 and not those of Figure 3-15 (because of the addition of the joule heating component). However, this approximation yields $R_b$ = 16 K/W given that two thermoelectrics are acting thermally in parallel. The actual value reasonably lies somewhere between these values.

The thermal resistance, $R_{si}$, is the sum of resistances of several components of the system. This resistance must account for the remaining thickness of alumina, that of the epoxy that bonds the alumina to the silicon, and that of the silicon. The resistance of the silicon to the point at which the RTD is bonded is defined by a silicon thickness of 1 mm and a cross section area 12 mm by 6 mm. Given silicon's thermal conductivity (k = 148 W/m·K), the resistance contributed by the silicon is 0.09 K/W. The resistance contributed by the epoxy can be computed assuming the epoxy bond is only 100 μm thick but 100× less conductive than the silicon. Therefore, $R_{epoxy}$ = 0.9 K/W. The sum of these resistances with that previously computed for the first half of the alumina thickness provides the total resistance for $R_{si}$ = 1.14 K/W.

The resistance, $R_w$, is defined by that of the water. While it should actually include some amount of resistance associated with the silicon and to their coupling, the resistance of the water itself is so high that it dominates these ancillary ones. The resistance shown in Table 3-4 assumes the water is a static conductor. Its thermal conductivity was referenced from www.matweb.com.

---

* Heat propagates through solids via two major mechanisms. The first is via the same carriers as those that transport electric charges. This thermal conductivity is called carrier conductivity, $\lambda_c$. The second mechanism is by thermal vibrations of the crystalline lattice of the material. This conductivity is called lattice conductivity, $\lambda_L$. In undoped silicon, 99.8% of the heat energy is transported via lattice vibration. In undoped Bi2Te3, with its softer lattice, only 75% is via lattice vibration. Variation in carrier concentration especially modifies the carrier conductivity but can also modify the lattice mechanics.

Table 3-4 does not attempt to define $R_S$, the resistance that connects the capacitance of the alumina to the constant temperature sink. This resistance should include that of half the thickness of the alumina plus the resistance of the epoxy bond plus the resistance of the copper plus some resistance associated with the pumped water and its interface to the copper (i.e., a convective heat transfer resistance). This last term is difficult to estimate but certainly non-negligible. Further discussion of its value is discussed later.

Reviewing Table 3-3, it is observed that the capacitance, $C_b$, is negligible relative to other the capacitances. While $C_w$ is also small relative to the other capacitances, it cannot be dropped. Ignoring this capacitance would eliminate the time constant formed by it and the (large) $R_w$. The lag that exists between the temperature of the silicon and the water would be lost.

In addition to the thermal resistances and capacitances, Figure 3-15 also depicts two heat flow sources. The amount of heat flow from these sources is a function of the current applied to the thermoelectrics. For the source, $Q_p$, the relationship between current and heat pumped can approximated as

$$Q_p = 2 \cdot \left(2 \cdot N \cdot S_b \cdot T_h\right) \cdot i, \qquad \textbf{3-5}$$

where N is the number of semiconductor junctions at each face of the thermoelectric, $S_b$ is the Seebeck coefficient, $T_h$ is the hot side temperature of the thermoelectric, and $i$ is the current. The factor of 2 that leads the equation is included to indicate that a pair of thermoelectrics acts in parallel in the design. This equation is consistent with Equation 3-2 since the product of the Seebeck coefficient and junction temperature ($T_h$) is equivalent to the difference in Peltier coefficients ($\prod_1 - \prod_2$) and 2N is the number of junctions over which the heat is transferred (there are N junctions of p-type with copper and N junctions with n-type and copper). The Seebeck coefficient has a nominal value of $2.2\times10^{-4}$ W/K for this material pair (www.melcor.com). For this particular thermoelectric, N = 18. At $T_h$ = 323 K, the correlation between the driving current and the heat pumped is $Qp = 5.12\times i$. This relationship is only approximate however; since, first, it is temperature dependent. This dependence occurs not only by the direct inclusion of temperature in the equation, but also through the temperature dependence of the Seebeck coefficient. As observed in Figure 3-17, the product $S_b \cdot T_h$ increases

approximately 20% as the temperature rises from 323 K to 363 K (a 12% rise in temperature). Second, as is illustrated in Figure 3-18, the Seebeck coefficient is critically dependent on the level of doping* where doping concentration is subject to manufacturing tolerances.

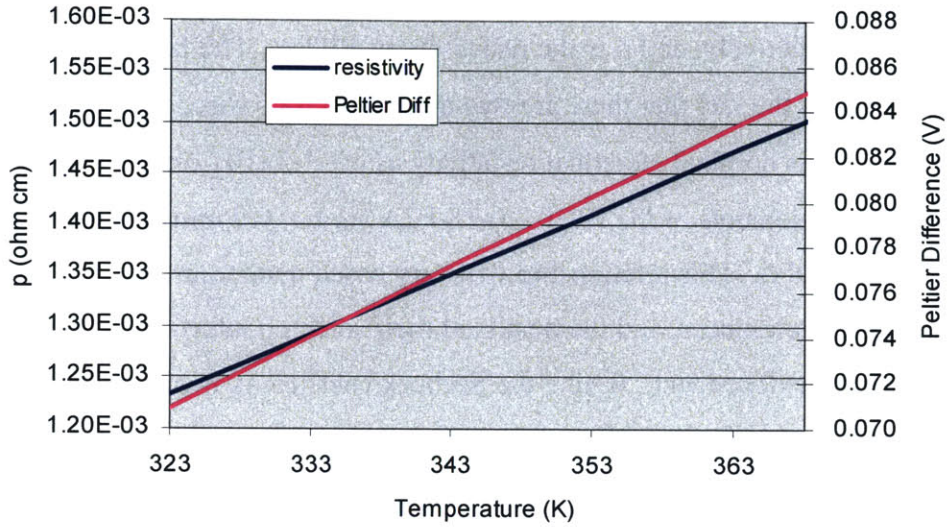


**Figure 3-17. Temperature sensitivities of the electrical resistivity and Peltier coefficient difference. Relationships based on data from www.melcor.com.**

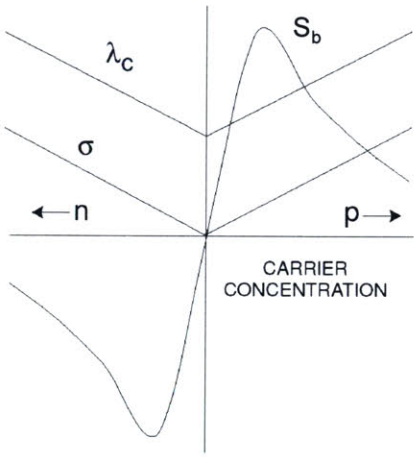


**Figure 3-18. Seebeck coefficient ($S_b$) and electric (σ) and heat ($\lambda_c$) conductivities of a semiconductor as a function of carrier concentration. Adapted from http://www.stanford.edu/class/ee293b/Fep7_X.pdf, page 15.**

* As described earlier, the polarity of the Peltier/Seebeck effect depends upon whether the semiconductor is of the p- or n- type. Intrinsic semiconductors have zero Seebeck coefficients. Therefore, for small doping levels, the coefficient grows rapidly as the doping level is increased.

The second heat source describes Joule heating and can be estimated based upon

$$Q_J = 2 \cdot \left( 2N \cdot \rho \cdot \frac{L}{A} \right) \cdot i^2, \qquad \textbf{3-6}$$

where N is as described before, L and A are the thickness and cross sectional area of a single element, respectively, and ρ is the resistivity of $Bi_2Te_3$. The factor of 2 that leads the equation reflects the fact that there are two thermoelectrics wired electrically in series. Melcor estimates this nominal electrical resistivity as $\rho = 1.3 \times 10^{-3}$ ohm-cm. The dimensions for the elements of the HOT-2.0-18-F2A are L = 0.9 mm and A = 0.47 $mm^2$. The result is $Q_J = 1.8\ i^2$. This relationship will vary based upon tolerances in doping levels, geometrical tolerances, and the details of their soldered interfaces. Resistivity is strongly temperature dependent. It, like the Seebeck coefficient, is observed to increase by ~20% when temperature shifts from 323 K to 363 K.

The possibility of neglecting Joule heating is explored in Table 3-5. Here the relative magnitudes of the two heat sources are compared where all values are computed at 50 °C. Clearly, unless very low currents are employed, joule heating cannot be neglected.

**Table 3-5. Comparison of outputs of each heat source at a specified current.**

| *I* (A) | Qp (W) | Qj (W) |
|---|---|---|
| 0.25 | 1.28 | 0.11 |
| 0.5 | 2.56 | 0.45 |
| 1 | 5.12 | 1.80 |
| 2 | 10.24 | 7.20 |

In order to test the accuracy of the estimated parameter values, the model was compared to experimental data. For this to be done, the model needed to include an additional resistance and capacitance summarizing the time constant of the RTD used to measure the temperature. The thin film RTD rests on a small slab of alumina (1.9 mm × 2.45 mm × 0.64 mm). Based on conductivity and specific heat data provided previously, a resistance of $R_{rtd}$ = 26 K/W and a capacitance of $C_{rtd}$ = 0.018 J/K were found. The updated model was created that included the RTD and neglected $C_b$. In addition,

experimental data was collected with no sample solution present. Therefore, the components $C_w$ and $R_w$ were also dropped from the model. The revised model is shown in Figure 3-19.

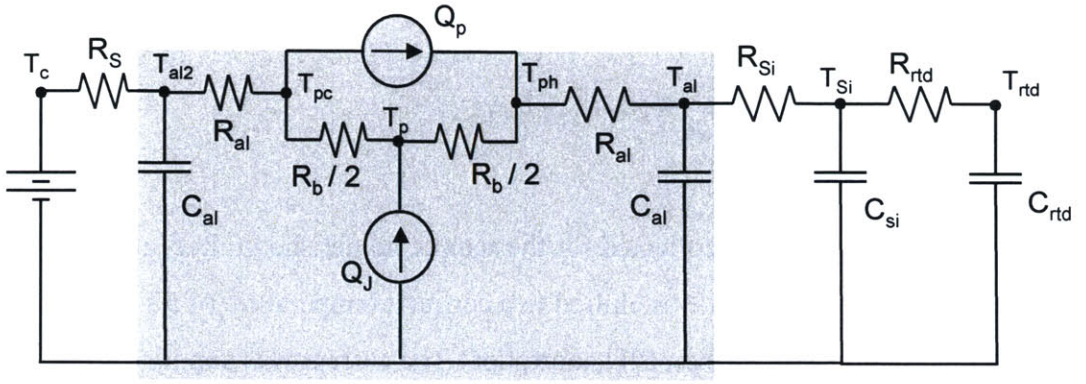


**Figure 3-19. Revised model to be fitted to experimental data.**

The equations that describe the model are given by Equations 3-7 through 3-13. These are derived by applying Kirchhoff's current law to each temperature node of the system. These were reduced to four state equations with states $T_{rtd}$, $T_{si}$, $T_{aL1}$, and $T_{aL2}$. State matrices are given in the Matlab code in the Appendix.

$$\frac{T_{Si}-T_{rtd}}{R_{rtd}} = C_{rtd}\cdot \dot{T}_{rtd} \qquad \textbf{3-7}$$

$$\frac{T_{AL1}-T_{Si}}{R_{Si}} + \frac{T_{rtd}-T_{Si}}{R_{rtd}} = C_{Si}\cdot \dot{T}_{Si} \qquad \textbf{3-8}$$

$$\frac{T_{ph}-T_{AL1}}{R_{AL}} + \frac{T_{Si}-T_{AL1}}{R_{Si}} = C_{AL}\cdot \dot{T}_{AL1} \qquad \textbf{3-9}$$

$$\frac{2\cdot\left(T_p-T_{ph}\right)}{R_b} + \frac{T_{AL1}-T_{ph}}{R_{AL}} + Q_p = 0 \qquad \textbf{3-10}$$

$$\frac{2\cdot\left(T_{pc}-T_p\right)}{R_b} + \frac{2\cdot\left(T_{ph}-T_p\right)}{R_b} + Q_J = 0 \qquad \textbf{3-11}$$

$$\frac{2\cdot\left(T_p - T_{pc}\right)}{R_b} + \frac{T_{AL2} - T_{pc}}{R_{AL}} = Q_p \qquad \textbf{3-12}$$

$$\frac{T_{pc} - T_{AL2}}{R_{AL}} + \frac{T_c - T_{AL2}}{R_S} = C_{AL}\cdot\dot{T}_{AL2} \qquad \textbf{3-13}$$

Step response data was collected for the sample holder shown in Figure 3-16. In these experiments, the heat sink was chilled to a constant temperature of 50.7 °C by a VWR water circulator with its own PID controller. The current was supplied by a KEPCO current supply commanded from a desktop computer via GPIB interface. The temperature was measured via a resistance temperature detector (RTDs, F3105, Omega, Inc.) by an Agilent 34970 data acquisition unit every 0.51 s. Three sets of data were collected including inputs of 0.25 A, 0.5 A, and 0.75 A. The resulting plots are shown in Figure 3-20.

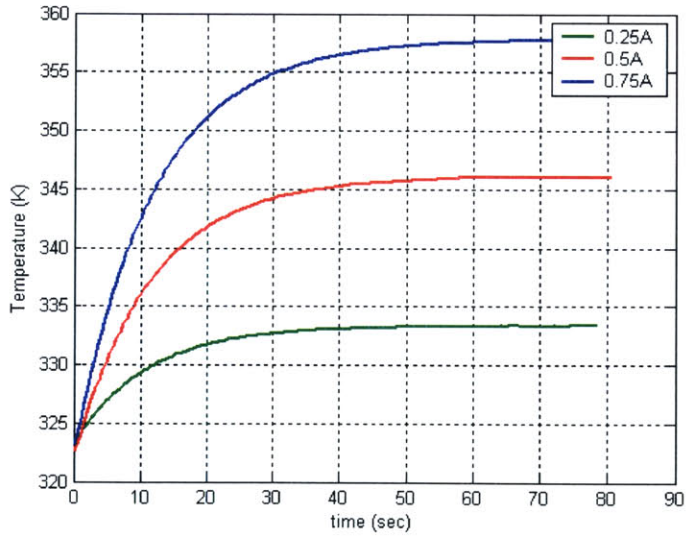


**Figure 3-20. Temperature response to step change in current to sample holder. Inputs of 0.25A (green), 0.5A (red), and 0.75A (blue) are shown.**

The step response predicted by the model was computed in Matlab using Simulink. The Simulink implementation is shown in Figure 3-21. There are two inputs, the constant temperature that cools the backside of the thermoelectric and the current (i)

driving the thermoelectric. Both $Q_p$ and $Q_J$ are defined by the driving current. $Q_p$ is linearly proportional to the current ($Q_p$ = itoQ·i, where itoQ is the conversion factor representing the Peltier effect as defined in Equations 3-2 and 3-5). $Q_J$ is proportional to the square of the current ($Q_J = Re \cdot i^2$, where Re is the conversion factor representing the electrical resistance of the thermoelectrics). .

The predicted response is compared to the actual response for a step in current to 0.25A in Figure 3-22. A poor fit is observed in general and there is large error in steady state output in particular.

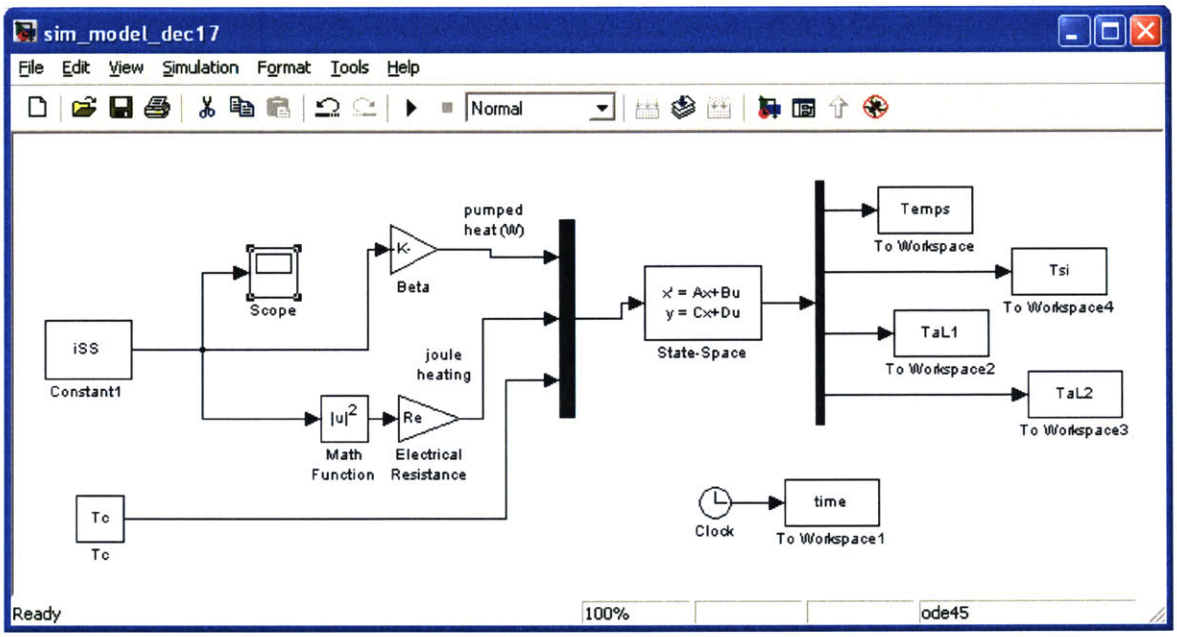


**Figure 3-21. Simulink implementation of step response simulation. The sample holder model is summarized by the state-space block.**

In order to improve the model, the parameters were iteratively adjusted. After each change, the sum of square errors between the model and all three of the experimental data sets shown in Figure 3-20 were computed. 170,100 combinations of different parameters were compared by incrementally varying each of 7 parameters. These included $R_s$, $R_{si}$, itoQ, Re, $C_{si}$, $R_{aL}$, and $R_{rtd}$. This optimization was run multiple times with narrowing ranges for the parameters to achieve a best fit condition. Because parameters such as $R_s$, $R_{si}$, and $R_{rtd}$ were initially estimated with limited confidence ($R_{si}$ and $R_{rtd}$ because of film resistances and $R_s$ because of convective transfer to water), the

optimization began with large ranges for these numbers. More accurately known parameters (itoQ, Re, and $C_{si}$) were allowed a range of only 0.5× to 2× initially, and then refined to smaller ranges when the global minimums seemed apparent.

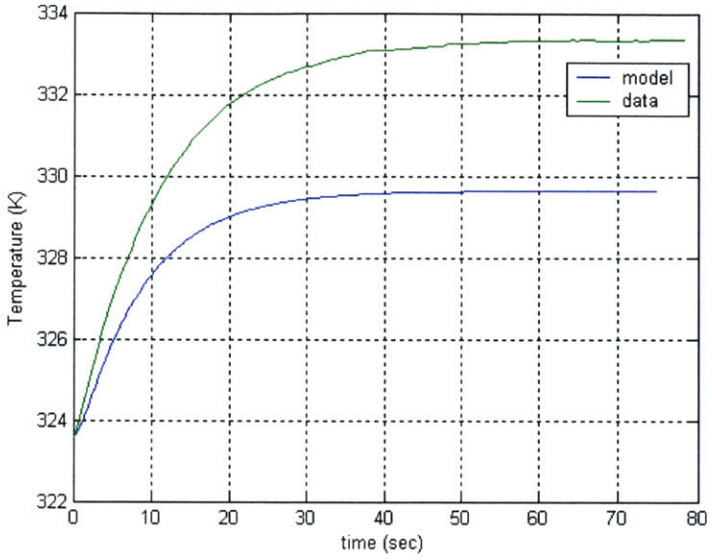


**Figure 3-22. Predicted response (blue) along with actual response (green) for a step input of 0.25A based on initial estimate of all parameters.**

In the search for improved parameters, it was noted that the steady state system provided a relationship that could be used to constrain a parameter. $R_b$ was chosen. Setting the time derivatives of Equations 3-7 through 3-13 to zero and solving for $R_b$ yields

$$R_b = \frac{-2 \cdot (Re \cdot i_{SS}^{\,2} \cdot (R_{aL} + R_s) + T_c - T_{ss})}{Re \cdot i_{SS}^{\,2} + 2 \cdot itoQ \cdot i_{SS}}, \qquad \textbf{3-14}$$

where $i_{ss}$ is the magnitude of the step in current and $T_{ss}$ is the steady state temperature. Note that if joule heating is neglected, i.e., Re = 0, Equation 3-14 simplifies to the steady state relationship implied by Equation 3-4.

Given a set of iterated parameters [$R_s$, $R_{si}$, itoQ, Re, $C_{si}$, $R_{aL}$, $R_{rtd}$], $R_b$ was constrained. These values were combined with those not iterated [Crtd, Cal] to compute a new step response. The best fit was found by the values given in Table 3-6. A comparison of the resulting model step response to the actual step response is shown in Figure 3-23.

**Table 3-6. Lumped Parameters found via iterative sum of square errors optimization compared to orginal parameter estimates. Note that last two parameters were not optimized.**

| | Best Fit Resistance (K/W) | Original Estimate of Resistance (K/W) |
|---|---|---|
| $R_S$ | 11.25 | 5 |
| $R_{al}$ | 0.11 | 0.15 |
| $R_b$ | 14.74 | 9 |
| $R_{si}$ | 2.85 | 1.14 |
| $R_{rtd}$ | 45 | 26 |
| $C_{si}$ | 0.21 | 0.17 |
| itoQ | 4.8 | 5.12 |
| Re | 3.16 | 1.8 |
| *$C_{al}$* | *0.146* | *0.146* |
| *$C_{rtd}$* | *0.018* | *0.018* |

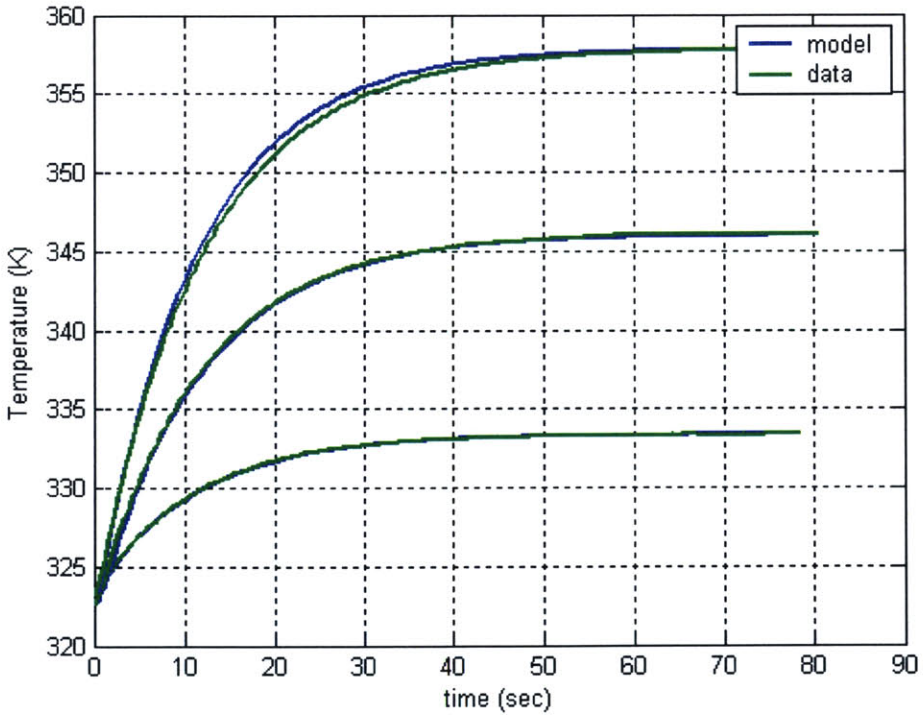


**Figure 3-23. Comparison of model step response (blue) and experimentally measured step response (green) after model parameters were best fit to the experimental data.**

The model shows an excellent fit for the first two data sets (0.25A and 0.5A inputs) with small error for the third data set. The deviation in the predicted response from that of the actual data is likely a result of the model's assumption of temperature independence for parameters including the Peltier coefficient and electrical resistivity terms (shown to be temperature dependent by Figure 3-17).

Table 3-6 indicates that estimates for a number of parameters are notably different that their original (physically) estimated value. Nearly all the thermal and electrical resistances differ from their estimated values by large percentages; however these can be explained by the reasons given previously. The capacitive values needed little adjustment to achieve this fit.

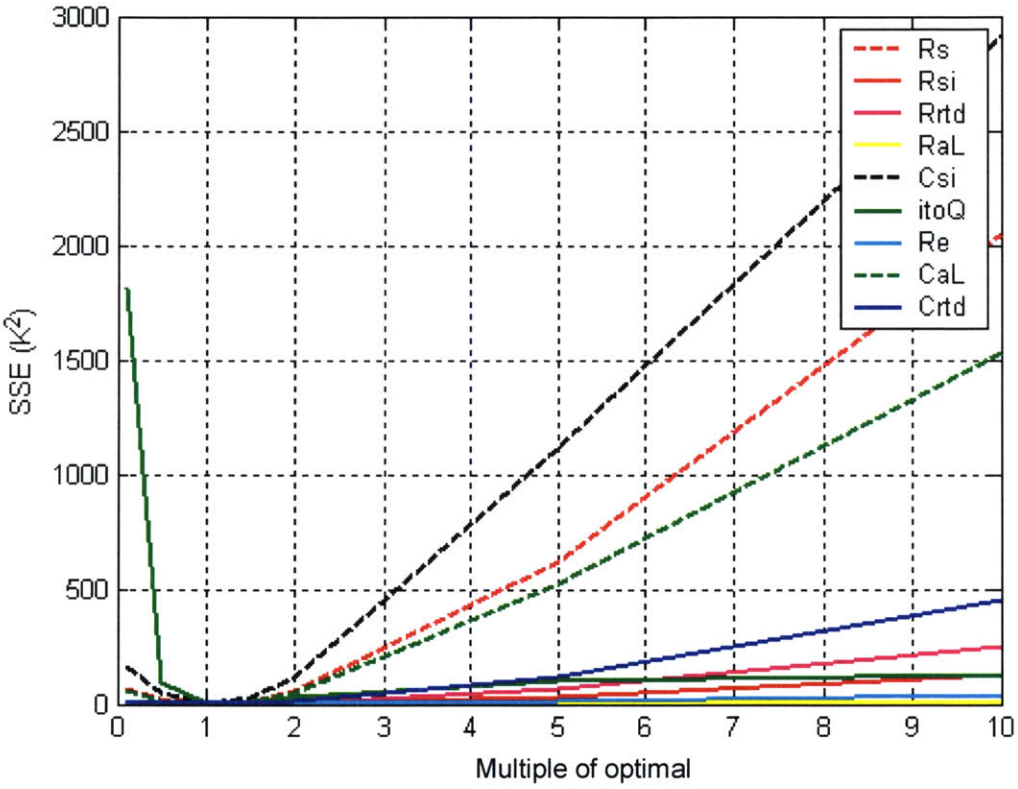


**Figure 3-24. Sum of square error (SSE) between the fitted model and all three data sets rises when any parameter deviates from the optimal. In the plot, SSE is evaluated for multiples of each parameters optimal value. SSE is most sensitive to capacitor values and the resistance Rs.**

It is interesting to consider the sensitivity of the solution fit to changes in each parameter. A summary of these sensitivities in the sum of square errors to changes in each parameter are shown in Figure 3-24. The error calculation is least sensitive to $R_{al}$, a

near negligible resistance. The error is most sensitive to $R_s$ and the model capacitances $C_{si}$, $C_{aL}$, and $C_{rtd}$, where the sensitivity is proportional to the magnitude of each capacitance. Parameters with the strongest sensitivity are expected to estimated with the least error. Note that the calculations of Figure 3-24 support the conclusion that the "best fit" solution truly is a global minimum.

Insight from the Model

Figure 3-25 shows the predicted response versus the actual response when joule heating is ignored. At currents above 0.25A, notable error results. Thus, the model indicates that this nonlinearity cannot be ignored if accurate representation of the plant is desired. As observed from Figure 3-23, the temperature dependence of some model parameters is also a non-negligible non-linearity if operating across a wide range of temperatures.

Disturbances can cause the system to perform differently than the ideal predictions of the model. The model treats $T_c$ as a constant input. In practice, variations are observed here. This disturbance must be minimized by hardware design or its affect may be minimized by closed loop control.

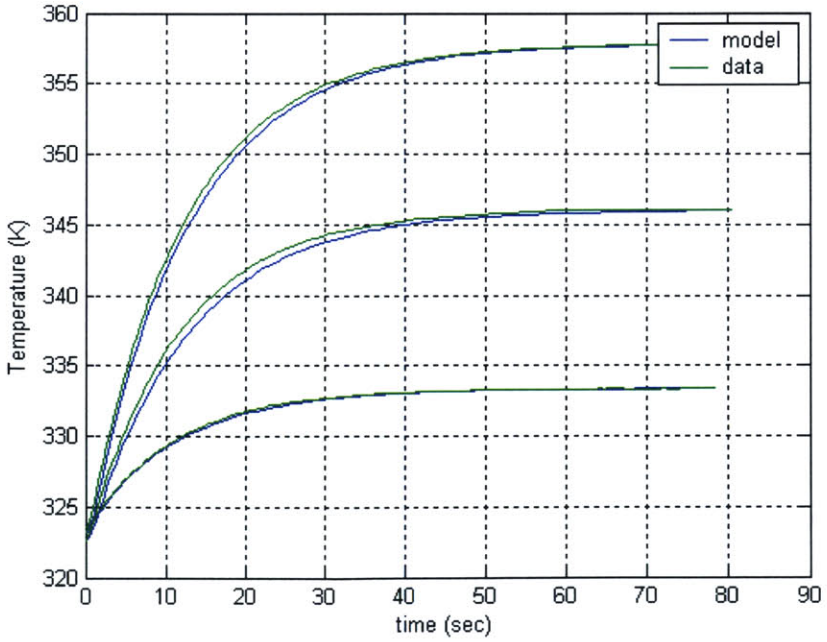


**Figure 3-25. Model results ignoring joule heating**

The model can also be used to define the required sampling time for the controller. As a rule of thumb, the sampling time should be shorter than the shortest time constant of the system. The "effective" time constants of the three capacitors (and their relevant resistors) shown in the right-hand half of Figure 3-19 are summarized by Table 3-7. It is observed that a sampling time several times shorter than 1 s should suffice.

The model and experimental data indicate a system time constant of ~12 s (as given in Table 3-7). Functioning open loop, such a system requires almost 50 s to step to 72 °C from 50 °C, an effective ramp rate of ~0.5 °C/s .

A final and important role of the plant model was in its implementation in the controller to predict steady state currents for any user selected temperature. This is discussed further in the next section.

**Table 3-7. Effective time constants of the thermal system.**

| | Time Constant (sec) |
|---|---|
| rtd | 1.00 |
| silicon | 2.17 |
| alumina | 1.09 |
| system | 12 |

### *3.3.e. Temperature Control for Prototype 2*

A controller was needed to speed up the system response as well as counter any disturbances. Simple proportional-integral-derivative (PID) control was again initially applied to the system but with unsatisfactory results. Model based control methods were considered, however an adequate model was shown to require several important non-linearities including joule heating and temperature dependent model parameters.

Instead, the non-linear control scheme previously described was selected. As depicted in Figure 3-6, two separate controllers were utilized in different stages of the response. In this second iteration, the first controller, H1, defined the current to the thermoelectric as some large value (lower than the maximum allowable current as

specified for the thermoelectric). This constant value was maintained regardless of the error; however, once the error reached a pre-set threshold, the H2 control algorithm replaced H1. H2 was a PID controller. Improved response characteristics were attained with the addition of the derivative term, a term which was not implemented in the first iteration of this type of controller. The derivative term adds damping allowing higher gains to be employed.

The control loop was closed by RTD temperature measurement as shown previously in Figure 3-16. The RTD was measured by an Agilent 34970 data acquisition unit. This resulting temperature was transmitted to a PC by GPIB communication. Control software was implemented in Visual Basic 6.0. At every cycle, a command was sent to a KEPCO current supply, again by GPIB, refining the current sent to the thermoelectric.

The PID controller was implemented via a discretized version of its continuous representation. The control equation for a PID controller in the (continuous) Laplace domain is

$$H(s) = \frac{i(s)}{e(s)} = K_P + \frac{K_I}{s} + K_D \cdot s\,, \qquad \textbf{3-15}$$

where $K_p$, $K_I$, and $K_D$ are the proportional, integral, and derivative gains, s is the Laplace operator, i(s) is the output current, and e(s) is the input error. The discrete approximation for the derivative is

$$sN \approx \frac{n_j - n_{j-1}}{\Delta t}\,. \qquad \textbf{3-16}$$

Applying this discretization to an expansion of Equation 3-15, the resulting implemented control equation is

$$i_j = i_{j-1} + K_P \cdot (e_j - e_{j-1}) + K_I \cdot e_j \cdot \Delta t + \frac{K_D \cdot (e_j - 2 \cdot e_{j-1} + e_{j-2})}{\Delta t}, \qquad \textbf{3-17}$$

which defines the new current command ($i_j$) as a function of the previous current command ($i_{j-1}$), the new temperature error ($e_j$) and previous temperature error ($e_{j-1}$), and the time interval between the new and previous error measurements, $\Delta t$ (sampling time).

In addition to the PID output calculation, the digital H2 controller shown in Figure 3-6 also contained a saturation limit. As noted in Table 3-1, the thermoelectrics

have specifications for maximum current. Therefore, the computed current, $i_j$, was compared to the maximum current by an if statement. If $i_j$ was larger than the maximum, the commanded current was modified to be only the maximum.

A key feature of the dual controller system was the ability to avoid integrating large error in the early part of the step change. Waiting to "turn on" the integral controller minimized problems with overshoot and "ringing"; however, switching controllers brings an additional complication, namely initializing previous values for the current and error. In the original implementation, undesirable temperature dynamics where observed when controllers were switched as seen in Figure 3-7. These resulted from a poor strategy of initializing previous values. In the final implementation of the controller, the previous values for the error were initialized such that all terms were made equal to the present error (i.e., the error measurement that caused the controller to be switched from H1 to H2). Thus for the very first calculation of the output current, $e_j = e_{j-1} = e_{j-2}$.

Since the switch from H1 to H2 did not occur until the control temperature was very near the target temperature (typically within 2 °C), the previous value of the current ($i_{j-1}$) was defined as the steady state current that would yield the correct steady state temperature. This current was easily predicted from the model discussed in detail in the previous section. Given the temperature of the heat sink, the required steady state temperature could be computed for any desired steady state temperature. Thus this strategy was not limiting in the user's ability to select temperatures.

A final caveat to the H2 controller's design was the ability to implement unique controller gains for each step in the FA-PCR process (denature, anneal, extend, and measure). Early in the development, it was observed that the best performance was achieved with unique gains for all four steps; however with the adoption of the strategy for initialization of previous values describe above, performance and robustness of the controller was improved. Subsequently, a set of control values were used for steps increasing in temperature (measure to denature, anneal to extend) and steps that would decrease the temperature (denature to anneal, extend to measure).

It was initially hoped that the model developed in the previous section would find great usefulness in tuning the control parameters; however, since the system is not single-

input, single output most design tools were unsuitable. It was possible to extend the model of Figure 3-21 by closing the feedback loop in Simulink. Unfortunately, problems were encountered adequately modeling the discrete nature of the controller both in converting the continuous state space model to its discrete form and in properly inserting delays and zero order holds. Solving these problems would only have allowed iterative trial and error modification of the control parameters. For systems with long time constants or rise times, such a strategy would be important to efficient parameter tuning. As shown, however, in this application the system time constants were quite short. Thus, rather than delay the development studying the problems associated with modeling the discrete controller, control parameters were tuned directly in hardware rather than in simulation.

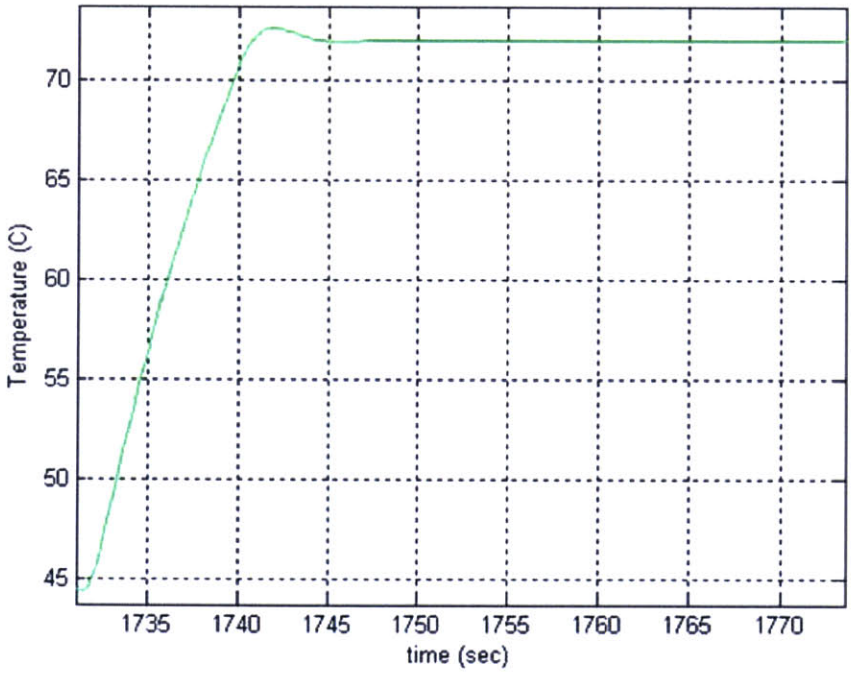


**Figure 3-26. Step response of dual-controller system.**

Results of the control strategy and implementation are shown in Figure 3-26, Figure 3-27, and Figure 3-28. All three plots are different views of the same experimentally measured step response. In Figure 3-26, the temperature is increased from 45 °C to 70 °C in under 9 s, a ramp rate of 2.8 °C/s . Figure 23 gives a closer look

at the 0.6 °C overshoot. Such an overshoot is not problematic for the PCR process. It can be eliminated by modification of the controller gains at the expense of longer settling time if desired. Note that in neither of these figures is the transition from the H1 controller to the H2 controller evident.

Figure 3-28 shows a zoomed view of the steady state stability. The controller is able to stabilize the temperature to a level near that of the resolution of the RTD. This figure shows evidence of the necessary thermal stability for precision FA measurement.

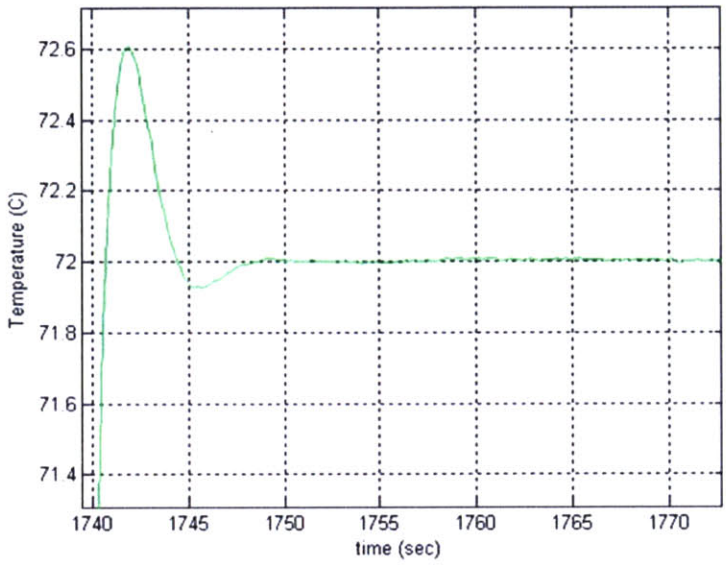


**Figure 3-27. Zoomed view of the overshoot for step response of dual-controller system**

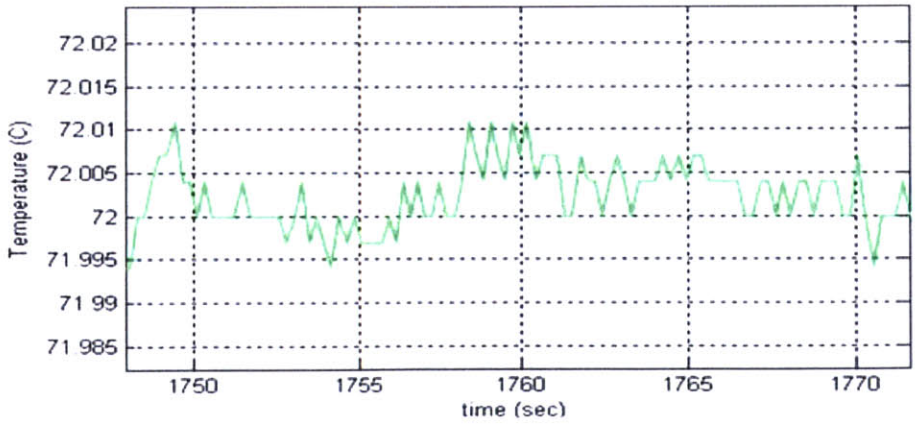


**Figure 3-28. Zoomed view of the steady state stability after a step response for the dual controller system.**

*3.3.f. Combating Evpaoration*

Evaporation was a significant problem in the second prototype. Because the sample chamber had no seal (such as the plastic cap in the first prototype), it did not act as a closed volume. This challenge was anticipated, and as such, countermeasures were at the ready.

Evaporation rates are a function of many environmental parameters but qualitatively, rates can be compared among different liquids under the assumption that the evaporation rate of each is proportional to its saturated vapor pressure, which is itself a function of temperature. The saturated vapor pressure of a liquid is the pressure exerted by its vapor in a closed system when its liquid and vapor are in dynamic equilibrium. This equilibrium occurs when the number of atoms leaving the liquid to go to the vapor phase equal those returning from the vapor to liquid phase. A liquid with a lower saturated vapor pressure typically has higher intermolecular forces thus requiring fewer molecules to move to the vapor phase to achieve evaporative equilibrium.
The first countermeasure applied to prevent evaporation was a layer of mineral oil over the PCR solution. At room temperature, the saturated vapor pressure of mineral oil is <66 Pa. This is 35× lower than the vapor pressure of water. Later, a substance called Fluorinert (FC-70, 3M) was used as the protective layer. The saturated vapor pressure of Fluorinert at room temperature is <13 Pa.

Increased relative humidity was employed as a second countermeasure. This was achieved by humidifying the chamber that enclosed the sample, as shown in Figure 3-29. The original implementation of the humidifier input, shown at the left of the figure, ported the output of an ultrasonic humidifier (model 572, ETS) straight into the sample chamber. The air within the chamber was stirred by a fan. The relative humidity in the chamber was regulated with an on/off controller (model 524, ETS) via sensor feedback. This configuration was problematic for optical measurement, however, because the vapor was not being adequately dispersed into the air volume. Tufts of water vapor were observed passing by the optical detector causing measurement fluctuations. To counter this problem, the configuration was modified to that shown in the figure's right. A housing was fabricated that contained hundreds of 2 mm diameter holes at its front face.

The stirring fan was mounted over a large hole on the back face of the housing. The humidifier output entered through the side. As the vapor was forced through the grid, its output was more evenly dispersed into the chamber air volume. This eliminated the observed optical fluctuations.

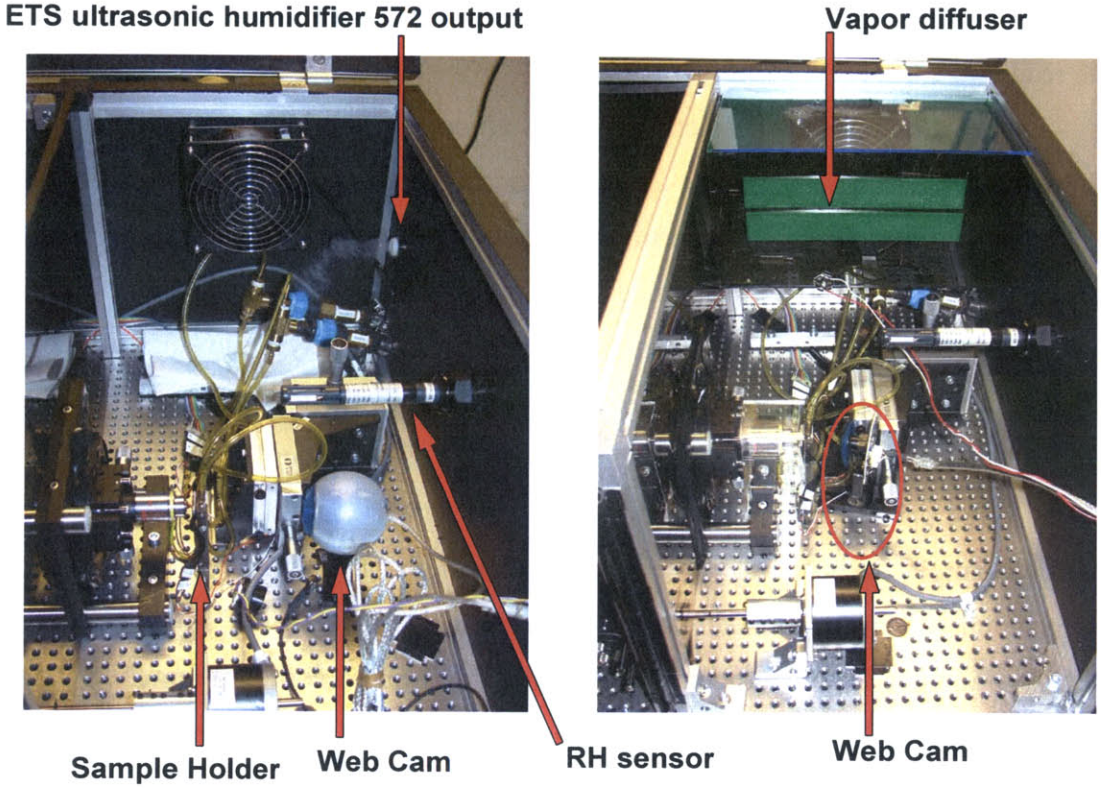


**Figure 3-29. The humidified sample chamber containing the prototype 2 sample holder. [Left]: originial installation of humidifier out put and diffusing fan, [Right]: improved configuration in which humidifier output is spatially filtered by grid of holes.**

Despite these countermeasures, evaporation continued to be a problem. Examples of experimental data afflicted by evaporation are shown in Figure 3-30 and Figure 3-31. In each experiments, 20 μL of PCR solution (See Appendix: 2nd Prototype PCR Protocol) was covered by 20 μL of Fluorinert (FC-70, 3M). Samples were subject to a four stage thermal cycle during the last of which, the FA was measured. For the experiment shown in Figure 3-30, the thermal cycling began with one 3 minute incubation at 95 °C followed by 55 cycles of 15 s at 95 °C, 15 s at 49 °C, 10 s at 72 °C, and 20 s at 50 °C. The relative humidity was set at 97%. After ~30 cycles, the sample level dropped below the point of optical interrogation because of evaporation. The

intensity plot at the left of the figure shows a sharp increase shortly before the loss of signal. Hypotheses for the cause of this intensity increase include scattering of the excitation light by the oil/water interface, an increased concentration of fluorophore at the oil water interface (perhaps due to some molecular hydrophobicity), or a non-linear evaporation rate leading to a non-linear increase in fluorophore concentration over the course of cycling. The computed FA, shown at the right side of the figure, is observed to remain relatively stable during the steep rise in intensity, indicating that light scattering by the oil/water interface is not likely the cause of the intensity increase.

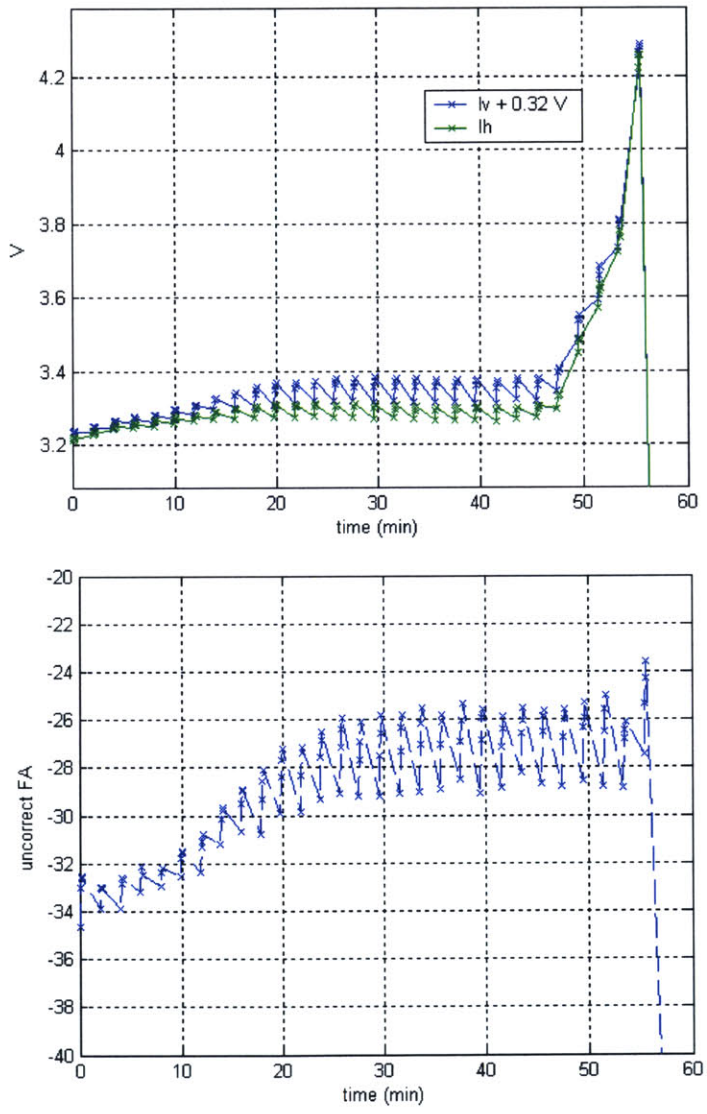


**Figure 3-30. Results from March 10, 2004 Exp 2, [Upper]:Vertical (Iv) and horizontal (Ih) intensities measured as sample evaporated over cycling., [Lower]: Uncorrected FA computed from measured intensities.**

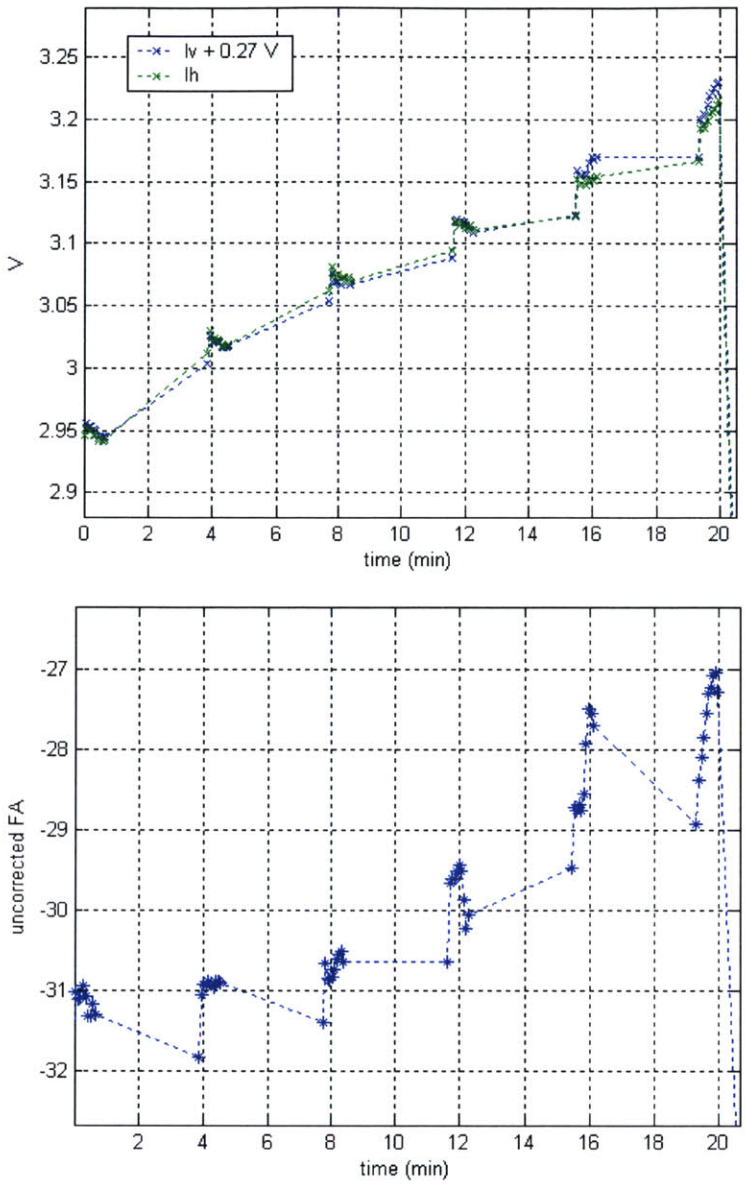


**Figure 3-31. Results from March 10, 2004 Exp 3, [Left]:Vertical (Iv) and horizontal (Ih) intensities measured as sample evaporated over cycling., [Right]: Uncorrected FA computed from measured intensities.**

The experiment of Figure 3-31 was conducted with a different thermal cycling profile that omitted the initial pre-incubation step. Step durations were also modified. The new profile was defined by 55 cycles of the series 45 s at 95 °C, 45 s at 49 °C, 45 s at 72 °C, and 45 s at 50 °C where again the FA measurement was made at the last step. The measurement chamber was humidified to 98% RH. The plot at the left shows intensities increased during cycling. After only 6 cycles, the solution evaporated below the level of

optical interrogation. The computed FA, shown at the right of the figure, is observed to drift upward along with the intensities. Increased inter-molecular interaction at increasing concentration was one early hypothesis for this observation. Given that the intensity only indicates a 7% increase before the solution drops below the optical interrogation level, the extent of evaporation would not have caused a sufficient change in the initial 200 nM fluorophore concentration to support this hypothesis.

A webcam (IBOT 2.0, Orange Micro) was installed in the chamber to get more insight into the evaporation problem. The webcam is visible in Figure 3-29. LEDs from Lumiled were also installed to provide light for the webcam imaging in the closed chamber. The video images from the webcam provided significant insight into the evaporation problem.

First, it became immediately clear that performance was very sensitive to pipetting errors. With poor technique, air could be trapped at the PCR solution/sample holder interface or at the solution/Fluorinert interface. During thermal cycling, expansion and contraction of this air bubble produced significant errors in the fluorescent measurements.

With careful technique, trapped air could be avoided, however, a second problem persisted. This problem is illustrated in Figure 3-32. With an experimental protocol similar to that of Figure 3-31, the entire PCR sample solution is observed to evaporate by the $10^{th}$ PCR cycle. Most interesting was that the PCR solution evaporated from underneath the thick, protective layer of Fluorinert. It appeared that the hydrophilic surface of the $SiO_2$ may have allowed some water to remain on its surface during the pipetting of the Fluorinert, effectively creating a thin capillary by which PCR solution could wick up to a point where it was unprotected from evaporation.

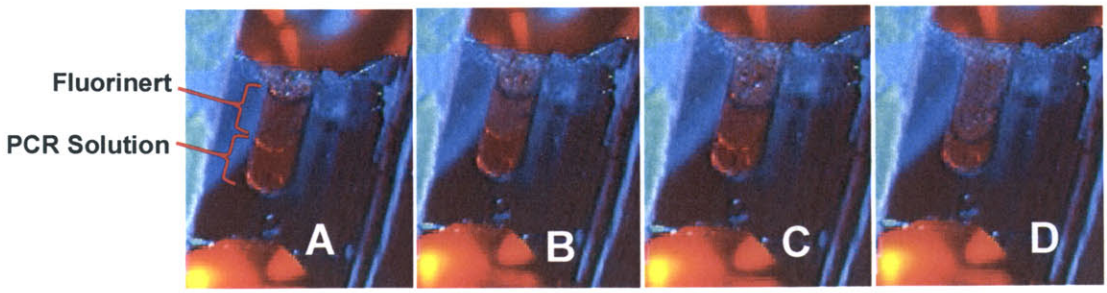


**Figure 3-32. Time lapse images demonstrating evaporation of PCR solution out-from-under the protective Fluorinert. Images are taken at ~3 min intervals during thermal cycling.**

Various solutions were attempted and/or contemplated to remedy the evaporation problem. Caps were fabricated from butyle rubber but did not provide effective seals. Capping with a soft wax was also attempted. The wax seal was not strong enough to counter the pressure rise of the trapped, heated air.

Surface modifications altering the hydrophobicity of the sample holder surfaces were also contemplated. Problems beyond evaporation such as difficulty cleaning this non-disposable sample holder and worries about enzyme-surface interactions motivated the decision to build a third prototype built around disposable PCR tubes shown in Figure 3-1.

These tubes have an integrated plastic cap that seals tightly. Thus, at first glance, the PCR solution is confined to a closed volume that can achieve evaporative equilibrium (and therefore halt evaporation). However, notice that in the design shown in Figure 3-1, only the bottom portion of the tube is heated. In their commercial implementation, these tubes are intended to hold 100 μL of PCR solution and the entire body of the tube is uniformly heated. Prototype 3 was designed to use only 20 μL of PCR solution that resided in the bottom of the tube. At 95 °C, water's saturated vapor specific volume is 1.982 $m^3/kg$. Thus, in order to bring 100 μL of dry air to saturation, 50 nL of PCR solution must evaporate from the liquid state. At first glance, this does not appear to be a problem. However, because only the base of the tube is heated, the water vapor would be expected to condense onto the sides of the tube above the heated portion. At each cycle, >50 nL of PCR solution would have been lost to condensation on the upper walls of the tube. After many cycles, this could have a measurable impact on the measurement. To counter this problem, the use of a protective layer was continued. Mineral oil was preferred over Fluorinert, despite its higher vapor pressure, because mineral oil's density is less than that of water (while Fluorinert has a higher density than water). This allowed a centrifugation step to be performed after the addition of the mineral oil to the tube while still leaving the PCR solution at the bottom. (A separate centrifugation step was also performed immediately after adding the PCR solution – before the mineral oil was added – to pull the solution down off the tube walls.)

*3.3.g. Non-standard thermal profiles*

In Figure 3-7, the first prototype is shown to have used a four stage thermal profile. Three of these stages are typical of PCR, as described in the Introduction. The fourth step was added to allow for FA measurement. This same four step thermal cycle was used for all experiments done in the first and second prototypes.

The fourth step in the thermal cycle was added based on measurements made with the first prototype comparing the FA of flourescein-labeled oligonucleotides (20 bp) and flourescein-labeled product (122 bp) at 30, 50, and 70 °C. The results are shown in Table 3-8.

**Table 3-8. Anisotropy of Primer ($r_{primer}$) and Product ($r_{product}$) Solutions at Elevated Temperatures. Standard deviations ($\sigma$) are given for each measurement to its right**

| Temperature (°C) | $r_{primer}$ (mP) | $\sigma_{primer}$ (mP) | $r_{product}$ (mP) | $\sigma_{product}$ (mP) | Range |
|---|---|---|---|---|---|
| 30 | 47 | 0.61 | 118 | 0.2 | 71 |
| 50 | 35 | 0.11 | 85.5 | 0.2 | 50.5 |
| 70 | 30 | 0.1 | 63 | 0.17 | 33 |

These results indicated that more than fifty percent of the measurement range was lost (compared to ambient) if anisotropy is measured at 70 °C (approximately the temperature used for polymerase extension). A less substantial loss of range is observed for 50 °C. The desire to maximize the change in FA motivated the decision to measure at a temperature below the extension temperature.

The results of this experiment are in disagreement with the theoretical analysis presented in Chapter 2 which indicated that the measurement range should rise with increasing temperature. The difference between measurement and the results predicted by Perrin's equation lies largely in the real and assumed shape of the fluorescing molecule. Perrin's equation is based on spherical masses while the actual measurements are made from fluorescent molecules attached by an amino linker to a 6 carbon chain which is attached to a flexible DNA strand. The effective stiffness of the structure between the fluorophore and the primary mass (the DNA) would be expected to drop with increasing temperature. Measurement at high temperatures would therefore simply reflect the motion of the fluorophore regardless of the mass to which it is attached. In

more recent measurements, the FA of primer and product were found to be indistinguishable at 95 °C.

Maximization of range is only one of many design goals. Another important requirement (for any measurement) is that the measurement does not affect the system that it is measuring. Therefore, an important concern was whether adding the extra temperature step would cause errors in amplification. Maximized range seemed best achieved at low temperatures. These low temperatures could allow primer-dimer formation or primer annealing to genomic DNA. At the completion of FA measurement, during the step to 95 °C for denaturation, the enzyme would be become briefly active. This could result in extended primer-dimers or partially extended target sequence.

An experiment testing the impact of adding a measurement step to the thermal cycle was performed by Heelo Sudo in August 2002. Two protocols, identical except that one included a $4^{th}$ step of 50 °C for 5 s, were run to amplify the APC target used in all experiments for this thesis (see Appendix: Sudo Protocol). The PCR products were analyzed by capillary electrophoresis. The electropherograms are shown in Figure 3-33. Unfortunately, these results were largely overlooked at the time of the experiment. The central peak that existed in the data from the protocol including the $4^{th}$ step was (in hindsight, mistakenly) assumed to have occurred by chance.

Concern over the consequences of the $4^{th}$ step in PCR were revisited as the third prototype's performance was being evaluated. This time, titrations of starting DNA template were compared in protocols with and without a $4^{th}$ step (50 °C for 20 s). The full experimental design is given in the Appendix (Protocol: $4^{th}$ Step Test).

The resulting amplification curves are shown in Figure 3-34. The results appear to indicate that more efficient amplification occurred when the fourth step was omitted.

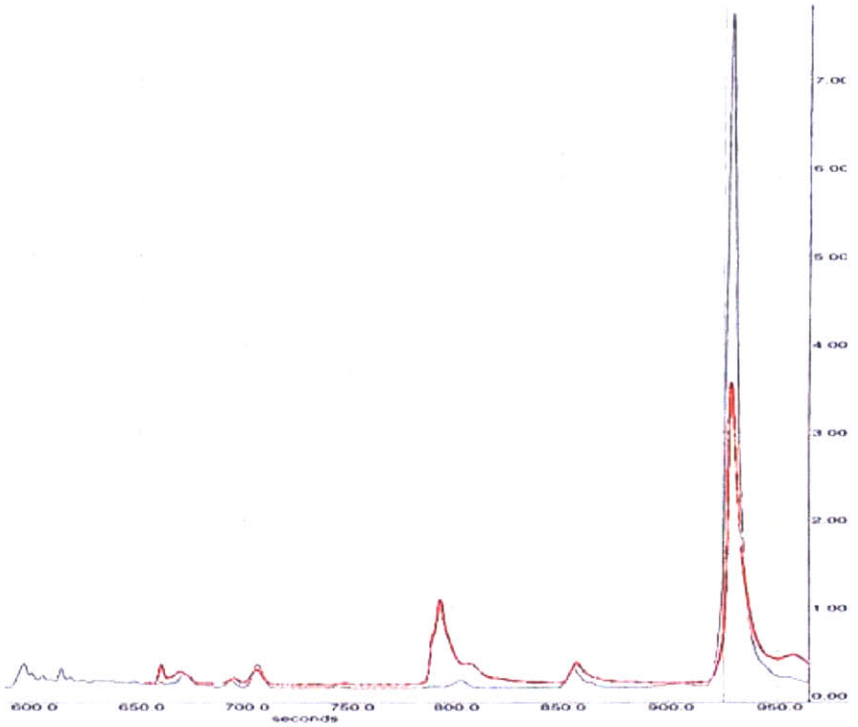


**Figure 3-33. Capillary electrophoresis data collected by Heelo Sudo comparing amplification with (red) and without (black) a fourth step (50 °C for 5 s ) in the PCR thermal cycle.**

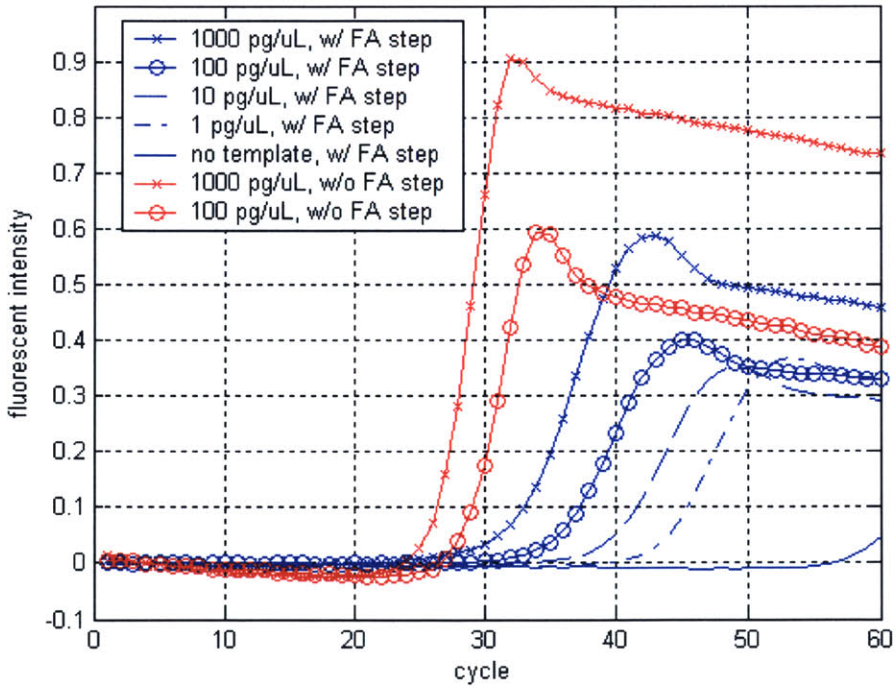


**Figure 3-34. Real-time PCR data from Roche LightCycler comparing amplification with (blue) and without (red) a fourth step (50 °C for 18 s ). A series of starting template concentrations are used as shown in the figure legend.**

The impact of the fourth step in the PCR was further studied by analysis of the PCR products. Instead of electrophoresis, melt profiles of the products were measured. Most commercial real-time PCR machines (including the Roche Lightcycler) have included in their functionality the ability to measure melt profiles. As discussed in Chapter 1, SYBR green measurement of real time PCR is susceptible to non-specific amplification. Analysis of PCR products by measurement of melt profiles enables confidence that amplification curves represent amplification of the specific target sequence.

Melt curves are generated by continuous fluorescence measurement while temperature is ramped from 50 °C to 95 °C at a slow rate (typically 0.1 °C/s). The analysis works best when the target sequence lies in an iso-melting domain. This means that all of the hydrogen bonds joining a double-stranded DNA molecule will be broken at essentially the same temperature. The temperature at which this event occurs is specific to the sequence of bases in the amplification target. Because SYBR green fluoresces more brightly when bound to double stranded than single stranded DNA, a sharp drop in the measured fluorescence occurs upon denaturation. Melt profiles are typically presented as the negative of the first derivative of the measured fluorescence to accentuate the temperature at which the sharp decline in fluorescence was observed.

Figure 3-35 shows the melt profiles comparing PCR products generated under thermal cycling protocols with and without the fourth step. Sharp peaks are observed for samples run without the fourth step. When the additional step was added, the peak is broadened, appearing to be the composite of two peaks. This broadening is evidence of non-specific amplification resulting in a product that is either longer or of sequence containing more G-C bases.

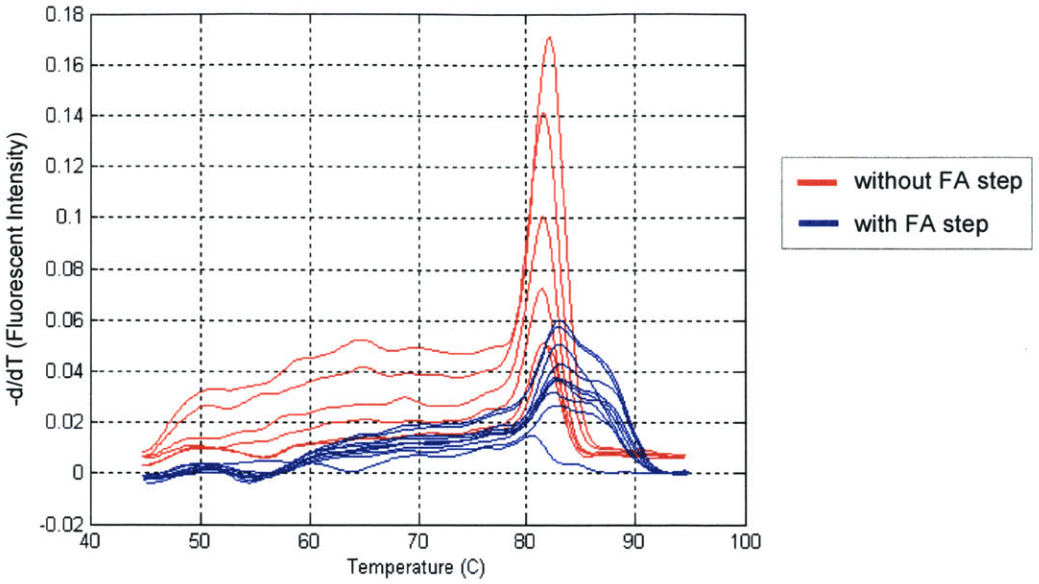


**Figure 3-35. Melt curves from Roche Lightcycler comparing melt profiles of PCR products to test the impact of a fourth step (50 °C for 18 s) in the PCR thermal cycle. Blue curves are those with the extra step. Red curves are those without a fourth step.**

The results of these experiments indicate that adding a fourth step at low temperature to improve FA range comes at the expense of non-specific amplification. Consequently, use of the fourth PCR step was eliminated. All future protocols included FA measurement during the extension step at 72 °C.

### *3.3.h. Avoiding Temperature Overshoot*

The dynamic response of the thermal profile also required some development. Published protocols typically list only steady state temperatures and dwells times. A controller, such as the one shown in Figure 3-2, is required to step the system between these temperatures. The amount of allowable overshoot is an important parameter in designing this controller.

Experiments with different thermal profiles made it clear that the Taq enzyme is easily damaged at temperatures above 95 °C. Indeed, product literature provided with the AmpliTaq Gold PCR Master Mix from Applied Biosystems, Inc. indicates that enzyme activity falls dramatically when exposed to 97 °C. Figure 3-36, taken from this product literature, illustrates the pre-incubation times and temperatures needed for degradation of

the "hot-start" modification of the enzyme. This degradation allows the enzyme to become fully activated. The figure also illustrates the decline in enzyme performance that occurs when the enzyme is exposed to temperatures greater than 97 °C.

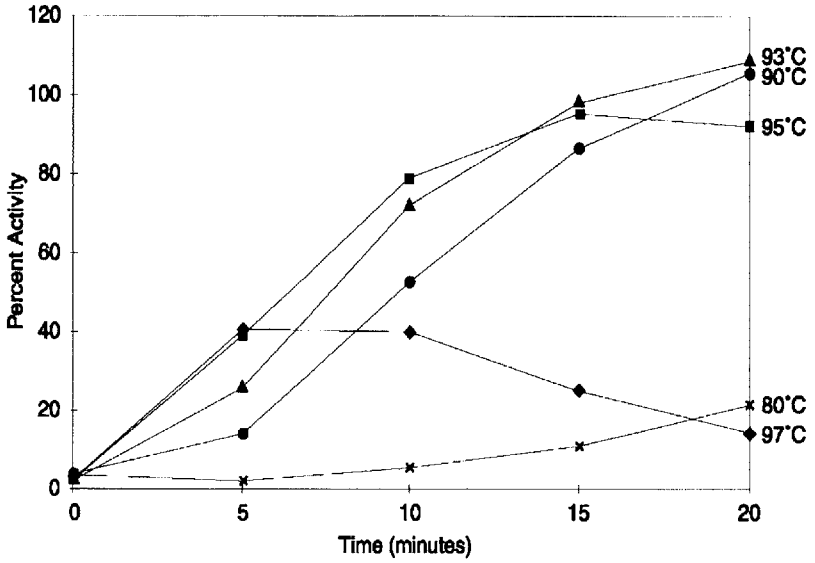


**Figure 3-36. Enzyme activation profile from AmpliTaq Gold PCR Master Mix Protocol. (Taken from http://docs.appliedbiosystems.com/pebiodocs/04317621.pdf)**

Several factors complicate the achievement of this design goal. First, all three of the prototypes relied on an external temperature measurement (see RTD placement in Figure 3-1) to estimate the temperature of the PCR solution. The control loop was closed on the basis of the external temperature and not on direct observation of the solution temperature.

The second complication was the desire to rapidly move the temperature from one set point to another. Thermal resistances, especially that of the glass and air gap at the glass-copper interface, slowed the conduction of thermal energy to the PCR sample. The solution was to program the controller to overshoot the target temperature at the point of measurement, and then sharply return that temperature to the target temperature. That strategy is illustrated in Figure 3-4.

Along the way to achieving the results shown in Figure 3-4, problems were encountered. The RTD used to measure the PCR solution temperature in calibration experiments was large (2 mm × 2.4 mm × 1mm) with respect to the PCR capillary tube

(2.5 mm ID). As such, the RTD reflected a spatially averaged temperature of the solution, low pass filtered by the thermal mass of the RTD. In addition, without enough care, air bubbles could be trapped around the RTD further slowing its response. The result was that early calibration experiments under-represented the temperature of the PCR solution, and it was allowed to become too hot. When measurement was improved by avoiding air bubbles and minimizing epoxy coating (applied for electrical isolation of RTD lead wires), overshoot was observed with the original settings as shown in Figure 3-37.

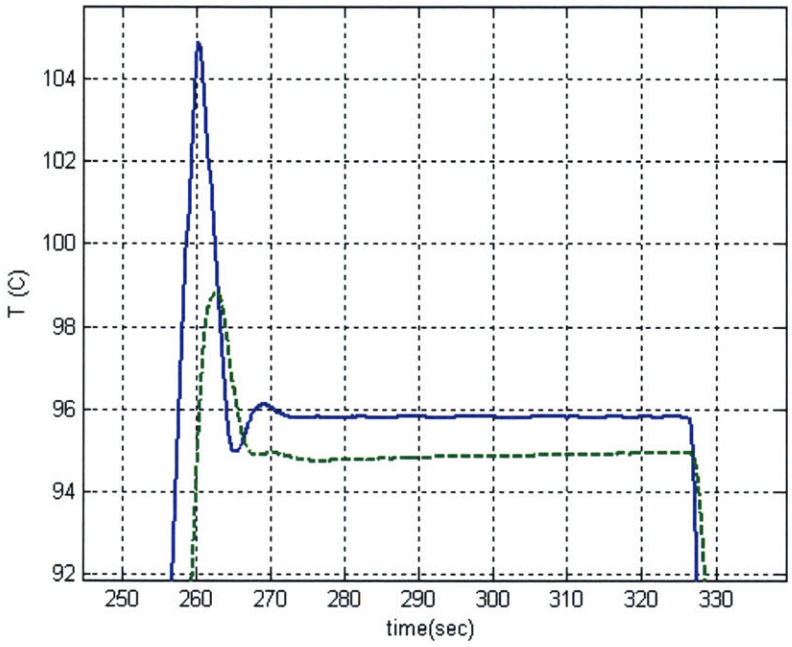


**Figure 3-37. Temperature profile of denaturation step with settings that caused overshoot of PCR solution temperature. Blue curve is external RTD measurement. Green curve is RTD submerged in PCR solution for calibration.**

The discovery that the PCR sample temperature was going too high and likely damaging the Taq polymerase was key to explaining the poor reproducibility and amplification efficiency that had plagued experiments up to that point. A collection of results illustrating this problem is shown in Figure 3-38.

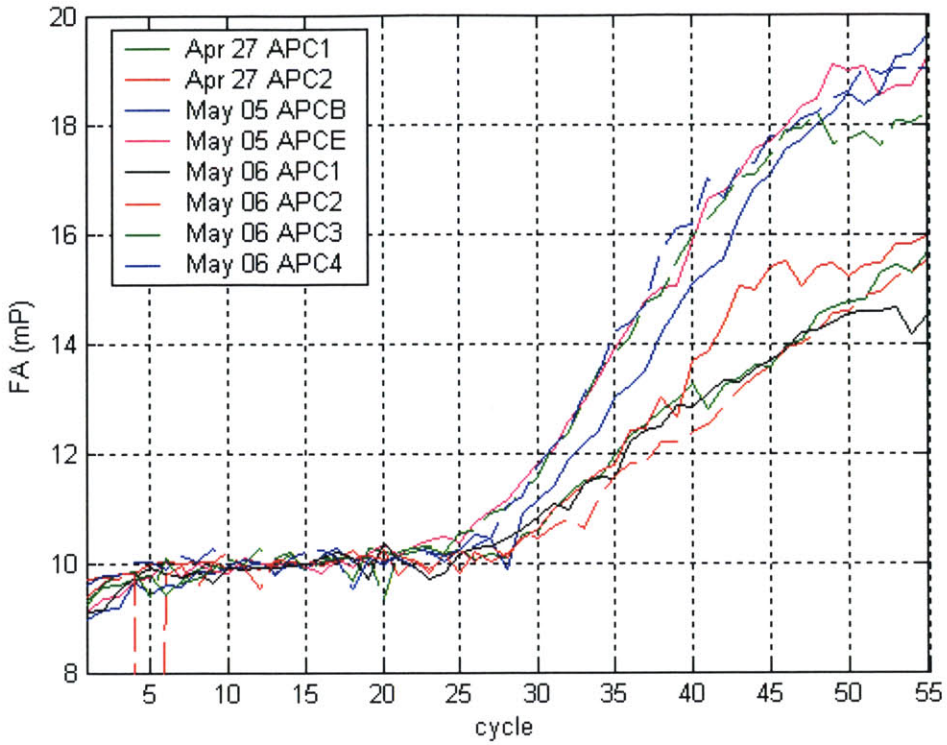


**Figure 3-38. A series of amplification curves generated before it was discovered that the temperature controller was allowing the PCR sample temperature to overshoot to detrimental levels. As enzyme was progressively damaged in each cycle, poor amplification efficiency was assured. This problem disappeared after temperature overshoot was eliminated.**

Once calibration methods were improved, it was a simple matter to modify the controller to eliminate the overshoot of the PCR sample temperature. In this controller correction, a less aggressive controller was implemented to provide additional allowance for the spatial-averaging and low pass filtering of the RTD. The results of the improved controller are shown in Figure 3-4.

# Chapter 4

# Design of Optical System

## 4.1. Design Requirements

The optical system must accurately and reproducibly measure the fluorescence anisotropy (FA) of the PCR sample. As described in Chapter 2, FA is the normalized difference between the vertical and horizontal intensities of the emitted fluorescence given by

$$FA=\frac{I_V-I_H}{I_V+2\cdot I_H}. \qquad 4\text{-}1$$

The optical system seeks to accurately measure $I_V$ and $I_H$, isolating them from light intensities other than emitted fluorescence.

The range of the FA measurements (i.e., the difference between the FA of product and the FA of primer) is fundamentally not a property of the optical system but of the measured molecules and their environment. Experiments for this thesis were primarily conducted with Alexa Fluor 488-labeled primers (20 bp) amplifying a 122 bp sequence from the APC gene. The FA range between primers and product labeled with Alex Fluor 488, measured at 72 °C, was ~10 mP. In contrast, the resolution of the FA measurement is determined by the optical system. In Chapter 2, a target dynamic range (the ratio of the measurement range and its resolution) of 200/1 was identified. Thus, the design requirement for FA measurement resolution (standard deviation) was 0.05 mP.

To the benefit of achieving these specifications, the fluorophore concentration used in PCR is relatively high (typically > 200 nM).

## 4.2. Final Design

A diagram of the optical system is shown in Figure 4-1. A photograph of the hardware is shown in Figure 4-2. A solid state laser set to full power (20 mW, 488 nm, Sapphire, Coherent, Inc.) provides the excitation intensity. Immediately after leaving the laser, the beam is attenuated by a neutral density (ND) filter (OD 3). The ND filter is mounted slightly out of perpendicular alignment so that the reflected beam does not return to the laser cavity. Next, a lens pair is used to expand the beam 5× (to 5 mm diameter). The expanded beam is reflected 90° by a mirror mounted on an adjustable support providing the mirror 4 degrees of freedom. The mirror was incorporated both because of space constraints and the desire to aid in beam alignment. An automated shutter serves as the next component in the system. The shutter is programmed to open immediately before and close after FA measurement. When allowed to pass the shutter, the beam continues on through a Glan-Thompson polarizer (Karl Lambrecht Corp.) which sharply attenuates the horizontal intensity. The collimated beam is then focused by a convex lens (f = 50mm). When allowed to pass the shutter, the excitation beam is reflected by a dichroic mirror and condensed onto the sample via an objective (0.3 NA, Zeiss Plan-NeoFluar 10X).

The excitation intensity collected by the same objective was transmitted back through the dichroic mirror. Wavelengths other than those of interest were attenuated by the band pass emission filter (UHP48030, Custom Scientific). A polarizing beam splitter then separated the vertical and horizontal components into the two detection arms of the instrument. Each detection arm contained an additional polarizer (Glan Thompson, Karl Lambrecht Corp.), a condensing lens, and a photomultiplier tube module (PMT) (H7422 PMT and M9012 controller, Hamamatsu).

The PMT controllers were powered by two single output power supplies (3632A, Agilent). Dynode array voltages are set using a multi-turn potentiometer on board the M9012 controllers. Optional external I/O control that bypasses this potentiometer is not

used because the PMT was observed to perform poorly in this mode. The output current from each PMT was amplified by $10^6$ with a Keithley 428 current amplifier. Each amplifier's built in low pass filter is set to a 300 ms time constant. The current suppress feature of these amplifiers is used to subtract background intensity. The output from each amplifier is measured by a digital multimeter (DMM) (34401A, Agilent) coupled to a desktop computer (PC). Both DMMs were externally triggered by a single output from the PC so that measurement was simultaneous for each PMT (1.67 s analog-to-digital integration where integration triggering was within 500 μs for both DMMs). At the extension stage of each PCR cycle, five anisotropy measurements are taken.

Anisotropy is computed from these measurements as

$$FA=\frac{I_{VM}-G\cdot I_{HM}}{I_{VM}+2\cdot G\cdot I_{HM}}, \qquad \textbf{4-2}$$

where $I_{VM}$ and $I_{HM}$ are the measured intensities (transduced as voltages by the PMT) for the vertical and horizontal polarization states respectively. G is a calibration factor to account for differing sensitivities and or preferential transmission of the detection arms. This calibration factor is computed by measuring a sample of known or assumed anisotropy. Measurements of anisotropy are typically reported in units of P or mP despite being a unitless quantity. Multiplying Equation 4-2 by 1000 results in an anisotropy measurement in mP.

The entire instrument is enclosed in a light-tight housing, shown in Figure 4-3, to seal it from ambient light. The enclosure consisted of two compartments separating the optical system from the sample holder. The mean temperature of the sample holder chamber temperature was over 31 °C and exhibited oscillations due to the changing thermal loads of the thermal cycler. The optical system was housed in a separate compartment to isolate it from these thermal fluctuations. This compartment was temperature regulated by a thermoelectric heat pump (AC-027, TE Technology, Inc.) and controller (TC-24-25-RS232, TE Technology, Inc.). Typically it was set to hold a constant 29 °C and maintained this air temperature to with in ±0.1 °C.

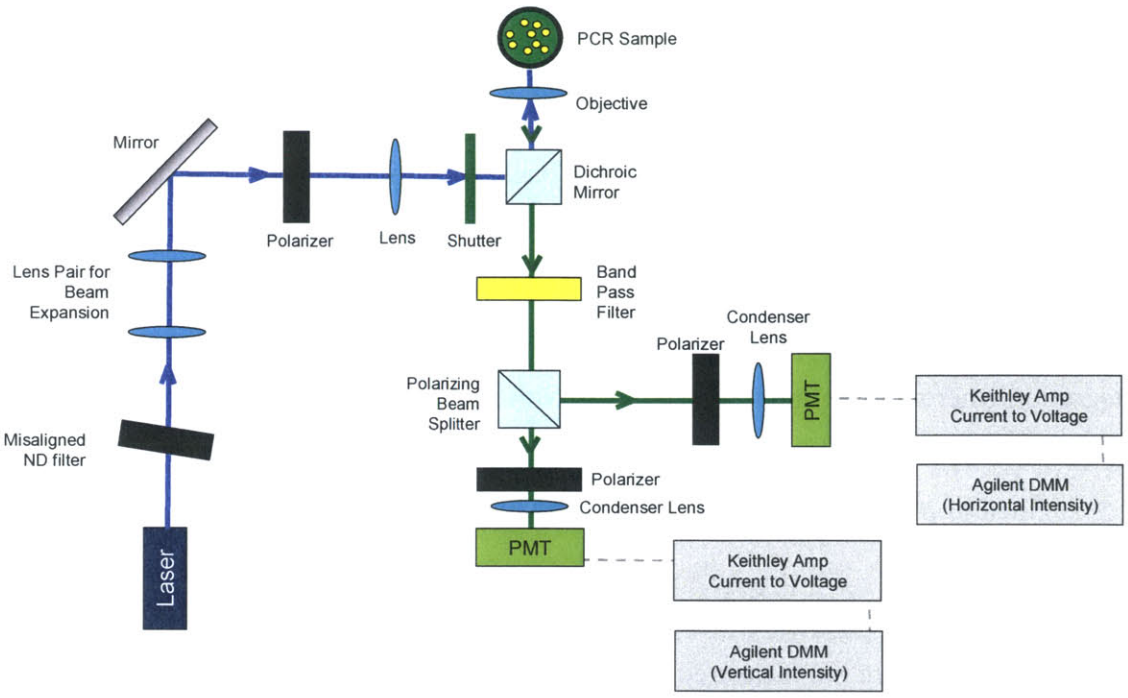


**Figure 4-1. Final optical system layout for FA measurement of real time PCR.**

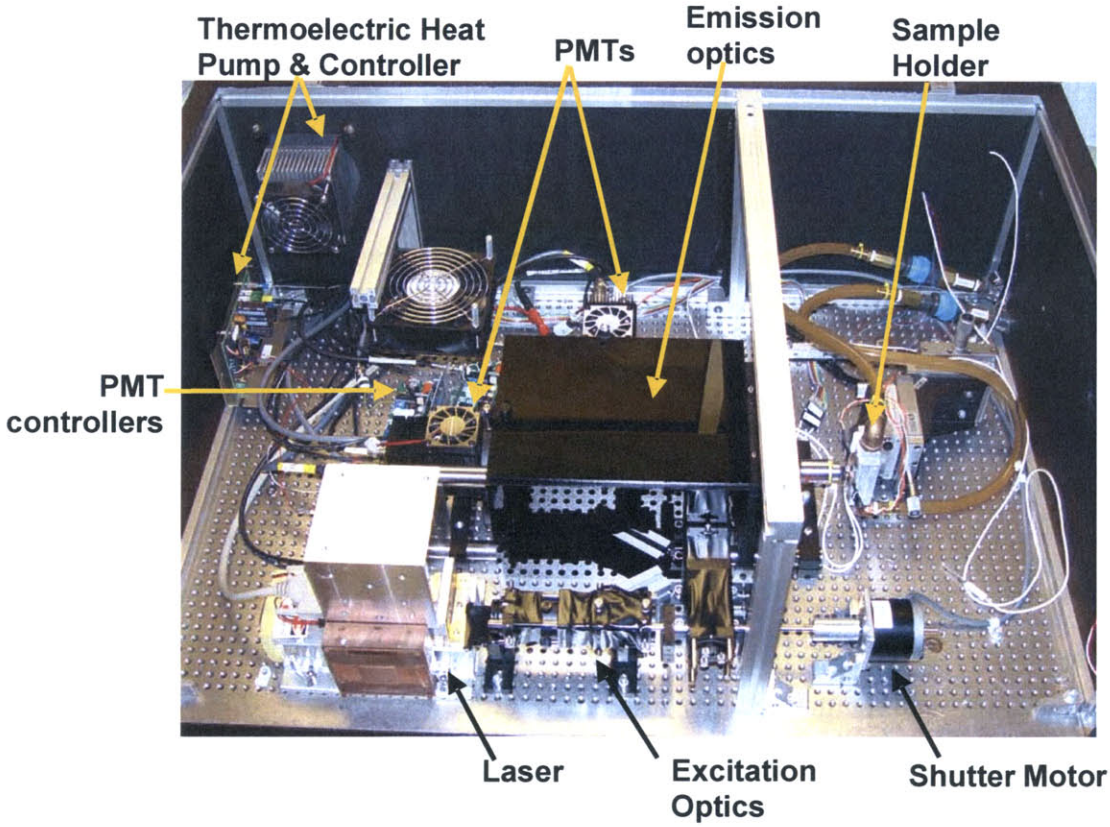


**Figure 4-2. The two compartments of the instrument. At left, the optical measurement compartment. At right, the sample holder compartment.**

**Figure 4-3. Instrument was housed in a light tight, temperature regulated enclosure consisting of two separate compartments.**

## 4.3. Performance Results

In this section, the performance of the optical system is analyzed via data taken in four experiments. The first three data sets are presented again in Chapter 5, however, the focus in that later chapter will be other than optical system characterization. Full experimental protocols for all experiments can be found in the Appendix.

### *4.3.a. Un-enriched DNA as starting template*

The first two sets of data illustrate typical results for purified genomic DNA. The experiment shown in Figure 4-4 began with a starting template concentration of 10 pg/μL, while the experiment of Figure 4-5 began with only 1 pg/μL (See experimental protocol for Dilution Series in Appendix). At the left in each figure is the computed FA, uncorrected (and thus shown as negative). Five FA measurements (data points marked by pink Xs) were taken at each cycle. The average of those data points is given by the blue line. The average of the five intensity measurements taken at each cycle for each polarization state are shown in the plot on the right of each figure. In these intensity plots, the horizontal intensity has been offset to make it more viewable.

Both experiments exhibit approximately the same total change in FA (~ 7 mP) as the primer is integrated into product DNA. The standard deviation of the five FA measurements at any given cycle are approximately the same in the first 20 cycles for both figures (~0.13 mP). The standard deviation across cycles 10 to 22 of the FA measurements averaged at each cycle is only 0.035 mP for Figure 4-4 and 0.11 mP for Figure 4-5.

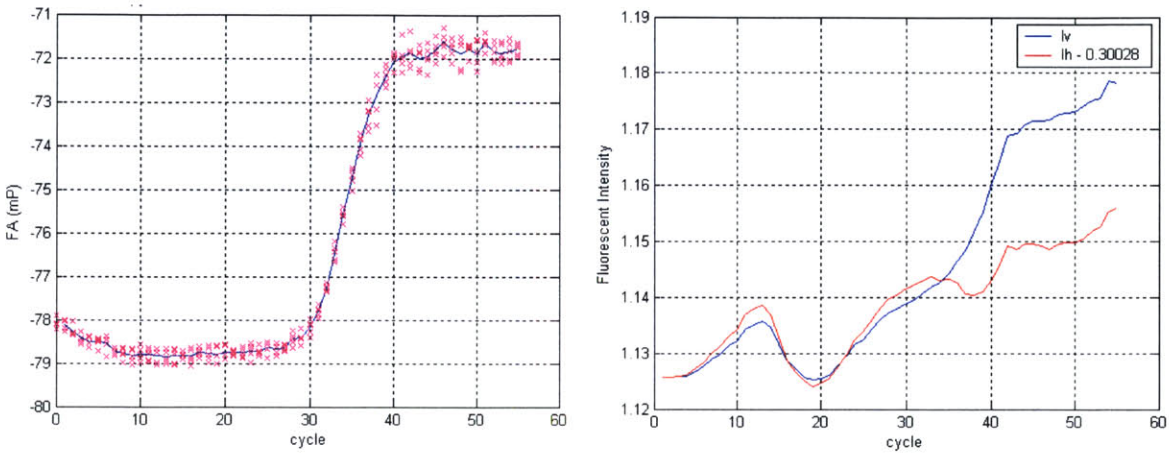


**Figure 4-4 Real-time PCR data for 10 pg/µL genomic DNA, [Left]: Uncorrected FA measurements (pink Xs) and average (blue) , [Right]: Vertical (blue) and horizontal (red) intensity measurements used to compute FA at left. Horizontal intensity measurement has been offset- see legend. (Exp: June9_2004_10pg-uL_B).**

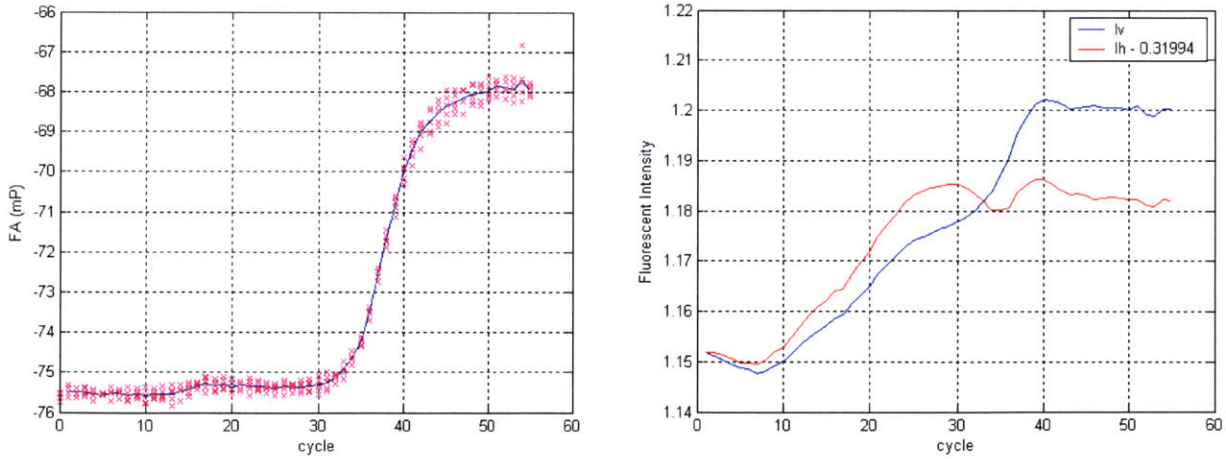


**Figure 4-5. Real-time PCR data for 1 pg/µL genomic DNA, [Left]: Uncorrected FA measurements (pink Xs) and average (blue) , [Right]: Vertical (blue) and horizontal (red) intensity measurements used to compute FA at left. Horizontal intensity measurement has been offset- see legend. (Experiment: June9_2004_1pg-uL_A).**

Other than the small drift observed in the early cycles of Figure 4-4, over the first 25 cycles of both figures, the FA measurement is essentially flat (i.e., primer molecules drastically outnumber product such that the net measurement reflects only the FA of the labeled primer). During these cycles, the mean FA would ideally be equal. In fact, they differ by ~ 3 mP. Likewise, the measured component intensities would ideally be constant, however some drift is observed. In both data sets, less than 3% drift is observed within the first 25 cycles relative to the intensities measured at the first cycle.

*4.3.b. Enriched DNA as starting template*

Better performance was observed when enriched DNA was used as the starting template. An example of data from amplification of enriched DNA is shown in Figure 4-6, again with the FA measurements on the left and component intensities on the right. The protocol used in this experiment can be found in the Appendix under Enriched DNA protocol.

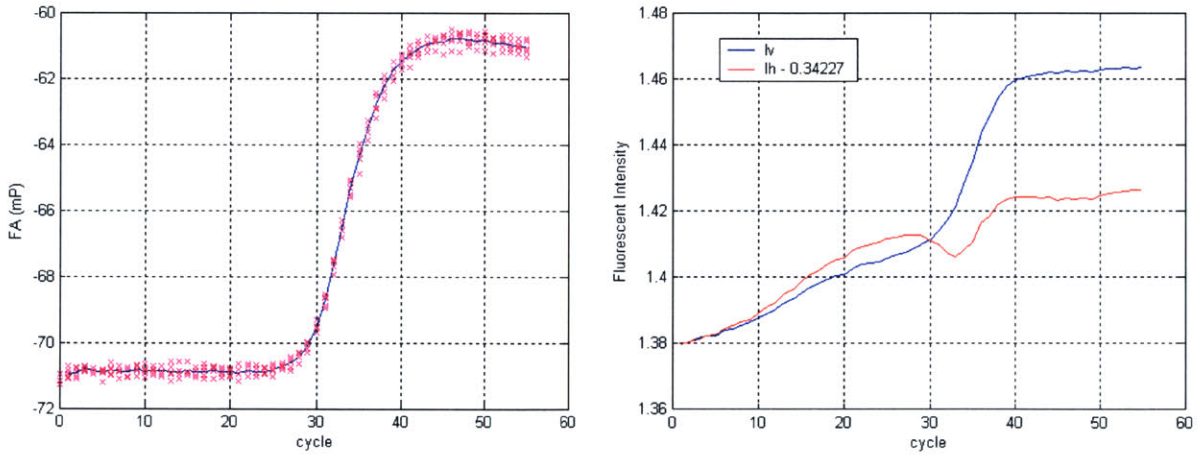


**Figure 4-6. Real-time PCR data for DNA template enriched for target, [Left]: Uncorrected FA measurements (pink Xs) and average (blue) , [Right]: Vertical (blue) and horizontal (red) intensity measurements used to compute FA at left. Horizontal intensity measurement has been offset- see legend. (Experiment: June17_2004_enrichedB).**

In three replicates of this experiment, none exhibited the early-cycle drift present in Figure 4-4. The measurement range was also 20-35% larger than for amplification of un-enriched template. The standard deviation of the five FA measurements taken at any

cycle (pink X's) was essentially the same as for the un-enriched experiments (0.14 mP). However, consistent with the elimination of the early cycle drift, the averaged FA (blue line) was more stable. The standard deviation across the averaged measurements of cycles 10 to 22 was 0.02 mP. The average FA over the first 25 cycles is -71 mP which is again different from both that observed in Figure 4-2 (-78.5 mP) and Figure 4-3 (-75.5 mP).

The component intensities in enriched template experiments were observed to be 20-30% greater than in un-enriched experiments. The intensity drift over the first 25 cycles was similar for both types of starting template (~3%).

*4.3.c. Long time-span FA measurements*

In order to further characterize the FA measurement, experiments were performed to measure the FA over longer time intervals than the typical 20 s used in real-time PCR experiments.

The long time span experiment shown in Figure 4-7 measured 20 μL of Alexa Fluor 488 labeled primer diluted to 200 nM in Millipore water. $MgCl_2$ was added to a concentration of 3 mM. This solution was covered by 15 μL of mineral oil as per typical protocol. The thermal cycling profile was also typical (Denature: 95 °C for 15 s ; Anneal: 45 °C for 45 s ) except that the "extension" stage in which the FA was measured was increased to 1000 s at 72 °C.

The uncorrected FA measurement from these experiments is shown in the upper half of Figure 4-7. A drift with a long time constant ($\tau \sim 180$ s) is observed at each measurement. At each cycle, the initial FA measurement repeatably returns to an initial value of -75 mP. When the FA response has reached its steady state value, its standard deviation around that steady state over a four second window is 0.05 mP.

The component intensity measurements, shown in the lower half of Figure 4-7 also exhibit a first-order drift, but one that is not a function of thermal cycling. The response of the component intensities has a time constant of almost 10 minutes. The intensities become quite stable after 20 minutes varying by less than ±0.24%. In regions of flattest stability (such as the period from 27 minutes to 33 minutes) the intensities

exhibited a standard deviation of 0.348 mV and 0.364 mV for the vertical and horizontal component intensities, respectively.

The drift in the FA measurement is also visible in the data sets presented above. Figure 4-8 presents a zoomed view of the first 28 cycles of the data presented in Figure 4-6. Instead of plotting the uncorrected FA over cycle number, Figure 4-8 shows the data plotted against time. Each narrow vertical band of five data points (marked by + ) represents the FA measurements collected at the end of one cycle. The measurements are observed to sequentially increase at each cycle.

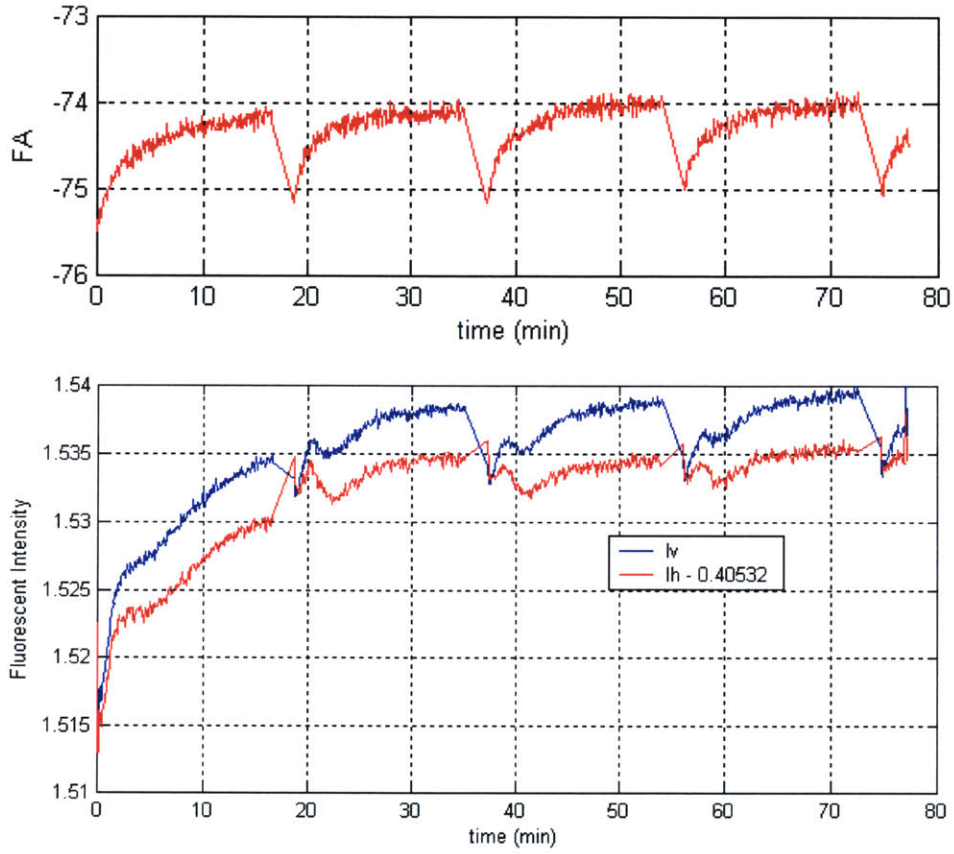


**Figure 4-7. Long term measurement of 200 nM primer solution over 1000 s interval at 72 °C. Between measurements, solution was thermal cycled as usual (Denature: 95 °C for 15 s ; Anneal: 45 °C for 45 s ). [Upper]: FA measurement; [Lower]: Component intensities where Ih (red) has been offset to make it more viewable with respect to Iv (blue).**

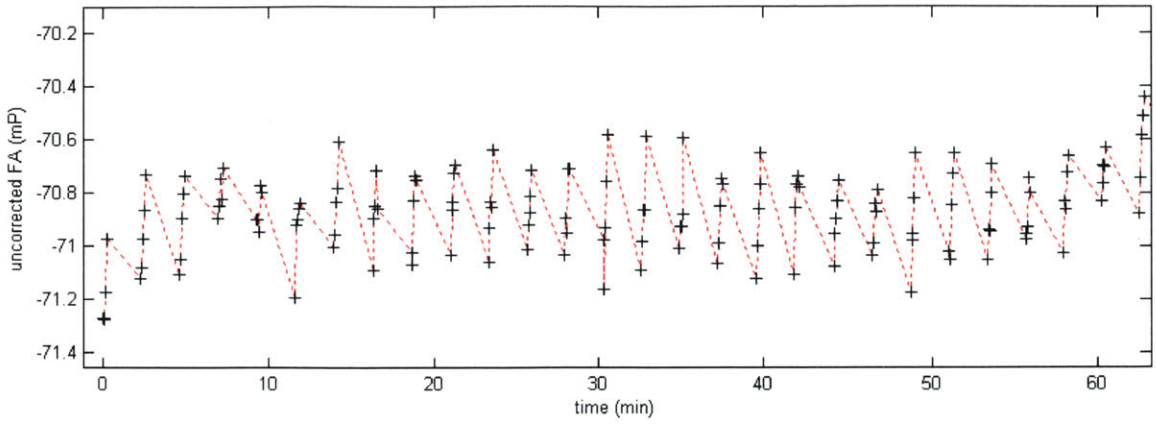


**Figure 4-8. Zoomed view of first 28 cycles of Figure 4-6 plotted against time (instead of cycles). Each narrow vertical band of five data points (+) represent the measurements taken at the end of one PCR cycle. A sequence of increasing FA values are observed at each cycle.**

### *4.3.d. Summary of Observations from Performance Data*

The goals of the optical system design are to make accurate, repeatable FA measurements of the amplification process with enough dynamic range for accurate quantification of the starting template number. In the results presented in Figure 4-4 through Figure 4-7, the limitations of the optical system are characterized. The remainder of this chapter is dedicated to analyzing the sources of error that define the observed measurement limitations. The limitations are summarized below with a brief preface on the limiting error source.

Summary observations from the above data include:

A. Component intensities drift ≤3% over a period of 25 cycles under what should have been constant measurement conditions. Possible cause include drift of either the excitation intensity or detection sensitivity. Chemical change of labeled fluorophores is also possible, however, this is not analyzed below.

B. Early cycle FA measurements do not agree across identically designed experiments, differing by ± 4 mP. This is most likely due to relative changes in detection sensitivity of the two intensity polarization states.

C. From Figure 4-7, FA drifts upward during measurement at each cycle, moving ~ 1 mP over a 1000 s window. Since only labeled primer (no other oligonucleotides or template) was included in the experiment, this is not believed to be representative of slow molecular interactions. Instead this is believed to be a drifting of one PMT relative to the other where the drifting is induced by the measurement itself.

D. In the long term measurements of Figure 4-7, when the drifting of intensities and FA was allowed to stabilize , the standard deviations were 0.348 mV, 0.364 mV, and 0.05 mP for the vertical intensity, horizontal intensity, and FA, respectively. These are measurements are limited by the shot noise inherent in photonic measurements.

E. When the five FA measurements of each cycle are averaged, the standard deviation of those FA averages, across 10 early cycles, is ~0.05 mP for un-enriched DNA and <0.02 mP for enriched DNA. The measurement ranges were 7 mP and 10 mP for genomic and enriched DNA, respectively. The result is a measurement dynamic range of 1:70 for genomic DNA and 1:250 for enriched DNA.

## 4.4. Sources of Error

In this section, sources of error in FA measurement are reviewed. The initial focus will be on sources of error that drive the Summary Observations above. Additional errors sources, minimized by the instrument design are also discussed.

### *4.4.a. Excitation drift*

The drifting in the component intensities described in Summary Observation A is due to drifting in the excitation energy or in emission measurement (where the major source of drift is the PMT). PMT drift is discussed as a subsequent topic.
Lasers with emission at 488 nm typically have a specified stability of ±2%. The Coherent Sapphire 488 laser employed in this instrument was specified to have a long

term (2 hour period) power stability of <2% given an environmental temperature stability of ±3 °C. Numerous attempts were made to characterize the laser's performance, however it was always difficult to distinguish sensor drift from laser drift. Early experiments after receipt of the laser indicated excellent stability (within ±0.5%) however subsequent failure of a current-to-voltage amplifier that had been used in those experiments called the validity of these results into question.

In addition to efforts to measure the laser stability with a custom measurement, the Sapphire laser has a built-in photodiode for closed-loop power regulation. The output of this photodiode could be read using the RS-232 communication capability on the laser. Variability in the laser output could be observed on the photodiode during warm-up but readings stabilized within the specified 5 minute warm up time. The photodiode typically reported deviations of less than 0.1 mW during operation when the laser was set at 20 mW output.

Excitation intensity stability is not a function of laser power stability alone. Laser pointing stability and thermal expansion shifts of optical components could also have modified the excitation intensity at the sample.

The data of Figure 4-5 and Figure 4-6 indicate drifting of the fluorescent emission intensity of as much as 3%. Figure 4-7 clearly shows a long term emission drifting of 1.3%. While evaporation at the sample holder (increasing the concentration of the fluorophore) or detector drift could also cause the measured intensities to drift, these observations indicate that the excitation intensity exhibited long term stability of at least as good as 3%.

The anisotropy of fluorescence emission is a function of the fluorophore properties and its rotational diffusion in the sample solution. Because it is a normalized difference, FA is independent of the excitation intensity. The ***measured*** FA ($FA_M$), however, can become a function of the excitation intensity in error of the true value.

In order to quantify this source of error, the analysis begins with a simplifying assumption that the excitation intensity is purely vertically polarized with intensity $I_o$. The total emission intensity is $I_V + 2 \cdot I_H$ (Lakowicz, 1999) where $I_V$ and $I_H$ are as defined for Equation 2-5. By conservation of energy, $I_V + 2 \cdot I_H = \beta \cdot I_o$ where $\beta$ is the effective

excitation efficiency. Combining this with Equation 2-5, component intensities are computed as

$$I_H = \frac{\beta}{3} \cdot (1 - FA) \cdot I_o, \quad \textbf{4-3}$$

$$I_V = \frac{\beta}{3} \cdot (1 + 2 \cdot FA) \cdot I_o, \quad \textbf{4-4}$$

where FA is the true fluorescence anisotropy of the fluorophore in its environment.

This fluorescent emission is collected by the objective and travels through the dichroic mirror and band pass filter before being split into the detection arms for measurement. Also collected by the objective is reflected laser light. In addition, the dichroic mirror scatters some amount of laser light into the optical path. Dust in the optical path can also cause laser excitation to become scattered into the detection optics.

A bandpass filter is implemented in the system to significantly attenuate the excitation wavelength. The interference filter employed (UHP48030, Custom Scientific) is specified to attenuate 488 nm light by a factor of $10^{-6}$. The filter achieves this attenuation by using thin film coatings having alternating indices of refraction that create reflective interfaces for the null bands. Much of the intensity is rejected by this reflection. The rest of the attenuation occurs by destructive interference. The thin film layer thicknesses are precisely deposited to coincide with quarter wavelengths. These thicknesses are designed under the assumption that incident light is collimated and arriving at normal incidence.

In practice, the reflected and scattered photons that arrive at the filter do not strictly comply with these assumptions. Off axis rays significantly reduce the attenuation performance of interference filters thereby allowing laser light to be transmitted through the filter. These photons, scattered through many independent events, are essentially fully depolarized. Thus, transmitted through the filter along with $I_V$ and $I_H$ of Equations 4-3 and 4-4 is a background intensity whose polarization components are of approximately equivalent magnitudes.

Ignoring any preferential transmission of one polarization state over the other (because it can be calibrated out by the G-factor), these intensities arrive at the detector. The PMT employs a scintillator which releases an electron when struck by a photon. These photons are accelerated through an electric field toward a dynode. The increased

momentum of the electron causes multiple electrons to be released from the dynode upon being struck by a photon-generated electron. An array of dynodes follows, amplifying the initial one to one ratio of photons to electrons by a factor of $10^8$ to $10^{10}$ (depending on the number of dynodes, field intensity, and PMT age) (Hamamatsu Corporation, 1998). The electron flux is measured as a current and sent through a low noise current-to-voltage amplifier. The voltage is read by a data acquisition system. Given constant gain (field intensity) and temperature, the output voltage is linear with input intensity over several orders of magnitude (i.e., $V_V = m_V \cdot I_V$).

In addition, the conversion can be accompanied by an offset voltage. Thermal vibrations in the scintillator cause electrons to be released randomly, independent of a photon strike. This false signal that can be measured in total darkness is called dark current and is proportional to the temperature of the scintillator and dynode chain. The measured voltages can be summarized as

$$V_H = m_H\left(\frac{\beta}{3}\cdot(1 - FA)\cdot I_o + I_{LBH}\right)+b_H, \qquad \textbf{4-5}$$

$$V_V = m_V\left(\frac{\beta}{3}\cdot(1 + 2\,FA)\cdot I_o + I_{LBV}\right)+b_V, \qquad \textbf{4-6}$$

where $m_H$ and $m_V$ are the photon to voltage conversion factors, $I_{LBV}$ and $I_{LBH}$ are the background laser intensities reaching each detector, and $b_H$ and $b_V$ are the dark currents for the photomultipliers.

In practice, the dark current is small relative to the background laser intensity and similar for both PMTs. This is true in particular for the PMTs implemented in the final setup (H7422, Hamamatsu). The housing temperature of these PMTs is cooled to 4 °C by a PID controlled thermoelectric. At this temperature, dark current is more than 10× lower than the already low level observed in ambient temperature PMTs. Therefore, in computing the measured FA, where $FA_M = (V_V - V_H)/(V_V + 2V_H)$, the difference in the dark currents is negligible in the numerator and their sum is negligible (relative to the rest of the summed term) in the denominator. The resulting equation for the measured FA is given by

$$FA_M = \frac{\frac{\beta \cdot I_o}{3}\left(m_V \cdot (1 + 2\,FA) - m_H \cdot (1 - FA)\right) + m_V \cdot I_{LBV} - m_H \cdot I_{LBH}}{m_V \cdot \left(\frac{\beta}{3} \cdot (1 + 2\,FA) \cdot I_o + I_{LBV}\right) + 2 \cdot m_H \cdot \left(\frac{\beta}{3} \cdot (1 - FA) \cdot I_o + I_{LBH}\right)} \cdot \qquad \textbf{4-7}$$

If the two PMTs have identical linearities ($m_V = m_H$) and the background intensity from the laser is completely depolarized ($I_{LBH} = I_{LVB}$), then Equation 4-7 simplifies to

$$FA_M = \frac{\beta \cdot I_o}{\beta \cdot I_o + I_{LB}} \cdot FA = \frac{1}{1 + I_{LB} / \beta \cdot I_o} \cdot FA\,. \qquad \textbf{4-8}$$

The term $\beta \cdot I_o$ is the total fluorescent intensity collected by the optical system and $I_{LB}$ is the scattered laser light collected in one detection arm. Under these assumptions, the blue (top-most) curve of Figure 4-9 shows the resulting measurement error given signal-to-background ratios ($\beta \cdot I_o / I_{LB}$) of $0^+$ to 1000. The true FA was assumed to be 100 mP. In the final instrument configuration, signal-to-background ratios were <45 (before any background subtraction). Figure 4-9 indicates that background laser light can cause substantial errors in FA measurement (1 to 2 mP at typically observed signal to background ratios). These errors cannot be removed by G factor correction. Note also, that the assumption that the background laser light was completely depolarized resulted in a computation of a lower threshold on the expected error. In practice, the backgrounds measured in each detection arm are different. This can add as much as 50% more error than predicted by Figure 4-9.

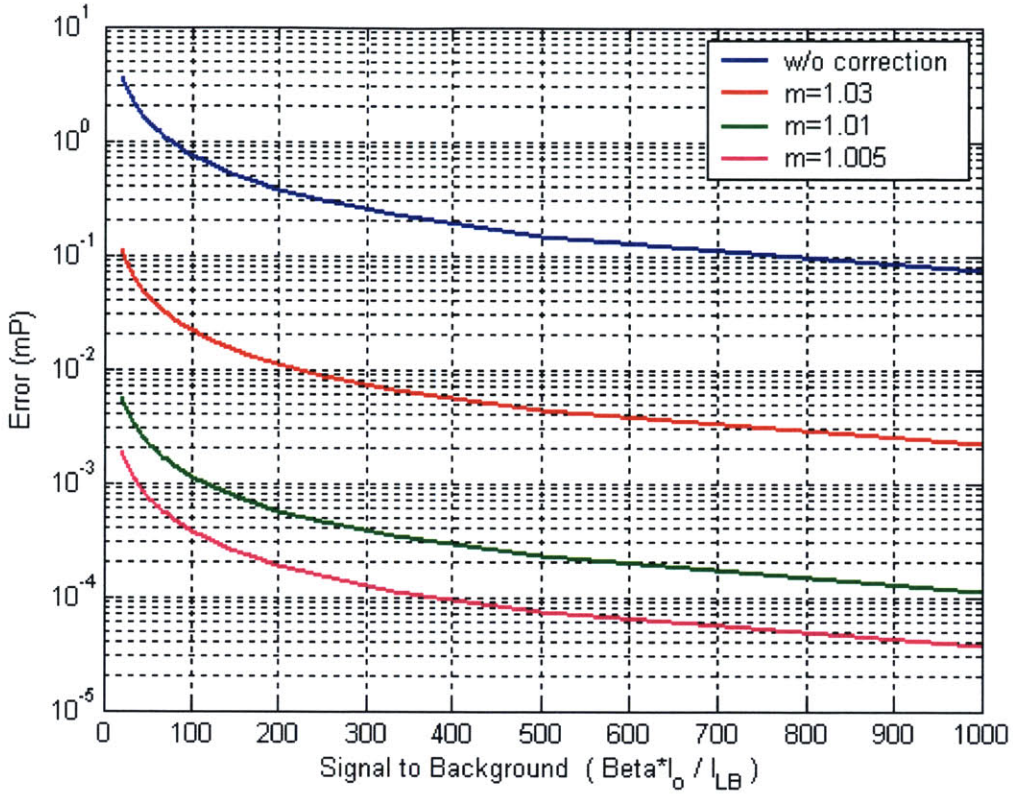


**Figure 4-9. Error between measured FA ($FA_M$) and the true FA as a function of signal-to-background ratio. True FA is taken as 100 mP in this example.**

To minimize this error, background subtraction can be implemented by measuring the voltages corresponding to the laser background intensities ($V_{VB}$ and $V_{HB}$) when the sample solution is a water blank. $FA_M$ is then computed as

$$FA_M = \frac{(V_V - V_{VB}) - G \cdot (V_H - V_{HB})}{(V_V - V_{VB}) + 2 \cdot G \cdot (V_H - V_{HB})}. \qquad \textbf{4-9}$$

While this can dramatically reduce the measurement error, it does not alleviate the problem of dynamic variation of the laser intensity. Background intensity measurement must be done prior to the experiment and any variation in the laser intensity after that will result in a change in the background and thus an error in the measured FA. Incorporating the benefits of background subtraction and assuming the excitation intensity variation is given as a percentage, m, of the intensity upon calibration ($I_o$), Equation 4-8 may be rewritten as

$$FA_M = \frac{1}{1 + \frac{(m-1)\cdot I_{LB}}{m\cdot\beta\cdot I_o}}\cdot FA \qquad \textbf{4-10}$$

where m is the ratio of the excitation intensity during FA measurement to the intensity during background measurement.

As noted, a drift of 3% was observed in the experiments of Figure 4-3 and Figure 4-6. A deviation of 3% from the original intensity provides an m = 1.03. Referencing this curve in Figure 4-9, the error caused by a 3% drift in excitation intensity is 0.05 mP (given a pre-subtraction signal-to-background ratio of 45). Errors caused by excitation drifting of 1% (m = 1.01) and 0.5% (m = 1.005) are also shown in the figure.

This analysis indicates that given adequate signal-to-background levels, long term drifting of as much as 3% in the excitation intensity provide insignificant error to FA measurements (<0.05 mP).

*4.4.b. PMT drift*

The drifting of component intensities described in Summary Observation A could have been caused by drifting in detector sensitivity (instead of or in parallel to the previously discussed drifting of excitation intensity). The component intensities are observed to change with similar, though not identical, shapes. Such similarity could be explained by thermal changes in the environment of the PMT affecting the photocathodes or the PMT controllers.

Any drifting in PMT sensitivity that affects both detectors equally will have minimal impact on the FA measurement and as such are of limited concern. However, any source of sensitivity drift has the potential to manifest itself in a way that is not uniform across the PMT pair. Non-uniform sensitivity changes can cause large errors in FA measurement.

To keep the analysis simple, assume that background intensity is zero. Then Equation 4-7 becomes

$$FA_M = \frac{m_V\cdot(1 + 2\,FA) - m_H\cdot(1 - FA)}{m_V\cdot(1 + 2\,FA) + 2\cdot m_H\cdot(1 - FA)}. \qquad \textbf{4-11}$$

Substituting $R = m_H/m_V$, Equation 4-11 reduces to

$$\Delta FA = \frac{(1-R)\cdot(1+FA)}{(1+2R)} \qquad \textbf{4-12}$$

and is plotted in Figure 4-10 for a ±2% change in $m_H$ relative to $m_V$. From this figure, it is apparent that for even a 0.5% change in relative sensitivity, significant (1.8 mP) error in FA measurement can result. Several potential sources of PMT sensitivity drift are discussed below.

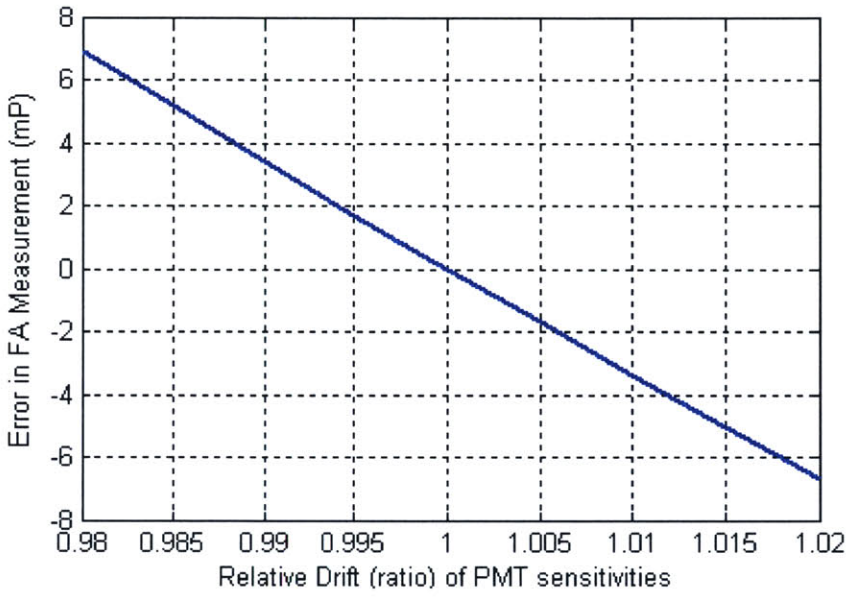


**Figure 4-10. Theoretical error between measured FA ($FA_M$) and the true FA resulting from the drift in $m_V$ relative to $m_H$. True FA is taken as 20 mP in this example.**

*Photocathode temperature sensitivity*

Figure 4-11 shows the temperature sensitivity of various photocathode materials to temperature. The H7422 PMT used in this instrument contains a multialkali photocathode. From the figure, the photocathode temperature sensitivity is –0.3 % / °C at 520 nm wavelengths.

The H7422 PMT has an integrated thermoelectric cooler placed near the photomultiplier tube to reduce thermal noise emitted from the photocathode. According to product literature, "The photomultiplier tube is maintained at a constant temperature by monitoring the output from a thermistor installed near the photomultiplier and then

regulating the current to the thermoelectric cooler (Hamamatsu Corporation, 2002)." The implementation is not ideal in that there is a non-ideal thermal pathway between the regulated surface and the photocathode (the photocathode is housed in a vacuum tube). However, effective dark current reduction is observed when the cooler is enabled. For all experiments, the controller was set to maintain a 0 °C set temperature. The thermoelectric cooler, in addition to reducing dark current, also served to stabilize the photocathode current against ambient temperature variations. At steady state, the cooler is specified to achieve a stability of at least ±0.2 °C. The H7422 PMT does not include the ability to externally communicate the thermistor readings, thus it was not possible to verify this stability. It was also not possible to measure the extent to which the photocathode was truly isolated from environmental temperature changes.

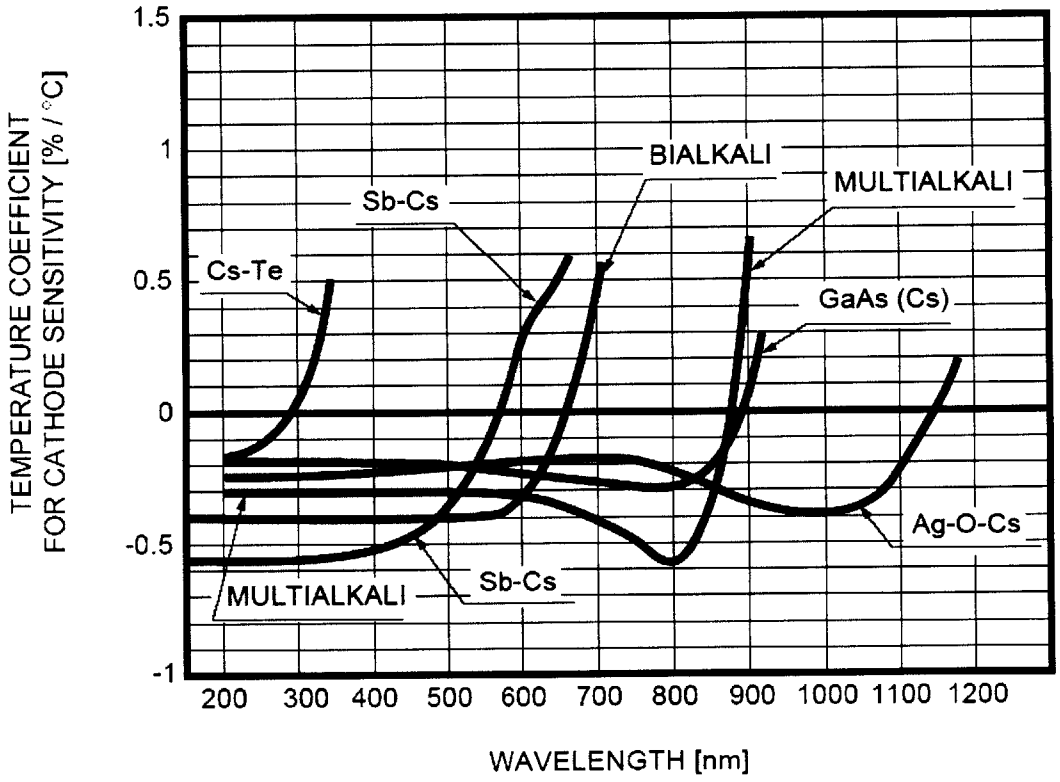


**Figure 4-11. Temperature sensitivity of the photocathodes in Hamamatsu PMT (Hamamatsu Corporation ,1998).**

Toward supporting improved stability for the optical system, an environmental temperature regulation system was installed (see Section 4.2) stabilizing the optical instrument enclosure to least ±0.5 °C.

regulating the current to the thermoelectric cooler (Hamamatsu Corporation, 2002)." The implementation is not ideal in that there is a non-ideal thermal pathway between the regulated surface and the photocathode (the photocathode is housed in a vacuum tube). However, effective dark current reduction is observed when the cooler is enabled. For all experiments, the controller was set to maintain a 0 °C set temperature. The thermoelectric cooler, in addition to reducing dark current, also served to stabilize the photocathode current against ambient temperature variations. At steady state, the cooler is specified to achieve a stability of at least ±0.2 °C. The H7422 PMT does not include the ability to externally communicate the thermistor readings, thus it was not possible to verify this stability. It was also not possible to measure the extent to which the photocathode was truly isolated from environmental temperature changes.

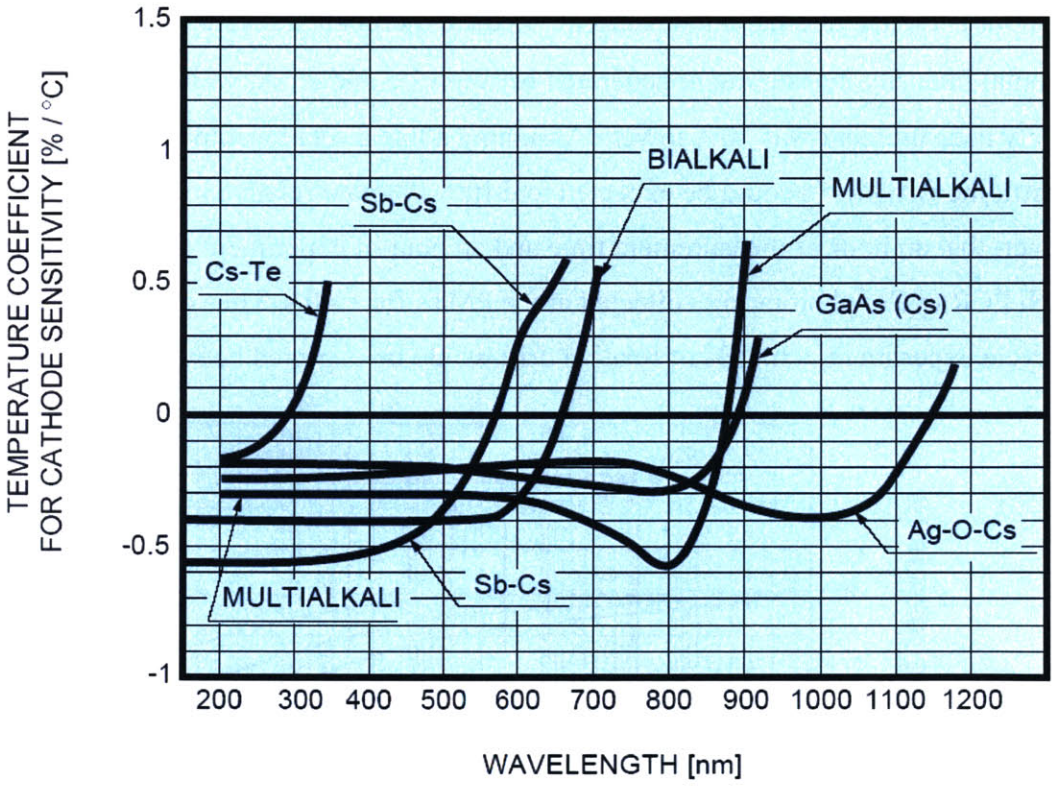


**Figure 4-11. Temperature sensitivity of the photocathodes in Hamamatsu PMT (Hamamatsu Corporation ,1998).**

Toward supporting improved stability for the optical system, an environmental temperature regulation system was installed (see Section 4.2) stabilizing the optical instrument enclosure to least ±0.5 °C.

Through these two design features, it was unlikely that the photocathode temperature could drift beyond ±0.2 °C relative to each other. Thus the expected change in PMT output would not be expected to exceed ±0.06%. A rising ambient temperature could cause larger drift but this drift would be identical for both PMTs.

*PMT sensitivity decline due to dynode wear*

When operating a PMT continuously over a long period, the anode output current of the PMT may decline over time despite constant operating conditions. This drift is primarily caused by damage to the last dynode by heavy electron bombardment. The rate of this drift is dependent on the rate of electron bombardment (the measured current). In a personal communication, Hamamatsu technical support reported that a drift of 0.5%/hour is typical at 2 μA anode current. In the experimental results shown above, the horizontal intensity measurement generated between 1.5 and 2 μA, while the vertical intensity measurement was 20% lower. Assuming a linear relationship between current and drift, the two PMTs could be expected to drift 0.1%/hour relative to each other. Note however, that an hour of measurement time and an hour of experiment time are different. In each PCR cycle, photons are collected at the PMTs for ~ 40 s. Thus over the course of a 55 cycle experiment, a 0.06% of relative drift would be expected between the PMTs.

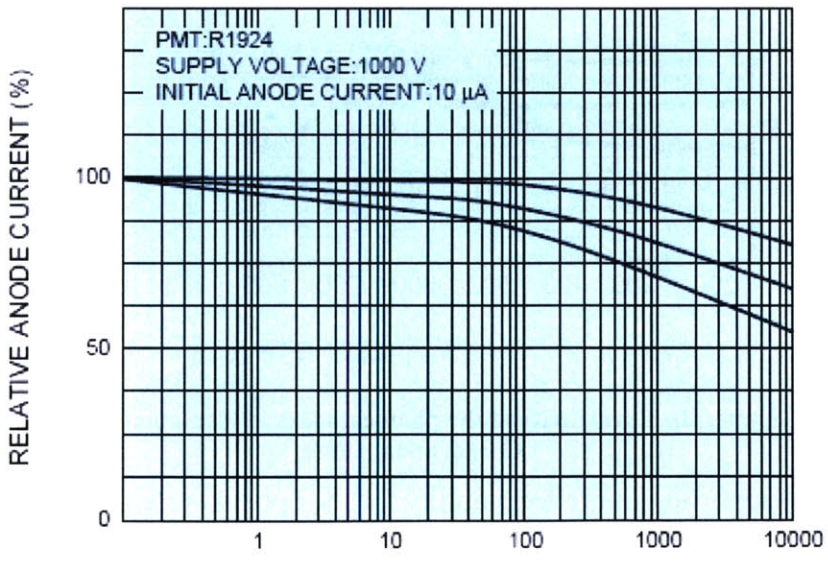


**Figure 4-12. PMT sensitivity decline with use caused by electron bombardment of last dynode (Hamamatsu Corporation ,1998).**

contain a manufacturing flaw and requested they be returned for inspection. Because of time constraints, this return was not completed. Digital I/O mode was simply avoided.

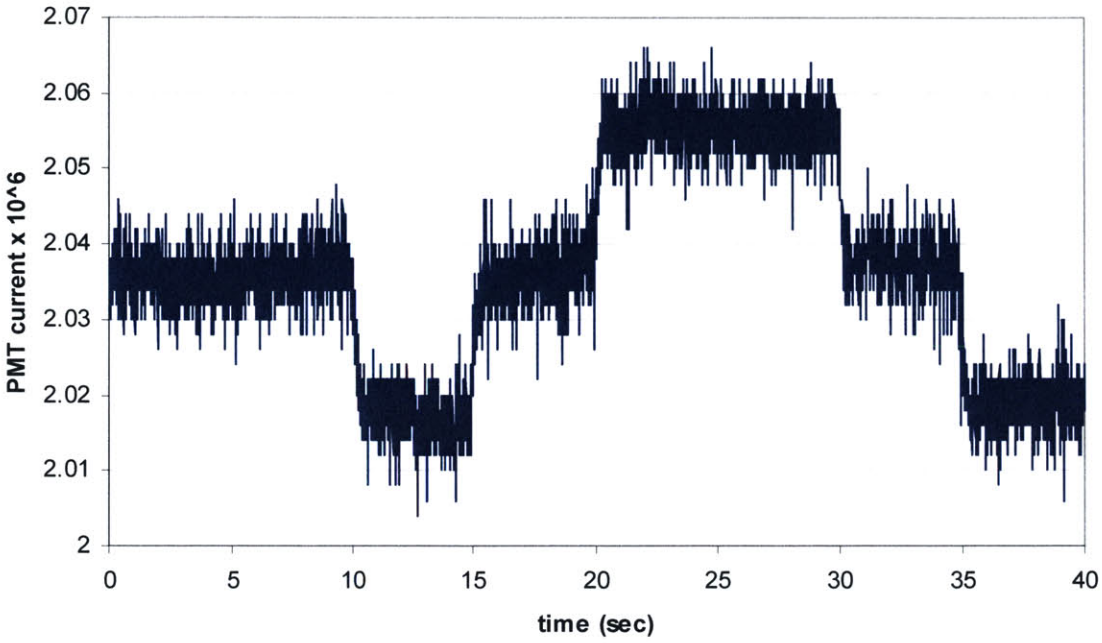


**Figure 4-13. PMT output current carried a square-wave noise when the digital I/O mode of the controller was enabled. This noise disappeared if thermoelectric regulation of the PMT was disabled.**

Ignoring the many problems that seem to plague this controller design, if performing to specification, one limit to stability would be the thermal coefficient of the potentiometer which defines the control voltage. The relationship of control voltage to PMT gain is shown in Figure 4-14. This curve is given by the relationship $Gain = 10^{6.38} \cdot (ControlVoltage)^{6.774}$. The typical operating point for the control voltage was 0.75 V. For a 1 °C change in the temperature of the potentiometer, the gain would be expected to change 0.07%.

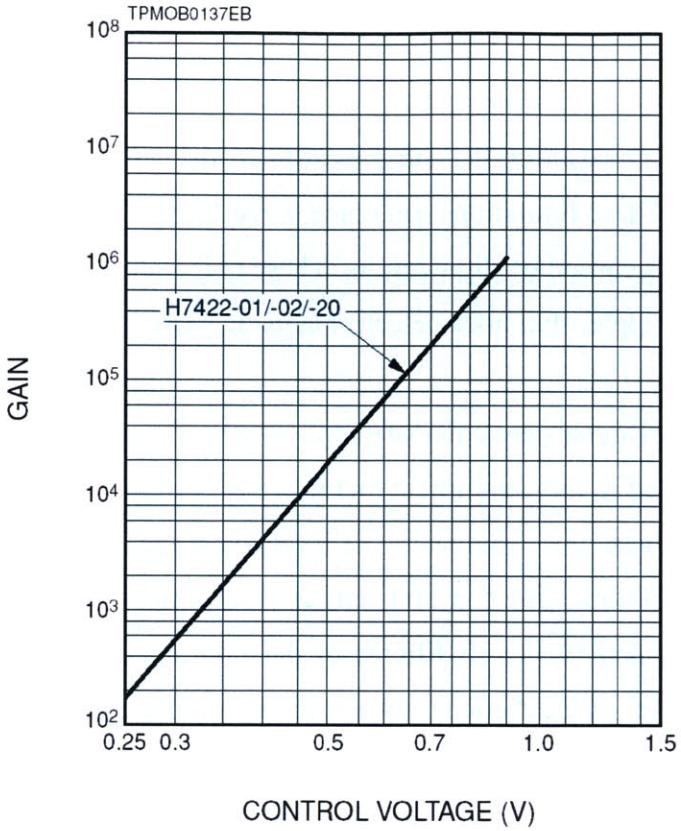


**Figure 4-14. The gain created by the dynode array is an exponential function of the dynode voltages. The dynode array voltages are proportional to the control voltage. Gain refers to the amplification of the number of measured electrons compared to the number of incident photons (Hamamatsu Corporation ,1998).**

*Summary for PMT drift errors*

Because of the ratio-metric nature of the FA measurement, some amount of drift in detector sensitivity can be tolerated, in particular drift that affects both detectors equally. These sources of drift play a role in data trends reported Summary Observations A, B, and C.

The PMTs used in this instrument provided adequate performance for this application. Photon counting PMTs stand as an alternative detector which would virtually eliminate long term drift, however current light levels are significantly larger than typical photon counting applications. Low noise CCD arrays also stand as an alternative. These detectors achieve their signal to noise ratios by integrating over extended intervals (seconds to hours) instead of via an amplification technique making them less prone to changes in their sensitivity.

*4.4.c. Noise*

Limitations in measuring the component intensities constrain the resolution of the FA measurements. These limitations can come in the form of noise on the measured signal and limitations caused by digitization. These noise sources include laser noise, PMT power supply ripple, shot noise, electromagnetic noise, and current-to-voltage amplifier noise.

These random signals are attenuated by low pass filtering. The current-to-voltage amplifier implemented in this instrument includes a $2^{nd}$ order-low pass filter which attenuates many of these noise sources to the levels recorded in Figure 4-15. The filter was operated at the 300 ms time constant setting which exhibits a -3 dB point at ~0.6 Hz.

The signal is also effectively filtered by the nature of the dual-slope analog-to-digital (A/D) converter of the Agilent 34401A digital multimeter used to record the amplifier output. Unlike comparator-based A/D chips used for high sample rate measurement, dual-slope A/D chips integrate charge on a precision capacitor over a set period of time. The voltage is read by measuring the time required to discharge the capacitor. Time periods for integration are typically set to integer multiples of 1/(60 Hz) to attenuate line noise. Integrating in this way not only nulls amplitudes at frequencies multiple of 60 Hz, but also effectively creates a first order filter with a -3dB point at a frequency corresponding to the reciprocal of the A/D integration time. The FA instrument was configured to have an integration time of 100 power line cycles (1.67 s) creating a cut-off point of 0.6 Hz.

The noise on the intensity measurements can be estimated from the steady state response data of Figure 4-7 under the assumption that the sources of drift described previously have stabilized. Figure 4-15 provides a zoomed view of the steady state response of the vertical intensity shown in Figure 4-7. The standard deviation of this data subset is $3.1\times10^{-4}$ V. This result is dominated by shot noise.

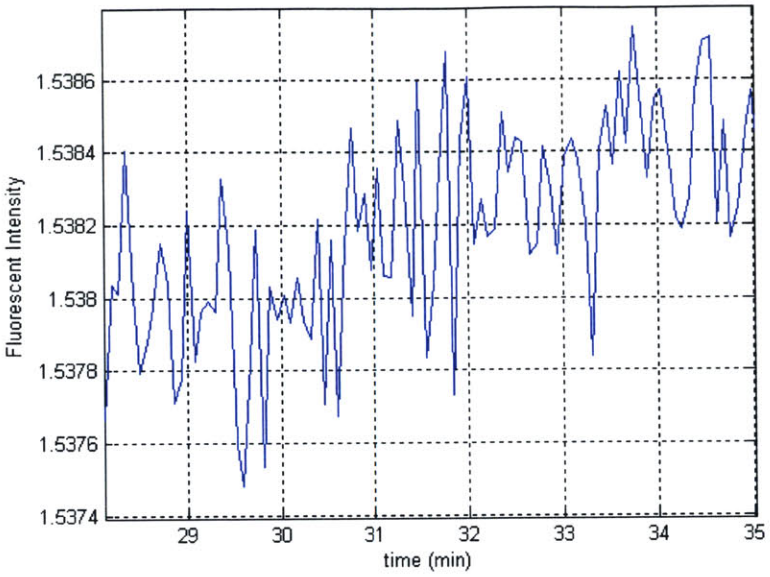


**Figure 4-15. Zoomed view of vertical intensity measurement of Figure 4-7 indicating variability of intensity measurement after it has reached a "steady state."**

*Shot Noise*

Measurement of light intensity is a process of counting photons. If the emission source has a very large number of independent emitters and each of which has a very small probability of emission, then the rate of photon arrival is Poisson distributed. A key feature of such distributions is that its variance ($\sigma^2$) is equal to its mean. Thus measurement of photon arrival rate will have a variance in the number of photons ($\sigma_N^2$) arriving at the detector equal to the mean number of arriving photons ($\bar{N}$) as stated by

$$\sigma_N^2 = \overline{\left(N - \bar{N}\right)^2} = \bar{N}\,. \qquad \textbf{4-13}$$

The average current output (from the anode) of the PMT, $\bar{i}$, is

$$\bar{i} = \frac{q \cdot G \cdot \bar{N}}{T}, \qquad \textbf{4-14}$$

where q is the charge of an electron ($1.6 \times 10^{-19}$ C), G is the photon to electron gain of the PMT dynode array, and T is the time interval over which the average is made.

The variance of this current, $i_N^2$, (caused by the random arrival of the photons) is referred to as shot noise and can be computed as

$$i_N^2 = \overline{(i-\bar{i})^2} = \frac{q^2 \cdot G^2}{T^2}\overline{\left(N-\bar{N}\right)^2} = \frac{q^2 \cdot G^2}{T^2} \cdot \sigma_N^2 = \frac{q^2 \cdot G^2}{T^2} \cdot \bar{N} \,. \qquad \textbf{4-15}$$

Combining this relationship with that of Equation 4-14, the shot noise can be described as a function of the average current as

$$i_N^2 = \frac{q \cdot G}{T} \cdot \bar{i} \,. \qquad \textbf{4-16}$$

Shot noise has a uniform spectral density. Thus, Equation 4-16 can be re-written as a function of the measurement bandwidth $\Delta f$ as

$$i_N^2 = 2 \cdot q \cdot G \cdot \bar{i} \cdot \Delta f \,. \qquad \textbf{4-17}$$

In the FA instrument, the current-to-voltage amplifier was set at a gain of $10^6$ V/A. Therefore, an amplifier output voltage of 1.5 V corresponds to an input current of $\bar{i} = 1.5\times10^{-6}$ A. From Figure 4-14, given the typical control voltage of 0.75 V, there are $G = 3.4\times10^5$ electrons expected per incident photon. As described earlier, the measurement bandwidth was limited to 0.6 Hz. Therefore, the variance on the PMT output current was expected to be $i_N^2 = 9.8\cdot10^{-20}\,\mathrm{A}^2$. Give the current-to-voltage gain of $10^6$ V/A, this current noise corresponds to a standard deviation on the voltage measurement of 0.3 mV. Note that this agrees closely with the values reported in Figure 4-15 and Summary Observation D.

*Shot Noise Impact on FA measurement*

The resolution of FA measurement is fundamentally constrained by the shot noise limit. In order to be quantitative about the expected variation in the signal due to the statistical nature of light, a few simplifying assumptions are needed. First, assume that the Poisson distribution function of the photon arrival rate may be assumed to approximate that of a normal distribution function. Second, to compute an upper bound on the variance of the FA, assume that the noise on the vertical and horizontal intensities are statistically independent (which they are not).

The probability distribution of the ratio of two independent variables of normal distribution is given by the Cauchy distribution (Weinsstein, ; Hamamatsu Corporation

,1998). Unfortunately, the variance for the Cauchy distribution is undefined because its integral is non-convergent. Under special assumptions, a solution can be found, however, for the purposes of this analysis, an alternative was found in simulation.

The simulation, conducted with MathCad 2001i, was begun by defining PMT current outputs for vertical and horizontal intensities consistent with those shown in Figure 4-7 ($i_v = 1.5 \times 10^{-6}$ A, $i_h = 1.9 \times 10^{-6}$ A). Next, two sets of noise data ($e_V$ and $e_H$) were generated using Mathcad's random number function. This function generates random numbers with a uniform distribution, however by summing 100 random values (specified to range from -1 to 1) and offsetting this sum by -50, each set of numbers became normally distributed (according to the central limit theorem) with zero mean. The mean ($\mu$) and standard deviation ($\sigma$) of this noise data were computed and then used to refine the data sets to ensure they exhibited the specified standard deviation ($std_C$) and a zero mean by the expression

$$e_C(j) = \mathrm{std}_C \cdot \frac{(e_C(j) - \mu)}{\sigma}, \qquad \textbf{4-18}$$

where C is a subscript used to denote that the equation was applied to both component noise data sets. For each component, the standard deviation was specified as the shot noise limit given by $i_N$ in Equation 4-23 above. Noisy data sets for each component current were then created by summation of the noise with the average currents. The FA was computed from these corrupted current data sets so that its mean and standard deviation could be computed. The mean was -75 mP as expected (same as what would be computed from the noiseless $i_V$ and $i_H$). The standard deviation of the FA was 0.08 mP which is actually slightly greater than that reported in Summary Observation D.

That the observed variation was less than the predicted may find explanation in the assumption of independence of the noise sources. Because each noise level is a function of its component intensity and these components are related by the FA of the imaged molecules, some correlation is expected. The effect of source correlation was explored by assuming that the horizontal component noise data set was the scaled sum of the $e_V$ and $e_H$ data sets (instead of just $e_H$) given as

$$e_H(j) = e_H(j) \cdot (1-p) + e_V(j) \cdot p, \qquad \textbf{4-19}$$

where p is defines the level of cross correlation. The mean and standard deviation of this data set were scaled as before with Equation 4-25 to the correct values. The relationship that resulted from this analysis is shown in Figure 4-16. The results indicate a declining standard deviation as the correlation between the noise sources is increased.

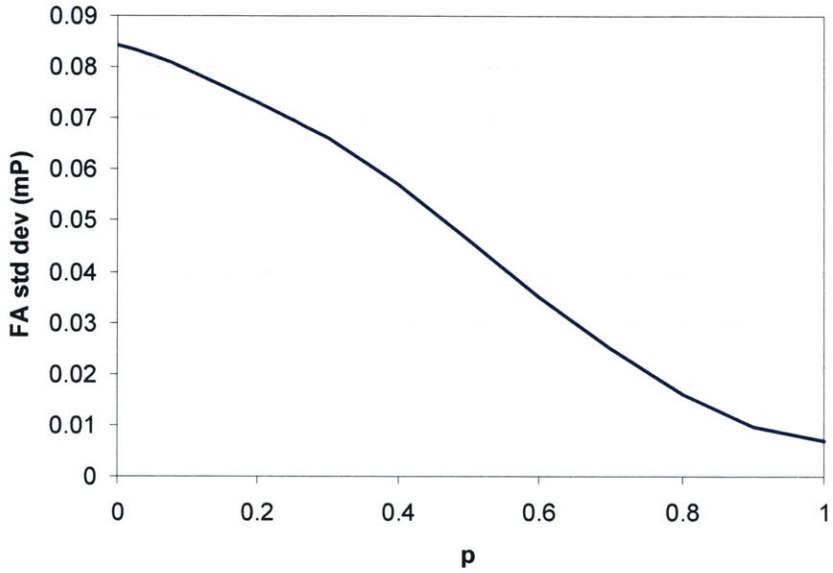


**Figure 4-16. A decline in the FA noise level (std dev) is observed in simulation as the correlation (p) between the noise on the vertical and horizontal component intensities is increased.**

Returning to the assumption of uncorrelated noise on each intensity signal, another important question observation is the dependence of signal strength of FA resolution. One motivation for applying FA to real-time PCR is to improve the assay robustness in order to reduce the burden on shrinking the assay to the sub-microliter scale. As the assay volume is reduced, the number of photons collected will likewise be reduced. The mean FA will not change, however because of the Poissonian nature of the noise on the intensity measurements, the noise on the FA measurement will rise. Using the previous example as a baseline, the intensity components ($i_v$ and $i_h$) were scaled in repeated simulations. Scaling was done by factors of 10 to investigate the noise level at $1/1000^{th}$ to 1000× of the originally assumed $i_v$ and $i_h$. The results are shown in Figure 4-17. The results indicate that critical importance of maximizing the number of collected photons.

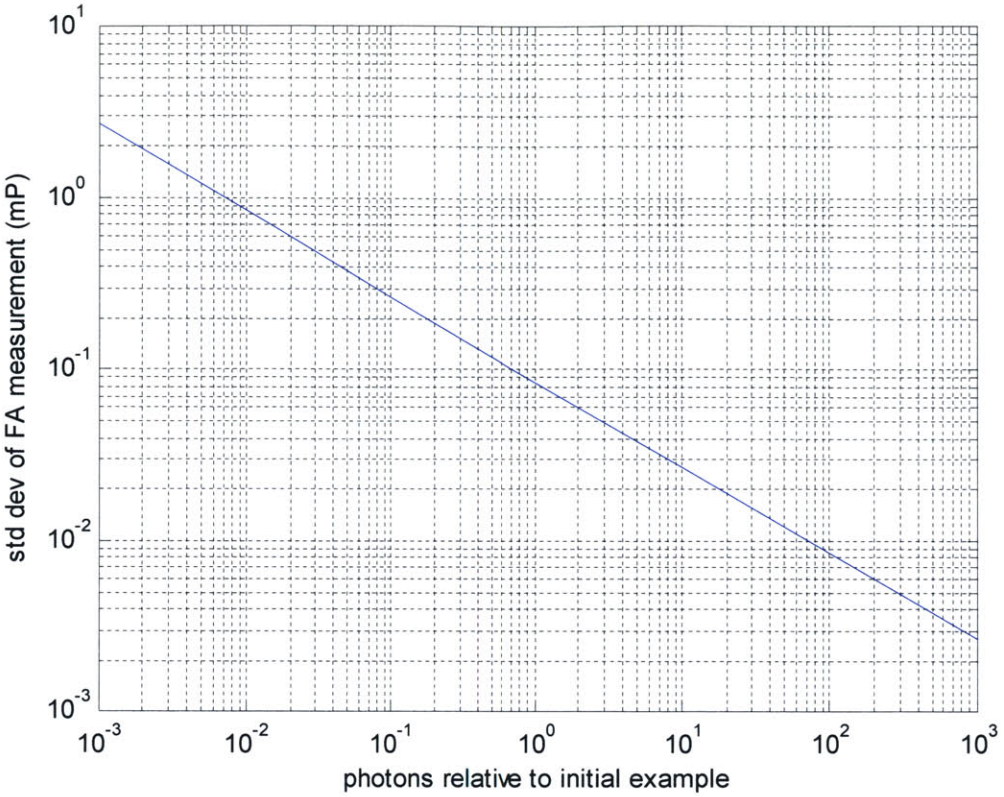


**Figure 4-17. When the component intensities get smaller, the noise on FA increases. Standard deviation of the measured FA is shown as a function of the relative number of photons in the component intensity measurement. The number of photons is taken relative to that of Figure 4-7 ($i_v$=1.5×10$^{-6}$ A, $i_h$=1.9×10$^{-6}$ A).**

Source Noise

The laser is specified to have an RMS noise of 0.25% when filtered to include frequencies between 20 Hz and 2 MHz. Assuming the noise is uniformly disturbed across this frequency band (i.e., Gaussian), an RMS noise of 0.25% is equivalent to a standard deviation of 3.75 mV on a 1.5 V signal. The low pass filters described above would be expected to sharply attenuate this noise.

*PMT Power Supply Ripple*

As discussed in the section on PMT drift above, the PMT sensitivity is an exponential function of the control voltage. The M9012 controller is specified to have less than 20 mV peak-to-peak (and therefore ~ 3 mV standard deviation) ripple noise on the control voltage. The frequency distribution of this noise is not specified.

A movement in the control voltage of one standard deviation creates an error in the amplifier gain given by

$$\% \text{ error} = \frac{(CV^{(6.77+\sigma_{CV})} - CV^{6.77})}{CV^{6.77}}. \qquad \textbf{4-20}$$

At a control voltage of 0.75V, this yields an error of 0.086%. Therefore, noise on a 1.5 V signal due to PMT power ripple would be expected to have a standard deviation of less than 1 mV before being attenuated by the low pass filters.

*Amplifier Noise*

The Keithley 428 current amplifiers used in this instrument are capable of both low noise and fast response time. At a V/A gain setting of $10^6$, the amplifier is specified to have an rms noise of less than 90 pA measured over a bandwidth of 3500 Hz. The frequency distribution is flat above 100 Hz. Below 100 Hz the typical noise current (in $fA/Hz^{0.5}$) goes approximately as $1260 \cdot \left(\frac{1}{f}\right)^{0.4}$. Integrating this response up to the 0.6 Hz filter bandwidth gives a noise standard deviation of 2.7 fA. Given the $10^6$ gain, this results in a 2.7 nV standard deviation on the voltage measurement.

*Digitization*

Two Agilent 34401A digital multimeters (DMM) are used to digitize the amplified signals. As described above, the shot-noise-limited standard deviation is ~0.3 mV for the 1.5 V signal. This signals required the units to be operated in the 10 V range setting. Thus the noise to range ratio was 1 part in $3\times10^4$. Therefore, an analog-to-digital converter (A/D) of at least 16 bits would be required to ensure that the bit resolution was smaller than the rms noise. The 34401A utilizes a dual-slope A/D to achieve very high bit resolution. For this work, these DMMs were operated in their 6.5 digit mode (21 bits) for a resolution of 1: $2\times10^6$.

*4.4.d. Dichroic Mirror*

A leading manufacturer of instrumentation for fluorescence anisotropy measurement, Cambridge Research Instruments (CRI), reports on their website (www.cri-inc.com) that "dichroic beamsplitters are the biggest source of [bias] error because the polarization bias is strongly wavelength dependent." They explain that typical dichroic beamsplitters have different spectral properties for parallel and perpendicular polarization states which necessitate a G-factor correction to the FA equation.

This is a well known fact reported in most of the literature regarding FA. Any component in the optical path that preferentially transmits one polarization state over another requires a correction to the equation defining FA such that this bias can be nulled. This is reflected in Equation 4-2.

CRI continues it arguments against dichroic beamsplitters explaining that spectral shifts in the fluorescent emission, occurring from well to well, plate to plate, or temporally, cause the appropriate G correction factor to be non-uniform across plates or varying with time. Their website presents a plot, shown here as Figure 4-18, summarizing the range of error caused by a shift in the peak fluorescent emission wavelength.

The point of zero emission peak shift in Figure 4-18, shows an instrument bias of ~76 mP. This is computed on the basis of an FA equation that has not used a G-factor correction. Measurement of a control sample of known FA would allow a G-factor to be added to the instrument, essentially zeroing the bias given in the vertical axis at zero peak shift (i.e., a G-factor would eliminate the no-shift bias). However, CRI's point is that small shifts in the emission wavelength yield large errors in the FA, more than 14 mP for a 3 nm shift! Such shifts would not be eliminated by a uniform or static G correction factor.

The assumptions used to generate this plot are not given in detail on the CRI website, nor is this argument available in published literature. Therefore, these calculations were duplicated for the real-time PCR FA instrument shown in Figure 4-1. Final optical system layout for FA measurement of real time PCR. in order to explore the error induced by use of a dichroic beamsplitter.

In order to focus attention on the effects of the dichroic beamsplitter and simplify the analysis, assume that none of the other components have any transmission bias. Second, assume that the excitation wavelength is completely eliminated by the band pass filter.

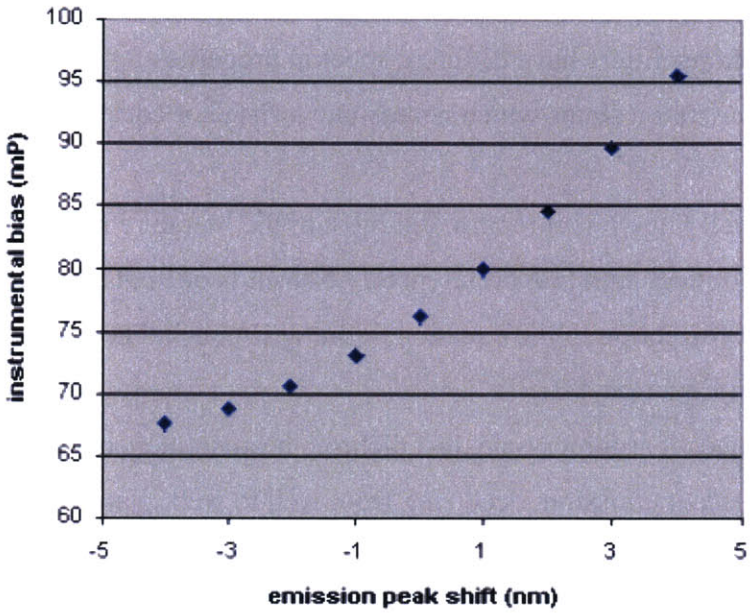


**Figure 4-18. Instrumental bias as a function of emission shift for Rhodamine Dichroic (Cambridge Research Instruments, 2002).**

The measured intensities of each polarization state ($I_{VM}$ and $I_{HM}$) can be described in terms of the original intensity spectrums emitted by the sample ($I_V(\lambda)$ and $I_H(\lambda)$). The relationships, given by Equations 4-21 and 4-22, are defined as the integral of the product of transmission spectrums $T_{Xn}(\lambda)$ and the emission spectrum $I_X(\lambda)$ for each of the n components of the optical path across the relevant spectral window. Note that $I_{XM}$ represent integrals of intensity across a spectral width while $I_X(\lambda)$ represent intensities at unique wavelengths.

$$I_{VM} = \int_{\lambda_1}^{\lambda_2} I_V(\lambda) \cdot \prod_n \{T_{Vn}(\lambda)\}\, d\lambda \qquad \textbf{4-21}$$

$$I_{HM} = \int_{\lambda_1}^{\lambda_2} I_H(\lambda) \cdot \prod_n \{T_{Hn}(\lambda)\}\, d\lambda \qquad \textbf{4-22}$$

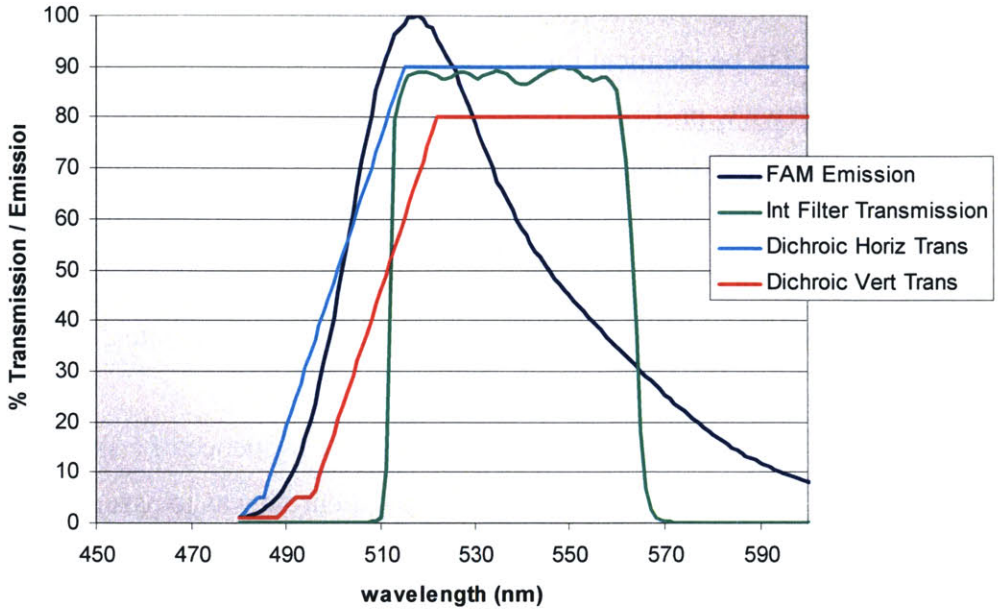


**Figure 4-19. Spectral Emission of fluorescein (FAM) overlain by transmission spectra for interference filter and dichroic mirror (rough recreation of data from CRI analysis) described at (Cambridge Research Instruments ,2002).**

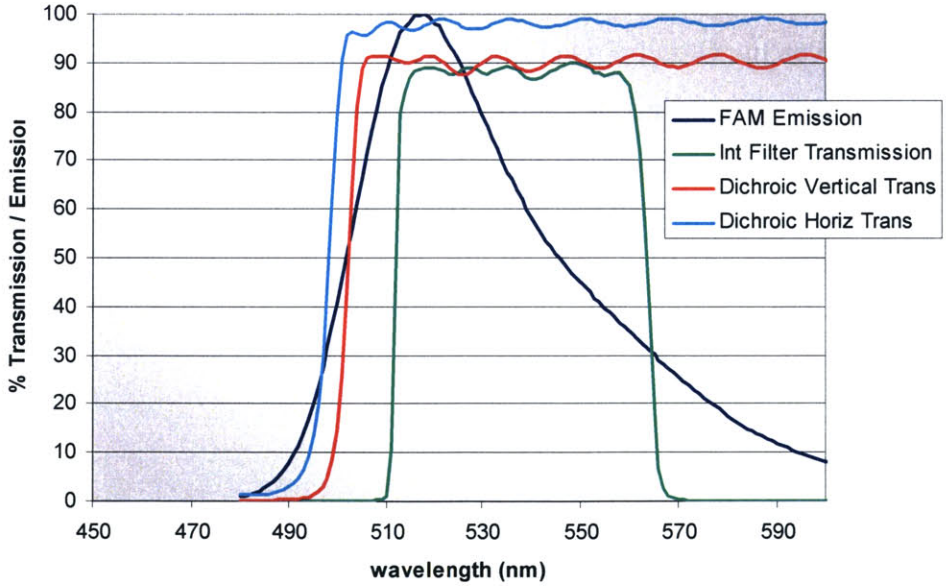


**Figure 4-20. Spectral Emission of fluorescein (FAM) overlain by transmission spectra for interference filter and a dichroic mirror designed by Barr & Associates. Mirror features a flat transmission band across the entire pass band of the interference filter.**

Given our assumptions, the only relevant spectral transmission profiles are that of the dichroic beamsplitter and the band pass filter, where the band pass transmission spectrums are assumed to be identical for both polarization states. The spectral emission of fluorescein (FAM) (www.probes.com) and the transmission spectrum for XF3084 band pass filter (www.omegafilters.com) are shown in both Figure 4-19 and Figure 4-20 below. Dichroic transmission spectra for each polarization state based on the example given by CRI are shown in Figure 4-19. The transmission spectra for each polarization state for a specialized dichroic beamsplitter designed by Barr & Associates, Inc. (www.barrassociates.com) is shown in Figure 4-20.

The first step in estimating the error caused by the confluence of a shifting emission spectra and the transmission properties of the dichroic was to assume a known FA for the emission at the sample, fixing the ratio of $I_V$ and $I_H$. A spectral profile for each of the component intensities was then generated, each being a scaled version of the FAM emission profile shown in the figures above. These served as un-shifted emission spectra. The measured intensities ($I_{VM}$ and $I_{HM}$) were then computed according to Equations 4-21 and 4-22. This was done separately for each dichroic beamsplitter. Next, a G-factor correction was computed that eliminated the bias for the un-shifted emission profile. This is given by, $G = (1\text{-}FA)/(1+2\cdot FA)\cdot(I_{VM}/I_{HM})$.

The next step was to shift the emission spectrum and recomputed $I_{VM}$ and $I_{HM}$. A measured FA was then computed from these intensities utilizing the previously computed G-factor. The error between the FA computed under conditions of shifted emission and the "ideal" (assumed) FA is shown in Figure 4-21.

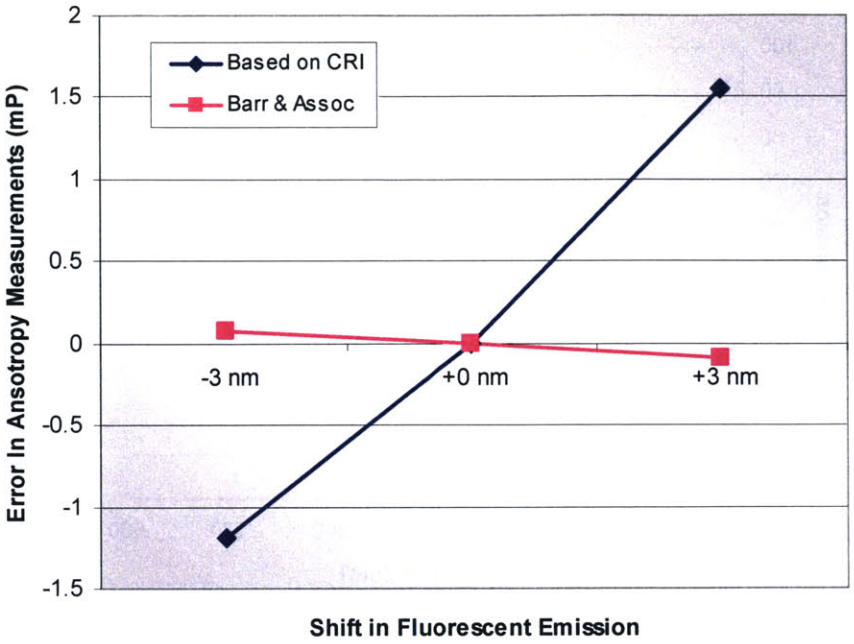


**Figure 4-21. Error between FA that results from shifted emission and the original FA from un-shifted emission. FA calculation utilized a G-factor to eliminate bias for the un-shifted condition.**

These results show that 3 nm shifts in emission wavelength result in an error of less than 1.6 mP for the CRI-described dichroic and less than 0.1 mP for the Barr & Associates dichroic. The much larger error that appears in the calculations based upon the CRI-described dichroic can be explained by referencing Figure 4-19. The dichroic transmission profile for the vertical polarized light has a knee which lies inside the pass band of the interference filter. It is the presence of this "internal" knee that creates error. Barr & Associates, Inc. manufactures custom optical components and was asked to provide specifications for a dichroic whose knees were outside the pass band of the interference filter. The error from a shifting emission spectrum is virtually eliminated with this dichroic design.

An alternative to a more sophisticated dichroic design is modification of the interference filter selection. The tighter pass band of the UHP48030 filter shown in Figure 4-22 better excludes the ramping portion of the transmission profiles of the CRI-described dichroic. Repeating the error analysis for this filter brings the maximum error down to 0.55 mP (from 1.6 mP for the XF3084 filter).

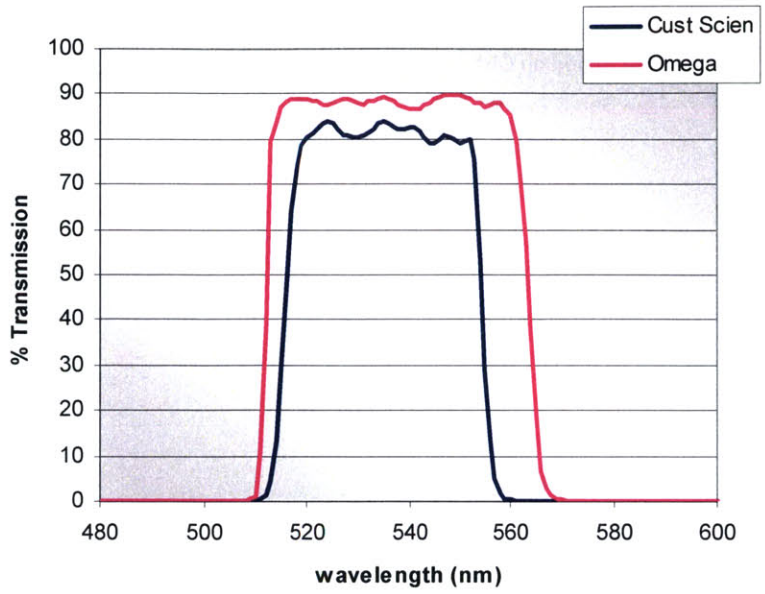


**Figure 4-22. Comparison of pass bands of XF3084 filter from Omega Filters and the UHP48030 from Custom Scientific.**

It remains somewhat unclear where the assumptions CRI used in its calculations differ from those presented here. No discussion is made in their arguments regarding the interference filter. Indeed, if the effects of the interference filter are removed, errors of the magnitude they describe do result. An interference filter with a broad pass band that encompassed a larger portion of the ramp region of the dichroic transmission profile would similarly result in much larger errors than calculated here.

Regardless of where the analyses differ, the analysis specific to the real-time PCR FA system shows that a dichroic beamsplitter can, in fact, be implemented without creating significant errors as a result of emission shifting. A static G-factor correction to remove the transmission bias is, however, clearly required in order to get accurate FA results.

### *4.4.e. Imperfect polarizer performance*

As shown in Figure 4-1, the system contains three polarizers. Several types of polarizers are available. The lowest cost polarizers are film polarizers. These are made from an anisotropic plastic that absorbs light oriented parallel to the polymer chains.

Glan-Taylor polarizers utilize a pair of mated calcite prisms. The crystalline structure of calcite allows one polarization component to propagate through the material faster than the other. This geometry of the prisms causes the slower traveling component to be directed along an alternate path which terminates at an opaque wall of the crystal housing. Thus only one polarization component of the light is transmitted. Glan-Thompson polarizers operate in the same way but utilize a different crystal plane oriented at a shallower angle.

There are several important differences in the performance of these polarizers. The first two are specifications that define the transmission characteristics of the polarization component to be transmitted (passed component) and the component that is to be attenuated (nulled component). These are typically defined by the transmission efficiency for the passed component and the extinction ratio (ratio between the transmission efficiencies of the nulled component and the passed component). Another difference in polarizer types is their "acceptance angle." The transmission efficiency specifications are true only when light entering the polarizer is within a cone defined by this acceptance angle. Reduced performance is observed for light that enters at a larger angle. A final difference is cost.

Film polarizers are the clear winner in terms of cost. Film polarizers, typically cost $50 to $100, are an order of magnitude less expensive than crystal polarizers. Costs for calcite polarizers are typically proportional to the size of the crystal. The geometry of Glan-Thompson polarizers require a larger crystal than Glan-Taylor, and thus they are more expensive. The prices specified in Table 4-1 are based on 25 mm optics. Larger diameter optics will see the span between the price of calcite polarizers grow rapidly. Because of the mechanism by which film polarizers absorb the nulled component, these polarizers also exhibit a much wider acceptance angle, typically ~30°, than crystal polarizers whose acceptance angles are less than 10°. The smaller angle of the crystal prism in Glan-Thompson polarizers gives them a larger acceptance angle than the Glan-Taylor type.

Crystal polarizers have a strong advantage in transmission of the passed component. While film polarizers may only transmit 60% of the passed component, crystal polarizers, depending upon anti-reflection coatings, have an efficiency greater

than 90%. The absorbance of the null and pass components by the film polarizers heats the thin film. This heating limits the intensity (and flux) for which film polarizers can be applied without damage. Similarly, heating and the associated thermal expansion can cause performance changes in the film polarizer that vary over time (as temperature changes).

Finally, crystal polarizers also have a strong advantage in extinction ratio (assuming acceptance angle specifications are met). While film polarizers are typically limited to extinction ratios of $5\times10^{-3}$, Glan-Taylor polarizers are specified to achieve $10^{-5}$, and Glan-Thompson polarizers are specified to achieve $10^{-6}$.

**Table 4-1. Summary of polarizer performance specifications**

| Polarizer Type | Film | Glan-Taylor | Glan-Thompson |
|---|---|---|---|
| %T of passed component | 60 | > 90 | > 90 |
| Extinction Ratio | $5\times10^{-3}$ | $10^{-5}$ | $10^{-6}$ |
| Acceptance Angle | 30 | 5 | 7 |
| Cost | $50 | $600? | $800? |

The sensitivity of FA measurement to the extinction ratio of the polarizers will determine whether calcite polarizers are preferable over film polarizers and the extent to which ideal performance must be achieved from the polarizer (for example, by only allowing light arriving within the acceptance angle to reach the polarizer).

The equations defining sensitivity to the extinction ratio start at the laser with its vertical and horizontal excitation intensities ($I_{VE}$ and $I_{HE}$). Given a laser output intensity of $I_o$ (where $I_o = I_{VE} + I_{HE}$) which is initially polarized with a ratio, R, ($R = I_{VE}/I_{HE}$) the initial excitation intensities are given by

$$I_{VE} = \frac{R}{1+R} \cdot I_o , \qquad \textbf{4-23}$$

$$I_{HE} = \frac{1}{1+R} \cdot I_o . \qquad \textbf{4-24}$$

Given a collimated, monochromatic input, polarizer performance can be modeled by the transmission efficiency (T) and the extinction ratio (ε). These assumptions are easily accepted for the laser beam; thus, the polarizer outputs are given by

$$I_{VE}=\frac{R\cdot T}{1+R}\cdot I_o, \qquad \textbf{4-25}$$

$$I_{HE}=\frac{T\cdot \varepsilon}{1+R}\cdot I_o. \qquad \textbf{4-26}$$

Assuming ideal performance (and therefore neglecting the influence) of all optical components except the polarizers, the intensities of Equations 4-25 and 4-26 arrive at the sample, exciting the fluorescent molecules. In Chapter 2, fluorescence anisotropy was described in detail. In this description, it was assumed that excitation was by vertically polarized light only. This light selectively excited molecules whose dipoles were oriented near vertical. In the present analysis, both vertical and horizontal excitation intensities are present. The horizontal excitation will preferentially excite any molecule having its dipole axis oriented near horizontal.

Using different notation than previously used in the thesis, this FA can be described as

$$FA=\frac{I_{\parallel}-I_{\perp}}{I_{\parallel}+2\cdot I_{\perp}}, \qquad \textbf{4-27}$$

where $I_{\parallel}$ and $I_{\perp}$ are the emission intensities parallel and perpendicular to excitation, respectively. By conservation of energy, $I_{\parallel} + I_{\perp} = \beta \times I_{excite}$ where $\beta$ is an efficiency and $I_{excite}$ is either the $I_{VE}$ or $I_{HE}$. Thus, the vertical excitation will give rise to component intensities

$$I_{\perp V} = \frac{\beta}{3}\cdot(1 - FA)\cdot I_{VE}, \qquad \textbf{4-28}$$

$$I_{\parallel V} = \frac{\beta}{3}\cdot(1 + 2\cdot FA)\cdot I_{VE}. \qquad \textbf{4-29}$$

Likewise, the horizontal excitation will give rise to

$$I_{\perp H} = \frac{\beta}{3} \cdot (1 - FA) \cdot I_{HE}, \quad \textbf{4-30}$$

$$I_{\parallel H} = \frac{\beta}{3} \cdot (1 + 2 \cdot FA) \cdot I_{HE}. \quad \textbf{4-31}$$

The polarized emission ($I_{VS}$ and $I_{HS}$) from the sample will then be the sum of these component intensities as

$$I_{HS} = I_{\parallel H} + I_{\perp V}, \quad \textbf{4-32}$$

$$I_{VS} = I_{\parallel V} + I_{\perp H}. \quad \textbf{4-33}$$

These intensities are collected by the optical system and propagate toward the detectors. The objective and dichroic mirror are assumed to transmit both states identically such that they may be neglected. The emission filter is assumed to block the excitation completely and transmit the components of the emission identically.

The next component in the light path is the polarizing beam splitter. Such splitters typically exhibit poor performance having an effective extinction ratio of only $\sim 10^{-1}$. As a worst case condition, assume the beamsplitter is not polarizing at all and that component intensities are split evenly into the two detection arms. In this case, roughly approximating the emission as collimated and (quasi-) monochromatic, the intensities transmitted through the polarizers and measured at the detectors are given by

$$I_{VM} = T \cdot I_{VS} + T \cdot \varepsilon \cdot I_{HS}, \quad \textbf{4-34}$$

$$I_{HM} = T \cdot I_{HS} + T \cdot \varepsilon \cdot I_{VS}. \quad \textbf{4-35}$$

Because all optical components were assumed to transmit the component intensities with the same efficiency, no G-factor correction is required and the measured fluorescence anisotropy is simply

$$FA_M = \frac{I_{VM} - I_{HM}}{I_{VM} + 2 \cdot I_{HM}}. \quad \textbf{4-36}$$

Solving Equations 4-25, 4-26 and 4-28 through 4-36 for $FA_M$, an expression relating the measured to the actual FA can be found that is given by

$$FA_M = \frac{(1-\varepsilon)\cdot(R-\varepsilon)\cdot FA}{R+\varepsilon\cdot(1+\varepsilon+FA+R+FA\cdot R)}. \qquad \text{4-37}$$

The error between $FA_M$ and the actual FA as a function of FA is shown graphically in Figure 4-23 below. This analysis indicates that in order to keep the error below 0.1 mP for a wide range of possible FA outputs, an extinction ratio of $10^{-4}$ is required. To hold the error to less than 0.01 mP, an extinction ratio of $10^{-5}$ is required. These extinction ratios cannot be achieved with film polarizers.

Both the Glan-Taylor and Glan-Thompson polarizers have adequate extinction ratios. Glan-Thompson polarizers were chosen for this instrument because of its greater extinction ratio but more importantly, its larger acceptance angle.

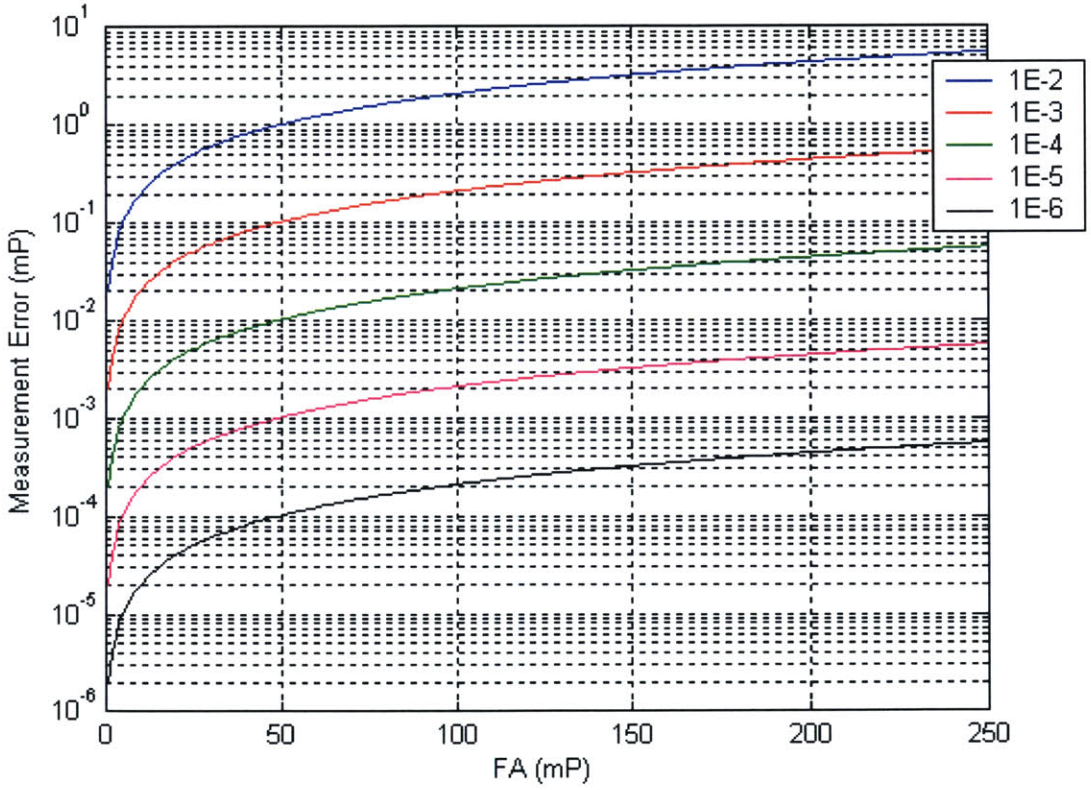


**Figure 4-23. Error between the measured FA ($FA_M$) and the actual FA as a function of FA given a set of polarizer extinction ratios.**

*4.4.f. Stray light*

Ambient light can also, obviously, cause error in FA measurement. This error propagates similarly to that for "leaked" laser light. Because ambient light is typically white (broad band), the energy in wavelengths overlapping the pass band of the interference filter is transmitted without attenuation. Wavelengths in the null band are also difficult to effectively attenuate with the filter since these photons arrive at disperse angles due to their tumultuous travel into the optical path.

In practice, it is relatively easy to design an enclosure that tightly seals the instrumentation from ambient lighting. The final instrument is enclosed in a black housing. Holes in the housing that allow data and power routing are carefully sealed. A rubber seal runs the perimeter of the enclosure lid that allows access to the sample holder. In addition to this enclosure, a second layer of defense is employed at the optical components themselves. The optical components of Figure 4-1 are assembled on a Spindler-Hoya optical framework. After assembly and alignment, this framework is wrapped in black electrical tape so that entry into the optical path requires passage through the interference filter. By creating a narrow optical path with opaque side walls, photons that are not traveling nearly parallel to the optical axis will strike and be absorbed by the side walls (the black tape).

Through these hardware features, error caused by stray light is negligible.

# Chapter 5

# Real Time PCR Results

In this chapter, four data sets are presented demonstrating the performance capability of the FA real time PCR instrument. As a benchmark, these results are compared against data from the Roche Lightcycler and against theoretical fundamental measurement limits. The experiments include dilution series data to demonstrate linearity across a wide range of starting template concentrations and repeatability data to establish quantitation accuracy. Additional data is presented demonstrating the observed performance enhancement when the starting template is isolated from genomic DNA. Finally, FA results using different fluorophores are compared.

## 5.1. Standard for comparison: Roche Light Cycler

The Roche Lightcycler real time PCR instrument was selected as a benchmark against which to compare FA measurement of real-time PCR. Up to 32 of the 100 μL capillaries shown in Figure 3-1 can be run simultaneously in the Lightcycler (FA instrument was designed to use the same PCR tubes as the Lightcycler). The instrument is shown in Figure 5-1.

In this instrument, the temperature of the capillaries is regulated by circulated, heated air. A temperature transition rate of up to 20 °C/s is specified. Actual observed ramp rates over broader ramp intervals were closer to 7.4 °C/s . An example of the measured air temperature profile during cycling is shown in Figure 5-2. Specifications for temperature control indicate that, at equilibrium, the mean PCR solution temperature

will be within ±0.3 °C of the temperature measurement. However, this specification is noted not to be an indication of the accuracy of the measurement hardware (thermocouple based).

The optical system images the capillaries end-on as shown in the schematic on the right of Figure 5-1. Filtered LED excitation is focused onto the capillary tip. The tip acts as a lens, illuminating the length of the capillary. The fluorescent emission is diverted by a dichroic mirror and ported into an array of photohybrid detectors. Six colors can be detected simultaneously. The Lightcycler does not monitor the polarization of the measured light in any way.

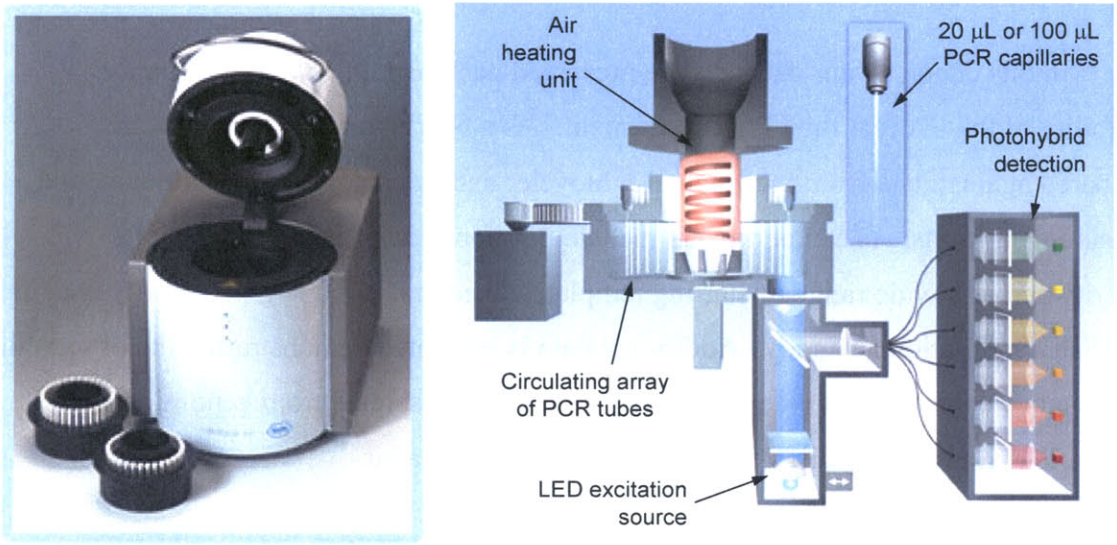


**Figure 5-1. Roche Lightcycler Real-Time PCR instrument, [Left]: A view with lid open of the Lightcycler 2.0 with cassettes for both 100 uL and 20 uL capillaries. [Right]: Schematic of Lightcycler hardware components.**

The Lightcycler includes sophisticated software to define the crossing point (see Chapter 1) of the amplification curve. It automatically compares this data across samples defined as controls to quantitate the starting copy number under a variety of different quantitation strategies.

The Lightcycler is amenable to both intercalating dye and hybridization probe chemistries. However, it is not able to monitor real time PCR through the polarization of the fluorescent emission of a labeled primer.

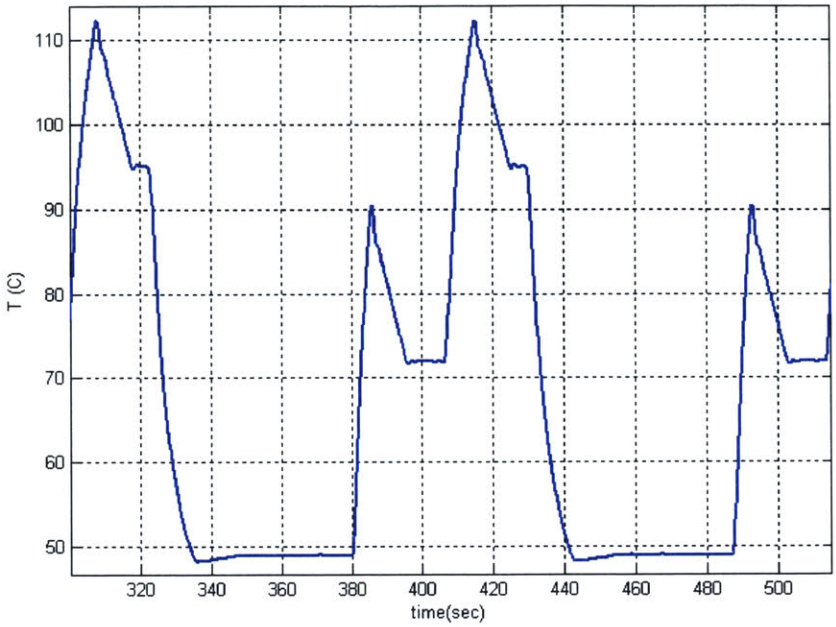


**Figure 5-2. Air temperature, as measured and reported by integrated hardware, during a typical Lightcycler thermal cycle. Target temperatures and times were 95 °C for 15 s, 49 °C for 45 s, and 72 °C for 20 s.**

## 5.2. Benchmarking the Benchmark

### *5.2.a. Fundamental Limits of Quantitation Accuracy*

Quantitation accuracy is fundamentally limited by the stochastic processes involved in preparing and running a PCR assay. That is to say that even if the amplification curve were measured without any error, the signal is still expected to exhibit some variation and the relative or absolute quantification is still known only to within bounds of uncertainty. The two stochastic processes which dominate this uncertainty are pipetting of starting template and the amplification process itself.

Using standard pipetting techniques, it is not possible to aliquot an exact number of template molecules into a reaction mix. Sampling error occurs due to the stochastic nature of the pipetting process. Assuming that the template molecules are evenly distributed in a dilute solution of known concentration, the probability of a certain number of molecules being present in an aliquot pipetted from this solution can be calculated according to the Poisson distribution (Wiesner, Beinbrech, and Ruegg, 1993).

A unique feature of the Poisson distribution is that its variance is equal to its mean. Thus, if the true template copy number is N copies, a pipetting process will, at best, aliquot an average of N copies with a standard deviation of $N^{0.5}$. Variations expected for starting copies of 1 to 1000 are shown in Table 5-1.

**Table 5-1. True target copy number in any aliquot will have a distribution about its expected value.**

| Expected Starting Copies ($N_o$) | std dev of $N_o$ | Coefficient of Variation of $N_o$ |
|---|---|---|
| 1000 | 31.62 | 3.16% |
| 100 | 10.00 | 10.00% |
| 10 | 3.16 | 31.62% |
| 1 | 1.00 | 85.20% |

The amplification process can also exhibit stochastic behavior. At the molecular level, the PCR yield is dependent on the probability of a template copy committing itself to the reaction. A dilute sample or small population size forces the consideration of the probability of reaction for each molecule and the stochastic behavior of the population. Branching process models have been used by several authors to describe the stochastic nature of the PCR (Krawczak, Reiss, Schmidtke, et. al, 1989; Sun, 1995; Peccoud, 1998). Specifically, the discrete time branching process that applies to PCR is known as the Galton-Watson-process. At each cycle, a molecule can either be copied with probability p or fail to be copied with probability (1-p). The duplication of each molecule is assumed to be independent of the duplication of other molecules since PCR is usually conducted with an excess of reagents. Peccoud and Jacob present an estimate ( $\hat{N}_0$ ) of the actual initial number of template copies ($N_o$) based on the number of molecules ($N_c$) observed at some cycle, c. The variance of the values of $\hat{N}_0$ was shown to plateau as the cycle number went to infinity. At this limit, the variance was $N_o \times (1-p)/(1+p)$, where p is the PCR efficiency. A summary of the variation expected given true starting copy numbers of 1 to 1000 and efficiencies ranging from 0.5 to 0.95 are shown in Table 5-2.

**Table 5-2. Theoretical limits to minimum coefficient of variation on starting copy quantitation based on crossing point (cp)**

| Expected Starting Copies ($N_0$) | Amplification Efficiency (p) | std dev of $\hat{N}_0$ | Coefficient of Variation of $\hat{N}_0$ |
|---|---|---|---|
| 1000 | 0.95 | 5.06 | 0.51% |
| 1000 | 0.9 | 7.25 | 0.73% |
| 1000 | 0.7 | 13.28 | 1.33% |
| 1000 | 0.5 | 18.26 | 1.83% |
| 100 | 0.95 | 1.60 | 1.60% |
| 100 | 0.9 | 2.29 | 2.29% |
| 100 | 0.7 | 4.20 | 4.20% |
| 100 | 0.5 | 5.77 | 5.77% |
| 10 | 0.95 | 0.51 | 5.06% |
| 10 | 0.9 | 0.73 | 7.25% |
| 10 | 0.7 | 1.33 | 13.28% |
| 10 | 0.5 | 1.83 | 18.26% |
| 1 | 0.95 | 0.16 | 16.01% |
| 1 | 0.9 | 0.23 | 22.94% |
| 1 | 0.7 | 0.42 | 42.01% |
| 1 | 0.5 | 0.58 | 57.74% |

Published literature does not address the variance on $\hat{N}_0$ when the stochastic processes of pipetting and amplification are combined. Because the amplification process must use the pipetting process as its starting point, the two processes are not independent. In order to study the variance that results from this series of stochastic processes, simulation was employed.

Matlab was used to simulate PCR (full code given in Appendix) from a set of expected starting copy quantities (1 to 1000) with efficiencies ranging from 0.5 to 0.95. For each combination of starting copy number and efficiency, 1000 PCR reactions were simulated.

Simulating the first stochastic process, pipetting, required the generation of the starting template quantity for each of the 1000 trials. Ideally, each reaction would begin with the expected number of molecules but, as discussed, in reality a Poisson distribution is expected. To simplify the simulation, a normal approximation was used. A set of normally distributed numbers was created by leveraging the central limit theorem and the random number generator of Matlab. According to the central limit theorem, a series of numbers having a normal distribution can be created by repeatedly summing a set of

random numbers from any distribution (including the uniform distribution of the random number generating function). After generating the normally distributed set, the values were modified to adjust the variance of the series to be the square root of the expected starting copy number. An example of the probability density function that resulted from this technique is shown in Figure 5-3.

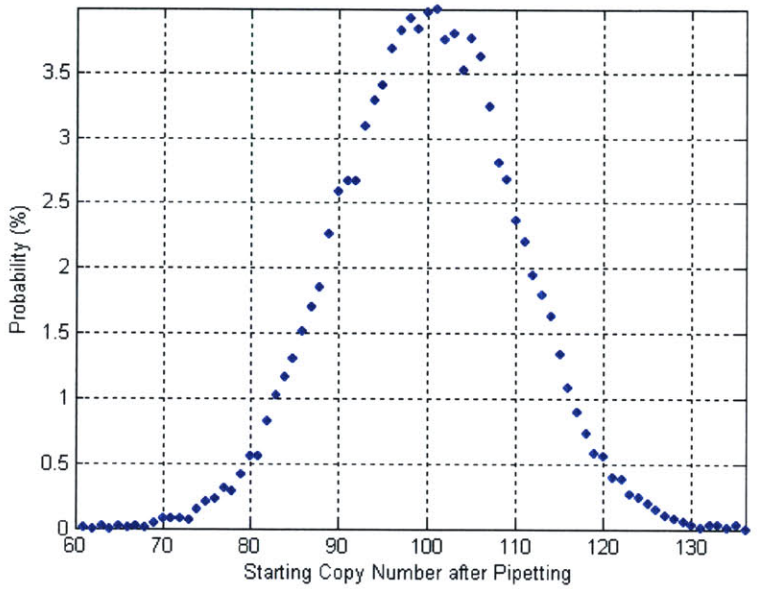


**Figure 5-3. Probability of pipetting starting copy quantities near the expected starting copy number of 100 copies. The simulation defines the distribution to be normal with variance that is the square root of the expected starting copy number.**

Having defined the normally distributed starting template number available for each of the 1000 trials of an experiment, amplification could then be simulated. To do so, the random number generator was used to define a duplication event for each molecule for each cycle of each trial. If the random number function, which outputs numbers only between 0 and 1, generated a number less than the reaction's pre-defined efficiency (p), duplication occurred. If the random number generator outputted a number greater than the efficiency, the molecule was not duplicated. While simple to implement, this algorithm requires substantial computation time when the starting copy number or efficiency is large but especially if the number of amplification cycles is large. When simulating reactions beginning with 1000 starting copies and 90% efficiency, it was only practical to run the simulation through 8 cycles. The typical output from a simulation is shown in Figure 5-4.

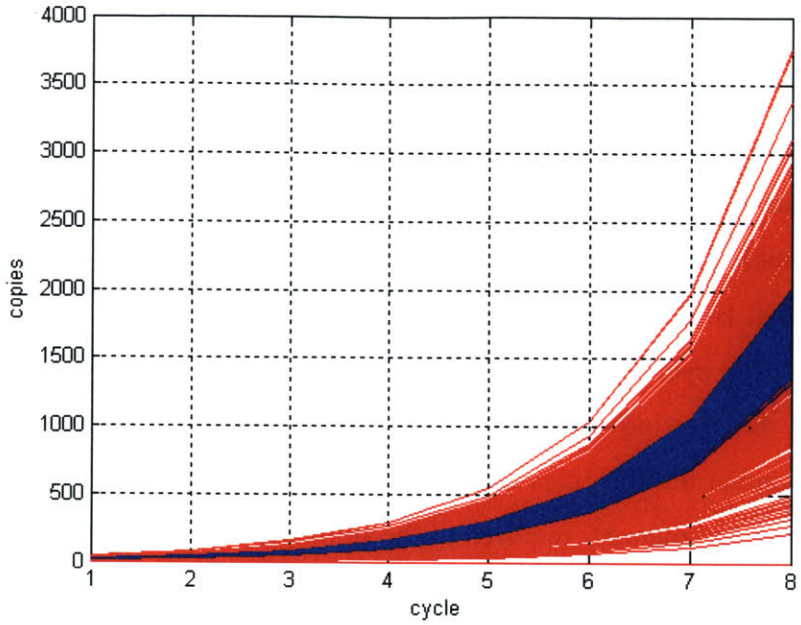


**Figure 5-4. Results of two simulation experiments both having an amplification efficiency of 90%. Shown in blue are the results of 1000 trials of a PCR experiment that began with exactly 10 starting copies. Shown in red are the results of 1000 trials of an experiment in which 10 starting copies was the expected number after a pipetting process.**

Once the simulation was complete, the estimated starting copy number ( $\hat{N}_0$ ) was computed under the assumption that all amplification occurred with the same efficiency (which is effectively a standard assumption in real-time PCR analysis in practice). Thus, the $\hat{N}_0$ for each trail was computed by dividing the copy number observed at the 8$^{th}$ cycle by $(1+p)^8$.

Correct implementation of this branching algorithm was confirmed by computing the variance of $\hat{N}_0$ that resulted from 1000 trials of an experiment that began with an exact number of starting copies (i.e., no pipetting error). These simulation results agreed very closely with the values of Table 5-2.

In addition to statistics regarding the initial copy number estimation, statistics regarding the variation of the measured "crossing point" were also desired since the variation in the crossing point for "identical" experiments is used to infer a PCR instrument's repeatability. From Chapter 1, recall that the crossing point is defined as

the cycle at which measured signal rises to some arbitrarily defined level above background. This threshold number of molecules that can be detected ($N_{CT}$) must be specified in order to compute the crossing points from the simulation. The crossing point variation was not sensitive to the selection of the level chosen. For the statistics shown in Table 5-3, it was assumed that the crossing point would be defined as the cycle at which the number of molecules would reach $N_{CT} = 1000\times(1+0.9)^{24}$ copies. In other words, the assumption is that 1000 starting copies amplified at 90% efficiency would be detected at the 24 amplification cycle.

Ideally, the crossing point statistics would be computed by simulating each PCR trial until the number of molecules was above the detection limit. In practice, the computation time and memory required of the simulation were not feasible. The alternative was to extrapolate the data. One method of extrapolation begins with the standard amplification equation,

$$N_c = N_0(1+p)^C \qquad \textbf{5-1}$$

where $N_c$ is the number of target copies present at cycle C, $N_0$ is the initial number of target copies before amplification, and p is the probability of amplification (amplification efficiency). Taking the base-10 logarithm of both sides of Equation 5-1, the expression becomes

$$\log_{10}(N_c) = \log_{10}(N_0) + C\cdot\log_{10}(1+p)\ . \qquad \textbf{5-2}$$

The cycle (C) at which the number of target copies ($N_c$) equals the threshold for the detectable number of copies ($N_{CT}$) is the crossing point (cp). In other words, when $N_c = N_{CT}$, cp = C. Substituting these identities and rearranging Equation 5-2, the expression for the crossing point is defined as

$$cp = \frac{\log_{10}(N_{CT}) - \log_{10}\left(\hat{N}_0\right)}{\log_{10}(1+p)}\ . \qquad \textbf{5-3}$$

where, as above, $\hat{N}_0$ represents the estimated number of starting copies based on the number of copies observed at the last cycle of the simulation.

The limitation in this approach to computing the crossing point is the assumption of constant amplification efficiency in the extrapolation. The variation in the observed

number of copies at the end of the simulation is inferred as a variation in the number of starting copies instead of a stochastic variation of the amplification efficiency. This assumption works well when the pipetting process errors dominate the variation of the observed copy number. In the parameter space analyzed by the simulation (i.e., PCR with low starting copies), it is, in fact, the pipetting errors which dominate as observed in Figure 5-4.

To clarify the ability of this extrapolation method to correctly estimate the statistics of the crossing point variation, one simulation was run beginning with 10 molecules and amplifying for 25 cycles. This simulation required substantial modification of the code that was used in previous simulations to improve its computational speed and memory use but 25 cycles remained an upper limit because of memory limitations (1 GB of RAM). When the same analysis was applied to $25^{th}$ cycle data instead of $8^{th}$ cycle data, the variation on $c_p$ was found to be the same with either approach.

**Table 5-3. Theoretical limits to minimum coefficient of variation on starting copy quantitation based on crossing point ($c_p$).**

| *simulation inputs* | | *simulation outputs* | | |
|---|---|---|---|---|
| **Expected Starting Copies ($N_o$)** | **Amplification Efficiency (p)** | **standard deviation of $c_p$** | **Coefficient of Variation of $c_p$** | **Coefficient of Variation of $\hat{N}_0$** |
| 1000 | 0.95 | 0.0 | 0.2% | 3.2% |
| 1000 | 0.9 | 0.1 | 0.2% | 3.2% |
| 1000 | 0.7 | 0.1 | 0.2% | 3.4% |
| 1000 | 0.5 | 0.1 | 0.2% | 3.6% |
| 100 | 0.95 | 0.2 | 0.6% | 10.2% |
| 100 | 0.9 | 0.2 | 0.6% | 10.3% |
| 100 | 0.7 | 0.2 | 0.6% | 10.8% |
| 100 | 0.5 | 0.3 | 0.7% | 11.6% |
| 10 | 0.95 | 0.6 | 1.9% | 32.3% |
| 10 | 0.9 | 0.6 | 1.9% | 32.8% |
| 10 | 0.7 | 0.7 | 1.95% | 33.9% |
| 10 | 0.5 | 1.0 | 2.1% | 36.9% |
| 1 | 0.95 | 0.7 | 2.0% | 87.4% |
| 1 | 0.9 | 0.8 | 2.2% | 87.6% |
| 1 | 0.7 | 1.2 | 2.9% | 92.8% |
| 1 | 0.5 | 1.9 | 3.4% | 103.2% |

The results of the simulation combining the stochastic processes of pipetting and amplification are shown in Table 5-3. Comparing the variation of $\hat{N}_0$ in Table 5-3 to that of Table 5-1 and Table 5-2, two points are clear. First, the variation caused by the pipetting process dominates that caused by the amplification process. Second, the variation that results from the series of the two processes is notably less than the sum of their variations when analyzed separately.

### *5.2.b. Lightcycler performance compared to fundamental limit*

The cleanest PCR amplification results are typically generated by amplification of plasmid DNA. Plasmids are autonomous self-replicating extra-chromosomal circular DNA often less than 10,000 base pairs in length. Plasmids can be effectively purified away from other cellular material. The combination of a pure sample of short DNA products makes an excellent template for PCR. As such, many instrumentation companies present performance data for their machines using plasmid DNA.

Real-time PCR data in the Lightcycler (taken from a sales brochure) for a dilution series of plasmid DNA is shown in Figure 5-5. The coefficient of variation (CV) of both the crossing point and the estimation of initial plasma concentration are shown in Table 5-4.

Comparing Table 5-3 to Table 5-4, it is observed that the CVs for the crossing point and estimates of the initial starting copy number of the Lightcycler in amplifying plasmid DNA is near the fundamental limit, especially for low copy numbers (10 -100). At higher copy numbers, when the stochastic processes of pipetting and amplification begin to have less inherent variation, some residual instrumentation error is more clear. Never the less, the Lightcycler yields impressive results.

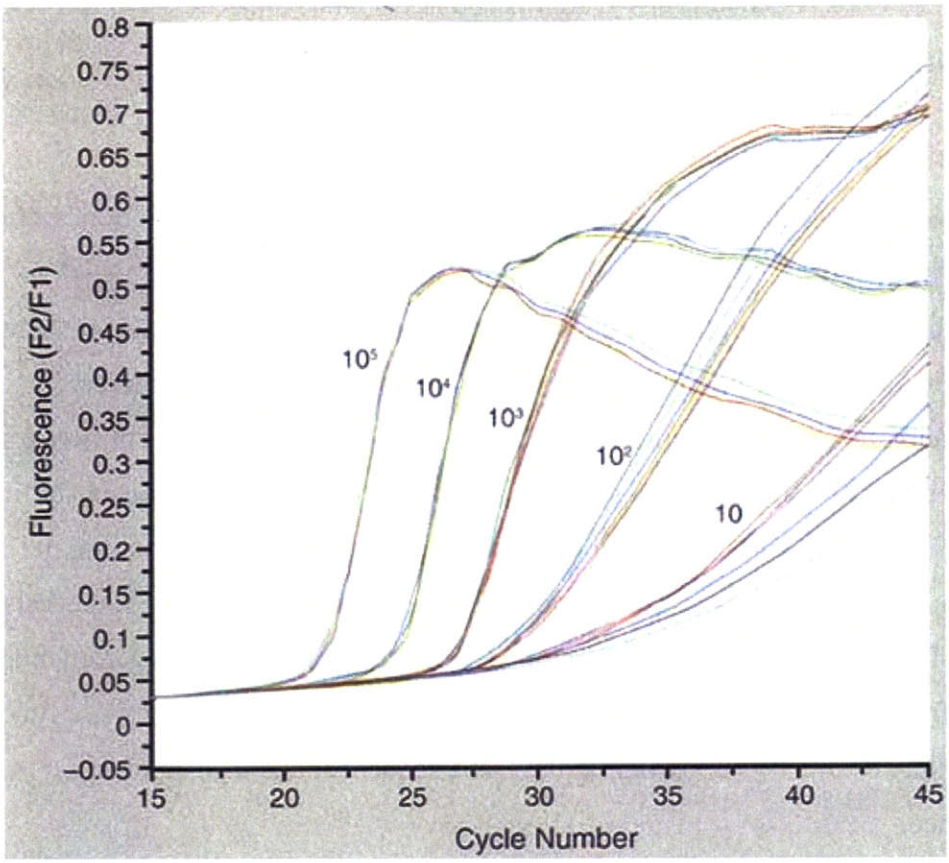


**Figure 5-5. Lightcycler amplification data for a dilution series of starting plasmid copies.**

**Table 5-4. Coefficient of Variation (CV) data on the crossing point and computed concentrations for amplification of a dilution series of plasmid DNA. Amplification data are shown above in Figure 5-5.**

| Starting concentration | $CV_{cr.\ point}$ | $CV_{conc.}$ |
|---|---|---|
| $10^5$ copies | 0.3% | 5.9% |
| $10^4$ copies | 0.3% | 5.1% |
| $10^3$ copies | 0.4% | 8.8% |
| $10^2$ copies | 0.7% | 16.5% |
| 10 copies | 1.7% | 41.0% |

## 5.3. Dilution series of starting template

*5.3.a. Results from real-time PCR by FA measurement*

The two strategies for quantitation, absolute and relative quantitation, were described in Chapter 1. Both strategies require reference curves against which to compare the unknown sample and thereby compute its original template copy content. For absolute quantification, this reference is a set of standard dilution curves.

Standards curves are typically generated by diluting a control sample to a series of starting copy numbers that evenly spans a range encompassing the expected starting copy number of the unknown sample. Because of their evenly spaced distribution, the standard curves should ideally rise above background at regularly spaced intervals (cycles). This will only be true if all samples across the range of starting copy numbers are amplified with the same efficiency. Uniform amplification efficiency is a function of both the assay chemistry (in particular the DNA sequence) and instrumentation performance.

To test the performance of the real-time PCR instrument created for this thesis, a PCR chemistry was chosen that was known to amplify efficiently at a broad range of concentrations. A dilution series was constructed consisting of four starting copy amounts including 20 pg, 200 pg, 2 ng, and 20 ng of genomic DNA. A no-template control was also run on a separate date. A single PCR master mix was prepared aliquoting equal amounts to all four dilution samples. Because the instrument only cycles one tube at a time, the samples were run one after the other through the course of a day. Instrument settings were identical across all experiments. The full details of the experimental protocol are given in the Appendix (Dilution Series Protocol).

The FA data from each experiment was scaled by G-factor correction so that all measurements had the same FA averaged over cycles 12 to 18. Such correction is necessary to account for long term drift of the optical system that changes the relative sensitivity of vertically to horizontally polarized light (see Chapter 4). The results of this experiment are shown in Figure 5-6.

Before discussing quantitative features of these results, a few qualitative observations are in order. First, the change in FA as all the free primer molecules are

incorporated into product is quite uniform across the samples (except for the control). The no-template control is observed to have been contaminated by an extremely small amount of DNA, on the order of a few copies. Because the control was mixed separately there is no guarantee that all reagents were in identical concentration to those of previous experiments. The difference in plateau levels is easily explained by a reaction that is ultimately limited not by a shortage of the fluorescently labeled primer but by a shortage of unlabeled primer used to prime the opposing DNA strand.

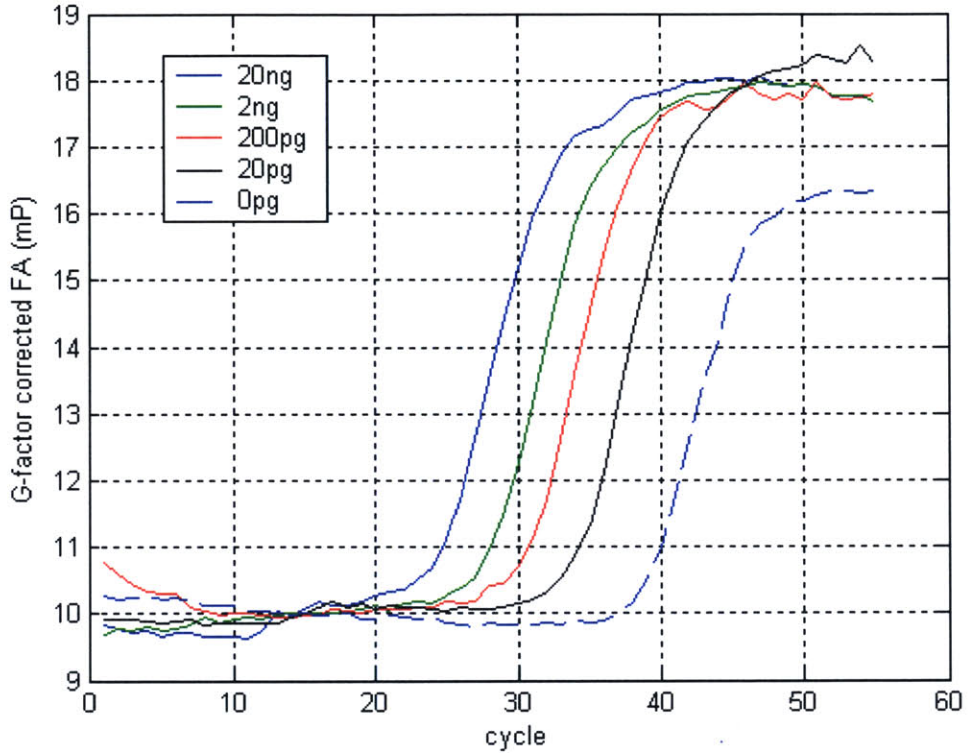


**Figure 5-6. Dilution series of starting template. Legend indicates mass of genomic DNA used as template in each experiment. One copy of the target sequence is present in each full genomic sequence. One copy of the full human genome has a mass of ~ 3 pg.**

FA measurements at early cycles are observed to be unsteady, drifting either up or down. One explanation for this was believed to be interaction of the primer molecules with genomic DNA. In later cycles, as the ratio of template copies to total genomic copies began rise, the measurements seemed to stabilize. This hypothesis was tested in an experiment with enriched DNA (instead of genomic DNA). The results of these experiments are discussed later in this chapter and are consistent with this hypothesis.

Quantitative evaluation of the results of Figure 5-6 focused on analyzing the level and uniformity of amplification efficiency. As discussed in the introduction, quantitative analysis of amplification curves typically focuses on the cycle at which the measured signal rises above background. Before presenting an analysis of the crossing points of this data, an explanation of their computation is necessary.

### *5.3.b. Calculating the Crossing Point*

Two methods of calculating the crossing points for the amplification data contained in this chapter were explored. The first was the more traditional method requiring manual definition of a threshold FA whose intersection with the amplification curves defined the crossing point. The second method was the use of the amplification signal first derivative maximum to define the crossing point. The first derivative maximum method is the one employed by the Lightcycler and is the method that yielded the best results for the FA data. This method's implementation is described below. The implementation of the manually defined threshold is given in the Appendix.

The first-derivative maximum method for crossing point definition began with an averaging of each of the FA data points taken at each cycle. (As discussed in Chapter 4, five FA measurements were taken at the end of each cycle. These were averaged to a single point for each cycle.) The discretized first derivative of the signal was computed by a simple forwarding-looking difference given by

$$\frac{D\big(FA(cycle)\big)}{d(cycle)} = FA(cycle+1) - FA(cycle) \ . \qquad \textbf{5-4}$$

Because measurement of FA only occurs at the end of every cycle, this signal and its derivative are very course. Accurate quantitation requires better-than integer cycle resolution. In order to interpolate a maximum in the derivatives signal to a point between cycles, a Gaussian function of the form

$$f(x) = \frac{A}{\sigma\sqrt{2\pi}} \cdot e^{-\frac{(x-\mu)^2}{2\sigma^2}} \ . \qquad \textbf{5-5}$$

was fit to the first derivative data using a non-linear least squares method in Matlab v6.5. An initial estimate for the mean ($\mu$) was taken as the cycle with the maximum derivative

value. The standard deviation ($\sigma$) was initially assumed as 1 and the amplitude (A) was initially approximated as the product $\sqrt{2\pi} \cdot$(maximum derivative value). All three parameters, A, $\sigma$, and $\mu$, were optimized to minimize the error between the data and model. An example of the first derivative data and the fitted Gaussian model is shown in Figure 5-7. The crossing point ($C_T$) is defined as the mean of the fitted model ($C_T = \mu$).

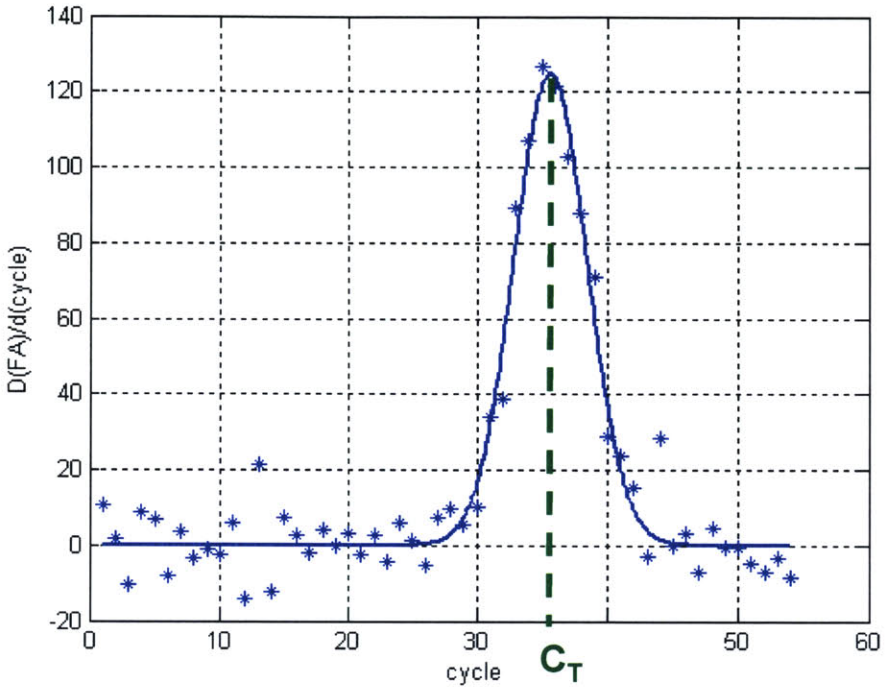


**Figure 5-7. Example of first derivative data and fitted Gaussian model.**

*5.3.c. Cross Point Analysis*

The computed crossing points for each curve of Figure 5-6 are shown in Figure 5-8. The starting copy numbers in the x-axis of this figure are based on the approximate mass of a single, full copy of the human genome (3 pg). One copy of the genome includes only one copy of the amplification target.

The slope of the crossing point versus the logarithm of the starting copy number is indicative of the efficiency of the PCR. This can be observed by manipulating the equation that models the PCR FA measurement which is given by

$$FA_{measured} = FA_{primer} + (FA_{product} - FA_{primer}) \cdot \frac{N_o}{P_o} \cdot (1+p)^{cycle} \quad \text{5-6}$$

This model arises from the integrative nature of the measured FA ($FA_{measured}$) described earlier in Chapter 2. Initially, there are $P_o$ primer molecules and $N_o$ target template copies. Since fluorophores are attached to primer molecules and $P_o >> N_o$, the early cycle measurements are dominated by the FA of primer molecules ($FA_{primer}$). As these primers are incorporated into product, the anisotropy of the product molecules ($FA_{product}$) becomes dominant.

To elucidate the linear relationship of crossing point with the logarithm of starting copy number, the logarithm is taken on both sides of Equation 2-5 and regrouping terms,

$$Log_{10}\left(\frac{P_o \cdot (FA_{measured} - FA_{primer})}{FA_{product} - FA_{primer}}\right) = Log_{10}(N_o) + cycle \cdot Log_{10}(1+p) \quad \text{5-7}$$

The crossing point (cp) is defined as the cycle at which the measured FA ($FA_{measured}$) is equal to the threshold ($FA_T$). Substituting these identities into Equation 5-7, a relationship between the crossing point and the staring copy number ($N_o$) can be found which is given by

$$cp = -\frac{1}{Log_{10}(1+p)} \cdot Log_{10}(N_o) - Log_{10}\left(\frac{P_o \cdot (FA_T - FA_{primer})}{FA_T - FA_{primer}}\right) \quad \text{5-8}$$

Thus the amplification efficiency may be calculated from the slope of the CP versus $Log_{10}(N_o)$ curve as

$$p = 10^{-\frac{1}{slope}} - 1 . \quad \text{5-9}$$

The computed crossing points of Figure 5-8 were least-squares fitted by a straight line having a slope of -3. This translates into an efficiency of p = 1.1. An error of at least 10% is obviously being made in the estimation of the amplification efficiency since p cannot be greater than 1. The $R^2$ value ($R^2$ = 1-(SSE / CSS), where SSE is the sum of squared errors and CSS is the corrected sum of squares) for the straight line fit was 99.6%, indicating that amplification efficiency was highly uniform across the starting copy dilution series.

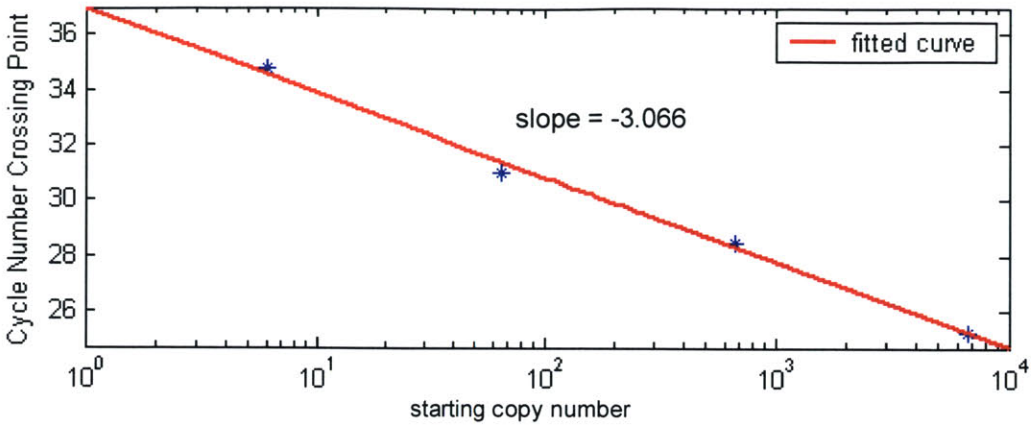


**Figure 5-8. Computed crossing points for the FA instrument amplification curves of Figure 5-6 with straight line fitted model.**

*5.3.d. Comparison to Lightcycler Data*

A dilution series was run in the Lightcycler for comparison. This experiment amplified the same target sequence with two replicates done for each starting copy amount. An error was made in experiment design such that the starting copy amounts are not identical to those of the above experiment; however, this difference is inconsequential. Full details of the experimental protocol can be found in the Appendix.

The results of the experiment are shown in Figure 5-9. Qualitatively, we observe that amplification results from the Lightcycler include an unsteady signal in the early cycles of the PCR (just as for the FA instrument). In addition, very consistently there is a slow downward drift on the intensities observable in the early and late cycles.
The signal plateaus occur at different intensity levels not only across dilution samples but even between replicates. The trend of a lower intensity plateau occurring for lower starting copy number is unexpected since the same primer concentration is used in each. In other words, since lack of primer availability ultimately stops the reaction, each reaction should finish with approximately the same number of product molecules. The SYBR green signal, expected to be proportional to the number of molecules, would therefore be expected to be a constant. One explanation may be that the fluorophore is being damaged over the course of the PCR.

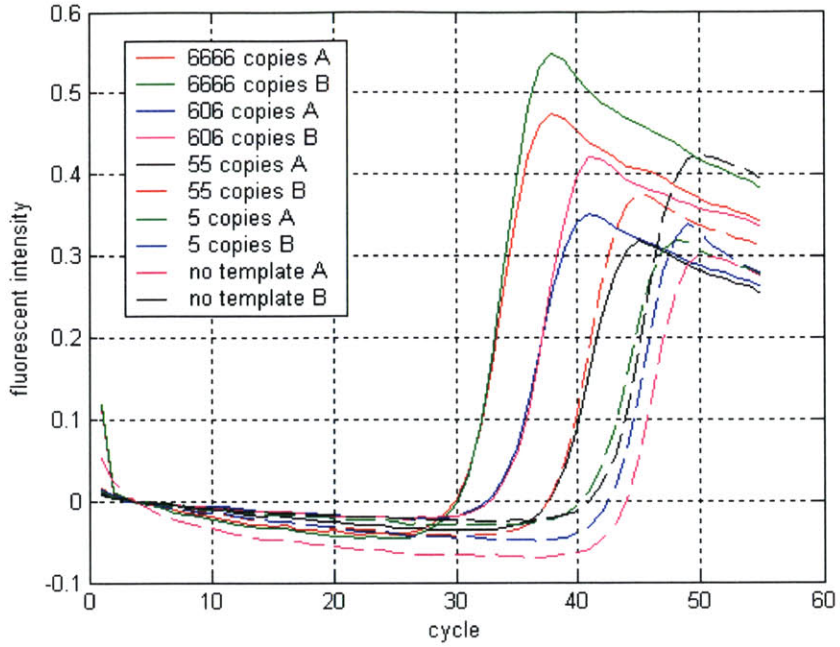


**Figure 5-9. Dilution series of starting template analyzed by SYBR green assay in the Lightcycler. Legend indicates starting copies of template. A & B designation identify separate tubes of otherwise identical reaction mix.**

The crossing point versus starting copy number curve is shown in Figure 5-10. Like the relationship derived for the FA instrument, the method of first-derivative maximum is used to determine the "crossing point." The fitted straight line has a slope of -3.5, corresponding to a constant efficiency of 93% across this range of starting copies. The $R^2$ for the fit is 99.14%.

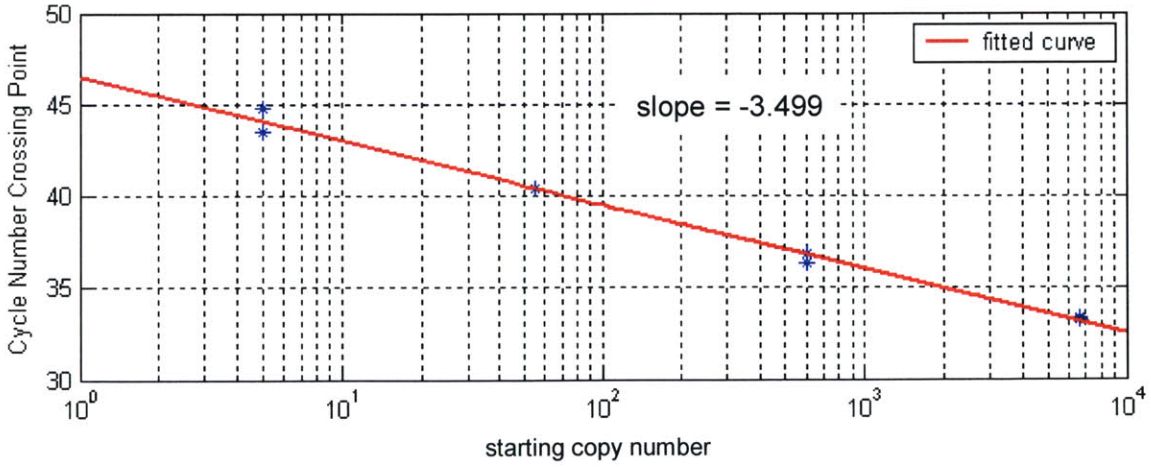


**Figure 5-10. Computed "crossing points" for Lightcycler amplification curves of Figure 5-9 with straight line fit.**

The efficiency observed in the Lightcycler analysis is a more reasonable value than that computed for the FA instrument (since it is less than 100%) but both data sets indicate near full efficiency. The difference in the observed performance may be due to pipetting errors. Another possible cause was the difference in evaluation periods of the samples. All the amplified samples were mixed simultaneously. For the Lightcycler, the ten samples that were mixed simultaneously were immediately placed in the cycler and run together. For the FA instrument, more than 8 hours passed between the first run and the last.

Another possible cause of the difference lies in the non-parallel format of the FA based instrument. Since only one tube is run at a time, a greater burden is placed on ensuring uniform conditions in run to run for the FA instrument. However, in the next section this uniformity is demonstrated.

## 5.4. Repeatability

*5.4.a. Results from real-time PCR by FA measurement*

The repeatability of the FA instrument was tested by amplifying two different starting copy amounts a series of times. Starting template quantities of 2 ng and 200 pg of human genomic DNA were tested. At 3 pg per complete genomic copy, these samples sizes corresponded to 666 and 66 template copies, respectively. The experimental protocol sought to minimize opportunities for pipetting error. First, a single PCR master mix was prepared without template. Equal amounts of master mix were aliquoted into two separate ependorf tubes (enough for three reactions each). 3× template was added to each of the tubes and gently mixed by pipette circulation. The contents of each tube were then aliquoted to three separate replicates. This whole procedure was intended to ensure that independent PCR tubes contained identical reagent concentrations. Instrument settings were identical across all experiments. The full details of the experimental protocol are given in the Appendix. The results of this experiment are shown in Figure 5-11.

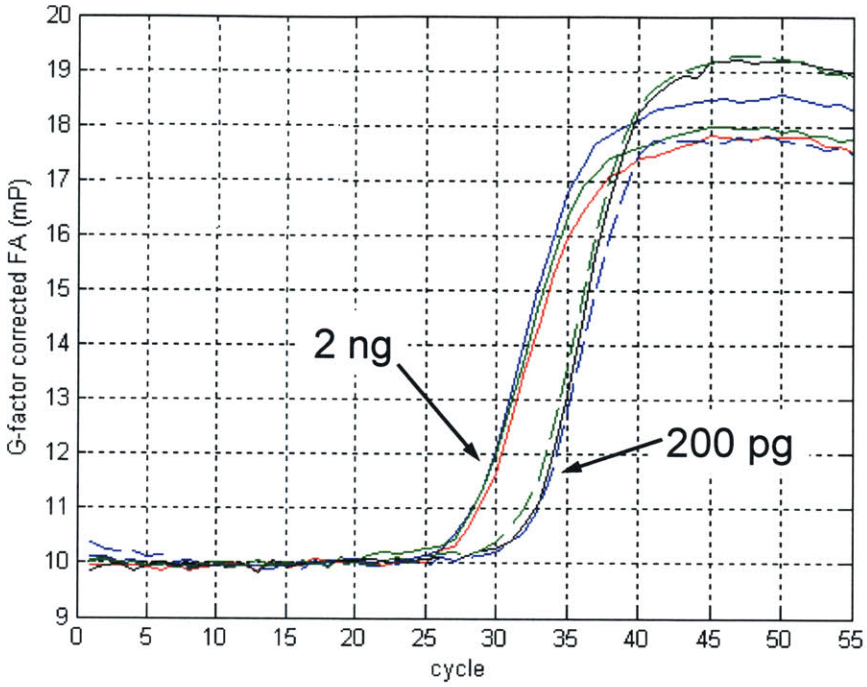


**Figure 5-11. Repeatability experiments amplifying two different starting template quantities over a series of trials under identical amplification parameters.**

Quantitative analysis of these amplification curves is performed as before using the first-derivative maximum method for defining the "crossing point." The first derivative data for the two starting copy numbers are shown in Figure 5-12. The maxima for all curves is given in the legends of this figure. For the samples beginning with an expected number of 66 template copies, the cross point mean is 35.54 cycles with a coefficient of variation of 0.5%. The samples beginning with an expected 666 template copies had a mean crossing point of 31.58 cycles with a coefficient of variation of 0.32%. These CVs align closely with the fundamental limits defined in our analysis of the stochastic processes of pipetting and amplification. From Table 5-3 at 95% amplification efficiency, crossing point CVs of 0.2%, 0.6%, and 1.9% are expected for expected starting copies numbers of 1000, 100, and 10 copies respectively. Thus, the observed CV of 0.5% for 66 starting copies is actually *lower* than would be expected given the stochastic nature of the experiment. The CV observed for the 666 starting copies is very close to the predicted fundamental limit.

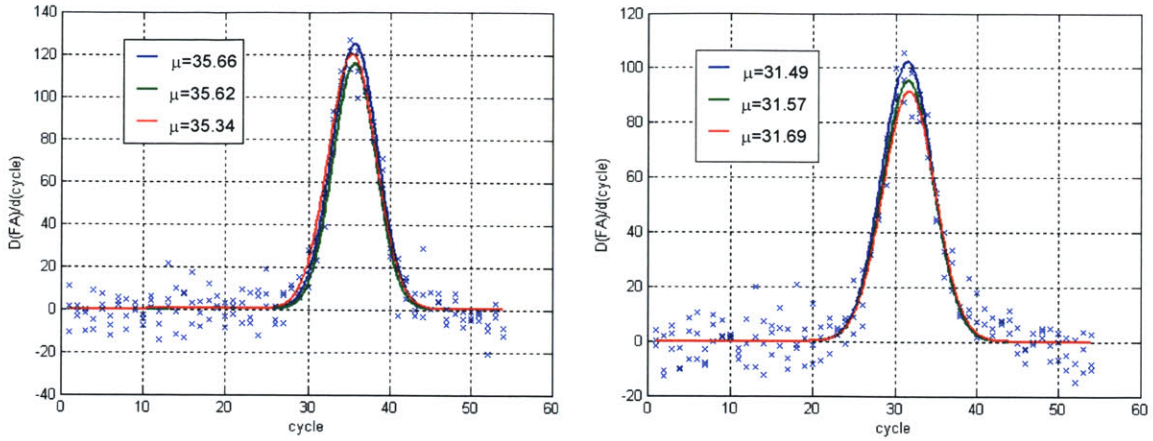


**Figure 5-12. First-derivatives of amplification curves for starting quantities of [Left] 66 template copies and [Right] 666 template copies. The legend of each figure gives the cycle at which the maximum of the fitted Gaussian model (i.e., its mean) occurs for each data set. This cycle is defined as the "crossing point" for each amplification curve.**

### *5.4.b. Comparison to Lightcycler Data*

For comparison, the same target sequence at the same starting copy concentrations were also amplified repeatedly on the Lightcycler. SYBR green detection was used in place of FA measurement, however thermal cycling parameters were the same as those used above. The four samples of each concentration were mixed in a single ependorf tube. After all reagents were added and mixed, samples were aliquoted to separate PCR tubes. Full details of the experimental protocol can be found in the Appendix.

Replicate amplification data for starting copy amounts of 2 ng and 200 pg of genomic DNA (666 and 66 genomic copies, respectively) are shown in Figure 5-13. Note the characteristic drift of the SYBR green chemistry in the early and late cycles of the PCR.

Quantitative analysis, again by the first-derivative maximum method, shows the curves to be very repeatable. Plots of the first-derivative curves are shown in Figure 5-14. For the samples beginning with an expected number of 66 template copies, the cross point mean is 34.6 cycles with a coefficient of variation of 0.66%. The samples beginning with an expected 666 template copies had a mean crossing point of 30.4 cycles with a coefficient of variation of 0.26%.

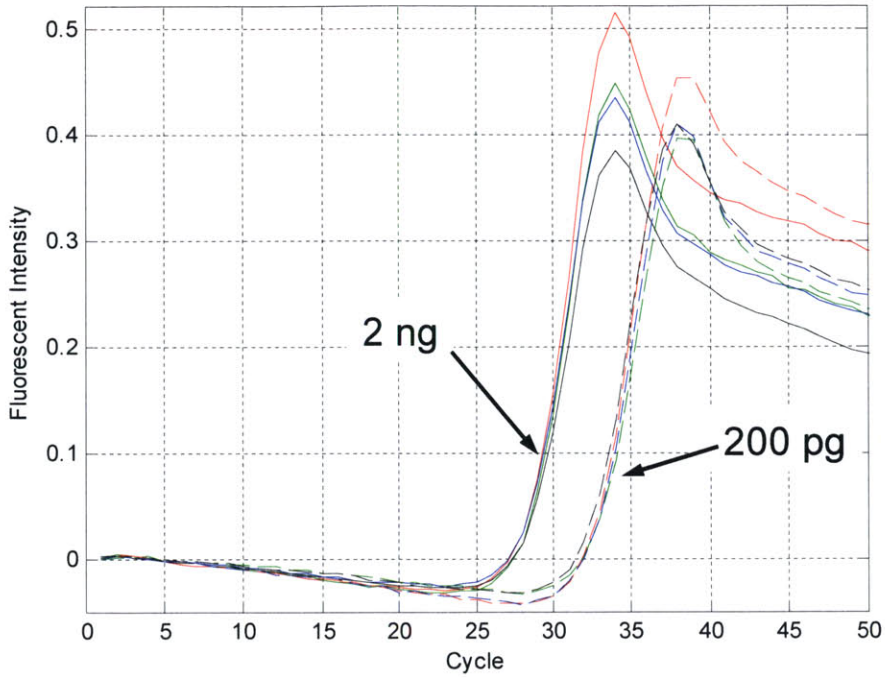


**Figure 5-13. Lightcycler repeatability experiments amplifying replicates of 2 ng and 200 pg of genomic DNA (666 and 66 template copies expected, respectively) under identical amplification parameters.**

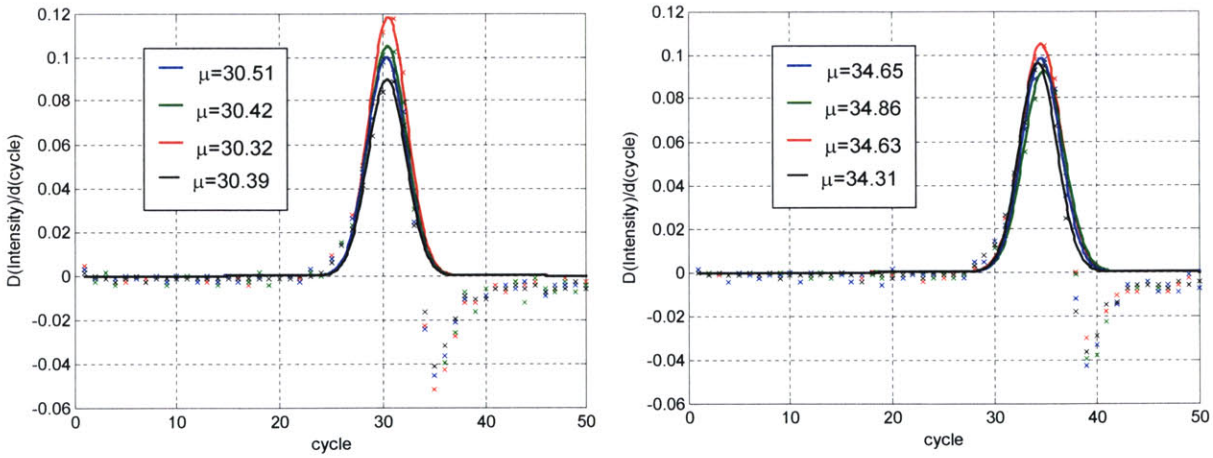


**Figure 5-14. First-derivatives of amplification curves of Figure 5-13. The legend gives the cycle at which maximum of the fitted Gaussian model (i.e., its mean) occurs for each data set. This cycle is defined as the "crossing point" for each amplification curve.**

The crossing point variation for the FA instrument and the Lightcycler are compared against the theoretical predictions in Table 5. The theoretical minimum CVs in the table are calculated for 666 and 66 expected starting copies via the same Matlab code earlier (90% amplification efficiency was assumed). For both expected starting copy amounts, both instruments yield results that are comparable to the theoretical best possible.

For each starting copy case one of the instruments exhibits a CV that is less than the theoretical minimum. There are several ways in which this could occur. First, it could be that the number of replicate experiments (3 for the FA instrument and 4 for the Lightcycler) was insufficient to accurately establish the CV. Another alternative is that the assumptions made in the theoretical analysis are in accurate. The pipetting process may not be adequately modeled under the Poisson distribution assumption. A final alternative is that the method of crossing point definition may be inadequate. Defining the crossing point relied on fitting the first derivative data with a Gaussian model via a non-linear least squares method. Such methods require initial conditions to begin the minimization. Because each data set from a replicate exhibited a maxima at essentially the same cycle (remember that the raw data is discretized per cycle), the fitting algorithm utilized effectively the same starting conditions. This may have, to some extent, biased definition of the crossing points for replicate curves, decreasing the CV. Efforts were made to minimize the impact of this last alternative by visually inspecting the quality of the fits. For example, in analyzing the results of Figure 5-13, the data beyond cycles 33 and 37 in the left and right figures, respectively, were excluded from the fit.

**Table 5. Comparison of coefficient of variation on crossing points for repeated amplification of an expected number of starting copies.**

| Starting Copies | FA Instrument | Lightcycler | Theoretical Minimum |
|---|---|---|---|
| 666 | 0.32% | 0.26% | 0.33% |
| 66 | 0.50% | 0.66% | 0.65% |

## 5.5. Enriched template

As mentioned earlier, real-time PCR instrumentation is often benchmarked using plasmid DNA as its template. It was hypothesized that a cleaner template would also improve FA based real time PCR measurement.

Because plasmid DNA for the target of interest was not readily available, an alternative was found in enrichment. The enrichment process was begun by cleaving genomic DNA with a cleavase enzyme (Taq$^{\alpha}$1). These enzymes cut the genomic DNA at sites exhibiting a particular "recognition sequence." In a separate, parallel process, biotin labeled oligonucleotides specific to the target of interest were bound to streptavidin coated magnetic beads. The cleaved genomic DNA was denatured by heating to 95 °C and then flash cooled in an ethanol water bath forming single stranded DNA (ssDNA). These ssDNA fragments were then mixed and incubated with the probe-bound beads. Unbound (non-target) DNA was eluted via repeated rinsing while the beads were held at the bottom of the container via the force of a magnet. The enriched target DNA was finally released from the beads and resuspended in Millipore water. The full details of the enrichment protocol are given in the Appendix.

Enriched DNA was amplified with the same protocol as that used for the genomic DNA repeatability experiments. Protocol details are given in the Appendix. The results of three replicate amplifications of ~300 starting copies (mixed together then aliquoted to three separate PCR tubes) are shown in Figure 5-15.

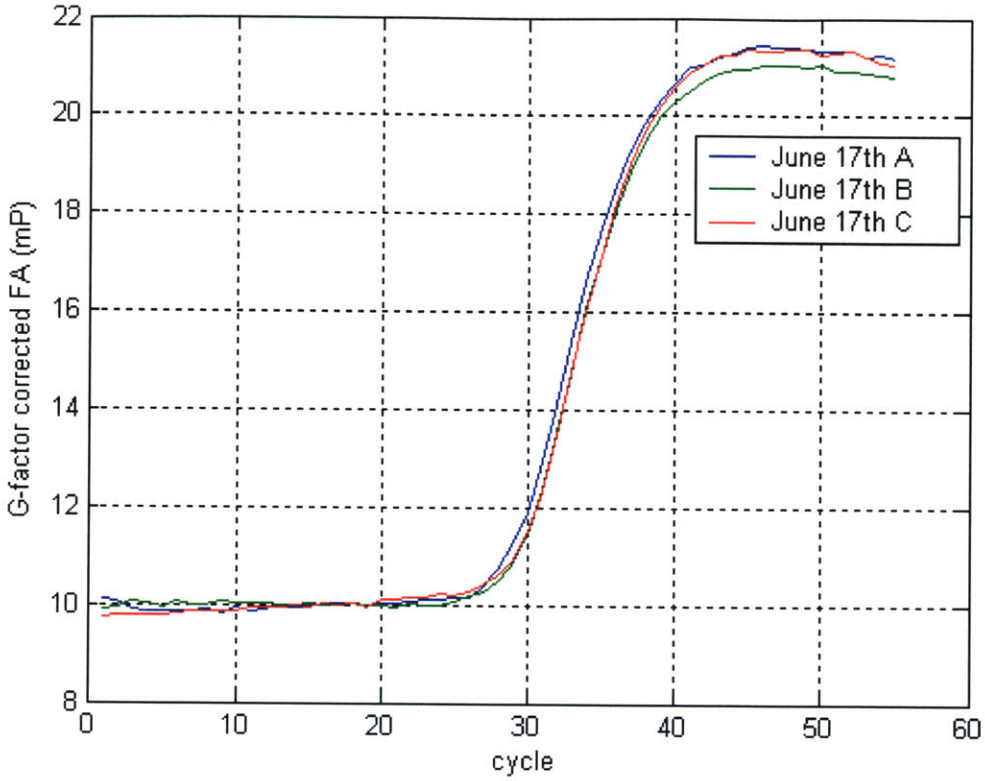


**Figure 5-15. Three replicate amplifications of enriched DNA template exhibiting a larger FA change when compared to genomic DNA as the template.**

*5.5.a. Range Improvement*

One important change that resulted from making the switch to enriched DNA was that the measurement range has noticeably increased as compared to amplification done with genomic DNA as the starting template. This is more clearly presented in Figure 5-16 where both genomic and enriched template amplification results are plotted together. The enriched samples exhibit a change from 10 mP during early cycles to 21 mP at the plateau of late cycles. In the genomic samples, the late cycle plateau 18-19 mP.

The exact mechanism of the improvement is not known. One explanation could be that specific binding of primers to unrestricted genomic DNA produces a substantial shift in FA. In subsequent cycles, when primers are only incorporated into template-length fragments, the change in FA contributed by these molecules would be smaller. For amplification of enriched DNA, the offsets provided by primer binding to genomic DNA would not be present, thereby enlarging the observed change during the course of PCR. In Figure 5-16, the baseline FA measurements have been adjusted for each

experiment to begin at the same value. This correction may mask a difference in the early-cycle FA.

This hypothesis seems unlikely given that the primers outnumber the genomic template by more than a $10^{27}$ to 1. Only an extremely small percentage of the primers would be expected to specifically bind to the genomic DNA in early cycles. Even if the few primers that specifically bound to genomic DNA became completely immobile, a 2-3 mP offset in the net FA of all molecules would not be observed.

An extension of this theory is that the genomic DNA is experiencing non-specific binding with the DNA and thereby biasing a much larger percentage of the primers. Casting doubt on this hypothesis is the lack of evidence of non-specific amplification however, it remains a possibility that non-specific binding, insufficient for extension but adequate to inhibit free rotation of the primers, causes the measured FA in the early cycles of genomic DNA amplification to be higher than the FA in enriched template amplification.

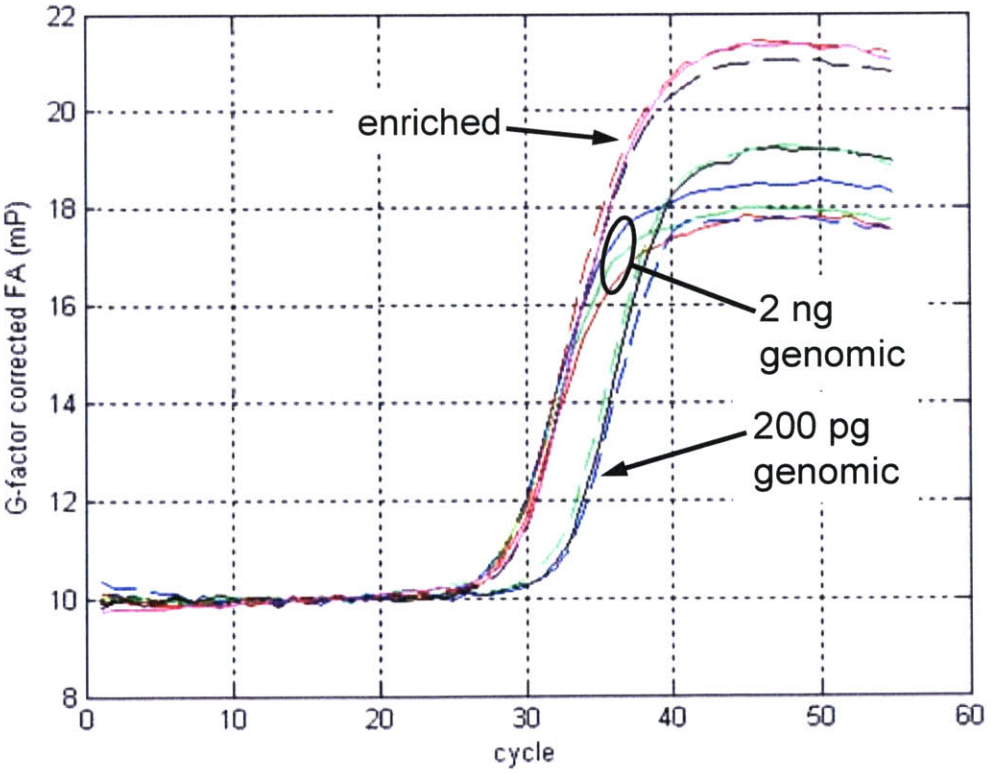


**Figure 5-16. Comparing the amplification results from the enriched template to the 2ng and 200 pg genomic template results, an improved net change in fluorescence anisotropy is observed.**

*5.5.b. Dynamic Range*

In Chapter 2, dynamic range was defined as the signal range divided by the measurement resolution, where the resolution is typically taken as twice the standard deviation of the measurement. In Chapter 2, it was argued that achieving a dynamic range comparable to that of existing instrumentation was desirable. In results from the Lightcycler, a dynamic range of 1:85 with the hybridization probes and 1:200 with SYBR green was demonstrated. Using enriched DNA, it is observed that the range displayed in Figure 5-16 is ~ 10 mP. The standard deviation of the early cycle variation is 0.02 mP. Thus, the measurement has achieved a dynamic range of better than 1:250.

*5.5.c. Repeatability*

The repeatability of the enriched template amplification did not show an improvement compared to the genomic DNA amplification. The fitted first derivative curves are shown in Figure 5-17, where the mean of each fitted Gaussian model is given in the figure legend. These mean values exhibit a coefficient of variation of 0.87%. The variation on the comparable quantity of genomic DNA was only 0.3%. The cause of this increased crossing point variability is assumed to lie in pipetting error.

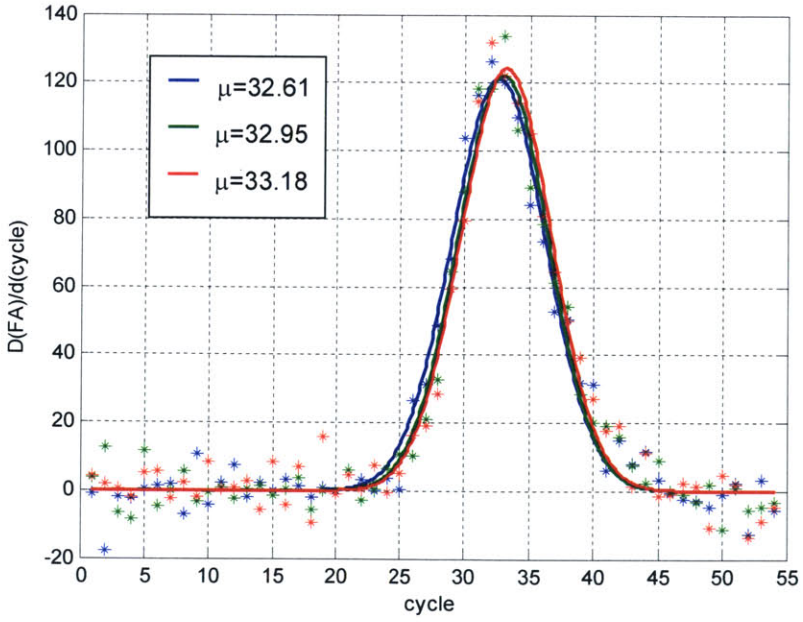


**Figure 5-17. First-derivatives of amplification curves of Figure 5-16. The legend gives the cycle at which maximum of the fitted Gaussian model (i.e., its mean) occurs for each data set.**

# Chapter 6

# Conclusion

## Accomplishments

This thesis presents a new method for monitoring real-time PCR which excludes the use of intercalating dyes or hybridization probes. Instead, the incorporation of labeled primer molecules is monitored via fluorescence anisotropy. The work is motivated by the desire to maintain the specificity that accompanies a detection method founded on oligonucleotide binding (such as in hybridization probes) but without the expense and added complexity of hybridization probes.

The most significant contribution of this work has been the demonstration that adequate dynamic range can be achieved with FA detection to achieve accurate, repeatable real time PCR measurement. Previous attempts to use FA for real time DNA applications (Walker, Linn, and Nadeau, 1996a) were not successful without modifying the amplification assay to include binding proteins. Real-time PCR assays amplifying a wide range of starting copy numbers were presented for both FA and intercalator dye methods. Comparably constant, high (>92%) amplification efficiencies were observed across the range of starting copy numbers for both measurement methods (Section 5.3).

Beyond experimental data, this thesis has analyzed the theoretical limits to FA resolution that result from shot noise limited optical measurements (Section 4.4.c). These

fundamental limits provide the basis for instrument evaluation and future development. The experimental results indicate that, when instrument drift is under control, the theoretical best possible measurement resolution is achieved with this instrument design. Future work in parallelizing and reducing the analyzed PCR assay volume must keep a close eye on the increased noise expected at lower signal levels (Figure 4-17).

This thesis has also included calculation of the theoretical minimum expected variability in repeated real-time PCR measurement of an expected number of starting copies (Section 5.2.a). While both stochastic pipetting and amplification variability have been considered individually in the literature, their combined affects have not been presented before. The results show that pipetting error dominates the combined error providing focus to future effort toward high accuracy, low copy number real-time PCR measurements. Experimental results (Section 5.4) indicate monitoring real-time PCR with FA provides repeatability in the crossing point consistent with the theoretical best possible.

## Future Work

The use of FA to monitor real time PCR is motivated by the desire to eliminate a costly, complicating reagent (hybridization probes) with minimal compromise on assay specificity. While elimination of the hybridization probes, alone, provides an important means of cost reduction, the real cost reductions will only be gained by leveraging the improved robustness of the simpler FA assay to enable reduced PCR assay volume. Therefore, the main goals of future work should focus on scaling this instrument to smaller reaction volumes with significant parallelization.

To be feasible, no more than a 2× increase in measurement noise is allowable if the measurement range is to remain at 7 to 10 mP. Very low noise measurements of parallel samples can be maintained with cooled charge coupled devices (CCD) (or potentially the rapidly evolving complimentary metal oxide semiconductor (CMOS) detectors). Affordable implementations of such devices are not likely to include any means of signal amplification (such as in the PMT), however the roughly 6× higher quantum efficiency of CCDs and their ability to integrate incoming photons over long

periods of time make the prospect of low noise, parallel measurement realizable. This application is particularly suited to integrative photonic measurement since polymerase extension (the step at which the FA is measured) requires a minimum of several seconds. Maintaining shot noise limited measurement is further aided by maximizing incoming signal. Careful and creative optical system design will be required to maintain maximal signal transmission efficiency. The use of a high numerical aperture (NA = 0.3 to 0.5) coupling of polarization-conserving optical fibers provides one interesting alternative[♣]. At one end, a bundle of, for example, nine fibers could tightly couple a sample plate via a micro-lens. The bundle would be separated into two groups at the detection end, each group interfacing with an optical filter, polarizer, and detector. Parallelization would be achieved by using many fiber bundles and a micro lens array. Another interesting option is the use of liquid crystal polarizers such as used by the CRI instrument discussed in Section 4.4.d

Measurement range may likely also hold room for improvement as new fluorophores and new methods of more rigid coupling of those fluorophores to oligonucleotides are developed.

Finally, other design requirements such as prevention of evaporation and adequate thermal stability will also remain important challenges in achieving parallization of micro to nano-scale PCR volumes.

Even as the number of correlations between genes and disease continues to rise, the promise of pharmocogenetics and molecular diagnostics will not be realized without a low cost, high throughput means of screening individuals in a clinical setting. It is the author's hope that this work may contribute toward that goal.

---

[♣] The extent to which high numerical aperture (NA) can be used to achieve large signals is limited in FA measurement. The FA measurement becomes increasingly biased toward unity at increasing NA (Lakowicz ,1999).

# References


1. Abramson, R. D. PCR Strategies: San Diego; 1995.

2. Amir, R. E.; Van den Veyver, I. B.; Wan, M.; Tran, C. Q.; Francke, U., and Zoghbi, H. Y. Rett syndrome is caused by mutations in X-linked MECP2, encoding methyl-CpG-binding protein 2. Nat Genet. 1999 Oct; 23(2):185-8.

3. Armitage, P. and Doll, R. The age distribution of cancer and a multi-stage theory of carcinogenesis. Br J Cancer. 1954 Mar; 8(1):1-12.

4. Avery, O. T.; MacLeod, C. M., and McCarty, M. Studies on the Chemical Nature of the Substance Inducing Transformation of Pneumococcal Types: Induction of Transformation by a Deoxyribonucleic Acid Faction Isolated from Pneumococcus Type III. Journal of Experimental Medicine . 1979 Feb; 149:297-326.

5. Bassler, H. A.; Flood, S. J.; Livak, K. J.; Marmaro, J.; Knorr, R., and Batt, C. A. Use of a fluorogenic probe in a PCR-based assay for the detection of Listeria monocytogenes. Appl Environ Microbiol. 1995 Oct; 61(10):3724-8.

6. Beadle, G. W. and Tatum, E. L. Genetic Control of Biochemical Reactions in Neurospora . *Proceedings of the National Academy of Sciences of the United States of America.* 1941 Nov 15; 27 (11):499-506.

7. Bezieau, S.; Devilder, M. C.; Avet-Loiseau, H.; Mellerin, M. P.; Puthier, D.; Pennarun, E.; Rapp, M. J.; Harousseau, J. L.; Moisan, J. P., and Bataille, R. High incidence of N and K-Ras activating mutations in multiple myeloma and primary plasma cell leukemia at diagnosis. Hum Mutat. 2001 Sep; 18(3):212-24.

8. Brash, D. E.; Rudolph, J. A.; Simon, J. A.; Lin, A.; McKenna, G. J.; Baden, H. P.; Halperin, A. J., and Ponten, J. A role for sunlight in skin cancer: UV-induced p53 mutations in squamous cell carcinoma. Proc Natl Acad Sci U S A. 1991 Nov 15; 88(22):10124-8.

9. Bustin, S. A. Absolute quantification of mRNA using real-time reverse transcription polymerase chain reaction assays. J Mol Endocrinol. 2000 Oct; 25(2):169-93.

10. Bustin, S. A. Quantification of mRNA using real-time reverse transcription PCR (RT-PCR): trends and problems. J Mol Endocrinol. 2002 Aug; 29(1):23-39.

11. Bustin, S. A. and Dorudi, S. Molecular assessment of tumour stage and disease recurrence using PCR-based assays. Mol Med Today. 1998 Sep; 4(9):389-96.

12. Cambridge Research Instruments. Instrument Bias with Dichroic Mirror [Web Page]. Accessed 2002. Available at: http://www.cri-inc.com/instruments/data/pdf/SBS_2001_Gfactor_B.mov.

13. Cardullo, R. A.; Agrawal, S.; Flores, C.; Zamecnik, P. C., and Wolf, D. E. Detection of nucleic acid hybridization by nonradiative fluorescence resonance energy transfer. Proc Natl Acad Sci U S A. 1988 Dec; 85(23):8790-4.

14. Cha, R. S.; Zarbl, H.; Keohavong, P., and Thilly, W. G. Mismatch amplification mutation assay (MAMA): application to the c-H- ras gene. PCR Methods Appl. 1992 Aug; 2(1):14-20.

15. Chen, T.; Harrington-Brock, K., and Moore, M. M. Mutant frequencies and loss of heterozygosity induced by N-ethyl-N-nitrosourea in the thymidine kinase gene of L5178Y/TK(+/-)-3.7.2C mouse lymphoma cells. Mutagenesis. 2002 Mar; 17(2):105-9.

16. Chen, X.; Levine, L., and Kwok, P. Y. Fluorescence polarization in homogeneous nucleic acid analysis. Genome Res. 1999a May; 9(5):492-8.

17. Cheng, J.; Shoffner, M. A.; Hvichia, G. E.; Kricka, L. J., and Wilding, P. Chip PCR. II. Investigation of different PCR amplification systems in microbabricated silicon-glass chips. Nucleic Acids Res. 1996a Jan 15; 24(2):380-5.

18. Cotton, R. G. H. Mutation Detection. New York , NY: Oxford University Press; 1997.

19. Couzin, J. Genomics. New mapping project splits the community. Science. 2002 May 24; 296(5572):1391-3.

20. Crane, B.; Sudo, H.; Thilly, W. G., and Hunter, I. W. Towards Fluorescence Anisotropy Detection for Real Time PCR assays. 25th Annual International Conference of the IEEE Engineering in Medicine and Biology Society.

21. Desjardin, L. E.; Perkins, M. D.; Wolski, K.; Haun, S.; Teixeira, L.; Chen, Y.; Johnson, J. L.; Ellner, J. J.; Dietze, R.; Bates, J.; Cave, M. D., and Eisenach, K. D. Measurement of sputum Mycobacterium tuberculosis messenger RNA as a surrogate for response to chemotherapy. Am J Respir Crit Care Med. 1999 Jul; 160(1):203-10.

22. Dobrovolsky, V. N.; Chen, T., and Heflich, R. H. Molecular analysis of in vivo

mutations induced by N-ethyl-N-nitrosourea in the autosomal Tk and the X-linked Hprt genes of mouse lymphocytes. Environ Mol Mutagen. 1999; 34(1):30-8.

23. Evans, W. E. and Relling, M. V. Moving towards individualized medicine with pharmacogenomics. Nature. 2004 May 27; 429(6990):464-8.

24. Gabriel, S. B.; Schaffner, S. F.; Nguyen, H.; Moore, J. M.; Roy, J.; Blumenstiel, B.; Higgins, J.; DeFelice, M.; Lochner, A.; Faggart, M.; Liu-Cordero, S. N.; Rotimi, C.; Adeyemo, A.; Cooper, R.; Ward, R.; Lander, E. S.; Daly, M. J., and Altshuler, D. The structure of haplotype blocks in the human genome. Science. 2002 Jun 21; 296(5576):2225-9.

25. Ghossein, R. A. and Rosai, J. Polymerase chain reaction in the detection of micrometastases and circulating tumor cells. Cancer. 1996 Jul 1; 78(1):10-6.

26. Gibson, N. J.; Gillard, H. L.; Whitcombe, D.; Ferrie, R. M.; Newton, C. R., and Little, S. A homogeneous method for genotyping with fluorescence polarization. Clin Chem. 1997 Aug; 43(8 Pt 1):1336-41.

27. Glaab, W. E. and Skopek, T. R. A novel assay for allelic discrimination that combines the fluorogenic 5' nuclease polymerase chain reaction (TaqMan) and mismatch amplification mutation assay. Mutat Res. 1999 Nov 29; 430(1):1-12.

28. Halapi, E. and Hakonarson, H. Advances in the development of genetic markers for the diagnosis of disease and drug response. Expert Rev Mol Diagn. 2002 Sep; 2(5):411-21.

29. Hamamatsu Corporation. Photomultiplier Tubes: Construction and Operating Characteristics [Web Page]. 1998 Jan; Accessed 2002. Available at: http://www.phys.uni.torun.pl/~lab2/library/pdf/pmt_caoc.pdf.

30. Hamamatsu Corporation. M9011/M9012 Temperature Control & Power Supply For H7421/H7422 Series Instruction Manual. 1st ed.; 2002 Apr.

31. Heid, C. A.; Stevens, J.; Livak, K. J., and Williams, P. M. Real time quantitative PCR. Genome Res. 1996 Oct; 6(10):986-94.

32. Higuchi, R.; Dollinger, G.; Walsh, P. S., and Griffith, R. Simultaneous amplification and detection of specific DNA sequences. Biotechnology (N Y). 1992 Apr; 10(4):413-7.

33. Hill, W. E. The polymerase chain reaction: applications for the detection of foodborne pathogens. Crit Rev Food Sci Nutr. 1996 Jan; 36(1-2):123-73.

34. Holden, A. L. The SNP consortium: summary of a private consortium effort to

develop an applied map of the human genome. Biotechniques. 2002 Jun; Suppl:22-4, 26.

35. Holland, P. M.; Abramson, R. D.; Watson, R., and Gelfand, D. H. Detection of specific polymerase chain reaction product by utilizing the 5'----3' exonuclease activity of Thermus aquaticus DNA polymerase. Proc Natl Acad Sci U S A. 1991 Aug 15; 88(16):7276-80.

36. Holodniy, M. Clinical application of reverse transcription-polymerase chain reaction for HIV infection. Clin Lab Med. 1994 Jun; 14(2):335-49.

37. Horikoshi, T.; Lenz, H. J.; Danenberg, K.; Koch, O. M.; Bertino, J. R., and Danenberg, P. V. Quantitative determination of the ratio of mutated to normal ras genes in the blood of leukemia patients by allele-specific PCR. Leuk Res. 1994 Sep; 18(9):693-702.

38. Khrapko, K.; Hanekamp, J. S.; Thilly, W. G.; Belenkii, A.; Foret, F., and Karger, B. L. Constant denaturant capillary electrophoresis (CDCE): a high resolution approach to mutational analysis. Nucleic Acids Res. 1994 Feb 11; 22(3):364-9.

39. Kirby, G. M.; Batist, G.; Fotouhi-Ardakani, N.; Nakazawa, H.; Yamasaki, H.; Kew, M.; Cameron, R. G., and Alaoui-Jamali, M. A. Allele-specific PCR analysis of p53 codon 249 AGT transversion in liver tissues from patients with viral hepatitis. Int J Cancer. 1996 Sep 27; 68(1):21-5.

40. Knudson, A. G. Jr. Mutation and cancer: statistical study of retinoblastoma. Proc Natl Acad Sci U S A. 1971 Apr; 68(4):820-3.

41. Krawczak, M.; Reiss, J.; Schmidtke, J., and Rosler, U. Polymerase chain reaction: replication errors and reliability of gene diagnosis. Nucleic Acids Res. 1989 Mar 25; 17(6):2197-201.

42. Laghi, L.; Orbetegli, O.; Bianchi, P.; Zerbi, A.; Di Carlo, V.; Boland, C. R., and Malesci, A. Common occurrence of multiple K-RAS mutations in pancreatic cancers with associated precursor lesions and in biliary cancers. Oncogene. 2002 Jun 20; 21(27):4301-6.

43. Lakowicz, J. R. Principles of Fluorescence Spectroscopy. New York, NY: Kluwer Academic/Plenum Publishers; 1999.

44. Lander, E. S.; Linton, L. M.; Birren, B.; Nusbaum, C.; Zody, M. C.; Baldwin, J.; Devon, K.; Dewar, K.; Doyle, M.; FitzHugh, W.; Funke, R.; Gage, D.; Harris, K.; Heaford, A.; Howland, J.; Kann, L.; Lehoczky, J.; LeVine, R.; McEwan, P.; McKernan, K.; Meldrim, J.; Mesirov, J. P.; Miranda, C.; Morris, W.; Naylor, J.; Raymond, C.; Rosetti, M.; Santos, R.; Sheridan, A.; Sougnez, C.; Stange-Thomann, N.; Stojanovic, N.; Subramanian, A.; Wyman, D.; Rogers, J.; Sulston, J.; Ainscough, R.; Beck, S.; Bentley, D.;

Burton, J.; Clee, C.; Carter, N.; Coulson, A.; Deadman, R.; Deloukas, P.; Dunham, A.; Dunham, I.; Durbin, R.; French, L.; Grafham, D.; Gregory, S.; Hubbard, T.; Humphray, S.; Hunt, A.; Jones, M.; Lloyd, C.; McMurray, A.; Matthews, L.; Mercer, S.; Milne, S.; Mullikin, J. C.; Mungall, A.; Plumb, R.; Ross, M.; Shownkeen, R.; Sims, S.; Waterston, R. H.; Wilson, R. K.; Hillier, L. W.; McPherson, J. D.; Marra, M. A.; Mardis, E. R.; Fulton, L. A.; Chinwalla, A. T.; Pepin, K. H.; Gish, W. R.; Chissoe, S. L.; Wendl, M. C.; Delehaunty, K. D.; Miner, T. L.; Delehaunty, A.; Kramer, J. B.; Cook, L. L.; Fulton, R. S.; Johnson, D. L.; Minx, P. J.; Clifton, S. W.; Hawkins, T.; Branscomb, E.; Predki, P.; Richardson, P.; Wenning, S.; Slezak, T.; Doggett, N.; Cheng, J. F.; Olsen, A.; Lucas, S.; Elkin, C.; Uberbacher, E.; Frazier, M.; Gibbs, R. A.; Muzny, D. M.; Scherer, S. E.; Bouck, J. B.; Sodergren, E. J.; Worley, K. C.; Rives, C. M.; Gorrell, J. H.; Metzker, M. L.; Naylor, S. L.; Kucherlapati, R. S.; Nelson, D. L.; Weinstock, G. M.; Sakaki, Y.; Fujiyama, A.; Hattori, M.; Yada, T.; Toyoda, A.; Itoh, T.; Kawagoe, C.; Watanabe, H.; Totoki, Y.; Taylor, T.; Weissenbach, J.; Heilig, R.; Saurin, W.; Artiguenave, F.; Brottier, P.; Bruls, T.; Pelletier, E.; Robert, C.; Wincker, P.; Smith, D. R.; Doucette-Stamm, L.; Rubenfield, M.; Weinstock, K.; Lee, H. M.; Dubois, J.; Rosenthal, A.; Platzer, M.; Nyakatura, G.; Taudien, S.; Rump, A.; Yang, H.; Yu, J.; Wang, J.; Huang, G.; Gu, J.; Hood, L.; Rowen, L.; Madan, A.; Qin, S.; Davis, R. W.; Federspiel, N. A.; Abola, A. P.; Proctor, M. J.; Myers, R. M.; Schmutz, J.; Dickson, M.; Grimwood, J.; Cox, D. R.; Olson, M. V.; Kaul, R.; Raymond, C.; Shimizu, N.; Kawasaki, K.; Minoshima, S.; Evans, G. A.; Athanasiou, M.; Schultz, R.; Roe, B. A.; Chen, F.; Pan, H.; Ramser, J.; Lehrach, H.; Reinhardt, R.; McCombie, W. R.; de la Bastide, M.; Dedhia, N.; Blocker, H.; Hornischer, K.; Nordsiek, G.; Agarwala, R.; Aravind, L.; Bailey, J. A.; Bateman, A.; Batzoglou, S.; Birney, E.; Bork, P.; Brown, D. G.; Burge, C. B.; Cerutti, L.; Chen, H. C.; Church, D.; Clamp, M.; Copley, R. R.; Doerks, T.; Eddy, S. R.; Eichler, E. E.; Furey, T. S.; Galagan, J.; Gilbert, J. G.; Harmon, C.; Hayashizaki, Y.; Haussler, D.; Hermjakob, H.; Hokamp, K.; Jang, W.; Johnson, L. S.; Jones, T. A.; Kasif, S.; Kaspryzk, A.; Kennedy, S.; Kent, W. J.; Kitts, P.; Koonin, E. V.; Korf, I.; Kulp, D.; Lancet, D.; Lowe, T. M.; McLysaght, A.; Mikkelsen, T.; Moran, J. V.; Mulder, N.; Pollara, V. J.; Ponting, C. P.; Schuler, G.; Schultz, J.; Slater, G.; Smit, A. F.; Stupka, E.; Szustakowski, J.; Thierry-Mieg, D.; Thierry-Mieg, J.; Wagner, L.; Wallis, J.; Wheeler, R.; Williams, A.; Wolf, Y. I.; Wolfe, K. H.; Yang, S. P.; Yeh, R. F.; Collins, F.; Guyer, M. S.; Peterson, J.; Felsenfeld, A.; Wetterstrand, K. A.; Patrinos, A.; Morgan, M. J.; Szustakowki, J.; de Jong, P.; Catanese, J. J.; Osoegawa, K.; Shizuya, H.; Choi, S., and Chen, Y. J. Initial sequencing and analysis of the human genome. Nature. 2001 Feb 15; 409(6822):860-921.

45. Latif, S.; Bauer-Sardina, I.; Ranade, K.; Livak, K. J., and Kwok, P. Y. Fluorescence polarization in homogeneous nucleic acid analysis II: 5'-nuclease assay. Genome Res. 2001a Mar; 11(3):436-40.

46. Lewin, B. Genes. 6th ed. New York, NY: Oxford Univsersity Press; 1997.

47. Livak, K. J.; Flood, S. J.; Marmaro, J.; Giusti, W., and Deetz, K. Oligonucleotides with fluorescent dyes at opposite ends provide a quenched probe system useful for detecting PCR product and nucleic acid hybridization. PCR Methods Appl. 1995 Jun; 4(6):357-62.

48. Lunge, V. R.; Miller, B. J.; Livak, K. J., and Batt, C. A. Factors affecting the performance of 5' nuclease PCR assays for Listeria monocytogenes detection. J Microbiol Methods. 2002 Nov; 51(3):361-8.

49. Mackay, I. M.; Arden, K. E., and Nitsche, A. Real-time PCR in virology. Nucleic Acids Res. 2002 Mar 15; 30(6):1292-305.

50. Marino, M. A.; Devaney, J. M.; Davis, P. A.; Smith, J. K., and Girard, J. E. Spectral measurements of intercalated PCR-amplified short tandem repeat alleles. Anal Chem. 1998 Nov 1; 70(21):4514-9.

51. Meselson, M. and Stahl, F. W. The Replication of DNA in Escherichia Coli. Proceedings of the National Academy of Science. 1958; 44:671-682.

52. Mokdad, A. H.; Marks, J. S.; Stroup, D. F., and Gerberding, J. L. Actual causes of death in the United States, 2000. JAMA. 2004 Mar 10; 291(10):1238-45.

53. Morrison, T. B.; Weis, J. J., and Wittwer, C. T. Quantification of low-copy transcripts by continuous SYBR Green I monitoring during amplification. Biotechniques. 1998 Jun; 24(6):954-8, 960, 962.

54. Murakami, A.; Nakaura, M.; Nakatsuji, Y.; Nagahara, S.; Tran-Cong, Q., and Makino, K. Fluorescent-labeled oligonucleotide probes: detection of hybrid formation in solution by fluorescence polarization spectroscopy. Nucleic Acids Res. 1991 Aug 11; 19(15):4097-102.

55. Nazarenko, I. A.; Bhatnagar, S. K., and Hohman, R. J. A closed tube format for amplification and detection of DNA based on energy transfer. Nucleic Acids Res. 1997 Jun 15; 25(12):2516-21.

56. Newton, C. R.; Graham, A.; Heptinstall, L. E.; Powell, S. J.; Summers, C.; Kalsheker, N.; Smith, J. C., and Markham, A. F. Analysis of any point mutation in DNA. The amplification refractory mutation system (ARMS). Nucleic Acids Res. 1989 Apr 11; 17(7):2503-16.

57. Nikiforov, T. T.; Rendle, R. B.; Goelet, P.; Rogers, Y. H.; Kotewicz, M. L.; Anderson, S.; Trainor, G. L., and Knapp, M. R. Genetic Bit Analysis: a solid phase method for typing single nucleotide polymorphisms. Nucleic Acids Res. 1994 Oct 11; 22(20):4167-75.

58. Nordling, C. O. A new theory on cancer-inducing mechanism. Br J Cancer. 1953

Mar; 7(1):68-72.

59. Orou, A.; Fechner, B.; Utermann, G., and Menzel, H. J. Allele-specific competitive blocker PCR: a one-step method with applicability to pool screening. Hum Mutat. 1995; 6(2):163-9.

60. Owicki, J. C. Fluorescence polarization and anisotropy in high throughput screening: perspectives and primer. J Biomol Screen. 2000 Oct; 5(5):297-306.

61. Parsons, B. L. and Heflich, R. H. Genotypic selection methods for the direct analysis of point mutations. Mutat Res. 1997 Oct; 387(2):97-121.

62. Pease, A. C.; Solas, D.; Sullivan, E. J.; Cronin, M. T.; Holmes, C. P., and Fodor, S. P. Light-generated oligonucleotide arrays for rapid DNA sequence analysis. Proc Natl Acad Sci U S A. 1994 May 24; 91(11):5022-6.

63. Peccoud, J. and Jacob C. "Statistical Estimations of PCR Amplification Rates". In: *Gene Quantification.* New York: Birkhäuser; 1998; (F. Ferre (ed.).

64. Perrin, F. Polarization de la lumiere de fluorescence. Vie moyenne de molecules dans l'etat excite. J. Phys. Radium. 1926; 7:390-401.

65. Ramachandran, C. and Melnick, S. J. Multidrug resistance in human tumors--molecular diagnosis and clinical significance. Mol Diagn. 1999 Jun; 4(2):81-94.

66. Roche Applied Science. LightCycler 2.0 Instrument Operator's Manual. Germany: Roche Diagnostics GmbH; 2003 Oct.

67. Ronaghi, M.; Uhlen, M., and Nyren, P. A sequencing method based on real-time pyrophosphate. Science. 1998 Jul 17; 281(5375):363, 365.

68. Roses, A. D. Pharmacogenetics and the practice of medicine. Nature. 2000 Jun 15; 405(6788):857-65.

69. Ross, J. S. and Ginsburg, G. S. Integrating diagnostics and therapeutics: revolutionizing drug discovery and patient care. Drug Discov Today. 2002 Aug 15; 7(16):859-64.

70. Saiki, R. K.; Scharf, S.; Faloona, F.; Mullis, K. B.; Horn, G. T.; Erlich, H. A., and Arnheim, N. Enzymatic amplification of beta-globin genomic sequences and restriction site analysis for diagnosis of sickle cell anemia. Science. 1985 Dec 20; 230(4732):1350-4.

71. Sailer, B. L.; Nastasi, A. J.; Valdez, J. G.; Steinkamp, J. A., and Crissman, H. A. Differential effects of deuterium oxide on the fluorescence lifetimes and intensities of dyes with different modes of binding to DNA. J Histochem

Cytochem. 1997 Feb; 45(2):165-75.

72. Schmith, V. D.; Campbell, D. A.; Sehgal, S.; Anderson, W. H.; Burns, D. K.; Middleton, L. T., and Roses, A. D. Pharmacogenetics and disease genetics of complex diseases. Cell Mol Life Sci. 2003 Aug; 60(8):1636-46.

73. Shoffner, M. A.; Cheng, J.; Hvichia, G. E.; Kricka, L. J., and Wilding, P. Chip PCR. I. Surface passivation of microfabricated silicon-glass chips for PCR. Nucleic Acids Res. 1996 Jan 15; 24(2):375-9.

74. Sommer, S. S.; Cassady, J. D.; Sobell, J. L., and Bottema, C. D. A novel method for detecting point mutations or polymorphisms and its application to population screening for carriers of phenylketonuria. Mayo Clin Proc. 1989 Nov; 64(11):1361-72.

75. Spears, P. A.; Linn, C. P.; Woodard, D. L., and Walker, G. T. Simultaneous strand displacement amplification and fluorescence polarization detection of Chlamydia trachomatis DNA. Anal Biochem. 1997 Apr 5; 247(1):130-7.

76. Sun, F. The polymerase chain reaction and branching processes. J Comput Biol. 1995 Spring; 2(1):63-86.

77. Taylor, T. B.; Winn-Deen, E. S.; Picozza, E.; Woudenberg, T. M., and Albin, M. Optimization of the performance of the polymerase chain reaction in silicon-based microstructures. Nucleic Acids Res. 1997 Aug 1; 25(15):3164-8.

78. Thilly, W. G. Have environmental mutagens caused oncomutations in people? Nat Genet. 2003 Jul; 34(3):255-9.

79. Tyagi, S. and Kramer, F. R. Molecular beacons: probes that fluoresce upon hybridization. Nat Biotechnol. 1996 Mar; 14(3):303-8.

80. Venter, J. C.; Adams, M. D.; Myers, E. W.; Li, P. W.; Mural, R. J.; Sutton, G. G.; Smith, H. O.; Yandell, M.; Evans, C. A.; Holt, R. A.; Gocayne, J. D.; Amanatides, P.; Ballew, R. M.; Huson, D. H.; Wortman, J. R.; Zhang, Q.; Kodira, C. D.; Zheng, X. H.; Chen, L.; Skupski, M.; Subramanian, G.; Thomas, P. D.; Zhang, J.; Gabor Miklos, G. L.; Nelson, C.; Broder, S.; Clark, A. G.; Nadeau, J.; McKusick, V. A.; Zinder, N.; Levine, A. J.; Roberts, R. J.; Simon, M.; Slayman, C.; Hunkapiller, M.; Bolanos, R.; Delcher, A.; Dew, I.; Fasulo, D.; Flanigan, M.; Florea, L.; Halpern, A.; Hannenhalli, S.; Kravitz, S.; Levy, S.; Mobarry, C.; Reinert, K.; Remington, K.; Abu-Threideh, J.; Beasley, E.; Biddick, K.; Bonazzi, V.; Brandon, R.; Cargill, M.; Chandramouliswaran, I.; Charlab, R.; Chaturvedi, K.; Deng, Z.; Di Francesco, V.; Dunn, P.; Eilbeck, K.; Evangelista, C.; Gabrielian, A. E.; Gan, W.; Ge, W.; Gong, F.; Gu, Z.; Guan, P.; Heiman, T. J.; Higgins, M. E.; Ji, R. R.; Ke, Z.; Ketchum, K. A.;

Lai, Z.; Lei, Y.; Li, Z.; Li, J.; Liang, Y.; Lin, X.; Lu, F.; Merkulov, G. V.; Milshina, N.; Moore, H. M.; Naik, A. K.; Narayan, V. A.; Neelam, B.; Nusskern, D.; Rusch, D. B.; Salzberg, S.; Shao, W.; Shue, B.; Sun, J.; Wang, Z.; Wang, A.; Wang, X.; Wang, J.; Wei, M.; Wides, R.; Xiao, C.; Yan, C.; Yao, A.; Ye, J.; Zhan, M.; Zhang, W.; Zhang, H.; Zhao, Q.; Zheng, L.; Zhong, F.; Zhong, W.; Zhu, S.; Zhao, S.; Gilbert, D.; Baumhueter, S.; Spier, G.; Carter, C.; Cravchik, A.; Woodage, T.; Ali, F.; An, H.; Awe, A.; Baldwin, D.; Baden, H.; Barnstead, M.; Barrow, I.; Beeson, K.; Busam, D.; Carver, A.; Center, A.; Cheng, M. L.; Curry, L.; Danaher, S.; Davenport, L.; Desilets, R.; Dietz, S.; Dodson, K.; Doup, L.; Ferriera, S.; Garg, N.; Gluecksmann, A.; Hart, B.; Haynes, J.; Haynes, C.; Heiner, C.; Hladun, S.; Hostin, D.; Houck, J.; Howland, T.; Ibegwam, C.; Johnson, J.; Kalush, F.; Kline, L.; Koduru, S.; Love, A.; Mann, F.; May, D.; McCawley, S.; McIntosh, T.; McMullen, I.; Moy, M.; Moy, L.; Murphy, B.; Nelson, K.; Pfannkoch, C.; Pratts, E.; Puri, V.; Qureshi, H.; Reardon, M.; Rodriguez, R.; Rogers, Y. H.; Romblad, D.; Ruhfel, B.; Scott, R.; Sitter, C.; Smallwood, M.; Stewart, E.; Strong, R.; Suh, E.; Thomas, R.; Tint, N. N.; Tse, S.; Vech, C.; Wang, G.; Wetter, J.; Williams, S.; Williams, M.; Windsor, S.; Winn-Deen, E.; Wolfe, K.; Zaveri, J.; Zaveri, K.; Abril, J. F.; Guigo, R.; Campbell, M. J.; Sjolander, K. V.; Karlak, B.; Kejariwal, A.; Mi, H.; Lazareva, B.; Hatton, T.; Narechania, A.; Diemer, K.; Muruganujan, A.; Guo, N.; Sato, S.; Bafna, V.; Istrail, S.; Lippert, R.; Schwartz, R.; Walenz, B.; Yooseph, S.; Allen, D.; Basu, A.; Baxendale, J.; Blick, L.; Caminha, M.; Carnes-Stine, J.; Caulk, P.; Chiang, Y. H.; Coyne, M.; Dahlke, C.; Mays, A.; Dombroski, M.; Donnelly, M.; Ely, D.; Esparham, S.; Fosler, C.; Gire, H.; Glanowski, S.; Glasser, K.; Glodek, A.; Gorokhov, M.; Graham, K.; Gropman, B.; Harris, M.; Heil, J.; Henderson, S.; Hoover, J.; Jennings, D.; Jordan, C.; Jordan, J.; Kasha, J.; Kagan, L.; Kraft, C.; Levitsky, A.; Lewis, M.; Liu, X.; Lopez, J.; Ma, D.; Majoros, W.; McDaniel, J.; Murphy, S.; Newman, M.; Nguyen, T.; Nguyen, N.; Nodell, M.; Pan, S.; Peck, J.; Peterson, M.; Rowe, W.; Sanders, R.; Scott, J.; Simpson, M.; Smith, T.; Sprague, A.; Stockwell, T.; Turner, R.; Venter, E.; Wang, M.; Wen, M.; Wu, D.; Wu, M.; Xia, A.; Zandieh, A., and Zhu, X. The sequence of the human genome. Science. 2001 Feb 16; 291(5507):1304-51.

81. Walker, G. T.; Linn, C. P., and Nadeau, J. G. DNA detection by strand displacement amplification and fluorescence polarization with signal enhancement using a DNA binding protein. Nucleic Acids Res. 1996a Jan 15; 24(2):348-53.

82. Walker, G. T.; Nadeau, J. G., and Linn, P., inventors. Fluorescence Polarization Detection of Nucleic Acid Amplification. Becton, Dickinson and Company, assignee. 5,593,867. 1997 Jun 14.

83. Waterfall, C. M. and Cobb, B. D. SNP genotyping using single-tube fluorescent bidirectional PCR. Biotechniques. 2002 Jul; 33(1):80, 82-4, 86 passim.

84. Watson, J. D. and Crick , F. H. C. Molecular structure of nucleic acids - A structure for deoxyribose nucleic acid . Nature. 1953; 171:737-738.

85. Weinsstein, E. W. "Cauchy Distribution" [Web Page]. Available at: http://mathworld.wolfram.com/NormalRatioDistribution.html).

86. Whitcombe, D.; Theaker, J.; Guy, S. P.; Brown, T., and Little, S. Detection of PCR products using self-probing amplicons and fluorescence. Nat Biotechnol. 1999 Aug; 17(8):804-7.

87. Wiesner, R. J.; Beinbrech, B., and Ruegg, J. C. Quantitative PCR. Nature. 1993 Dec 2; 366(6454):416.

88. Wittwer, C. T.; Herrmann, M. G.; Moss, A. A., and Rasmussen, R. P. Continuous fluorescence monitoring of rapid cycle DNA amplification. Biotechniques. 1997 Jan; 22(1):130-1, 134-8.

89. Yano, T.; Uchida, M.; Yuasa, M.; Murakami, A.; Hagiwara, K., and Ichikawa, T. The inhibitory effect of vitamin E on K-ras mutation at an early stage of lung carcinogenesis in mice. Eur J Pharmacol. 1997 Mar 26; 323(1):99-102.

90. Ye, B. C.; Ikebukuro, K., and Karube, I. Quantitative analysis of polymerase chain reaction using anisotropy ratio and relative hydrodynamic volume of fluorescence polarization method. Nucleic Acids Res. 1998 Aug 1; 26(15):3614-5.

# Appendix

1. Analysis of Primers
2. $2^{nd}$ Prototype PCR Protocol
3. Sudo Protocol
4. $4^{th}$ Step Test Protocol
5. $MgCl_2$ Optimization Protocol
6. Dilution Series Protocol in FA Instrument
7. Dilution Series Protocol in Lightcycler
8. Repeatability Protocol in FA Instrument
9. Repeatability of Genomic DNA Amplification in LightCycler
10. Target Sequence Enrichment
11. An Alternate Method of Calculating the Crossing Point
12. Matlab Code for Simulating Stochastic Processes of PCR
13. Matlab Code for Modeling Sample Holder Heat Transfer

# 1. Analysis of Primers

**Target: APC gene (NCBI entry #: M74088)**

**History**: This is the sequence that Heelo and I originally used to simulate FA measurement of PCR. She designed the primers and conducted the PCR.

**Sequence**:
GACAAACCATGCCACCAAGCAGAAGTAAAACACCTCCACCACCTCCTCAAA
CAGCTCAAACCAAGCGAGAAGTACCTAAAAATAAAGCACCTACTGCTGAAAA
GAGAGAGAGTGGACCTAAG

**Fwd Primer**: 5'- GAC AAA CCA TGC CAC CAA GC
Primer3 data
melt temperature = 63.77 C
GC% = 55%
any = 4.0
3' = 2.0
rep = 11.0
Synthegen melt temp = 57.6 C

**Rvs Primer**: 5'- CTT AGG TCC ACT CTC TCT CT
Primer3 data
melt temperature = 50.07 C
GC% = 50%
any = 3.0
3' = 0.0
rep = 12.0
Synthegen melt temp = 52.5 C

**Surrounding Sequence (221 bases before, 258 bases after):**
TTCTTCAGGAGCGAAATCTCCCTCCAAAAGTGGTGCTCAGACACCCAAAAG
TCCACCTGAACACTATGTTCAGGAGACCCCACTCATGTTTAGCAGATGTACT
TCTGTCAGTTCACTTGATAGTTTTGAGAGTCGTTCGATTGCCAGCTCCGTTC
AGAGTGAACCATGCAGTGGAATGGTAAGTGGCATTATAAGCCCCAGTGATC
TTCCAGATAGCCCTG[GACAAACCATGCCACCAAGCAGAAGTAAAACACCTC
CACCACCTCCTCAAACAGCTCAAACCAAGCGAGAAGTACCTAAAAATAAAGC
ACCTACTGCTGAAAAGAGAGAGAGTGGACCTAAG]CAAGCTGCAGTAAATGC
TGCAGTTCAGAGGGTCCAGGTTCTTCCAGATGCTGATACTTTATTACATTTT
GCCACGGAAAGTACTCCAGATGGATTTTCTTGTTCATCCAGCCTGAGTGCTC
TGAGCCTCGATGAGCCATTTATACAGAAAGATGTGGAATTAAGAATAATGCC
TCCAGTTCAGGAAAATGACAATGGGAATGAAACAGAATCAGAGCAGCCTAA
AGAATCAAATGAAAACCAAGAGAAAGAGGCAGAA

# 2. 2nd Prototype PCR Protocol

*This protocol describes the steps used to set up a PCR in the second prototype.*

To prepare a 20 μL PCR solution, 4 μL of water were mixed with 2 μL of both the forward and reverse APC primers in a 400 μL micro-centrifuge tube,. Next, 10 μL of Master Mix was added. Qiagen Master Mix (P/N: 203443, Hot Start Taq Master Mix, Qiagen) contains 1.5 mM $MgCl_2$ and 200 μM of each dNTP. Finally, 20 ng of male genomic DNA (4312660, Taqman Control Genomic DNA (Human), Applied Biosystems) were added. Mixing was done by gently pipetting the solution up and down (no vortexing as recommended by Qiagen protocol).

| Component | Initial Conc | Final Conc | Volume (uL) |
|---|---|---|---|
| H20 | | | 4 |
| APC Fwd | 2 uM | 0.2 uM | 2 |
| APC Rev | 2 uM | 0.2 uM | 2 |
| Qiagen Master Mix | 2X | 1X | 10 |
| Male Genomic DNA | 10 ng/uL | | 2 |
| Total | | | 20 |

20 μL of PCR solution was pipetted into the sample holder followed by ~20 μL of Fluorinert (FC-70, 3M). The volume of Fluorinert is marked as approximate because its viscosity dramatically reduced the repeatability of pipetting performance. Each liquid was pipetted into the sample volume of prototype 2 using long, narrow pipette tips (MultiFlex Round Tips, Sorenson Bioscience, Inc).

Qiagen's protocol specifies a 3 minute pre-incubation period at 94 °C to activate the hot-start Taq Enzyme. The amplification thermal profile is given below. Amplification for 55 cycles was typical.

Thermal cycle profile:

| | |
|---|---|
| Pre-incubation | 3 min @ 94 °C |
| Amplification | 94 °C for 15s; |
| | 49 °C for 15s; |
| | 72 °C for 10s; |
| | 50 °C for 20s; |

# 3. Sudo Protocol

*This protocol describes the steps used in an experiment to test the use of a 4$^{th}$ PCR step using electrophoresis. Experiments performed by Heelo Sudo.*

Genomic DNA was isolated from suspended human TK-6 lymphoblast cells using the Blood and Cell Culture DNA Maxi Kit (Qiagen, Valencia CA) according to the manufacturer's specifications followed by isopropanol precipitation of the DNA. It was then digested by restriction endonuclease BstNI (New England Biolabs, Beverly, MA). The 122 bp DNA fragment from the APC gene (NCBI entry#: M74088) was amplified with Taq DNA polymerase (New England Biolabs, Beverly, MA). The primers used in the amplification, purchased from MWG Biotech (High Pt, NC), were 5'-fluorescein-labeled U2 (5'GACAAACCATGCCACCAAGC) and unlabeled L1 (5'-CTTAGGTCCACTCTCTCTCT). PCR was conducted in 20 μL volumes in an Eppendorf Mastercycler in 0.2 mL PCR thin walled tubes. The PCR mix included 1× Taq Polymerase Buffer (New England Biolabs, Beverly, MA), 100 μg/mL BSA, 200 nM each primer, 0.1 mM dNTPs, and 0.05 U/μL Taq polymerase.

PCR began with activation of the polymerase at 94 °C for 2 min., followed by 45 cycles of a four part temperature profile. These included denaturization at 94 °C for 12 s, annealing at 50 °C for 17 s, extension at 72 °C for 17 s, and a final measurement stage at 50 °C for 5 s. A control was also performed, run for 45 cycles under identical conditions as above, with the exception that the temperature cycle profile for the control omitted the 5 s at 50 °C.

One microliter from each of the tubes representing various stages of the PCR process was analyzed via capillary electrophoresis. Details of capillary electrophoresis method can be found in (Khrapko, Hanekamp, Thilly, et. al, 1994).

# 4. 4th Step Test Protocol

*This protocol describes the steps used in an experiment to test the use of a 4th PCR step.*

This experiment was conducted in the Lightcycler under conditions intended to mimic that of the FA PCR instrument. Two thermal profiles were compared with several tubes of different starting copy numbers used in each thermal profile experiment.

## A. Without 4th Step

For the experiment without a 4th step, two starting template copy amounts were amplified at three different salt concentrations. The combination of these parameters (and replicates) are shown in the table below.

| Tube | M. Mix | Salt | DNA (ng/uL) |
|---|---|---|---|
| 1 | LC FastStart | 2 | 1 |
| 2 | LC FastStart | 3 | 1 |
| 3 | LC FastStart | 4 | 1 |
| 4 | LC FastStart | 4 | 1 |
| 5 | LC FastStart | 4 | 1 |
| 6 | LC FastStart | 2 | 0.1 |
| 7 | LC FastStart | 3 | 0.1 |
| 8 | LC FastStart | 4 | 0.1 |
| 9 | LC FastStart | 4 | 0.1 |
| 10 | LC FastStart | 4 | No Template |

As a first step, APC forward and reverse primers, and master mix (P/N 3003230, Lightcycler Fast Start DNA Master SYBR Green I, Roche) were combined in a single micro-centrifuge tube. Subsequently, the required total amounts for each salt concentration were aliquoted into three tubes. To these tubes, distilled water and $MgCl_2$ was then added. The Roche Master Mix when diluted to 1× concentration yielded a PCR solution at 1μM $MgCl_2$, 400 μM of each dNTP, and an undisclosed quantity of SYBR green intercalating dye (along with other supporting and undisclosed reagents). The final quantities in each of the three tubes (no template DNA has been added yet) is shown in the table below.

LC Fast Start 4 mM

| Component | Initial Conc | Final Conc | Volume (uL) | 6x |
|---|---|---|---|---|
| H20 | | | 9.6 | 57.6 |
| MgCl2 | | 4 mM | 2.4 | 14.4 |
| APC Fwd | 2 uM | 0.2 uM | 2 | 12 |
| APC Rev | 2 uM | 0.2 uM | 2 | 12 |
| LC faststart SYBR | 10X | 1X | 2 | 12 |
| Total | | | 18 | 108 |

LC Fast Start 3 mM

| Component | Initial Conc | Final Conc | Volume (uL) | 2x |
|---|---|---|---|---|
| H20 | | | 10.4 | 20.8 |
| MgCl2 | | 3 mM | 1.6 | 3.2 |
| APC Fwd | 2 uM | 0.2 uM | 2 | 4 |
| APC Rev | 2 uM | 0.2 uM | 2 | 4 |
| LC faststart SYBR | 10X | 1X | 2 | 4 |
| Total | | | 18 | 36 |

LC Fast Start 2 mM

| Component | Initial Conc | Final Conc | Volume (uL) | 2x |
|---|---|---|---|---|
| H20 | | | 11.2 | 22.4 |
| MgCl2 | | 2 mM | 0.8 | 1.6 |
| APC Fwd | 2 uM | 0.2 uM | 2 | 4 |
| APC Rev | 2 uM | 0.2 uM | 2 | 4 |
| LC faststart SYBR | 10X | 1X | 2 | 4 |
| Total | | | 18 | 36 |

These three tubes of different salt concentration were split into seven micro-centrifuge tubes to account for the seven combinations of salt and template quantity (including the no template control). Male genomic DNA (4312660, Taqman Control Genomic DNA (Human), Applied Biosystems), originally at 10 ng/uL concentration, was diluted with distilled water in two separate micro-centrifuge tubes to concentrations of 1 ng/uL and 0.1 ng/uL. Volumes from these dilutions were then transferred to the set of seven tubes to achieve the desired template quantity. Mixing was done by gentle pipetting.

Aliquots of 20 μL of PCR solution was taken from each of these seven microcentrifuge tubes to fill ten 100 μL glass capillaries as shown in the first table. The tubes were then sealed with caps and centrifuged to pull the PCR solution to the bottom of each tube. The tubes were removed from the centrifuge and placed in a special chilled tube holder. Caps

were removed and ~15 μL of mineral oil was dispensed into each tube. This volume is marked as approximate because the viscosity of the mineral oil dramatically reduced the repeatability of pipetting performance. Often a significant amount remained in the pipette after an attempt to dispense the full volume. With cap back in place, the PCR tubes were centrifuged a second time to eliminate any air between the PCR solution and mineral oil.

This is not the typical protocol for 100 μL glass tubes for the Lightcycler. Typical protocol would use either 20 μL of solution in 20 μL tubes or 100 μL of solution in their 100 μL tubes. The experimental design, placing only 20 μL of solution plus 15 μL of mineral oil was meant to make these results more comparable to those observed in the FA PCR instrument.

Roche's protocol specifies a 10 minute pre-incubation period at 95 °C to activate the hot-start Taq Enzyme. The amplification thermal profile is given below. Amplification was conducted over 55 cycles.

| | Temperature ( C ) | Hold Time (sec) | Ramp Rate (C/sec) | Measurement Type |
|---|---|---|---|---|
| Pre-Incubation | 95 | 180 | 20 | none |
| Amplification | | | | |
| Denature | 95 | 15 | 20 | none |
| Anneal | 49 | 45 | 20 | none |
| Extend | 72 | 20 | 20 | single |
| Melt | | | | |
| Denature | 95 | 0 | 20 | none |
| Anneal | 45 | 45 | 20 | none |
| Denature | 95 | 0 | 0.1 | continuous |
| Cool | 40 | 45 | 20 | none |

## A. With 4th Step

Because the results of the first experiment showed that 4 mM amplification provided the greatest efficiency, only 4 mM concentration was used in the second experiment, simplifying its protocol. Three replicates were run for starting copy quantities of 20 ng and 2 ng, and 2 replicates were run for starting copy quantities of 200 pg and 20 pg. One no-template control was also run.

The same approach of combined mixing was used for the second experiment. Since everything was done with the same salt concentration, the reagents (excluding DNA template) for what would eventually be 11 tubes could be mixed at once. Volumes and concentrations are given in the table below. The same reagents described above are used here.

| Component | Initial Conc | Final Conc | Volume (uL) | 11x |
|---|---|---|---|---|
| H20 | | | 9.6 | 105.6 |
| MgCl2 | | 4 mM | 2.4 | 26.4 |
| APC Fwd | 2 uM | 0.2 uM | 2 | 22 |
| APC Rev | 2 uM | 0.2 uM | 2 | 22 |
| LC faststart SYBR | 10X | 1X | 2 | 22 |
| Total | | | 18 | 198 |

After splitting this single tube of reagents into four tubes, appropriate quantities of DNA were added. Mixing was performed by gently pipetting the solution up and down. These solutions were then transferred to 11 separate glass tubes. Centrifugation and mineral oil were done as above.

All eleven tubes were run simultaneously in the Lightcycler under the following conditions:

| | Temperature ( C ) | Hold Time (sec) | Ramp Rate (C/sec) | Measurement Type |
|---|---|---|---|---|
| Pre-Incubation | 95 | 180 | 20 | none |
| Amplification | | | | |
| Denature | 95 | 15 | 20 | none |
| Anneal | 49 | 45 | 20 | none |
| Extend | 72 | 20 | 20 | single |
| "FA step" | 50 | 20 | 20 | none |
| Melt | | | | |
| Denature | 95 | 0 | 20 | none |
| Anneal | 45 | 45 | 20 | none |
| Denature | 95 | 0 | 0.1 | continuous |
| Cool | 40 | 45 | 20 | none |

# 5. $MgCl_2$ Optimization Protocol

*This protocol describes the steps used to optimize the $MgCl_2$ concentration.*

In this optimization experiment several parameters were varied including the salt concentration, the type of master mix, and the template DNA concentration. All experiments used 200 nM forward and reverse APC primer (pipetted from a stock solutions at 2 μM). $MgCl_2$ concentrations were varied by pipetting from a 25 mM stock solution. Two master mixes were used, both originally at 10× concentration. These included the Lightcycler Fast Start DNA Master SYBR Green I (P/N 3003230, Roche) and the Lightcycler Fast Start DNA Master Hybridization Probes (P/N 3003248, Roche). When diluted to 1× concentration, both master mixes contain hot-start Taq polymerase at 0.5 U/μL, 400 μM of each dNTP, and 1 mM $MgCl_2$. The SYBR master mix includes SYBR green intercalating dye at undisclosed concentration. Male genomic DNA (4312660, Taqman Control Genomic DNA (Human), Applied Biosystems) supplied at 10 ng/μL was diluted to create an additional separate stock solution at a concentrations of 1 ng/μL.

Six micro-centrifuge tubes were prepared. The water, primers, and $MgCl_2$ for the first four tubes were prepared as one (blue highlighted cells in table below) and then aliquotted in appropriate volumes to their four respective tubes. The final target reaction size was 20 μL. As such, tube #1 was intended to produce five replicate 20 μL reactions.

| | | Volume of Reagents (uL) | | | | | | | |
|---|---|---|---|---|---|---|---|---|---|
| Description | Tube # | Water | Fwd Primer | Rev Primer | MgCl2 | Hyb Master Mix | SYBR Master Mix | 10 ng/uL DNA | 1 ng/uL DNA |
| 4 mM $MgCl_2$ / Hyb / 20 ng | 1 | 48 | 10 | 10 | 12 | 10 | | 10 | |
| 4 mM $MgCl_2$ / SYBR / 20 ng | 2 | 9.6 | 2 | 2 | 2.4 | | 2 | 2 | |
| 4 mM $MgCl_2$ / Hyb / 2 ng | 3 | 9.6 | 2 | 2 | 2.4 | 2 | | | 2 |
| 4 mM $MgCl_2$ / SYBR / 2 ng | 4 | 9.6 | 2 | 2 | 2.4 | | 2 | | 2 |
| 3 mM $MgCl_2$ / Hyb / 20 ng | 5 | 9.6 | 2 | 2 | 1.6 | 2 | | 2 | |
| 2 mM $MgCl_2$ / Hyb / 20 ng | 6 | 9.6 | 2 | 2 | 0.8 | 2 | | 2 | |

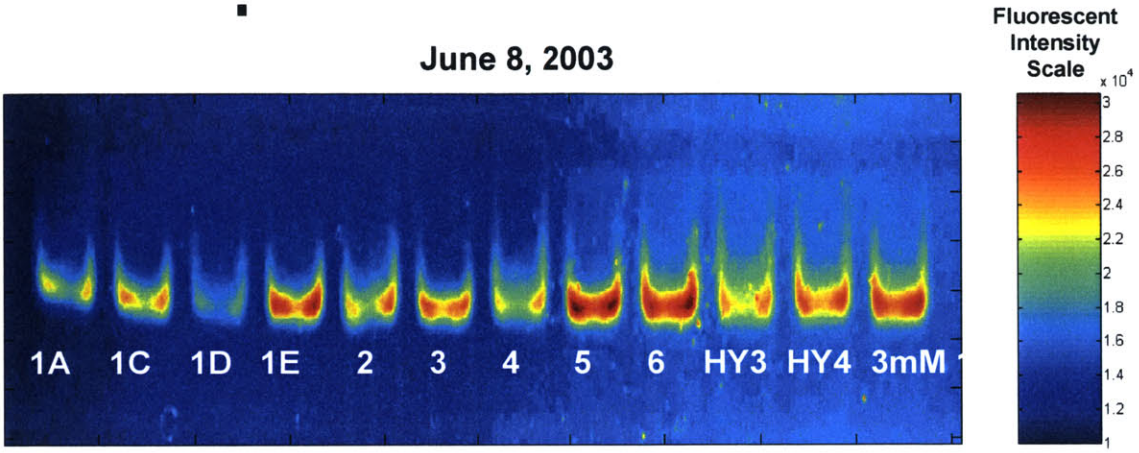
June 8, 2003
1A
1C
1D
1E
2
3
4
5
6
HY3
HY4
3mM
Fluorescent Intensity Scale
x 10^4
3
2.8
2.6
2.4
2.2
2
1.8
1.6
1.4
1.2
1

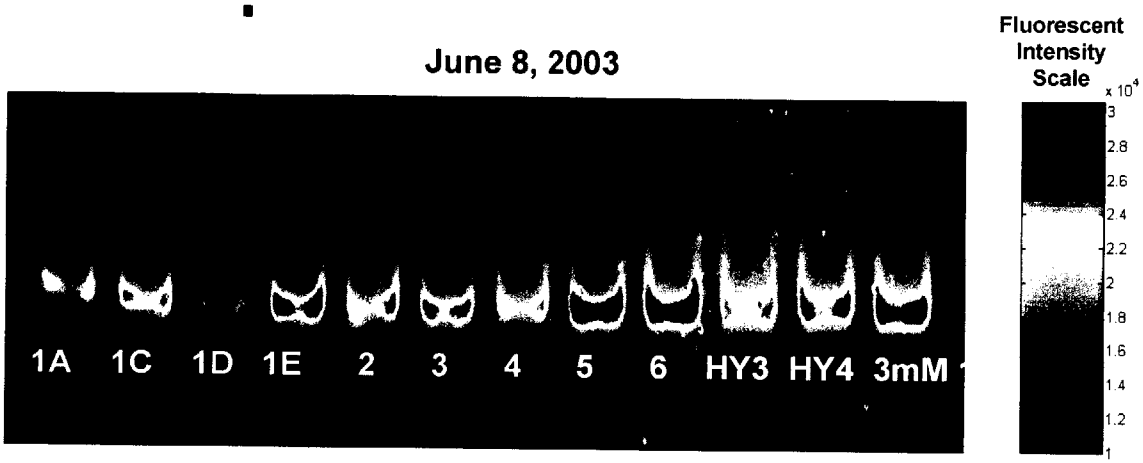
June 8, 2003
1A
1C
1D
1E
2
3
4
5
6
HY3
HY4
3mM
Fluorescent Intensity Scale
x 10^4
3
2.8
2.6
2.4
2.2
2
1.8
1.6
1.4
1.2
1

# 6. Dilution Series Protocol in FA Instrument

*This protocol describes the steps used to test the repeatability of amplification of genomic DNA in the final prototype.*

The first step was to mix the volumes of all PCR reagents except the template DNA required for 10 reactions. Premixing ensured that all samples contained equal concentrations of PCR reagents (except DNA). Ten reactions were prepared so that replicates would be available in the event of operator error. In at least one case, the PCR tube was broken while trying to insert it into the sample holder.

Distilled water, $MgCl_2$, APC forward and reverse primers, and master mix (3003248, Lightcycler Fast Start DNA Master Hybridization Probes, Roche) were combined in a single micro-centrifuge tube as shown in the table below. Note that this Master Mix is not the same as used in the previously described Lightcycler experiments. This master mix is intended for use with fluorogenic probes (probes are not present in the master mix) and therefore does not contain intercalating dye.

| Component | Initial Conc | Final Conc | Volume (uL) | 6x |
|---|---|---|---|---|
| H20 | | | 10.4 | 62.4 |
| MgCl2 | | 3 mM | 1.6 | 19.2 |
| APC Fwd | 2 μM | 0.2 μM | 2 | 12 |
| APC Rev | 2 μM | 0.μM | 2 | 12 |
| LC FastStart HYB | 10X | 1X | 2 | 12 |
| Total | | | 18 | 108 |

This mixed PCR solution was then aliquoted into two micro-centrifuge tubes (54 μL each).

Male genomic DNA (4312660, Taqman Control Genomic DNA (Human), Applied Biosystems) supplied at 10 ng/μL was diluted to two concentrations including 0.1 ng/μL and 0.01 ng/μL in distilled water. Each of these tubes provided the template for one of the micro-centrifuge tubes containing the PCR solution. 6 μL of template were added to each 54 μL of PCR solution.

After mixing by gentle pipetting, the contents of these five tubes were transferred to six glass PCR tubes as described in the table below (20 μL into each tube).

| Tube Number | Final Template Concentration in 20 uL (ng/uL) | whole genome copies |
|---|---|---|
| 1 | 0.1 | 667 |
| 2 | 0.1 | 667 |
| 3 | 0.1 | 667 |
| 4 | 0.01 | 67 |
| 5 | 0.01 | 67 |
| 6 | 0.01 | 67 |

The tubes were then covered with mineral oil and capped as described in earlier protocols. Only one reaction could be run at a time in the FA instrument. All tubes were stored at 4 °C until they were ready to be run. All runs occurred in succession on the same day.

Immediately before being loaded into the FA instrument, thermally conductive silicon paste (OT-201, www.omega.com) was applied to the PCR tube to improve thermal conductivity between the sample holder and the PCR tube. The glass tube was wiped clean on two opposing regions to allow a clear imaging path. The tube was carefully slid down into the sample holder, avoiding rotation, so that a thermal paste would not be smeared onto the imaged region. After insertion, the laser shutter was opened allowing the image of the laser to be checked behind the sample holder. If the tube had successfully been inserted with a clean window, a uniform intensity field was observed.

Thermal cycle profile:

| | | |
|---|---|---|
| Pre-incubation | 3 min @ 94 °C | |
| Amplification | 94 °C for 15s; | 55 cycles |
| | 49 °C for 45s; | |
| | 72 °C for 20s; | |

Not all tubes that were mixed were actually cycled since the long wait in 4 °C was believed to diminish the value of such data.

# 7. Dilution Series Protocol in Lightcycler

Template:
Male genomic DNA (4312660, Taqman Control Genomic DNA (Human), Applied Biosystems)

| | |
|---|---|
| 1 ng/uL (20,000 pg = 6667 copies) | TUBE 1 |
| 0.1 ng/uL (2,000 pg = 667 copies) | TUBE 2 |
| 0.01 ng/uL (200 pg = 67 copies) | TUBE 3 |
| 0.001 ng/uL (20 pg = 7 copies) | TUBE 4 |
| 0 ng/uL (no template control) | TUBE 5 |
| 1 ng/uL (20,000 pg = 6667 copies) | TUBE 6 |
| 0.1 ng/uL (2,000 pg = 667 copies) | TUBE 7 |
| 0.01 ng/uL (200 pg = 67 copies) | TUBE 8 |
| 0.001 ng/uL (20 pg = 7 copies) | TUBE 9 |
| 0 ng/uL (no template control) | TUBE 10 |

LC FastStart SYBRgreen Master Mix (P/N3003230) @ 3 mM MgCl2

I will perform the experiments in 100 uL capillaries, but I will use only 20 uL of DNA solution covered by 15 uL of mineral oil.

Thermal cycle profile:

| | |
|---|---|
| Preincubation | 3 min @95 C; 20 C/s; none |
| Amplification | 95 C for 15s; 20C/s; none. |
| | 49 C for 45s; 20C/s; none. |
| | 72 C for 24s; 20C/s; Single. |
| Melt | 95C for 0 sec; 20C/s; none. |
| | 45 C for 45 sec; 20C/s; none. |
| | 95C for 0 sec; 0.1 C/s; continuous |
| Cool | 40 C for 45 sec; 20C/s; none |

To improve repeatability of individual runs, I will mix up 11x of the PCR mix without DNA, then alliquot that into 0.5 mL tubes. I will add DNA template to these tubes. I will then alliquote these tubes into the capillaries. I will use Cathy's pippetters as well.

| Component | Initial Conc | Final Conc | Volume (uL) | 11x |
|---|---|---|---|---|
| H20 | | | 10.4 | 114.4 |
| MgCl2 | | 3 mM | 1.6 | 17.6 |
| APC Fwd | 2 uM | 0.2 uM | 2 | 22 |
| APC Rev | 2 uM | 0.2 uM | 2 | 22 |
| LC faststart SYBR | 10X | 1X | 2 | 22 |
| Total | | | 18 | 198 |

# 8. Repeatability for Genomic DNA in FA Instrument

*This protocol describes the steps used to set up a dilution series of starting template in the final prototype.*

The first step was to mix the volumes of all PCR reagents except the template DNA required for 10 reactions. Premixing ensured that all samples contained equal concentrations of PCR reagents (except DNA). Ten reactions were prepared so that replicates would be available in the event of operator error. In at least one case, the PCR tube was broken while trying to insert it into the sample holder.

Distilled water, $MgCl_2$, APC forward and reverse primers, and master (3003248, Lightcycler Fast Start DNA Master Hybridization Probes, Roche) were combined in a single micro-centrifuge tube as shown in the table below. Note that this Master Mix is not the same as used in the previously described Lightcycler experiments. This master mix is intended for use with fluorogenic probes (probes are not present in the master mix) and therefore does not contain intercalating dye.

| Component | Initial Conc | Final Conc | Volume (uL) | 10x |
|---|---|---|---|---|
| H20 | | | 10.4 | 104 |
| MgCl2 | | 3 mM | 1.6 | 16 |
| APC Fwd | 2 μM | 0.2 μM | 2 | 20 |
| APC Rev | 2 μM | 0.μM | 2 | 20 |
| LC FastStart HYB | 10X | 1X | 2 | 20 |
| Total | | | 18 | 180 |

This mixed PCR solution was then aliquotted into five micro-centrifuge tubes (36 μL each).

Male genomic DNA (4312660, Taqman Control Genomic DNA (Human), Applied Biosystems) supplied at 10 ng/μL was diluted to four concentrations including 1 ng/μL, 0.1 ng/μL, and 0.01 ng/μL in distilled water. Each of these tubes provided the template for one of the micro-centrifuge tubes containing the PCR solution. 4 μL of template were added to each 36 μL of PCR solution. The $5^{th}$ tube was a no-template control to which only distilled water was added.

After mixing by gentle pipetting, the contents of these five tubes were transferred to ten glass PCR tubes as described in the table below (20 μL into each tube).

| Tube Number | Final Template Concentration in 20 uL (ng/uL) | whole genome copies |
|---|---|---|
| 1 | 1 | 6667 |
| 2 | 0.1 | 667 |
| 3 | 0.01 | 67 |
| 4 | 0.001 | 7 |
| 5 | 0 | 0 |
| 6 | 1 | 6667 |
| 7 | 0.1 | 667 |
| 8 | 0.01 | 67 |
| 9 | 0.001 | 7 |
| 10 | 0 | 0 |

The tubes were then covered with mineral oil and capped as described in earlier protocols. Only one reaction could be run at a time in the FA instrument. All tubes were stored at 4 °C until they were ready to be run. All runs occurred in succession on the same day.

Immediately before being loaded into the FA instrument, thermally conductive silicon paste (OT-201, www.omega.com) was applied to the PCR tube to improve thermal conductivity between the sample holder and the PCR tube. The glass tube was wiped clean on two opposing regions to allow a clear imaging path. The tube was carefully slid down into the sample holder, avoiding rotation, so that a thermal paste would not be smeared onto the imaged region. After insertion, the laser shutter was opened allowing the image of the laser to be checked behind the sample holder. If the tube had successfully been inserted with a clean window, a uniform intensity field was observed.

Thermal cycle profile:

| | | |
|---|---|---|
| Pre-incubation | 3 min @ 94 °C | |
| Amplification | 94 °C for 15s; | 55 cycles |
| | 49 °C for 45s; | |
| | 72 °C for 20s; | |

Not all tubes that were mixed were actually cycled since the long wait in 4 °C was believed to diminish the value of such data.

# 9. Repeatability for Genomic DNA in Lightcycler

Templates:
Male genomic DNA (4312660, Taqman Control Genomic DNA (Human), Applied Biosystems)

| | |
|---|---|
| 1 ng/μL (20,000 pg = 6667 copies) | TUBE 1,2,3 |
| 0.1 ng/μL (2,000 pg = 667 copies) | TUBE 4,5,6,7 |
| 0.01 ng/μL (200 pg = 67 copies) | TUBE 8,9,10,11 |
| 0 ng/μL (no template control) | TUBE 12 |

LC FastStart SYBRgreen Master Mix (P/N3003230) @ 3 mM MgCl2

I will perform the experiments in 100 μL capillaries, but I will use only 20 μL of DNA solution covered by 15 μL of mineral oil.

Thermal cycle profile:

| | |
|---|---|
| Pre-incubation | 3 min @95 C; 20 C/s; none |
| Amplification | 95 C for 15s; 20C/s; none. |
| | 49 C for 45s; 20C/s; none. |
| | 72 C for 24s; 20C/s; Single. |
| Melt | 95C for 0 s ; 20C/s; none. |
| | 45 C for 45 s ; 20C/s; none. |
| | 95C for 0 s ; 0.1 C/s; continuous |
| Cool | 40 C for 45 s ; 20C/s; none |

To improve repeatability of individual runs, I will mix up 12x of the PCR mix without DNA, then aliquot that into 0.5 mL tubes. I will add DNA template to these tubes. I will then aliquot these tubes into the capillaries.

| Component | Initial Conc | Final Conc | Volume (uL) | 12x |
|---|---|---|---|---|
| H20 | | | 9.6 | 115.2 |
| MgCl2 | | 4 mM | 2.4 | 28.8 |
| APC Fwd | 2 μM | 0.2 μM | 2 | 24 |
| APC Rev | 2 μM | 0.2μM | 2 | 24 |
| LC FastStart SYBR | 10X | 1X | 2 | 24 |
| Total | | | 18 | 216 |

# 10. Target Sequence Enrichment

Cleaving with Taq$^{\alpha}$1 Enzyme

The first step in the enrichment process was to cleave the DNA using the Taq$^{\alpha}$1 restriction enzyme (R0149S, New England Biolabs). Initially, 1 μg of male genomic DNA (4312660, Taqman Control Genomic DNA (Human), Applied Biosystems) was diluted with 10× NEBuffer 3 (New England Biolabs) and water according to the table below.

| | Initial Conc | Final Conc | Volume (uL) |
|---|---|---|---|
| DNA | 10 ng/uL | 5 ng/uL | 100 |
| Buffer | 10X | 1X | 20 |
| Water | | | 80 |
| Total | | | 200 |

Next, the enzyme was diluted 40-fold in the same buffer.

| | Initial Conc | Final Conc | Volume (uL) |
|---|---|---|---|
| Buffer | 10X | 1X | 8 |
| Enzyme | 10 U/uL | 0.5 U/uL | 2 |
| Water | | | 70 |
| Total | | | 80 |

Finally, the diluted DNA and enzyme were combined with bovine serum albumin (BSA, 100 μg/mL = 100X, New England Biolabs), buffer, and water such that 3 Units of enzyme were present for every 1 μg of DNA.

| | Initial Conc | Final Conc | Volume (uL) |
|---|---|---|---|
| DNA | 5 ng/uL | | 100 |
| Buffer | 10X | 1X | 15 |
| Enzyme | 0.5 U/uL | | 3 |
| Water | | | 30.5 |
| BSA | 100X | 1X | 1.5 |
| Total | | | 150 |

This mixture was incubated for > 4hours at 65 °C.

Target Capture with Magnetic Beads

**This protocol was modified from that described by Heelo Sudo 2004.*

Enrichment of the desired target sequence from genomic DNA was previously demonstrated by Li-Sucholeiki and Thilly (2000). The protocol is based on probe-target hybridization coupled with a biotin-streptavidin capture system. The probes were designed as to minimize intra-probe hairpins and inter-probe duplex formations and to share similar melting temperatures so that they can be simultaneously used in the same hybridization reaction.

To begin, 0.6 mg of each streptavidin-coated paramagnetic beads per 60 μg of DNA were washed twice with 3x SSPE (0.56M NaCl, 30 mM sodium phosphate, pH 7.4, 3mM EDTA)at a concentration of 10 μg of beads per 50 μL of 3× SSPE. After resuspending with 3x SSPE, 1 pmole ($6x10^{11}$ copies) of biotin-labeled probes (BP) for both strands, BP1 (7GAACCTGGACCCTCTGAACTG)* and BP2 (7CATGCAGTGGAATGGTAAGTGG)*, were added to the magnetic beads per 1 μg of DNA ($3x10^5$ target copies). This mixture was incubated in a microthermomixer at room temperature for 30 minutes. The probe-bound beads were then washed three times with 3x SSPE at a concentration of 10 μg of beads per 50 μL of solution. Meanwhile, digested genomic DNA in a 1.6 mL ependorf tube was denatured by boiling water bath for 2 min and immediately chilled in an ethanol-water ice bath for 10 min. Magnetic, probe-bound beads where then added to single-stranded DNA samples. 20x SSPE was added to each sample to a final concentration of 6x SSPE and hybridized in a microthermomixer at 50 °C for 2 hr, rotating at the maximum speed. After incubation, the target-bead hybrids were washed with 6x SSPE at a concentration of 10 μg beads per 50 μL of 6x SSPE at 50 °C for 5 min, then with 6x, 3x, and 1x SSPE at the same concentration at room temperature. Beads were washed for a final time in ice-chilled 1/3x SSPE and resuspended with 20 μL of ddH20. The target DNA sequence was eluted from the probe-bound beads twice at 72C for 2 min using a magnet to retain the beads.

---

* In the given primer sequence, the number 7 indicates the position of the biotin label.

Enrichment recovery was poor but adequate. The preparation initially began with 1 μg of DNA ($3x10^5$ target copies). According to a real-time PCR analysis conducted in the Lightcycler, only 1 in 100 target copies was successfully captured.

# 11. An Alternate Method of Calculating the Crossing Point

An example set of real-time PCR data with FA measurement is shown in Figure 6-1. Computation of the crossing point for this curve had three steps.

1. A threshold ($FA_T$) was defined at a level just above the FA exhibited by the primer molecules ($FA_{primer}$).
2. A model was fitted to the exponential portion of curve (more details below).
3. The intersection of the model and the threshold was computed.

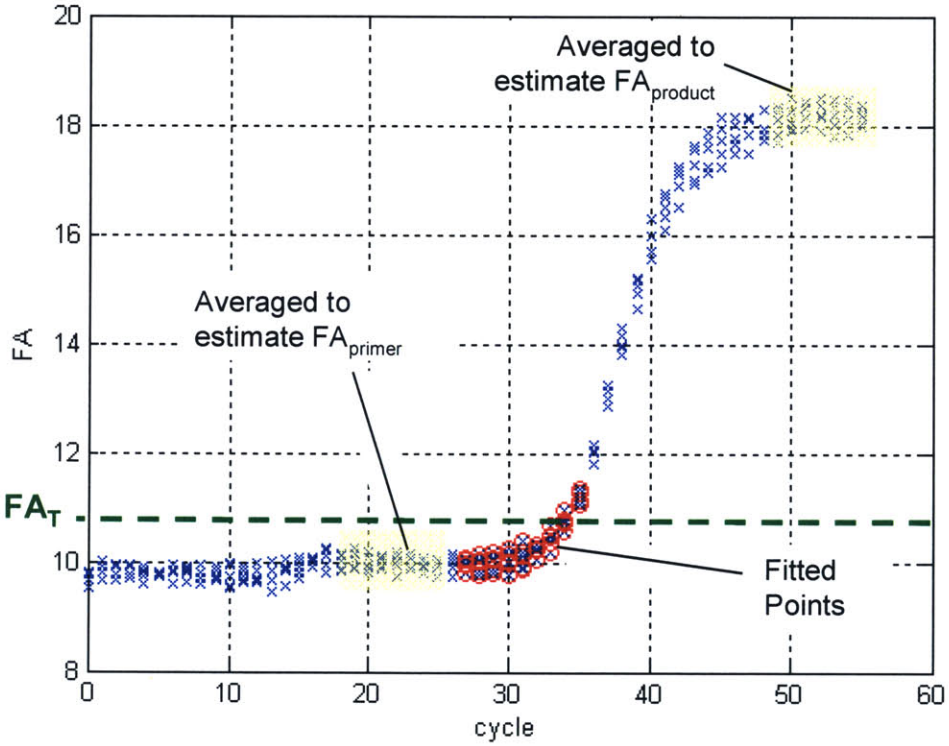


**Figure 6-1. Example of raw amplification data highlighting regions and features used in the computation of the crossing point. Data is from 20 pg amplification shown in Figure 5-6.**

Fitting a model across the cycles of exponential growth provides a means of reducing the measurement noise and utilizing all five data points taken at each cycle. The model also allowed more accurate calculation of the crossing point between the discretized

measurements of each cycle. Some method of interpolation is required to provide enough resolution for accurate quantification.

The model used to fit the data is given by

$$FA_{measured} = FA_{primer} + (FA_{product} - FA_{primer}) \cdot \frac{N_o}{P_o} \cdot (1+p)^{cycle}. \qquad \textbf{6-1}$$

$FA_{primer}$ and $FA_{product}$ are inputs to the model calculated by averaging data points in the early and late stage portions of the measurement, respectively (shown highlighted in yellow in Figure 6-1). The model, therefore, had two unknown parameters including the amplification efficiency (p) and the original ratio of template to primer ($N_o/P_o$). These unknowns were solved by non-linear least-squares fitting of Equation 2-5 to $FA_{measured}$ versus cycle data windowed to include only those data points from exponential growth of the signal immediately after it has risen above background. This data region is marked by red circles in Figure 6-1. All fitting was done in Matlab v6.5. A zoomed-view of the data from Figure 6-1 and the resulting data fit is shown in Figure 6-2.

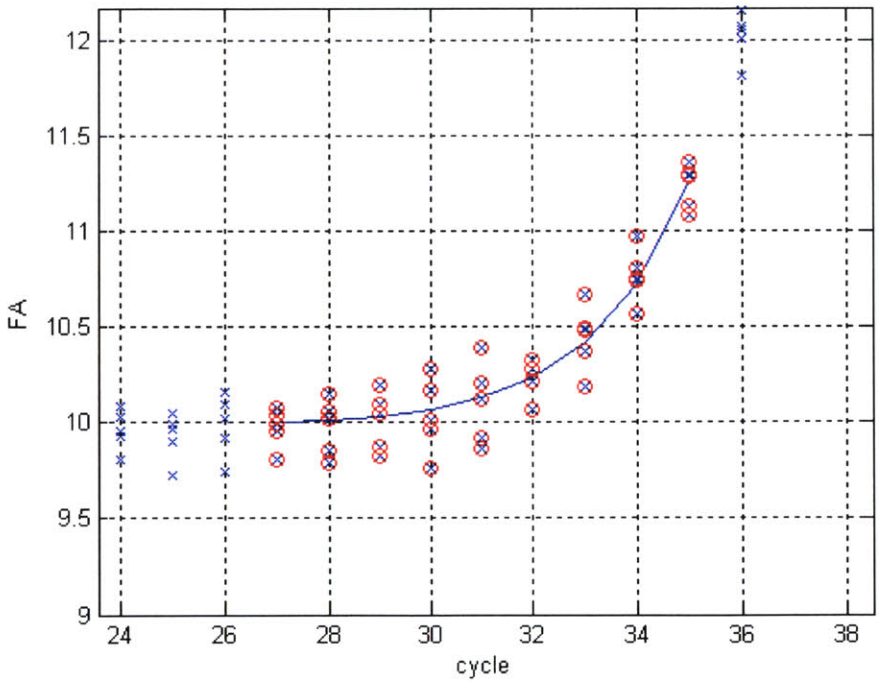


**Figure 6-2. Zoomed view of data from Figure 6-1. Best-fit result is shown by blue line.**

# 12. Matlab Code for Simulating Stochastic Processes of PCR

```
clear;

%Let us perform t trials of this PCR experiment.
t =1000;

%In each trial of the experiment, the PCR efficiency will be eff
%and the reaction will include n_max cycles.  Each trial will begin
%with an expect number of starting copies E_S0.
eff = 0.9;
n_max = 8;
E_S0 = 1;

%-----------------------------------
%Pipetting Error will cause a Poisson
%distribution of the number of starting
%copies (S0) in each of the t trials.

%a normal distribution is used to approximate the
%desired Poisson distribution. A set of numbers (S0)
%is generated by summing 1000 outputs
%from the random number generating function.
%This function generates uniformly distributed numbers.
%A set of numbers that are themselves the sum of many
%numbers of non-specified distribution will take a normal
%distribution according to the central limit theorem.

for k = 1:t
    y = rand(1000,1);
    Pd(k) = (sum(y))-500;
end;

Desired_std = sqrt(E_S0);

%after generating the numbers, the variance is adjusted
%to that expected for the Poisson distribution and the mean
%refined to zero.

S0 = Pd - mean(Pd);
S0 = Desired_std*S0/std(Pd);
S0 = S0 + E_S0;

S0 = round(S0);

%for low copy numbers, it is necessary to throw out any
%random number that is less than zero since this is not
%physically possible.
for k=1:t
    if S0(k) < 0
        S0(k)=0;
    end;
```

```
end;
%-------------------------------------


% Plot Probability Density Function *****
%define bins
inc = 1;
i = 0:inc:max(S0)+inc;

y=S0;

%what bin is y(j) in?
for j = 1:length(y)
    k=1;
    while y(j) > i(k)
        k=k+1;
    end;
    y_bin(j) = k;
end;

%how many are in each bin?
total_bin(1:length(i))=0;

for j = 1:length(y)
    for k = 1:length(i)
        if y_bin(j) == k
            total_bin(k) = total_bin(k)+1;
        end;
    end;
end;

%find probability of being in each bin
    prob_bin = 100*total_bin / sum(total_bin);

figure
plot(i,prob_bin)
xlabel('Starting Copy Number after Pipetting')
ylabel('Probability (%)')
axis([0 max(i) 0 max(prob_bin)])
title('Normal Probability Density Function')
grid on
%^^^^^^^^^^^^^^^^^^^^^^^^^^^^^^^^^^^^^^^^^^^^^^^^^^^^^^^^^^^^^^^^^^^^^^^^^^^^


%Now that we have estabilished the number of starting copies that
%are actually present at the beginning of each of t trials, we can
%begin the amplification process.  The first cycle (n=1) is done
%seperately.  The remaining n cycles are done in a loop.

%Each molecule present in each of the t trials will be duplicated
%with probablility, eff.  To do this, the random number function
%is again employed.

%-----------------------------------------------
n = 1
```

```
    for k = 1:t

        if S0(k)==0
            amp=0;
        end;

        for m = 1:S0(k)
            amp(m) = 1;
            if rand(1) <= eff
                amp(m) = 2;
            end;
        end;

        S(n,k) = sum(amp);
        clear amp
    end;
%---------------------------------------------


%---------------------------------------------
for n = 2:n_max
    n
    n_max
    for k = 1:t
        clear m
        clear amp

        if S0(k)==0
            amp=0;
        end;

        for m = 1:S(n-1,k)
            amp(m) = 1;
            if rand(1) <= eff
                amp(m) = 2;
            end;
        end;

        S(n,k) = sum(amp);
    end;
end;
%---------------------------------------------

%compute distribution of simultion results
Var_N = var(S(n_max,:))
Mean_N = mean(S(n_max,:))
const = (1+eff)^n_max;
Var_No = Var_N / const^2
Mean_No = Mean_N / const
CV_No_percent = sqrt(Var_No)/Mean_No*100
Var_Pec = (1-eff)/(1+eff)*E_S0


%----------------------------------
%Crossing Point Calculations

    %Some artificial definition of instrument detection
```

```
    %must be defined.  Results are not sensitive to this definition.
    %assume that 1000 copies amplified at 90% efficient should be
    %detectable by the 24th cycle.
    Ncp = 1000*(1+0.9)^24;
    E_cp = (log10(Ncp) - log10(E_S0)) / log10(1+eff)

    %compute crossing point for all simulations
    %assume that efficiency is same for all samples.
    for k=1:t
        if S(n_max,k)~=0
            N_est = S(n_max,k)/const;
            cp(k) = (log10(Ncp) - log10(N_est)) / log10(1+eff);
        else
            cp(k) = 50;
        end;
    end

    Mean_cp = mean(cp)
    Std_cp = std(cp)
    CV_cp_percent = std(cp)/mean(cp)*100
%---------------------------------------

%Plot Results
figure
for i=1:t
    plot(1:n_max,S(:,i),'r-')
    hold on
end;
grid on
xlabel('cycle')
ylabel('copies')
title_string = strcat('E_S0 =', num2str(E_S0), 'eff =',
num2str(eff));
title(title_string);
```

# 13. Matlab Code for Modeling Sample Holder Heat Transfer

```
clear;
%The intent of this program is to best fit a dynamic response measurement
%from my experimental set up with a parametized model that is built in
%Simulink.  I will do it by searching all possible combinations of the
%range of reasonable values for the model parameters.  The sum of squared
%errors between the actual data and the real model will be compared.


%Plotting the collected Data*****************************************

    dtpt = 150;

    data1 = load('Sept5_0.25Astep_bkside49.5C.txt');
    time_d(:,1) = data1(1:dtpt,1)-data1(1,1);
    temp_d(:,1) = data1(1:dtpt,2)+273;  %K

    data2 = load('Sept5_0.5Astep_bkside49pt5.txt');
    time_d(:,2) = data2(2:dtpt+1,1,1)-data2(2,1);
    temp_d(:,2) = data2(2:dtpt+1,2)+273;  %K

    data3 = load('Sept5_0.7Astep.txt');
    time_d(:,3) = data3(2:dtpt+1,1)-data3(2,1);
    temp_d(:,3) = data3(2:dtpt+1,2)+273;  %K

%
%     figure
%     plot(time_d(:,1), temp_d(:,1),'g');
%     hold on
%     plot(time_d(:,2), temp_d(:,2),'r');
%     plot(time_d(:,3), temp_d(:,3),'b');
%     grid on
%     hold off
%     xlabel('time (s )')
%     ylabel('Temperature (K)')
%     legend('0.25A', '0.5A', '0.75A')
%^^^^^^^^^^^^^^^^^^^^^^^^^^^^^^^^^^^^^^^^^^^^^^^^^^^^^^^^^^^^^^^^^^^^^^^^^^^^

timespan = [0 75];

iSS = 0.25/2; %A
Tc = 50.6+273; %K
Rs = 11.25;
Rsi = 2.85;
Rrtd = 45;
RaL = 0.11;
Csi = 0.21;
CaL = 0.146 ;
Crtd = 0.018;
itoQ = 4.796;
Re = 0; %3.157;

%Experiment Conditions **********************************************

    %Experimental data showed that for 0.25A of current, Tss = 60.36C
    iSSL(1) = 0.25/2; %A
    TssL(1) = 60.36+273; %K
    TcL(1) = 50.6+273; %K  %Initial temperature of system (temperature of cold
                           %side of Peltier)
```

```
%Experimental data showed that for 0.5A input, Tss = 346K
iSSL(2) = 0.5/2; %A
TssL(2) = 346; %K
TcL(2) = 322.65;  %K

%Experimental data showed that for 0.75A input, Tss = 357.82K
iSSL(3) = 0.75/2;
TssL(3) = 357.82; %K
TcL(3) = 323.2; %K

%Timespan for Simulink simulation
timespan = [0 75];

for dataset = 1:3
    iSS = iSSL(dataset);
    Tss = TssL(dataset);
    Tc = TcL(dataset);
    time_data=time_d(:, dataset);
    temp_data = temp_d(:,dataset);

    Rb = -2*(Re*iSS^2*(RaL+Rs) + Tc - Tss)/(Re*iSS^2 + 2*itoQ*iSS);

   %State Space Matrices Describing system*********************************

A = [ -1/(Crtd*Rrtd)      1/(Crtd*Rrtd)                    0                                0;
      1/(Csi*Rrtd)      -1/(Csi*Rsi) - 1/(Csi*Rrtd)        1/(Csi*Rsi)                      0;
      0                  1/(CaL*Rsi)     -(2*RaL + Rb + Rsi)/(CaL*Rsi*(2*RaL + Rb))   1/(CaL*(2*RaL + Rb));
      0                       0                 1/(CaL*(2*RaL+Rb))     -(1/(CaL*(2*RaL+Rb)) + 1/(CaL*Rs))];

B = [          0                      0                      0;
               0                      0                      0;
      Rb/(CaL*(2*RaL+Rb))         1/(2*CaL)                  0;
      -Rb/(CaL*(2*RaL+Rb))        1/(2*CaL)              1/(CaL*Rs)];

   C = [   1   0   0   0
           0   1   0   0
           0   0   1   0
           0   0   0   1 ];

   D = [   0   0   0
           0   0   0
           0   0   0
           0   0   0 ]   ;

   %^^^^^^^^^^^^^^^^^^^^^^^^^^^^^^^^^^^^^^^^^^^^^^^^^^^^^^^^^^^^^^^^^^^^^^^^^^^^

         %Run simulink Program.
         sim('sim_model_dec17',timespan);


         %for the purposes of the test version, I'll plot the outputs.
         plot(time,Temps,'b');
         hold on
         plot(time_data, temp_data,'g');
%        plot(time, TaL1,'r');
%        plot(time, TaL2,'m');
         legend('Tsi', 'data')  %, 'TaL1', 'TaL2')
   grid on
   xlabel('time (s )')
   ylabel('Temperature (K)')
   legend('model', 'data')  %, 'TaL1', 'TaL2')
end;
```

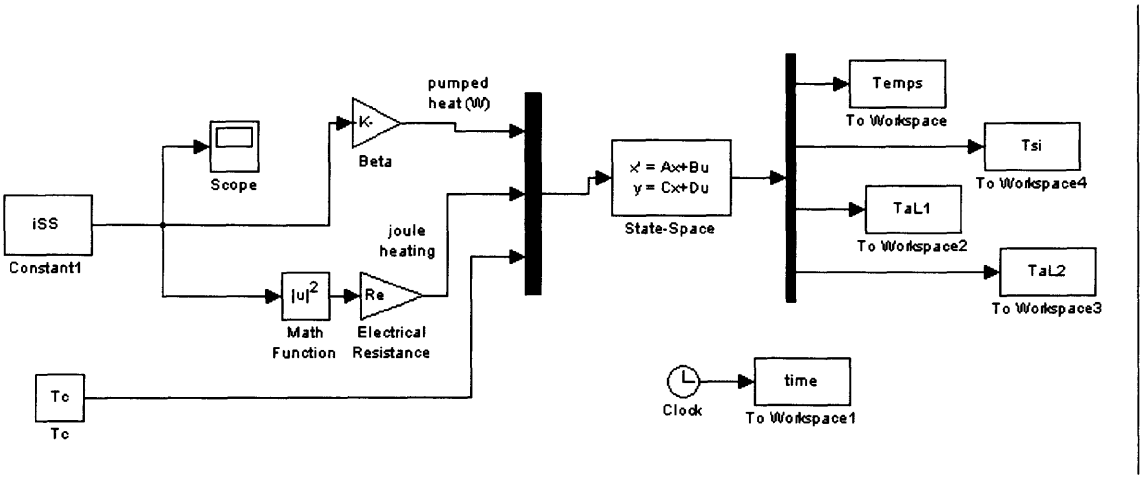


**Simulink Model: sim_model_dec17.mdl**